Fast 3D forward modeling of single scattered elastic wave fields for borehole configurations

Zur Erlangung des akademischen Grades eines

DOKTORS DER NATURWISSENSCHAFTEN

der Fakultät für Physik des
Karlsruher Instituts für Technologie (KIT)

genehmigte

DISSERTATION

von

Dipl.-Geophys. Ines Veile
aus Leimen

Tag der mündlichen Prüfung:	20. Dezember 2013
Referent:	Prof. Dr. Thomas Bohlen
Korreferent:	PD Dr. Joachim Ritter

Contents

Chapter 1

Introduction

The reliable detection and exploration of hydrocarbon reservoirs (e.g., gas or oil) represents an important field of application in geophysics. Usually, seismic reflection imaging methods (such as surface seismics and vertical seismic profiling (VSP)) are used to locate these reservoirs. Although these methods provide a great depth of penetration (i.e., 100 m - 10 km) the resolution they provide is very limited (i.e., 10 - 100 m) because various attenuation effects (such as intrinsic and scattering attenuation) lead to an energy loss of seismic waves that are used to illuminate the earth's interior. As a result, the mentioned methods provide a suitable compromise between depth of penetration and resolution to obtain large-scale structural images of the subsurface and thereby they are well suited to delineate potential reservoirs. However, seismic methods are not suited to resolve sub seismic wavelength reservoir features (e.g., certain fractures, faults). In addition, imaging below salt domes that often serve as reservoir (hydrocarbon) seals, is known to be problematic for surface seismic methods. This is mainly due to the high reflectivity of the salt and due to complex structures within the salt dome leading to strong seismic wave attenuation and to very complex wave fields (Ravaut et al., 2008). However, the reliable and efficient detection of these reservoir features does not only affect the costs for exploration projects but it also plays an important role for safety and sustainability for people and the environment, respectively. Hence, once a reservoir is detected, complementary sounding methods are required that image crucial reservoir features which are not visible to seismic methods. Figure 1.1 visualizes the current situation of available acoustic sounding methods. Obviously, there is a clear depth of penetration/resolution gap between surface seismic/VSP measurements in the top right corner of the plot and the ultrasonic/acoustic measurements in the bottom left corner of the plot. Hence, new methods have to be developed that fill this gap.

Ideally suited for this purpose is the further development of 'While Drilling' (WD) and 'WireLine' (WL) measurements that can be classified as conventional acoustic logging methods. Their original aim was the investigation of the direct surrounding of boreholes, e.g., the measurement of the compressional and shear-wave velocity parallel to the borehole and gamma ray logging. Their potential to investigate reflections coming from formations up to 30 m away from the borehole remained unrecognized for a long time. Figure 1.2 displays a schematic view of a WD tool (left) and a WL tool (right), both consisting of a source section, an isolater section and a receiver section. The isolator section is typically 2.5 - 4 m long (tool-dependent) and separates the source from the receiver array. This separation is necessary in order to gain the desired depth

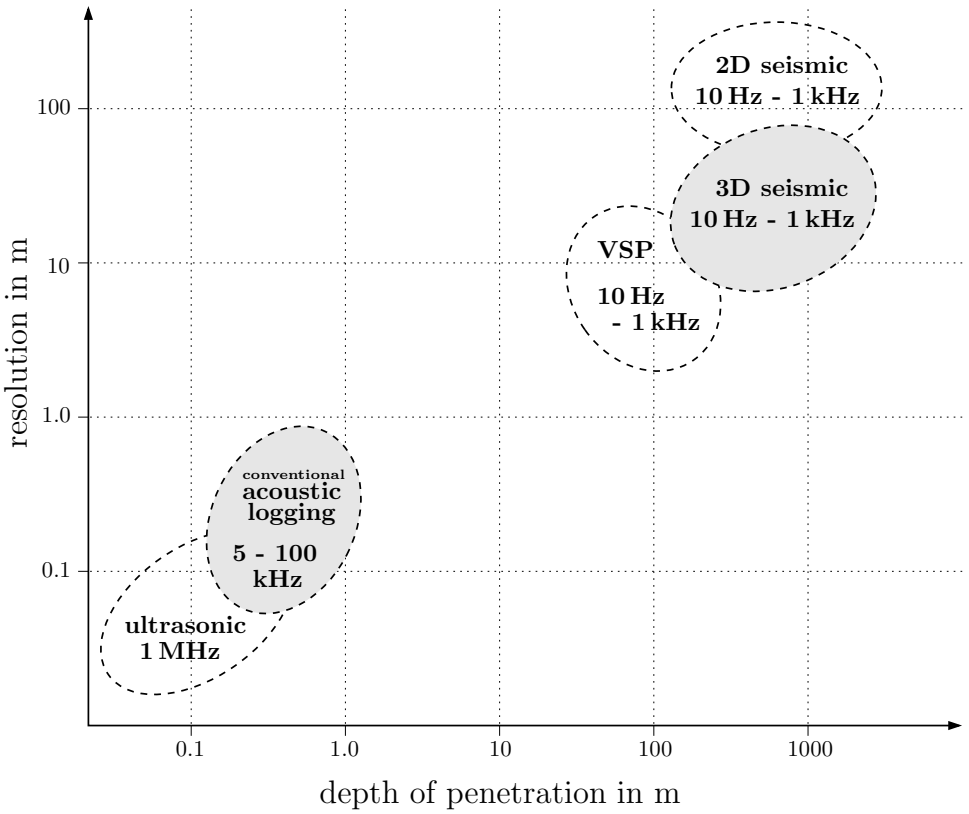

Figure 1.1: Depth of penetration versus resolution for available geophysical prospecting methods: there is a clear depth of penetration/resolution gap between surface seismic/VSP measurements (top right corner) and the ultrasonic/acoustic measurements (bottom left corner).

of penetration and to attenuate borehole guided wave modes (e.g., Stoneley or flexural waves).

In order to illustrate a potential application, Figure 1.3 visualizes a typical borehole setup. The borehole with an integrated drilling tool including a source and receiver array dives underneath a stratigraphic boundary and aims to detect structural changes on decimeter-scale that are present in the surrounding of the borehole. While the tool is moving, the source emanates signals that propagate through the background medium and are reflected by the stratigraphic boundaries. The integrated receivers record then the reflected waves. Based on the discussed small array apertures that these tools provide, obviously the illumination of the image point results mainly from the spatial progress of the moving tool. Therefore, building a velocity model of the subsurface to gain a structural image (as it is the case in seismics) is not possible. Because of high drilling noise levels in combination with a very limited number of receivers, high signal-to-noise levels are required in a typical Logging While Drilling (LWD) measurement in order to make imaging possible at all.

During the last three decades acoustic WireLine logging tools (cf. Figure 1.2, right) have been further developed to go beyond their usual measurements (e.g., Tang and Cheng, 2004). For this, the order of used multipole sources and the source frequency content have been lowered which has resulted in 'low' frequency (i.e., $f = 0.5 - 5\,\text{kHz}$) monopole and dipole sources that are currently employed. Apart from borehole guided modes, these sources also excite (low frequency) P- and S-(body)waves (with wavelengths between 0.2 m and 2 m) that propagate away from the well-bore and which potentially reflect from geological boundaries (due to impedance contrasts). It was not until the mid-eighties that geophysicists noticed the presence of these formation reflections in the later part of WL borehole acoustic wave trains and started to develop wave separation and migration techniques to image structural features in the direct vicinity ($\leq$10 m) of the well-bore (e.g., Hornby, 1989). Over the last two decades, with the development of cross-dipole WireLine logging, signal-to-noise levels have improved significantly and thereby the overall image quality and the depth of penetration ($\leq 30\,\text{m}$) (e.g., Tang, 2004; Tang et al., 2007, 2008; Tang and Patterson, 2009).

Although the above mentioned depth of penetration/resolution gap is (at least partly) filled with modern WireLine measurements, these measurements only become available after a well has been drilled. This is partly due to the fact that there is unfortunately, no efficient data modeling and processing scheme available that is able to keep up with the drilling progress. Therefore, so far most of the mentioned investigations are not carried out during the on-going drilling process. Hence, the drilling process either has to be interrupted until a specific analysis has been performed, or the analysis of the data has to be run post acquisition. In the latter case, the on-going drilling process cannot benefit from live updates. Unfortunately, both cases come along with numerous disadvantages. Firstly, the survey time increases and therefore the costs. Secondly, the technical expertise and scientific finding obtained throughout the initial part of a survey cannot be applied to the subsequent part of a survey which might affect the safety and successful outcome. It is clear that for the efficient and effective as well as save completion of a well (i.e., making it ready for production after it has been drilled), it would be extremely helpful if certain information was available already during the drilling process, i.e., if one could investigate the volume away from the well-bore while drilling. With current Bottom Hole Assembly steering technologies one could then pro-actively steer the well in the preferred direction and thereby optimize a subsequent completion. As typical drilling rig costs average about 500,000 USD per day this

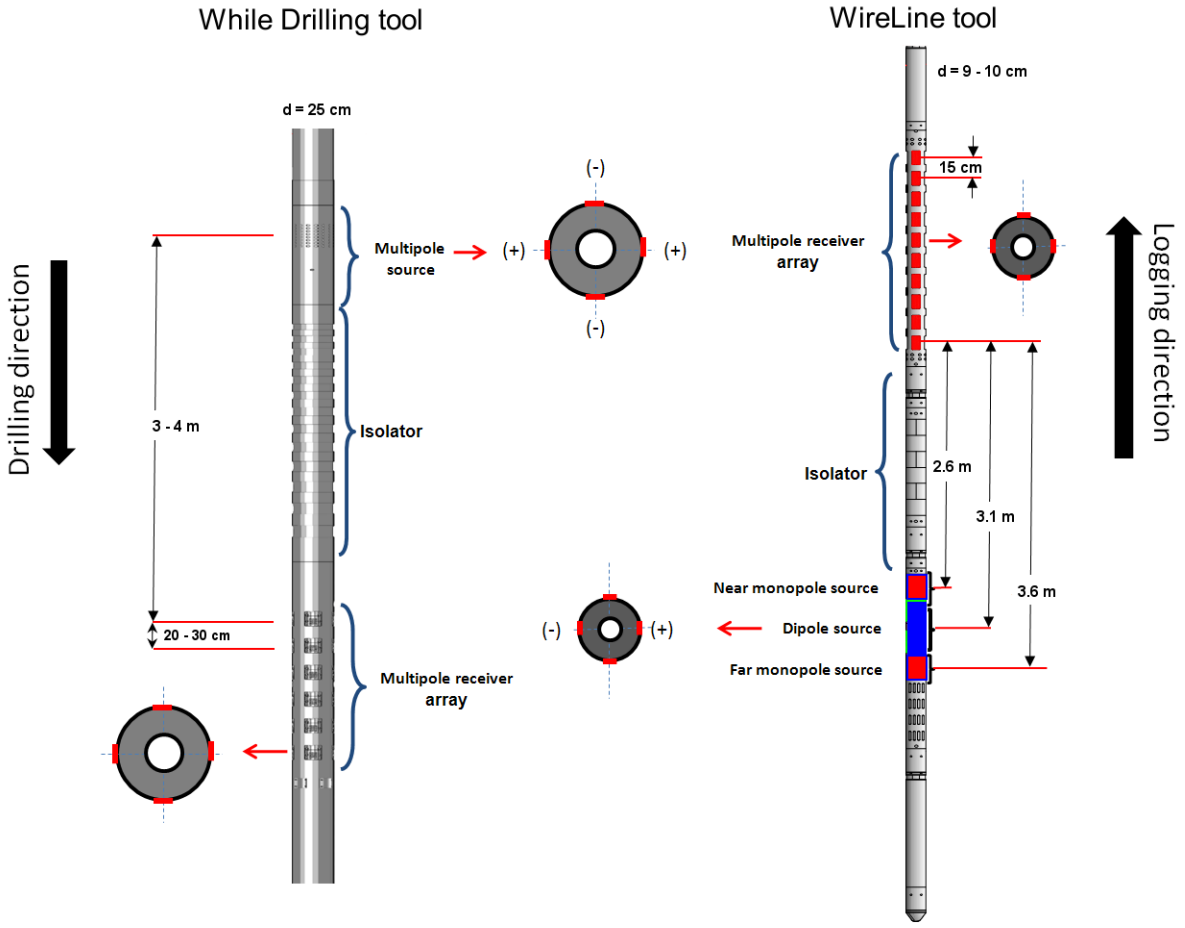

Figure 1.2: Sketch of a 'While Drilling' (WD) and a 'WireLine' (WL) tool. The figures were provided by Baker Hughes Inc. and slightly modified. The tools consist of a source section, an isolater section and a receiver section. The multipole source of the WD tool is a segmented piezoelectric source consisting of four segments that azimuthally offset by 90°. Polarity-wise these segments can be excited in ways that three different excitation types result: a monopole, dipole or quadrupole excitation. The source of the WL tool consists of three units: one piezoelectric ring source exciting a monopole and two dipole sources. The isolator section separates the source from the receiver array in order to gain the desired depth of penetration and to attenuate borehole guided wave modes. The receiver array typically consists of six (WD) or eight (WL) multipole receivers, each consisting of four piezoelectric sensors that azimuthally offset by 90°. The receivers typically offset by 20 - 30 cm (WD) or 15 cm (WL) from each other and their output is stacked in order to improve the signal-to-noise ratio of the recorded data. In WD measurements the drilling direction is from source to receiver. As the drilling noise propagates from the drill bit to the receiver array, drill bit induced borehole modes have an opposite array moveout than the source induced borehole modes. In this way, a clear separation of the occurring modes is possible. Accordingly, in WL measurements the logging direction is from source to receiver while the surface noise propagates from the surface to the receiver array. Hence, surface noise induced borehole modes have an opposite array moveout than source induced borehole modes. This is very advantageous for applications where, e.g., the slowness of source induced borehole modes is determined, such as Slowness Time Coherency (STC).

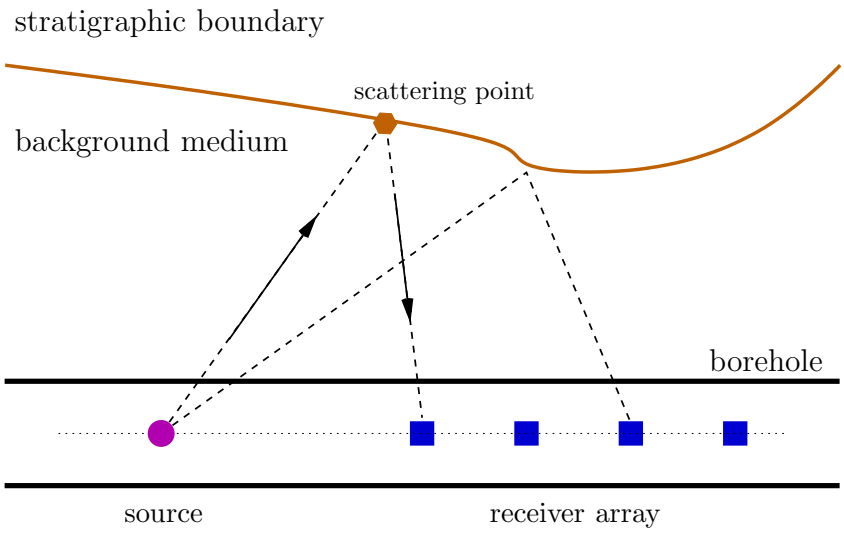

Figure 1.3: Schematic view of a typical borehole simulation setup: the borehole with an integrated drilling tool including a source and a receiver array dives underneath a stratigraphic boundary. The source excites a signal that is scattered by the stratigraphic boundary in the vicinity of the borehole and recorded by the receiver array. This is a modified sketch Veile et al. (2012).

possibility would significantly reduce costs in terms of lost time and completion efficiency. In transferring this WireLine technology to the WD environment, acoustic Logging While Drilling tools were developed (cf. Figure 1.2, left). As a part of this effort it is important to have fast and efficient 3D forward modeling techniques available that are able to accurately simulate the WD acoustic reflection measurement. In addition to the mentioned real-time application during the drilling process, such a modeling technique would be of great help for designing corresponding tools and for the development of processing algorithms, such as wave separation and migration under different circumstances (i.e., varying signal-to-noise ratio, different source excitations). As a consequence, in borehole geophysics there is an ever increasing demand for fast and accurate 3D forward modeling techniques that are able to efficiently model wave field variations due to structural changes around the borehole. In this thesis some key aspects of the afore mentioned modeling technique are addressed.

In general, there are plenty of seismic modeling techniques available. However, each technique has its own characteristics and is therefore suited sometimes better and sometimes worse for certain applications. Carcione et al. (2002) give an overview of the available methods and classify them into three main groups:
Direct methods rely on a spatial discretization of the geological model. If this discretization is sufficiently dense, these methods are very accurate as they implicitly deliver the full wave field. In addition, they are not restricted in terms of material variability. However, the computational effort may increase significantly due to the dense model discretization.
Ray-tracing methods are widely used in seismic modeling as they are extremely efficient. This efficiency is due to the fact that these methods are high-frequency approximations and do not model the complete wave field. However, especially for large 3D models and/or the identification of specific events on seismic records these methods are well suited.

Integral-equation methods model the wave field excited by point sources and go back to Huygens' principle (Huygens, 1996). Technically speaking, his work reveals that the total wave field can be described as a superposition of individual point source wave fields. In some cases these wave fields result from volume point sources and in some cases from point sources located on a boundary. Although these methods are restrictive in some aspects, they represent a good compromise between efficiency and accuracy and are particularly suited for bounded objects in a homogeneous medium and borehole applications.

Based on these observations, the so-called Born approximation, being an integral-equation method, has consistently been subject of research in the context of forward modeling techniques. However, most of the existing publications on this topic are either based on 2D (plane) wave propagation and investigate scattering caused by spherical inclusions (e.g., Gubernatis et al., 1977; Korneev and Johnson, 1993b,a) or on 3D (spherical) wave propagation caused by omnidirectional sources, investigating again the scattered wave field caused by spherical inclusions (e.g., Gritto et al., 1995; Eaton, 1999). Furthermore, there are numerous papers discussing the various limitations of this approximation (e.g., Hudson and Heritage, 1981; De Hoop, 1991; Murch, 1992; Panning et al., 2009). But there are only very few publications explicitly investigating the potential of the Born approximation to deliver a suitable solution for a fast and efficient forward modeling technique (Moradi Tehrani and Slob, 2009). Especially with respect to the forward modeling of the 3D scattered wave field occurring in a homogeneous and isotropic layered elastic medium, there is hardly any publication. The scientific findings of Tang (2004) and Tang et al. (2007) however prove that this question is of particular interest for borehole applications as investigations show that in borehole acoustics mainly primary reflections occur and multiply scattered wave modes are only rarely observed. Thus, the first-order Born approximation could in principle fit the borehole acoustic modeling needs.

Although the theory that describes the propagation and attenuation of multipole borehole modes (i.e., head and guided waves) is well established (e.g., Tsang and Radar, 1979; Kurkjian, 1985; Kurkjian and Chang, 1986; Schmitt, 1988, 1993; Geerits et al., 2010) there is no useful theory available that describes the joint occurrence of borehole guided waves and formation scattered waves in a fluid-filled borehole (cf. section 1.3 for the used definition of the word scatterer in this thesis). As a consequence, in this thesis the first-order elastodynamic Born scattering theory (De Hoop, 1995) is revisited in order to develop a suitable modeling algorithm for the single scattered wave field in borehole configurations. Of course, such a modeling technique has to fulfill several requirements. Apart from the fact that the algorithm should include the incident and the scattered 3D elastic wave field in terms of all single scattered and converted wave types (i.e., PP, PSV, SVP, SVSV, SHSH) the algorithm should also include the fluid-filled borehole with an integrated tool and simulate the tool movement. Furthermore, there should be the possibility to superpose drilling noise to the modeled synthetic wave field and the algorithm should be, of course, computationally inexpensive to allow for real-time applications. However, to more easily assess the validity of the Born approximation in this context, the fluid-filled borehole is initially excluded with the motivation that one or two wavelengths away from the borehole, radiating borehole mode amplitudes (e.g., Stoneley waves, formation dipole waves) are small compared to body wave amplitudes (P-, SV-, SH-waves). Consequently, for scatterers one or two wavelengths away from the fluid-filled borehole, it is sufficient to only consider their interaction with body waves (Geerits et al., 2013).

1.1 Topic of this thesis

The main topic of this thesis is the development of a new fast and efficient 3D elastodynamic forward modeling technique that addresses the moving source-receiver configuration, which is essential for logging and LWD reflection measurements. For this, the elastodynamic forward scattering formulation of De Hoop (1995) is revisited. The first-order approximation to this scattering approach provides the opportunity to separate the background medium, where the wave propagation takes place from the scatterer. This has huge computational advantages as will be shown in the course of this thesis (e.g., Veile et al., 2012; Geerits et al., 2013).

1.2 Outline of this thesis

After the initial remarks in this introduction, Chapter 2 shows the derivation of the underlying theoretical concept. Based on the elastodynamic forward scattering theory an explicit expression for the far-field first-order scattered wave field due to a multipole force source is derived. Furthermore, analytic zero-offset formulas for the scattered wave particle velocity and displacement in both the frequency and time domain, respectively, are derived. In this context, the simplest type of scatterer is considered, i.e., one characterized by a (Heaviside) step function change in at least one parameter (of three) describing the material contrast between the background medium and the scatterer. More complicated layered configurations can be derived from superposition of the given types of solutions. Explicit results are given for the dipole excitation, where the dipole direction is allowed to have an arbitrary orientation relative to the scatterer.

In chapter 3 the validation of the derived first-order zero-offset solution is investigated by a detailed sensitivity and accuracy analysis with respect to three independent perturbation parameters that uniquely define the contrast between background medium and scatterer. As to the topology (shape) of the contrast, the simplest type of shape, i.e., a Heaviside step function in one or more of the independent contrast (perturbation) parameters, is considered. A dipole excitation is considered as source of which the excitation direction is allowed to make an arbitrary angle with the Heaviside plateau. The zero-offset analytic Born results are compared with a full waveform benchmark code which is a wavenumber integration code that has implemented the reflectivity method for a horizontally stratified medium (Kennett, 1983). Hereafter, this benchmark code will be referred to as *qseis* (Wang, 1999).

In chapter 4 the parallel numerical implementation of the derived theoretical concept is presented. The implementation, called *FMBORN*, is based on the assumption that the background medium and the scatterer can be separated which provides huge computational advantages. Furthermore, the chapter presents a convergence study for the scattering integral and a discretization study in order to develop a criterion for the spatial discretization of the numerical implementation. In addition, the performance of the code is discussed for the static case (i.e., without a movement of the fixed source-receiver geometry) and the dynamic case (i.e., with a movement of the fixed source-receiver geometry). Finally, the corresponding computer memory requirements are presented in detail.

In chapter 5 forward modeling results of *FMBORN* are presented for static and dynamic cases as

well as for zero-offset and non-zero-offset configurations. These results are analyzed in terms of the accuracy in near-field configurations and the applicability of the method in multiple-layer setups. Furthermore, they are compared to results obtained by an established finite-difference-based method in order to classify the developed approach in terms of accuracy and performance among other numerical approaches. The corresponding quasi-analytic reference results of *qseis* are also presented.

Finally, in chapter 6 a summary of the main results and conclusions are presented.

1.3 Notation

At this point I would like to make some comments about the notation used in this thesis. Especially for geophysicists with a background in seismics the word 'scatterer' usually describes a small spherical inclusion that is significantly smaller than one wavelength. Hence, a straight bonded object that extends in one or more arbitrary dimensions for more than one wavelength is usually denoted a reflector. In this thesis, however, as the theoretical basis lies in scattering theory, each reflecting object, independent of its spatial extension, is denoted as 'scatterer', consisting of many scattering points.

Furthermore, it should be noted that in the following all vectors are printed in bold, while their components are printed in standard font. To give an example, this means that the vector $\mathbf{x}$ has three components x_r with $r \in \{1, 2, 3\}$.

In the following, the Einstein summation convention (Einstein, 1916) is used for convenience. This convention states that indices occurring twice in a single term of an expression implys summation over the corresponding term for all values of the index. For example,

$$\hat{v}_r = \sum_{k=1}^{3} \hat{G}_{r,k} \hat{f}_k = \hat{G}_{r,1} \hat{f}_1 + \hat{G}_{r,2} \hat{f}_2 + \hat{G}_{r,3} \hat{f}_3$$

can be briefly written as

$$\hat{v}_r = \hat{G}_{r,k} \hat{f}_k \, .$$

Moreover, it should be noted that whenever two spatial coordinates occur in the argument of a Green's tensor or function the left one refers to the observation location and the right one to the source location. In addition, it should be noted that whenever two spatial coordinates separated by a semicolon occur in the argument of a function, this function depends only on the left one referring to the observation location while the right one refers to the source location.

Chapter 2

Far-field elastodynamic Born scattering theory

Based on the full elastodynamic forward scattering theory presented by De Hoop (1995), in this chapter a theoretical approach for the calculation of the single scattered wave field is presented. In order to derive an explicit expression for the far-field first-order single scattered wave field due to a dipole excitation, I focus on the contrast-source stress-velocity forward scattering (integral equation) formulation for solid configurations of De Hoop (1995). A shortened overview of the presented derivations was published by Tim Geerits, myself and Olaf Hellwig in Geerits et al. (2013).

2.1 The full elastodynamic forward source and forward scattering formulation

In forward modeling there are two approaches to model the (elastodynamic) wave field: the forward source approach and the forward scattering approach. Using the global reciprocity theorem of the time-convolution type (De Hoop, 1990), both, the elastodynamic forward source formulation and the elastodynamic forward scattering formulation can be derived (De Hoop, 1995). In the following, both formulations are summarized by one set of integral equations (Veile et al., 2012; Geerits et al., 2013) by introducing the placeholder $\star$. In case of the forward source formulation this placeholder is replaced by 'T'. In case of the forward scattering formulation it is replaced by 'scat'. In the complex frequency domain this set of integral equations is

$$\begin{bmatrix} -\hat{\tau}^{\star}_{i,j} \\ \hat{v}^{\star}_{r} \end{bmatrix}(\mathbf{x}') = \int\limits_{\mathbf{x}\in\mathcal{D}^{\star}} \begin{bmatrix} \hat{G}^{\tau,f}_{i,j,k} & \hat{G}^{\tau,h}_{i,j,p,q} \\ \hat{G}^{v,f}_{r,k} & \hat{G}^{v,h}_{r,p,q} \end{bmatrix}(\mathbf{x}',\mathbf{x}) \begin{bmatrix} \hat{f}^{\star}_{k} \\ \hat{h}^{\star}_{p,q} \end{bmatrix}(\mathbf{x})\, dV \quad \text{with} \quad \mathbf{x}' \in \mathcal{D}\,, \tag{2.1}$$

where the dynamic stress tensor $\hat{\tau}^{\star}_{i,j}$ and the particle velocity vector $\hat{v}^{\star}_{r}$ denote the elastic wave field quantities at an arbitrary observation point $\mathbf{x}'$ within $\mathcal{D}$ as indicated in Figure 2.1. $\mathcal{D}$ represents the

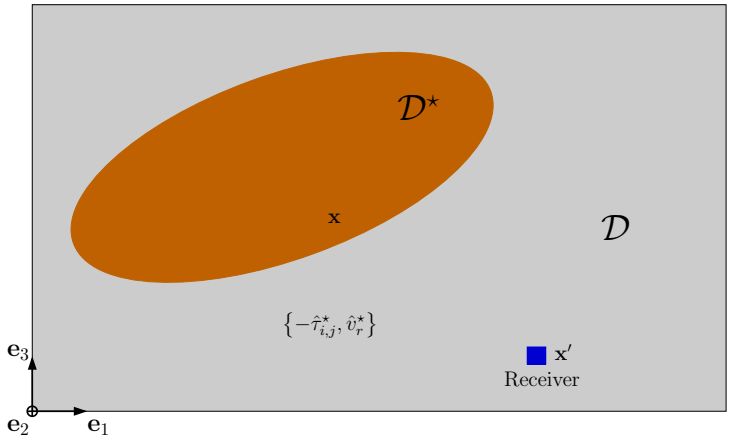

Figure 2.1: Schematic view of the occurring domains in the forward source and forward scattering formulation. In the forward source formulation $\mathcal{D}^\star = \mathcal{D}^{\mathrm{T}}$, denoting the spatial support of the known elastodynamic sources. The aim is to calculate the resulting wave field $\left\{-\hat{\tau}^{\mathrm{T}}_{i,j}, \hat{v}^{\mathrm{T}}_r\right\}(\mathbf{x}')$ at any receiver location $\mathbf{x}'$ in $\mathcal{D}$. In the forward scattering formulation $\mathcal{D}^\star = \mathcal{D}^{\mathrm{scat}}$, denoting the spatial support of the contrast sources, i.e., the scatterer. In this case, the aim is to calculate the resulting scattered wave field $\left\{-\hat{\tau}^{\mathrm{scat}}_{i,j}, \hat{v}^{\mathrm{scat}}_r\right\}(\mathbf{x}')$ at any receiver location $\mathbf{x}'$ in $\mathcal{D}$.

domain of a solid background medium. $\hat{f}^\star_k$ and $\hat{h}^\star_{p,q}$ denote the complex frequency domain source distribution terms for which the intergal adds up all contributions coming from the source domain $\mathcal{D}^\star$ that is located within the solid embedding. Figure 2.1 visualizes the fundamental domains in this context. The Green's tensors $\hat{G}^{\tau,f}_{i,j,k}(\mathbf{x}',\mathbf{x})$, $\hat{G}^{\tau,h}_{i,j,p,q}(\mathbf{x}',\mathbf{x})$, $\hat{G}^{v,f}_{r,k}(\mathbf{x}',\mathbf{x})$ and $\hat{G}^{v,h}_{r,p,q}(\mathbf{x}',\mathbf{x})$ can be seen as field quantity specific transfer functions that mediate the interaction between a specific source distribution and an associated medium observable (field quantity). In this notation the first superscript denotes the field quantity the associated Green's tensor pertains to and the second superscript denotes the assciated (Dirac) source type excitation. Furthermore, it should be noted that, whenever two spatial coordinates occur in the argument of a Green's tensor or function, the left one refers to the observation location and the right one to the source location.

In the forward source formulation the elastic wave field in the complex frequency domain $\left\{-\hat{\tau}^{\mathrm{T}}_{i,j}, \hat{v}^{\mathrm{T}}_r\right\}(\mathbf{x}')$ is expressed in terms of the known elastodynamic source distributions $\left\{\hat{f}^{\mathrm{T}}_k, \hat{h}^{\mathrm{T}}_{p,q}\right\}(\mathbf{x})$, having a spatial support $\mathcal{D}^{\mathrm{T}}$. In this context $\hat{f}^{\mathrm{T}}_k(\mathbf{x})$ denotes the solid volume source density of force and $\hat{h}^{\mathrm{T}}_{p,q}(\mathbf{x})$ denotes the solid volume source density of deformation rate.

In the forward scattering formulation for solid configurations, however, an arbitrarily shaped scatterer with a spatial support $\mathcal{D}^{\mathrm{scat}}$ is assumed to be located within a solid embedding $\mathcal{D}$, while the elastodynamic properties of both differ from each other (cf. Figure 2.2). As borehole forward scattering applications are considered, the scatterer can always be identified as a domain exterior to the bore tool including the source. Hence, the source having a spatial extension $\mathcal{D}^{\mathrm{T}}$ is located in the background medium outside $\mathcal{D}^{\mathrm{scat}}$ irradiating the scatterer. In the solid background medium with known elastodynamic properties, the radiation from given, arbitrarily distributed sources can be calculated via the just explained forward source formulation. As already indicated in equation 2.1, the forward scattering formulation can also be viewed as a forward source

formulation. However, in this case the source terms $\left\{\hat{f}_k^{\text{scat}}, \hat{h}_{p,q}^{\text{scat}}\right\}(\mathbf{x})$ are replaced by so-called contrast sources, that have a spatial support corresponding to the scattering domain $\mathcal{D}^{\text{scat}}$. The left hand side wave field quantities do then represent the total scattered wave field quantities $\left\{-\hat{\tau}_{i,j}^{\text{scat}}, \hat{v}_r^{\text{scat}}\right\}(\mathbf{x}')$. Moreover, it can be shown that the contrast sources can be expressed as (De Hoop, 1995)

$$\begin{bmatrix} \hat{f}_k^{\text{scat}} \\ \hat{h}_{p,q}^{\text{scat}} \end{bmatrix}(\mathbf{x}) = i\omega \begin{bmatrix} (\rho_{k,r}(\mathbf{x}) - \rho_{k,r})\, \hat{v}_r^{\text{total}} \\ -(S_{p,q,r,s}(\mathbf{x}) - S_{p,q,r,s})\, \hat{\tau}_{i,j}^{\text{total}} \end{bmatrix} = i\omega \begin{bmatrix} \overline{\rho}_{k,r}(\mathbf{x})\, \hat{v}_r^{\text{total}} \\ -\overline{S}_{p,q,r,s}(\mathbf{x})\, \hat{\tau}_{i,j}^{\text{total}} \end{bmatrix}, \tag{2.2}$$

where $\overline{\rho}_{k,r}(\mathbf{x}) = \rho_{k,r}(\mathbf{x}) - \rho_{k,r}$ denotes the actual contrast in density and $\overline{S}_{p,q,r,s}(\mathbf{x}) = S_{p,q,r,s}(\mathbf{x}) - S_{p,q,r,s}$ denotes the actual contrast in compliance. The total wavefield $\left\{-\hat{\tau}_{i,j}^{\text{total}}, \hat{v}_r^{\text{total}}\right\}(\mathbf{x}')$ can be decomposed in two parts

$$\begin{bmatrix} -\hat{\tau}_{i,j}^{\text{total}} \\ \hat{v}_r^{\text{total}} \end{bmatrix}(\mathbf{x}') = \begin{bmatrix} -\hat{\tau}_{i,j}^{\text{inc}} \\ \hat{v}_r^{\text{inc}} \end{bmatrix}(\mathbf{x}') + \begin{bmatrix} -\hat{\tau}_{i,j}^{\text{scat}} \\ \hat{v}_r^{\text{scat}} \end{bmatrix}(\mathbf{x}'), \tag{2.3}$$

where the incident wave field $\{-\hat{\tau}_{i,j}^{\text{inc}}, \hat{v}_r^{\text{inc}}\}$ is the wave field that would exist in absence of any contrast. This is the wave field that follows from the earlier explained forward source formulation. (cf. equation 2.1). It should be noted that in equation 2.2 the contrast weighted total wave field acts as a source distribution, but now with $\mathcal{D}^{\text{scat}}$ as spatial support.

It is a matter of convenience which formulation (i.e., the forward source or forward scattering formulation) is used for forward modeling. However, if the ultimate aim is to recover the scatterer from the scattered wave field, the forward scattering formulation deserves preference over the forward source formulation. This is due to the fact that the forward scattering formulation, under certain conditions, has a clearly defined and unique inverse (De Hoop, 1995), which exactly meets our aim, i.e., to recover the scatterer. The inversion process is also denoted as migration and represents a major subject in geophysics. In this thesis I will focus on the first order approximation of the scattered wave field (often referred to as the Born approximation). The far field (high frequency limit) approximation to this first order scattered wave field has a unique inverse (Beylkin, 1985; Miller et al., 1987; Beylkin and Burridge, 1990) and forms the foundation of many practically applied migration algorithms.

2.2 The first order iterative (Born) solution to the forward scattering problem

It is well known (De Hoop, 1995; Colton and Kress, 1998) that the total wave field $\{-\hat{\tau}_{i,j}^{\text{total}}, \hat{v}_r^{\text{total}}\}$ at an arbitrary position $\mathbf{x}'$ in $\mathcal{D}$ (cf. Figure 2.2) can be expressed as the sum of an incident wave field $\{-\hat{\tau}_{i,j}^{\text{inc}}, \hat{v}_r^{\text{inc}}\}$ and a scattered wave field $\{-\hat{\tau}_{i,j}^{\text{scat}}, \hat{v}_r^{\text{scat}}\}$ as done in equation 2.3. The incident wave field is the undisturbed wave field that would be present if no contrast between the background medium and the scatterer exists. Hence, it can be determined using the forward source formulation (cf. equation 2.1). The scattered wave field is simply the difference between the total wave field that can be recorded and the incident wave field.

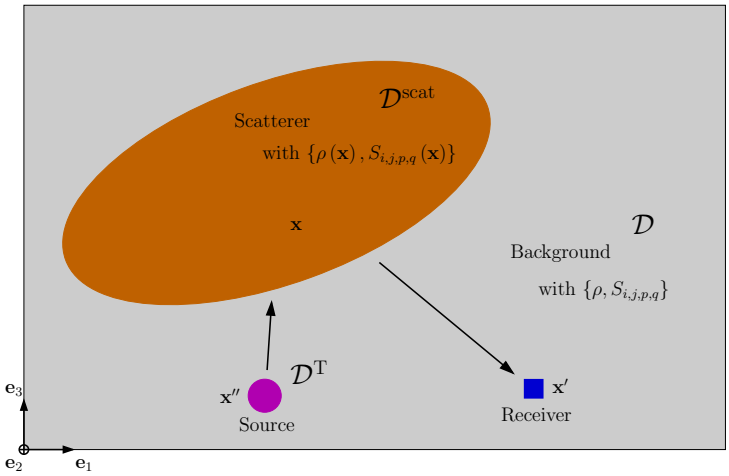

Figure 2.2: Schematic view of the occurring domains in the forward scattering formulation. $\mathcal{D}$ denotes the background domain, whereas $\mathcal{D}^{\text{scat}}$ represents the scatterer. Both domains are defined by elastodynamic properties, which differ from each other. The scatterer occurs as a penetrable bordered object and is irradiated by the source having a spatial extension $\mathcal{D}^{\text{T}}$, located in the background medium.

The so-called iterative Neumann Ansatz (De Hoop, 1995) assumes that the total wave field can be expressed in terms of a uniformly converging series

$$\begin{bmatrix} -\hat{\tau}_{i,j}^{\text{total}} \\ \hat{v}_r^{\text{total}} \end{bmatrix}(\mathbf{x}') = \sum_{n=0}^{\infty} \begin{bmatrix} \hat{\tau}_{i,j}^{[n]} \\ \hat{v}_r^{[n]} \end{bmatrix}(\mathbf{x}') \tag{2.4}$$

$$= \begin{bmatrix} -\hat{\tau}_{i,j}^{[0]} \\ \hat{v}_r^{[0]} \end{bmatrix}(\mathbf{x}') + \sum_{n=0}^{\infty} \begin{bmatrix} -\hat{\tau}_{i,j}^{[n+1]} \\ \hat{v}_r^{[n+1]} \end{bmatrix}(\mathbf{x}') \,. \tag{2.5}$$

As a consequence, the total wave field can be mathematically expressed as the sum of the number of scattering interactions n the wave field experiences. In this case, the incident wave field is the undisturbed wave field that experiences no scattering interactions. The scattered wave field is summarized in the most right had side term of equation 2.5, where the different terms of the sum correspond to the number of scattering interactions the scattered wave has experienced.

Using the iterative Neumann Ansatz, it is possible to arrive at an explicit first-order solution for the spectral scattered wave quantities in equation 2.1. Therefore, the left hand side term of equation 2.1 is replaced by the most right hand side term of equation 2.5. In addition, the contrast sources are expressed in terms of the total wave field particle velocity and the total wave field dynamic stress (cf. equation 2.2). Finally, this yields the following n-th term iterative solution

$$\begin{bmatrix} -\hat{\tau}_{i,j}^{[n+1]} \\ \hat{v}_r^{[n+1]} \end{bmatrix}(\mathbf{x}') = \int_{\mathbf{x}\in\mathcal{D}^{\text{scat}}} \begin{bmatrix} \hat{G}_{i,j,k}^{\tau,f} & \hat{G}_{i,j,p,q}^{\tau,h} \\ \hat{G}_{r,k}^{v,f} & \hat{G}_{r,p,q}^{v,h} \end{bmatrix}(\mathbf{x}',\mathbf{x}) \begin{bmatrix} \hat{f}_k^{\text{scat},[n]} \\ \hat{h}_{p,q}^{\text{scat},[n]} \end{bmatrix}(\mathbf{x}) \; dV, \tag{2.6}$$

where

$$\begin{bmatrix} \hat{f}_k^{\text{scat},[n]} \\ \hat{h}_{p,q}^{\text{scat},[n]} \end{bmatrix}(\mathbf{x}) = i\omega \begin{bmatrix} (\rho_{k,r}(\mathbf{x}) - \rho_{k,r})\, \hat{v}_r^{[n]} \\ -(S_{p,q,r,s}(\mathbf{x}) - S_{p,q,r,s})\, \hat{\tau}_{r,s}^{[n]} \end{bmatrix}. \tag{2.7}$$

This iterative solution is initialized by setting $n = 0$ and has to be pursued until the series expansion has converged, whereas the convergence is conjectured only for sufficiently small contrast parameters (Hudson and Heritage, 1981; Korneev and Johnson, 1993a; Gritto et al., 1995; Bohlen, 2004) and has only been proven for the acoustic case (De Hoop, 1991). However, as the aim here is to arrive at a first-order solution for the spectral scattered wave quantities, the series expansion is truncated after the first iteration. This yields a first-order solution to the scattered wave field which is called the first-order Born approximation:

$$\begin{bmatrix} -\hat{\tau}_{i,j}^{\text{scat},[1]} \\ \hat{v}_r^{\text{scat},[1]} \end{bmatrix}(\mathbf{x}') = \int_{\mathbf{x}\in\mathcal{D}^{\text{scat}}} \begin{bmatrix} \hat{G}_{i,j,k}^{\tau,f} & \hat{G}_{i,j,p,q}^{\tau,h} \\ \hat{G}_{r,k}^{v,f} & \hat{G}_{r,p,q}^{v,h} \end{bmatrix}(\mathbf{x}',\mathbf{x}) \begin{bmatrix} \hat{f}_k^{\text{scat},[0]} \\ \hat{h}_{p,q}^{\text{scat},[0]} \end{bmatrix}(\mathbf{x})\, dV \tag{2.8}$$

where

$$\begin{bmatrix} \hat{f}_k^{\text{scat},[0]} \\ \hat{h}_{p,q}^{\text{scat},[0]} \end{bmatrix}(\mathbf{x}) = i\omega \begin{bmatrix} (\rho_{k,r}(\mathbf{x}) - \rho_{k,r})\, \hat{v}_r^{[0]} \\ -(S_{p,q,r,s}(\mathbf{x}) - S_{p,q,r,s})\, \hat{\tau}_{r,s}^{[0]} \end{bmatrix}. \tag{2.9}$$

As the incident wave fields $\hat{v}_r^{[0]}$ and $-\hat{\tau}_{r,s}^{[0]}$ are known and the contrast parameters are assumed to be known the first-order Born approximation can be calculated.

2.3 The far-field first-order forward scattering solution in an unbounded homogeneous and isotropic background

For an unbounded homogeneous, isotropic, solid medium De Hoop (1995) presents the following definitions of the Green's tensors occurring in equation 2.1.

$$\hat{G}_{i,j,k}^{\tau,f}(\mathbf{x}',\mathbf{x}) = \frac{1}{\rho} C_{i,j,p,q} \partial_p \hat{G}_{r,k}(\mathbf{x}',\mathbf{x}), \tag{2.10}$$

$$\hat{G}_{r,k}^{v,f}(\mathbf{x}',\mathbf{x}) = \frac{-i\omega}{\rho} \hat{G}_{r,k}(\mathbf{x}',\mathbf{x}), \tag{2.11}$$

$$\hat{G}_{i,j,p,q}^{\tau,h}(\mathbf{x}',\mathbf{x}) = \frac{1}{i\omega} C_{i,j,p,q} \delta(\mathbf{x}'-\mathbf{x}) \frac{1}{i\omega\rho} C_{i,j,n,r}\, C_{k,m,p,q} \partial_n \partial_m \hat{G}_{r,k}(\mathbf{x}',\mathbf{x}), \tag{2.12}$$

$$\hat{G}_{r,p,q}^{v,h}(\mathbf{x}',\mathbf{x}) = -\frac{1}{\rho} C_{k,m,p,q} \partial_m \hat{G}_{r,k}(\mathbf{x}',\mathbf{x}) \tag{2.13}$$

where the fundamental homogeneous, isotropic elastodynamic Green's tensor $\hat{G}_{r,k}(\mathbf{x}', \mathbf{x})$ (De Hoop, 1995) is defined as

$$\hat{G}_{r,k}(\mathbf{x}', \mathbf{x}) = s_{\mathrm{S}}^2 \hat{G}_{\mathrm{S}}(\mathbf{x}', \mathbf{x}) \delta_{r,k} - \frac{1}{\omega^2} \partial_r \partial_k \left(\hat{G}_{\mathrm{P}}(\mathbf{x}', \mathbf{x}) - \hat{G}_{\mathrm{S}}(\mathbf{x}', \mathbf{x}) \right), \tag{2.14}$$

with the definition for the scalar Green's function pertaining to the P-wave

$$\hat{G}_{\mathrm{P}}(\mathbf{x}', \mathbf{x}) = \frac{\exp\left[i\omega s_{\mathrm{P}} |\mathbf{x}' - \mathbf{x}|\right]}{4\pi |\mathbf{x}' - \mathbf{x}|} \tag{2.15}$$

and the definition for the scalar Green's function pertaining to the S-wave

$$\hat{G}_{\mathrm{S}}(\mathbf{x}', \mathbf{x}) = \frac{\exp\left[i\omega s_{\mathrm{S}} |\mathbf{x}' - \mathbf{x}|\right]}{4\pi |\mathbf{x}' - \mathbf{x}|}. \tag{2.16}$$

s_{S} and s_{P} in equations 2.14 - 2.16 correspond to the isotropic shear and compressional wave slownesses and $\delta_{r,k}$ corresponds to the Kronecker delta. $C_{i,j,p,q}$ in equations 2.10, 2.12 and 2.13 denotes the stiffness tensor. In case of a homogeneous, isotropic and perfectly elastic medium it has the following form

$$C_{i,j,p,q} = \lambda \delta_{i,j} \delta_{p,q} + \mu \left(\delta_{i,p} \delta_{j,q} + \delta_{j,p} \delta_{i,q} \right), \tag{2.17}$$

where λ and μ are the first and second Lamé constants. The inverse of the stiffness tensor $C_{i,j,p,q}$ is the compliance tensor $S_{i,j,p,q}$, which is defined accordingly as

$$S_{i,j,p,q} = \Lambda \delta_{i,j} \delta_{p,q} + \mathrm{M} \left(\delta_{i,p} \delta_{j,q} + \delta_{j,p} \delta_{i,q} \right). \tag{2.18}$$

By definition, the two tensors are correlated through

$$S_{i,j,p,q} C_{i,j,p,q} = \frac{1}{2} \left(\delta_{i,p} \delta_{j,q} + \delta_{j,q} \delta_{j,q} \right) \tag{2.19}$$

which yields the following relations for the already mentioned Lamé constants

$$\Lambda = -\frac{\lambda}{(3\lambda + 2\mu) 2\mu} \tag{2.20}$$

and

$$\mathrm{M} = \frac{1}{4\mu}. \tag{2.21}$$

Using equation 2.20 and 2.21, in turn, leads to explicit definitions for the shear and compressional wave slownesses

$$s_{\mathrm{P}} = \left[\frac{\lambda + 2\mu}{\rho}\right]^{-\frac{1}{2}} = \sqrt{\frac{\rho\mathrm{M}\,(3\Lambda + 2\mathrm{M})}{\Lambda + \mathrm{M}}}\,, \tag{2.22}$$

$$s_{\mathrm{S}} = \sqrt{\frac{\rho}{\mu}} = 2\sqrt{\rho\mathrm{M}}\,, \tag{2.23}$$

occurring in equations 2.14 - 2.16.

2.3.1 The incident wave field

As mentioned in the introduction, in borehole acoustics mainly multipole ring sources are used with diameters in a range from 15 to 25 cm. Compared to typical observation distances that lie in a range from 10 to 30 m, (i.e., the distance from source to scattering point and from scattering point to receiver), the radii of these multipole ring sources are very small and can be neglected. Hence, a far-field approximation can be invoked. This approximation is applied to the scalar Green's functions in equations 2.15 and 2.16 as all other Green's vectors and tensors depend on them. In addition to the first-order singularity at $\mathbf{x}' = \mathbf{x}$ the multiple spatial differentiation of these scalar Green's functions introduces one more singularity (of one order higher) with each spatial differentiation. Hence, it can be assumed that the first-order term (i.e., the least singular term) contributes the dominant part to the incident and scattered wave amplitude. The spatial derivatives of first to fourth order with respect to the observation coordinate $\mathbf{x}'$ are given in appendix A. A detailed description of the multipole ring source employed here is given in appendix B.

Applying the mentioned far-field approximation to the scalar Green's functions (equations 2.15 and 2.16) in equation 2.14 and inserting the result in equations 2.10 and 2.11 leads to the following elastic quantities for the incident wave field

$$-\hat{\tau}^{\mathrm{inc}}_{i,j}\left(\mathbf{x};\mathbf{x}''\right) = -\frac{i\omega}{\rho}C_{i,j,n,q}n_n\left[s^3_{\mathrm{P}}n_q\left(n_l f^{\mathrm{P}}_l\right)\hat{G}_{\mathrm{P}}\left(\mathbf{x},\mathbf{x}''\right) + s^3_{\mathrm{S}}\left(\delta_{q,l} - n_q n_l\right) f^{\mathrm{S}}_l \hat{G}_{\mathrm{S}}\left(\mathbf{x},\mathbf{x}''\right)\right]\,, \tag{2.24}$$

$$\hat{v}^{\mathrm{inc}}_r\left(\mathbf{x};\mathbf{x}''\right) = -\frac{i\omega}{\rho}\left[s^2_{\mathrm{P}}n_r\left(n_l f^{\mathrm{P}}_l\right)\hat{G}_{\mathrm{P}}\left(\mathbf{x},\mathbf{x}''\right) + s^2_{\mathrm{S}}\left(\delta_{r,l} - n_r n_l\right) f^{\mathrm{S}}_l \hat{G}_{\mathrm{S}}\left(\mathbf{x},\mathbf{x}''\right)\right]\,, \tag{2.25}$$

where the former observation vector, $\mathbf{x}'$, is replaced by $\mathbf{x}$ and the former source vector, $\mathbf{x}$, is replaced by $\mathbf{x}''$. Furthermore, it should be noted that, whenever two spatial coordinates separated by ';' occur in the argument of a function, this function depends only on the left one referring to the observation location while the right one refers to the source location. $\hat{G}_{\mathrm{P}}\left(\mathbf{x},\mathbf{x}''\right)$ and $\hat{G}_{\mathrm{S}}\left(\mathbf{x},\mathbf{x}''\right)$ are the scalar Green's functions as defined in equations 2.15 and 2.16. f^{P}_l and f^{S}_l denote the directivity vectors for the P- and S-wave in the complex frequency domain and refer to (De Hoop, 1995)

$$f^{\odot}_l\left(\mathbf{k}^{\odot}\right) = \int\limits_{\mathbf{x}''\in\mathcal{D}^{\mathrm{T}}} \exp\left[ik^{\odot}_m x''_m\right]\hat{f}_l\left(\mathbf{x}''\right)\,dV \quad \text{with} \quad \odot \in \{\mathrm{P},\mathrm{S}\}\,, \tag{2.26}$$

where $ik_m^{\odot} = -i\omega s_{\odot} n_m$. The occurring unit vector $\mathbf{n}\,(n_k)$ from an arbitrary source coordinate $\mathbf{x}''$ to an arbitrary point of observation $\mathbf{x}$ can be written as

$$\mathbf{n} = \frac{\mathbf{x} - \mathbf{x}''}{|\mathbf{x} - \mathbf{x}''|} \tag{2.27}$$

with the components

$$n_k = \frac{\mathrm{x}_k - \mathrm{x}_k''}{\sqrt{(\mathrm{x}_m - \mathrm{x}_m'')\,(\mathrm{x}_m - \mathrm{x}_m'')}}. \tag{2.28}$$

A physical interpretation of equation 2.26 reveals that the directivity vectors $\mathbf{f}^{\mathrm{P}}$ and $\mathbf{f}^{\mathrm{S}}$ occurring in equations 2.24 and 2.25 are the spatial Fourier transforms of the (original) source distribution evaulated at $\mathbf{k}^{\mathrm{P}}$ and $\mathbf{k}^{\mathrm{S}}$, representing the P- and S-wavenumber, respectively.

2.3.2 The scattered wave field

Having calculated the incident wave field for a given source distribution $\hat{f}_k\,(\mathbf{x}'')$ the first-order scattered wave field can be calculated according to equation 2.8. For this, the result for the incident wave field (equations 2.24 and 2.25) is inserted in equation 2.9 and this outcome is then substituted in equation 2.8. Applying the definitions for the Green's tensors (equations 2.10 - 2.14), the evaluation of the integrand shows that the total scattered wave field is composed of five different wave types

$$\begin{aligned}
&\begin{bmatrix} -\hat{\tau}_{i,j}^{\mathrm{scat}} \\ \hat{v}_r^{\mathrm{scat}} \end{bmatrix}(\mathbf{x}';\mathbf{x}'') = \\
&\begin{bmatrix} -\hat{\tau}_{i,j}^{\mathrm{scat,PP}} \\ \hat{v}_r^{\mathrm{scat,PP}} \end{bmatrix} + \begin{bmatrix} -\hat{\tau}_{i,j}^{\mathrm{scat,PSV}} \\ \hat{v}_r^{\mathrm{scat,PSV}} \end{bmatrix} + \begin{bmatrix} -\hat{\tau}_{i,j}^{\mathrm{scat,SVP}} \\ \hat{v}_r^{\mathrm{scat,SVP}} \end{bmatrix} + \begin{bmatrix} -\hat{\tau}_{i,j}^{\mathrm{scat,SVSV}} \\ \hat{v}_r^{\mathrm{scat,SVSV}} \end{bmatrix} + \begin{bmatrix} -\hat{\tau}_{i,j}^{\mathrm{scat,SHSH}} \\ \hat{v}_r^{\mathrm{scat,SHSH}} \end{bmatrix}.
\end{aligned} \tag{2.29}$$

The dependencies of the different wave types are left due to lack of space. Including the far-field approximation in the derivation (following the same motivation as given for the calculation of the incident wave field) the following elastic quantities for the first order scattered wave field result:

$$-\hat{\tau}_{i,j}^{\mathrm{scat}}\,(\mathbf{x}';\mathbf{x}'') = i\omega^3 \sum_{\odot,\oplus} s_{\odot} s_{\oplus}^2 \int\limits_{\mathbf{x}\in\mathcal{D}^{\mathrm{scat}}} \hat{G}_{\odot}\,(\mathbf{x},\mathbf{x}'')\, A_{i,j}^{\odot\oplus}\,(\mathbf{x})\; \hat{G}_{\oplus}\,(\mathbf{x}',\mathbf{x})\; dV\,, \tag{2.30}$$

$$\hat{v}_r^{\mathrm{scat}}\,(\mathbf{x}';\mathbf{x}'') = \frac{i\omega^3}{\rho} \sum_{\odot,\oplus} s_{\odot}^2 s_{\oplus}^2 \int\limits_{\mathbf{x}\in\mathcal{D}^{\mathrm{scat}}} \hat{G}_{\odot}\,(\mathbf{x},\mathbf{x}'')\, A_{r}^{\odot\oplus}\,(\mathbf{x})\; \hat{G}_{\oplus}\,(\mathbf{x}',\mathbf{x})\; dV \tag{2.31}$$

with $\odot$ representing the incident and $\oplus$ representing the scattered wave type, respectively. The integral indicates that the first-order scattered wave field consists of all single scattered contributions that come from the scattering domain $\mathcal{D}^{\mathrm{scat}}$. Equation 2.29 shows that these contributions

pertain to PP, PSV, SVP, SVSV and SHSH reflections. The scalar Green's function $\hat{G}_{\odot}(\mathbf{x}, \mathbf{x}'')$ describes the wave propagation of the incident wave in terms of phase and amplitude (cf. equation 2.15), propagating in the background medium from the source location $\mathbf{x}''$ to the scattering point $\mathbf{x}$. Accordingly, the scalar Green's function $\hat{G}_{\oplus}(\mathbf{x}', \mathbf{x})$ describes the wave propagation of the scattered wave in terms of phase and amplitude (cf. equation 2.16), propagating in the background medium from the scattering point $\mathbf{x}$ to the observation location $\mathbf{x}'$.

$A_{i,j}^{\odot\oplus}$ and $A_{r}^{\odot\oplus}$ denote weighting factors that account for the perturbation describing the differences in material properties between the background medium and the scatterer. Furthermore, they account for the source signature, the directivity of the incident wave and the scattered wave polarization vector. Except for the source signature all named contributions are dimensionless. Hence, $A_{i,j}^{\odot\oplus}$ and $A_{r}^{\odot\oplus}$ have the dimension of the source signature. Explicitly written down, the weighting factors pertaining to the scattered dynamic stress are

$$A_{i,j}^{\mathrm{PP}} = \left[\left[\left(1 - 2\left(\frac{s_{\mathrm{P}}}{s_{\mathrm{S}}}\right)^2\right)\delta_{i,j} + 2\left(\frac{s_{\mathrm{P}}}{s_{\mathrm{S}}}\right)^2 n_i' n_j'\right]\left[3\left(\frac{s_{\mathrm{P}}}{s}\right)^2 \bar{\alpha} + 2\left(\frac{s_{\mathrm{P}}}{s_{\mathrm{S}}}\right)^2 (n_m n_m')^2\,\bar{\beta}\right]\right. \\ \left. + \left[\left(1 - 2\left(\frac{s_{\mathrm{P}}}{s_{\mathrm{S}}}\right)^2\right)(n_m n_m')\,\delta_{i,j} + 2\left(\frac{s_{\mathrm{P}}}{s_{\mathrm{S}}}\right)^2 n_i' n_j'\right]\bar{\rho}\right]\left(n_l f_l^{\mathrm{P}}\right), \tag{2.32}$$

$$A_{i,j}^{\mathrm{PSV}} = \left(\frac{s_{\mathrm{P}}}{s_{\mathrm{S}}}\right)\left(n_l f_l^{\mathrm{P}}\right)\left(e_k^{\mathrm{SV}'} n_k\right)\left[2\left(\frac{s_{\mathrm{P}}}{s_{\mathrm{S}}}\right)(n_m n_m')\,\bar{\beta} + \bar{\rho}\right]\left[e_j^{\mathrm{SV}'} n_i' + e_i^{\mathrm{SV}'} n_j'\right], \tag{2.33}$$

$$A_{i,j}^{\mathrm{SVP}} = \left[\left(1 - 2\left(\frac{s_{\mathrm{P}}}{s_{\mathrm{S}}}\right)^2\right)\delta_{i,j} + 2\left(\frac{s_{\mathrm{P}}}{s_{\mathrm{S}}}\right)^2 n_i' n_j'\right]\left[2\left(\frac{s_{\mathrm{P}}}{s_{\mathrm{S}}}\right)(n_m n_m')\,\bar{\beta} + \bar{\rho}\right]\left(p_k^{\mathrm{S}} e_k^{\mathrm{SV}}\right)\left(e_l^{\mathrm{SV}} n_l'\right), \tag{2.34}$$

$$A_{i,j}^{\mathrm{SVSV}} = \left(n_i' e_j^{\mathrm{SV}'} + n_j' e_i^{\mathrm{SV}'}\right)\left(p_k^{\mathrm{S}} e_k^{\mathrm{SV}}\right)\left[\left[\frac{\left(e_l^{\mathrm{SV}'} n_l\right)\left(e_m^{\mathrm{SV}} n_m'\right)}{\left(n_p n_p'\right)\left(n_p n_p'\right)} + 1\right]\left(n_p n_p'\right)\bar{\beta} + \bar{\rho}\right]\left(n_p n_p'\right), \tag{2.35}$$

$$A_{i,j}^{\mathrm{SHSH}} = \left(n_i' e_j^{\mathrm{SH}'} + n_j' e_i^{\mathrm{SH}'}\right)\left(p_k^{\mathrm{S}} e_k^{\mathrm{SH}}\right)\left[\left(n_p n_p'\right)\bar{\beta} + \bar{\rho}\right]. \tag{2.36}$$

The weighting factors pertaining to the scattered particle velocity are

$$A_{r}^{\mathrm{PP}} = \left[\left[3\left(\frac{s_{\mathrm{P}}}{s}\right)^2 \bar{\alpha} + 2\left(\frac{s_{\mathrm{P}}}{s_{\mathrm{S}}}\right)^2 (n_m n_m')^2\,\bar{\beta}\right] + \bar{\rho}\,(n_m n_m')\right]\left(n_l f_l^{\mathrm{P}}\right) n_r', \tag{2.37}$$

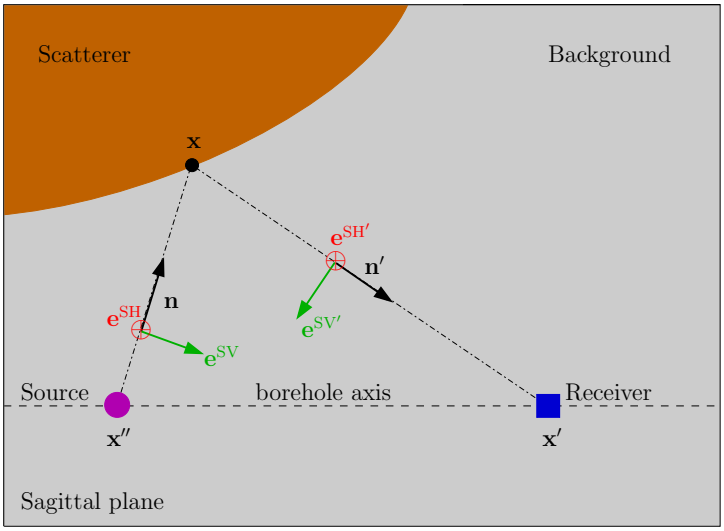

Figure 2.3: Visualization of the occurring polarization vectors of the incident and scattered wave particle velocity $\{\mathbf{n}, \mathbf{e}^{\mathrm{SV}}, \mathbf{e}^{\mathrm{SH}}\}$ and $\{\mathbf{n}', \mathbf{e}^{\mathrm{SV}'}, \mathbf{e}^{\mathrm{SH}'}\}$, respectively.

$$A_r^{\mathrm{PSV}} = \left[2\left(\frac{s_{\mathrm{P}}}{s_{\mathrm{S}}}\right)(n_m n'_m)\,\bar{\beta} + \bar{\rho}\right]\left(n_l f_l^{\mathrm{P}}\right)\left(e_k^{\mathrm{SV}'} n_k\right) e_r^{\mathrm{SV}'}\,, \tag{2.38}$$

$$A_r^{\mathrm{SVP}} = \left[2\left(\frac{s_{\mathrm{P}}}{s_{\mathrm{S}}}\right)(n_m n'_m)\,\bar{\beta} + \bar{\rho}\right]\left(p_k^{\mathrm{S}} e_k^{\mathrm{SV}}\right)\left(e_l^{\mathrm{SV}} n'_l\right) n'_r\,, \tag{2.39}$$

$$A_r^{\mathrm{SVSV}} = \left[\left[\frac{\left(e_l^{\mathrm{SV}'} n_l\right)\left(e_m^{\mathrm{SV}} n'_m\right)}{\left(n_p n'_p\right)\left(n_p n'_p\right)} + 1\right]\left(n_p n'_p\right)\bar{\beta} + \bar{\rho}\right]\left(n_p n'_p\right)\left(p_k^{\mathrm{S}} e_k^{\mathrm{SV}}\right) e_r^{\mathrm{SV}'}\,, \tag{2.40}$$

$$A_r^{\mathrm{SHSH}} = \left[\left(n_p n'_p\right)\bar{\beta} + \bar{\rho}\right]\left(p_k^{\mathrm{S}} e_k^{\mathrm{SH}}\right) e_r^{\mathrm{SH}'}\,, \tag{2.41}$$

where s_{P} and s_{S} are the slownesses of P- and S-wave, respectively, and

$$s = \sqrt{3\rho\left[3\Lambda + 2\mathrm{M}\right]}\,. \tag{2.42}$$

With reference to Figure 2.3 the occurring unitary polarization vector for the incident wave $\mathbf{n}\,(n_k)$ is defined in equation 2.27. Accordingly, the unitary polarization vector for the scattered wave $\mathbf{n}'\,(n'_k)$ from an arbitrary point $\mathbf{x}$ within the scattering domain to an arbitrary observation coordinate $\mathbf{x}'$ is defined as

$$\mathbf{n}' = \frac{\mathbf{x}' - \mathbf{x}}{|\mathbf{x}' - \mathbf{x}|}\,, \tag{2.43}$$

with the components

$$n'_k = \frac{\mathrm{x}'_k - \mathrm{x}_k}{\sqrt{\left(\mathrm{x}'_m - \mathrm{x}_m\right)\left(\mathrm{x}'_m - \mathrm{x}_m\right)}}\,. \tag{2.44}$$

Furthermore, Figure 2.3 shows the so-called Sagittal plane, which represents the plane in which the reflection occurs. It is defined by the center of the source location $\mathbf{x}''$, the scattering point $\mathbf{x}$ and the observation point $\mathbf{x}'$. By definition, in case of a homogeneous background medium the unitary polarization vectors for the incident and scattered wave lie in this plane. The equations for the incident wave (2.24, 2.25) and the calculations that lead to the equations for the scattered wave (2.30, 2.31) show that the particle motion of the incident and scattered P-wave is polarized parallel to $\mathbf{n}$ and $\mathbf{n}'$, respectively, and therefore occurs within the Sagittal plane. Since the particle motion of the incident and scattered S-wave is polarized perpendicular to $\mathbf{n}$ and $\mathbf{n}'$, respectively, but does not necessarily lie within or perpendicular to the Sagittal plane, a decomposition of the S-wave polarization direction is introduced. Hence, Figure 2.3 shows a right-handed reference frame for the incident wave, where the S-wave polarization direction is split into the SV polarization direction, denoted by $\mathbf{e}^{\mathrm{SV}}$ and defined perpendicular to $\mathbf{n}$ within the Sagittal plane and the SH polarization direction, denoted by $\mathbf{e}^{\mathrm{SH}}$ and defined perpendicular to $\mathbf{n}$ and the Sagittal plane. The same considerations have been applied to the scattered S-wave polarization direction as illustrated in Figure 2.3 which leads to $\mathbf{e}^{\mathrm{SH}} = \mathbf{e}^{\mathrm{SH}'}$.

As a result, the decomposed unitary polarization vectors for the incident $\left\{\mathbf{e}^{\mathrm{SV}},\, \mathbf{e}^{\mathrm{SH}}\right\}$ and the scattered $\left\{\mathbf{e}^{\mathrm{SV}'},\, \mathbf{e}^{\mathrm{SH}'}\right\}$ S-wave are defined as

$$\mathbf{e}^{\mathrm{SV}} = \frac{\left(\mathbf{e}^{\mathrm{W}} \times \mathbf{n}\right) \times \mathbf{n}}{\left|\mathbf{e}^{\mathrm{W}} \times \mathbf{n}\right|} \qquad \text{and} \qquad \mathbf{e}^{\mathrm{SV}'} = \frac{\left(\mathbf{e}^{\mathrm{W}} \times \mathbf{n}'\right) \times \mathbf{n}'}{\left|\mathbf{e}^{\mathrm{W}} \times \mathbf{n}'\right|}, \tag{2.45}$$

$$\mathbf{e}^{\mathrm{SH}} = \frac{\mathbf{e}^{\mathrm{W}} \times \mathbf{n}}{\left|\mathbf{e}^{\mathrm{W}} \times \mathbf{n}\right|} \qquad \text{and} \qquad \mathbf{e}^{\mathrm{SH}'} = \frac{\mathbf{e}^{\mathrm{W}} \times \mathbf{n}'}{\left|\mathbf{e}^{\mathrm{W}} \times \mathbf{n}'\right|} \tag{2.46}$$

with

$$\mathbf{e}^{\mathrm{W}} = \frac{\mathbf{n} - \mathbf{n}'}{\left|\mathbf{n} - \mathbf{n}'\right|} \tag{2.47}$$

being the resulting unitary ray vector. Equations 2.45 and 2.46 reveal that $\mathbf{e}^{\mathrm{SV}} \times \mathbf{e}^{\mathrm{SH}} = \mathbf{n}$ and $\mathbf{e}^{\mathrm{SV}'} \times \mathbf{e}^{\mathrm{SH}'} = \mathbf{n}'$.

According to this, the S-wave polarization vector $\mathbf{p}^{\mathrm{S}}\left(p_k^{\mathrm{S}}\right)$ occurring in equations 2.36 and 2.39 - 2.41 can also be decomposed and is defined as

$$\mathbf{p}^{\mathrm{S}} = \mathbf{n} \times \left(\mathbf{f}^{\mathrm{S}} \times \mathbf{n}\right) = \left(\mathbf{p}^{\mathrm{S}}\mathbf{e}^{\mathrm{SH}}\right)\mathbf{e}^{\mathrm{SH}} + \left(\mathbf{p}^{\mathrm{S}}\mathbf{e}^{\mathrm{SV}}\right)\mathbf{e}^{\mathrm{SV}} \tag{2.48}$$

with the components

$$p_k^{\mathrm{S}} = \left(\delta_{k,l} - n_k n_l\right) f_l^{\mathrm{S}} = \left(p_m^{\mathrm{S}} e_m^{\mathrm{SH}}\right) e_k^{\mathrm{SH}} + \left(p_m^{\mathrm{S}} e_m^{\mathrm{SV}}\right) e_k^{\mathrm{SV}}\,. \tag{2.49}$$

All weighting factors $A_{i,j}^{\odot\oplus}$ and $A_{r}^{\odot\oplus}$ occurring in equations 2.30 and 2.31 are composed of four terms:

- the directivity vector of the incident wave $\mathbf{f}^{\mathrm{P}}$ or $\mathbf{f}^{\mathrm{S}}$, which is projected along the polarization vector of the incident wave $\mathbf{n}, \mathbf{e}^{\mathrm{SV}}$ or $\mathbf{e}^{\mathrm{SH}}$;
- the inner product between the (unitary) polarization vector of the incident and the scattered wave, respectively, while $\mathbf{n} \cdot \mathbf{n}' = \mathbf{e}^{\mathrm{SV}} \cdot \mathbf{e}^{\mathrm{SV}'}$ and $\mathbf{e}^{\mathrm{SH}} = \mathbf{e}^{\mathrm{SH}'}$ (i.e., $\mathbf{e}^{\mathrm{SH}} \cdot \mathbf{e}^{\mathrm{SH}'} = 1$). Moreover, it should be noted that sometimes the angle between $\mathbf{n}$ and $-\mathbf{n}'$ is denoted as obliquity angle.
- the (unitary) polarization vector of the scattered wave $\mathbf{n}', \mathbf{e}^{\mathrm{SV}'}$or $\mathbf{e}^{\mathrm{SH}'}$, representing the (local) orientation of the scattered wave field quantities;
- a geometrically weighted dimensionless contrast function, that directly accounts for the differences in material properties between the background medium and the scatterer, i.e., the perturbation. Using the fundamental constant elastodynamic parameters of the background medium Λ, M and ρ and the fundamental elastodynamic parameters of the scatterer $\Lambda(\mathbf{x}), \mathrm{M}(\mathbf{x})$ and $\rho(\mathbf{x})$, the perturbation is expressed in terms of three dimensionless parameters $\delta\Lambda = \frac{\Lambda(\mathbf{x})}{\Lambda} - 1, \delta\mathrm{M} = \frac{\mathrm{M}(\mathbf{x})}{\mathrm{M}} - 1$ and $\delta\rho = \frac{\rho(\mathbf{x})}{\rho} - 1$. These perturbation parameters are directly related to the dimensionless coefficients $\bar{\alpha}, \bar{\beta}$ and $\bar{\rho}$, occurring in equations 2.32 - 2.41.

The dimensionless coefficients $\bar{\alpha}, \bar{\beta}$ and $\bar{\rho}$ are defined as

$$\bar{\alpha} = \frac{\Lambda}{(3\Lambda + 2\mathrm{M})}(\delta\Lambda - \delta\mathrm{M}) - \frac{\Lambda}{2\mathrm{M}}\delta\mathrm{M}\,, \tag{2.50}$$

$$\bar{\beta} = \frac{\mathrm{M}(\mathbf{x})}{\mathrm{M}} - 1 = \delta\mathrm{M}\,, \tag{2.51}$$

and

$$\bar{\rho} = \frac{\rho(\mathbf{x})}{\rho} - 1 = \delta\rho\,. \tag{2.52}$$

2.4 Zero-offset Born scattering

Generally, with respect to borehole logging imaging applications (Tang and Patterson, 2009; Tang et al., 2007, 2008) it is warranted to investigate zero-offset cases, as typical source-receiver distances (i.e., 3 - 6 m) are considerably small compared to typical observation distances (i.e., 30 - 40 m). Hence, in the following, a zero-offset approximation is applied to the derived expression for the scattered wave field (cf. equation 2.31). As in the context of this work only the formulation for the scattered wave particle velocity (and not the formulation for the scattered wave dynamic stress) has been explicitly implemented (Chapter 4) and investigated (Chapters 3 and 5), I restrict myself to this quantity of the scattered wave field concerning the following derivations.

Incorporating a multipole force source excitation as explicitly derived in appendix B in the expressions for the weighting factors by inserting equation B.7 in 2.37 - 2.41 allows to rewrite the weighting factors for the scattered particle velocity as

$$A_r^{\odot\oplus} = -\hat{T}\left(\omega\right) D_n^{\odot}\left(\mathbf{x}\right) \mathcal{R}^{\odot\oplus}\left(\mathbf{x}\right) \zeta_r^{\oplus}\left(\mathbf{x}\right) \quad \text{with} \quad \odot,\oplus \in \{\text{P,S}\}\,, \tag{2.53}$$

where $\hat{T}\left(\omega\right)$ is the spectral domain source signature and $D_n^{\odot}\left(\mathbf{x}\right)$ is the multipole directivity of the incident wave with n being the multipole excitation order (cf. appendix B). Furthermore, $\zeta^{\oplus}\left(\mathbf{x}\right)$ is the polarization vector of the scattered wave and $\mathcal{R}^{\odot\oplus}\left(\mathbf{x}\right)$ is a dimensionless and geometrically weighted contrast function (locally understood as scattering coefficient).

The scattering coefficients $\mathcal{R}^{\odot\oplus}\left(\mathbf{x}\right)$ pertaining to the scattered particle velocity (cf. equation 2.53) are

$$\mathcal{R}^{\text{PP}}\left(\mathbf{x}\right) = \left[\left[3\left(\frac{s_{\text{P}}}{s}\right)^2 \bar{\alpha} + 2\left(\frac{s_{\text{P}}}{s_{\text{S}}}\right)^2 \left(n_m n'_m\right)^2 \bar{\beta}\right] + \bar{\rho}\left(n_m n'_m\right)\right]\,, \tag{2.54}$$

$$\mathcal{R}^{\text{PSV}}\left(\mathbf{x}\right) = \left[2\left(\frac{s_{\text{P}}}{s_{\text{S}}}\right)\left(n_m n'_m\right)\bar{\beta} + \bar{\rho}\right]\left(e_k^{\text{SV}'} n_k\right)\,, \tag{2.55}$$

$$\mathcal{R}^{\text{SVP}}\left(\mathbf{x}\right) = \left[2\left(\frac{s_{\text{P}}}{s_{\text{S}}}\right)\left(n_m n'_m\right)\bar{\beta} + \bar{\rho}\right]\left(e_l^{\text{SV}} n'_l\right)\,, \tag{2.56}$$

$$\mathcal{R}^{\text{SVSV}}\left(\mathbf{x}\right) = \left[\left[\frac{\left(e_l^{\text{SV}'} n_l\right)\left(e_m^{\text{SV}} n'_m\right)}{\left(n_p n'_p\right)\left(n_p n'_p\right)} + 1\right]\left(n_p n'_p\right)\bar{\beta} + \bar{\rho}\right]\left(n_p n'_p\right)\,, \tag{2.57}$$

$$\mathcal{R}^{\text{SHSH}}\left(\mathbf{x}\right) = \left(n_p n'_p\right)\bar{\beta} + \bar{\rho}. \tag{2.58}$$

Inserting the expressions for the weighting factors (cf. equation 2.53) and the expressions for the scalar Greens functions (2.15, 2.16) in the equations for the first order scattered wave field (2.31) yields

$$\hat{v}_r^{\text{scat}}(\mathbf{x}';\mathbf{x}'') = \frac{-i\omega^3}{\left(4\pi\right)^2 \rho} \sum_{\odot,\oplus} s_{\odot}^2 s_{\oplus}^2 \hat{T}\left(\omega\right) \int\limits_{\mathbf{x}\in\mathcal{D}^{\text{scat}}} \frac{D_n^{\odot}\left(\mathbf{x}\right) \mathcal{R}^{\odot\oplus}(\mathbf{x}) \exp\left[i\omega\tau\left(\mathbf{x}',\mathbf{x},\mathbf{x}''\right)\right]}{\left|\mathbf{x}-\mathbf{x}''\right|\left|\mathbf{x}'-\mathbf{x}\right|} \zeta_r^{\oplus}(\mathbf{x})\; dV, \tag{2.59}$$

where τ describes the total travel time, i.e., the sum of the incident and the scattered wave travel time

$$\begin{aligned} \tau\left(\mathbf{x}',\mathbf{x},\mathbf{x}''\right) &= \tau\left(\mathbf{x},\mathbf{x}''\right) + \tau\left(\mathbf{x}',\mathbf{x}\right) \\ &= s_{\odot}\left|\mathbf{x}-\mathbf{x}''\right| + s_{\oplus}\left|\mathbf{x}'-\mathbf{x}\right| \\ &= s_{\odot}\mathbf{n}\cdot\left(\mathbf{x}-\mathbf{x}''\right) + s_{\oplus}\mathbf{n}'\cdot\left(\mathbf{x}'-\mathbf{x}\right) \\ &= \mathbf{s}_{\odot}\cdot\left(\mathbf{x}-\mathbf{x}''\right) + \mathbf{s}_{\oplus}\cdot\left(\mathbf{x}'-\mathbf{x}\right)\,, \end{aligned} \tag{2.60}$$

with $\mathbf{s}_{\odot} = s_{\odot}\mathbf{n}$ being the slowness vector of the incident wave and $\mathbf{s}_{\oplus} = s_{\oplus}\mathbf{n}'$ being the slowness vector of the scattered wave.

For fixed source-receiver positions and a fixed total travel time $\tau\left(\mathbf{x}', \mathbf{x}, \mathbf{x}''\right) = \tau_0$, equation 2.60 represents a quadratic surface, i.e., an isochronal surface. For all single scattered, non-converted waves (i.e., PP, SVSV, SHSH), this surface becomes a prolate spheroid. As a consequence, for $t = \tau_0$, (specular) reflections do only occur, if the corresponding isochronal surface becomes (locally) tangent to a scattering interface. To visualize the considered situation, Figure 2.4 shows a cross section of the mentioned spheroid in the plane in which the source-receiver line (i.e., the straight line between the source location $\mathbf{x}'' = (-c, 0, 0)$ and the receiver location $\mathbf{x}'' = (c, 0, 0)$ is located, i.e., the plane defined by $\mathbf{e}_2 = 0$. To further carve out the linked physical/mathematical meaning, it is to be mentioned that the application of a first-order Taylor expansion to equation 2.60 at $\mathbf{x}_0$ yields a first-order asymptotic solution for the scattered wave field. As a result, the spectral domain scattered wave field can be seen as being locally proportional to the spatial Fourier transform of the scatterer. With respect to the field of seismic exploration, this fact is of particular importance, since it provides the basis for many migration algorithms (Beylkin and Burridge, 1990; Miller et al., 1987; Beylkin, 1985).

As already mentioned, usually, for small source-receiver distances compared to the observation distance, the zero-offset approximation applies. With reference to Figure 2.4, this is the case, if $2c$, i.e., the source-receiver offset, is considerably smaller than $2a$, i.e., the sum of the incident and the scattered ray path, respectively. In this limting case, where $\frac{c}{a} \to 0$, the angle of incidence and the emergent angle approach zero, i.e., $\{i_1, i_2\} \to 0$. As a result, in zero-offset cases the prolate spheroid turns into a perfect sphere with the radius $R_0 = a$ and the center in the origin, as indicated in Figure 2.5.

With reference to Figures 2.3 and 2.4 it is clear that for zero-offset cases, where source and receiver coordinate coincide, the following relations arise

$$n_k \to -n'_k\,, \tag{2.61}$$

$$n_k n'_k \to -1\,, \tag{2.62}$$

and

$$e_k^{\mathrm{SV}} n'_k = -e_k^{\mathrm{SV}'} n_k \to 0\,. \tag{2.63}$$

Applying these relations to the weighting factors $A_r^{\odot\oplus}$ (equations 2.37 - 2.41) yields

$$A_r^{\mathrm{PP}} = \left[3\left(\frac{s_{\mathrm{P}}}{s}\right)^2 \bar{\alpha} + 2\left(\frac{s_{\mathrm{P}}}{s_{\mathrm{S}}}\right)^2 \bar{\beta} - \bar{\rho}\right]\left(n_l f_l^{\mathrm{P}}\right) n'_r\,, \tag{2.64}$$

$$A_r^{\mathrm{PSV}} = A_r^{\mathrm{SVP}} = 0\,, \tag{2.65}$$

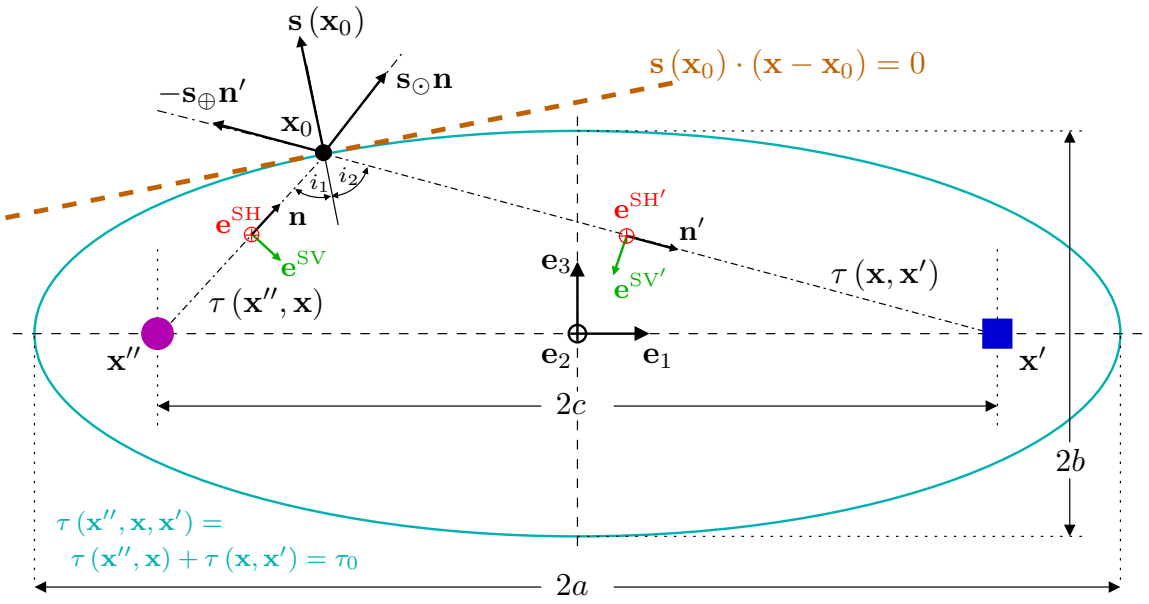

Figure 2.4: Cross section of the isochronal surface in the $\mathbf{e}_2 = 0$ plane for a fixed total traveltime τ_0 and a fixed source-receiver position. The isochronal surface is defined by the quantities $2a$ (i.e., the major axis), $2b$ (i.e., the minor axis) and $2c$, (i.e., the distance between the source location (pink) at $\mathbf{x}''$ and the receiver location (blue) at $\mathbf{x}'$). Reflections at $t = \tau_0$ can only arise when the corresponding isochronal surface becomes (locally) tangent to a scattering plane, as indicated by the brown tangent (at $\mathbf{x} = \mathbf{x}_0$) with the corresponding equation. The Figure was made after Geerits et al. (2013).

$$A_r^{\mathrm{SVSV}} = -\left[-\bar{\beta}+\bar{\rho}\right]\left(p_k^{\mathrm{S}} e_k^{\mathrm{SV}}\right) e_r^{\mathrm{SV}'}\,, \tag{2.66}$$

$$A_r^{\mathrm{SHSH}} = \left[-\bar{\beta}+\bar{\rho}\right]\left(p_k^{\mathrm{S}} e_k^{\mathrm{SH}}\right) e_r^{\mathrm{SH}'}\,, \tag{2.67}$$

and reveals that converted waves (PSV and SVP) vanish in zero-offset cases. For the introduced scattering coefficients $\mathcal{R}^{\odot\oplus}$ (cf. equations 2.54 - 2.58) this implies

$$\mathcal{R}^{\mathrm{PP}}(\mathbf{x}) = 3\left(\frac{s_{\mathrm{P}}}{s}\right)^2\bar{\alpha} + 2\left(\frac{s_{\mathrm{P}}}{s_{\mathrm{S}}}\right)^2\bar{\beta} - \bar{\rho}\,, \tag{2.68}$$

$$\mathcal{R}^{\mathrm{PSV}}(\mathbf{x}) = \mathcal{R}^{\mathrm{SVP}}(\mathbf{x}) = 0\,, \tag{2.69}$$

$$\mathcal{R}^{\mathrm{SVSV}}(\mathbf{x}) = -\mathcal{R}^{\mathrm{SHSH}}(\mathbf{x}) = \bar{\beta} - \bar{\rho}\,. \tag{2.70}$$

2.4.1 Zero-offset Born scattering in the presence of a plane scatterer

Since source and receiver coordinates coincide for zero offset, leading to equation 2.61, the Sagittal plane (introduced in Figure 2.3) is no longer clearly defined. Hence, a new Sagittal plane can be chosen. With regard to the calculations of the first-order scattered wave field in the presence of a plane scatterer, being parallel to the borehole axis (cf. Figure 2.3), the new Sagittal plane is chosen to be defined through the polarization vector of the incident wave $\mathbf{n}$ and the unit normal vector of the chosen scatterer, i.e., $\mathbf{e}_3$. Hence, the plane scatterer being parallel to the borehole axis is realized by a Heaviside step function change in all three elastodynamic compliance parameters $\delta\Lambda, \delta\mathrm{M}$ and $\delta\rho$ across a plane that is defined through $\mathbf{s}_0 \cdot \mathbf{x} = \mathbf{s}_0 \cdot \mathbf{x}_0$ (cf. Figure 2.5). Considering the scattering coefficients this leads to

$$\begin{aligned}\mathcal{R}^{\odot\oplus}(\mathbf{x}) &= \overline{\mathcal{R}}^{\odot\oplus} \times H\left[2s_{\odot}\mathbf{n}_0 \cdot (\mathbf{x} - \mathbf{x}_0)\right] \\ &= \overline{\mathcal{R}}^{\odot\oplus} \times \begin{cases} 1, & \mathbf{n}_0 \cdot \mathbf{x} > \mathbf{n}_0 \cdot \mathbf{x}_0 \\ \frac{1}{2}, & \mathbf{n}_0 \cdot \mathbf{x} = \mathbf{n}_0 \cdot \mathbf{x}_0 \\ 0, & \mathbf{n}_0 \cdot \mathbf{x} < \mathbf{n}_0 \cdot \mathbf{x}_0 \end{cases},\end{aligned} \tag{2.71}$$

where

$$\overline{\mathcal{R}}^{\mathrm{PP}} = 3\left(\frac{s_{\mathrm{P}}}{s}\right)^2 \alpha^* + 2\left(\frac{s_{\mathrm{P}}}{s_{\mathrm{S}}}\right)^2 \beta^* - \rho^* \tag{2.72}$$

and

$$\overline{\mathcal{R}}^{\mathrm{SVSV}} = -\overline{\mathcal{R}}^{\mathrm{SHSH}} = \beta^* - \rho^*\,, \tag{2.73}$$

with the corresponding dimensionless coefficients

$$\alpha^* = \frac{\Lambda}{(3\Lambda + 2\mathrm{M})}(\delta\Lambda - \delta\mathrm{M}) - \frac{\Lambda}{2\mathrm{M}}\delta\mathrm{M}\,, \tag{2.74}$$

where

$$\delta\mathrm{M} = \beta^* = \frac{\mathrm{M}^{\mathrm{scatterer}}}{\mathrm{M}} - 1\,, \tag{2.75}$$

$$\delta\Lambda = \frac{\Lambda^{\mathrm{scatterer}}}{\Lambda} - 1\,, \tag{2.76}$$

and

$$\delta\rho = \rho^* = \frac{\rho^{\mathrm{scatterer}}}{\rho} - 1\,, \tag{2.77}$$

while Λ, M and ρ denote the fundamental elastodynamic parameters of the background medium and $\Lambda^{\mathrm{scatterer}}, \mathrm{M}^{\mathrm{scatterer}}$ and $\rho^{\mathrm{scatterer}}$ denote the fundamental elastodynamic parameters of the scatterer, i.e., for $\mathbf{n}_0 \cdot \mathbf{x} > \mathbf{n}_0 \cdot \mathbf{x}_0$ (cf. Figure 2.5).

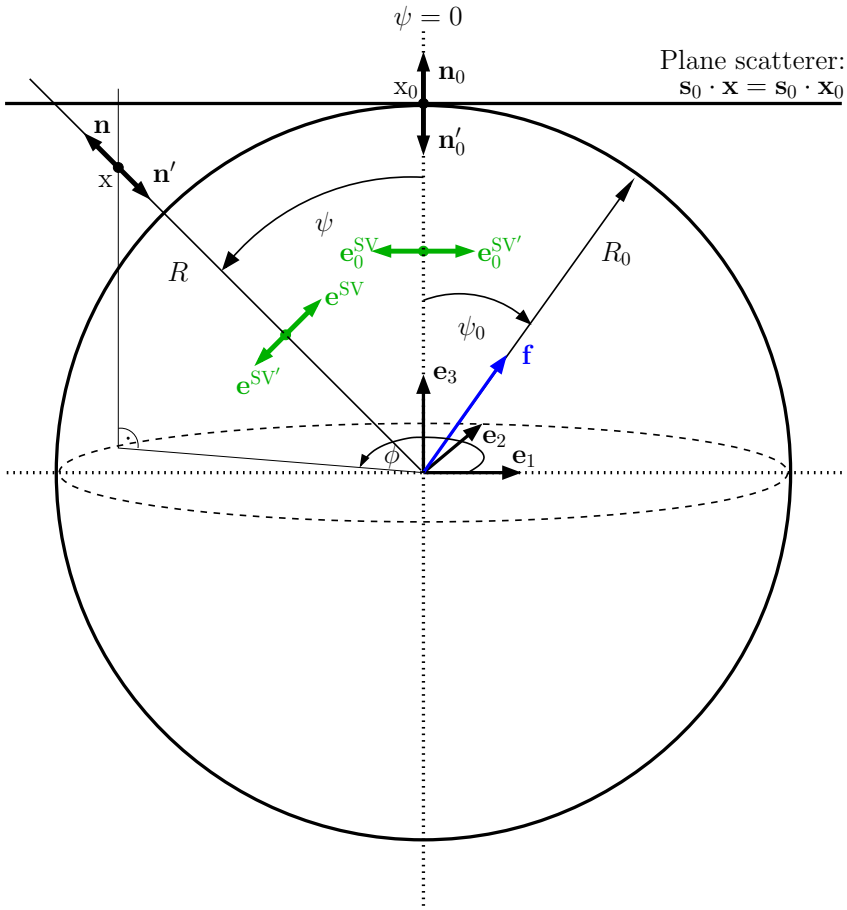

Figure 2.5: The introduced spherical coordinate system with $R = |\mathbf{x}|$, $0 \leq \psi \leq \pi$ and $0 \leq \phi < 2\pi$. Source and receiver coordinate $\mathbf{x}''$ and $\mathbf{x}'$, respectively, collapse in the center of the indicated sphere ($\mathbf{x}'' = \mathbf{x}' = 0$) with radius R_0 being the distance to the plane scatterer, which is described by a Heaviside step function. The originally used Cartesian coordinate system is also displayed. The Figure is taken from Geerits et al. (2013) and has been modified.

As illustrated in Figure 2.5, spherical coordinates are introduced, where

$$\begin{aligned} x_1 &= R\sin(\psi)\cos(\phi)\ , \\ x_2 &= R\sin(\psi)\sin(\phi)\ , \\ x_3 &= R\cos(\psi)\ , \end{aligned} \tag{2.78}$$

with $R = |\mathbf{x}|$, $0 \leq \psi \leq \pi$ and $0 \leq \phi < 2\pi$. Source and receiver coordinate $\mathbf{x}''$ and $\mathbf{x}'$, respectively, collapse in the center of the indicated sphere ($\mathbf{x}'' = \mathbf{x}' = 0$) with radius R_0 being the distance to the scatterer. This change of coordinate system facilitates the analytic solution of equation 2.59 considerably. Applying equation 2.78 to the definition of the Heaviside step function in case of $\mathbf{n}_0 = \mathbf{e}_3$ transforms equation 2.71 to

$$\begin{aligned} \mathcal{R}^{\odot\oplus}(\mathbf{x}) &= \overline{\mathcal{R}}^{\odot\oplus} \times H\left[2s_{\odot}\left(R\cos(\psi) - R_0\right)\right] \\ &= \overline{\mathcal{R}}^{\odot\oplus} \times \begin{cases} 1, & R\cos(\psi) > R_0 \\ \frac{1}{2}, & R\cos(\psi) = R_0 \\ 0, & R\cos(\psi) < R_0 \end{cases} . \end{aligned} \tag{2.79}$$

As a consequence $\mathbf{e}^{\mathrm{W}} = \mathbf{e}_3$ and the polarization vectors of the incident and the scattered wave, given in equations 2.45, 2.46 and 2.27 transform to

$$\mathbf{n} = -\mathbf{n}' = \begin{pmatrix} \sin(\psi)\cos(\phi) \\ \sin(\psi)\sin(\phi) \\ \cos(\phi) \end{pmatrix} , \tag{2.80}$$

$$\mathbf{e}^{\mathrm{SV}} = \mathbf{e}^{\mathrm{SV}'} = \begin{pmatrix} \cos(\psi)\cos(\phi) \\ \cos(\psi)\sin(\phi) \\ -\sin(\phi) \end{pmatrix} \tag{2.81}$$

and

$$\mathbf{e}^{\mathrm{SH}} = -\mathbf{e}^{\mathrm{SH}'} = \begin{pmatrix} -\sin(\phi) \\ \cos(\phi) \\ 0 \end{pmatrix} . \tag{2.82}$$

In consideration of equations 2.79 - 2.82 the transformation to spherical coordinates is also applied to equation 2.59, yielding $dV = R^2\sin(\psi)\,dR\,d\psi\,d\phi$ and

$$\hat{v}_r^{\mathrm{scat}} = -\frac{i\omega^3}{(4\pi)^2\rho}\sum_{\odot,\oplus} s_{\odot}^4\,\hat{T}\,\overline{\mathcal{R}}^{\odot\oplus}\hat{\mathcal{I}}_r^{\odot\oplus;n}(R_0, s_{\odot}) \quad \text{with} \quad \odot,\oplus \in \{\mathrm{P},\mathrm{S}\}\ , \tag{2.83}$$

where

$$\hat{\mathcal{I}}_r^{\odot\oplus;n}(R_0, s_\odot) = \\ -\int_{R=0}^{\infty}\int_{\psi=0}^{\frac{\pi}{2}}\int_{\phi=0}^{\pi} \exp\left[i\omega\left(2s_\odot R\right)\right] H\left[2s_\odot\left(R\cos\left(\psi\right) - R_0\right)\right] \times \zeta_r^{\oplus} D_n^{\odot}\left(\psi,\phi\right)\sin\left(\psi\right) dR\, d\psi\, d\phi \tag{2.84}$$

In equation 2.84, $s_\odot$ denotes the slowness of the incident wave, $\zeta_r^{\oplus} = \left\{n_r', e^{\mathrm{SV}'}, e^{\mathrm{SH}'}\right\}$ represents the polarization vector of the scattered wave (given in equations 2.80 - 2.82) and $D_n^{\odot}$ represents the directivity of order n of the incident wave.

2.4.2 Zero-offset Born scattering due to an arbitrary dipole excitation

To proceed with the calculation of the spectral scattered wave particle velocity in the presence of a plane scatterer, in the next step the source directivity has to be defined. Hence, an arbitrary dipole excitation is chosen, where the unitary dipole force source vector $\mathbf{f}$ is arbitrarily oriented relative to $\mathbf{e}_3$. With reference to Figure 2.5 this vector is defined as

$$\mathbf{f} = \sin\left(\psi_0\right)\cos\left(\phi_0\right)\mathbf{e}_1 + \sin\left(\psi_0\right)\sin\left(\phi_0\right)\mathbf{e}_2 + \cos\left(\psi_0\right)\mathbf{e}_3\,. \tag{2.85}$$

According to the superposition principle, the unitary dipole source vector is composed of three fundamental dipole excitations that are oriented along the three spatial directions $\mathbf{e}_1$, $\mathbf{e}_2$ and $\mathbf{e}_3$ and weighted by the factors $\sin\left(\psi_0\right)\cos\left(\phi_0\right)$, $\sin\left(\psi_0\right)\sin\left(\phi_0\right)$ and $\cos\left(\psi_0\right)$, respectively. The three corresponding fundamental dipole directivities for the incident wave can easily be derived from equations B.5 and B.6 and then be superimposed according to equation 2.85. Accordingly, they are

$$D_1^{\mathrm{P}}\left(\mathbf{x}\right) = \mathbf{n}\cdot\mathbf{e}_r\,, \tag{2.86}$$

$$D_1^{\mathrm{SV}}\left(\mathbf{x}\right) = \mathbf{D}_1^{\mathrm{S}}\cdot\mathbf{e}^{\mathrm{SV}} = \left[\mathbf{n}\times\left(\mathbf{e}_r\times\mathbf{n}\right)\right]\mathbf{e}^{\mathrm{SV}}\,, \tag{2.87}$$

$$D_1^{\mathrm{SH}}\left(\mathbf{x}\right) = \mathbf{D}_1^{\mathrm{S}}\cdot\mathbf{e}^{\mathrm{SH}} = \left[\mathbf{n}\times\left(\mathbf{e}_r\times\mathbf{n}\right)\right]\mathbf{e}^{\mathrm{SH}}\,, \tag{2.88}$$

with $r \in \{1,2,3\}$.

Following this line of argument, I show the first-order scattered wave field particle velocity for all three fundamental dipole excitations below. Since the mathematical derivations corresponding to the three excitations are quite similar, only the derivation for a dipole excitation along $\mathbf{e}_3$ (i.e., an excitation perpendicular to the earlier defined scatterer) is carried out explicitly. The other two results are summarized afterwards.

Dipole excitation perpendicular to the scatterer, i.e. along $\mathbf{e}_3$

In this case, $\mathbf{e}_r = \mathbf{e}_3$ in equations 2.86 - 2.88. The transformation of the resulting dipole directivities for the incident wave to spherical coordinates yields

$$D_1^{\mathrm{P}}(\psi) = \cos(\psi) \,, \tag{2.89}$$

$$D_1^{\mathrm{SV}}(\psi) = -\sin(\psi) \,, \tag{2.90}$$

$$D_1^{\mathrm{SH}}(\psi) = 0 \,. \tag{2.91}$$

In the next step the polarization vectors for the scattered wave, given in equations 2.80-2.82 are substituted in equation 2.84 which has to be evaluated separately for each type of reflection. According to equation 2.91 the SHSH-reflection vanishes. Since in zero-offset cases no converted waves occur, only the PP- and the SVSV-reflection remain. Hence,

$$\begin{pmatrix} \hat{\mathcal{I}}_1^{\mathrm{PP};1} \\ \hat{\mathcal{I}}_2^{\mathrm{PP};1} \\ \hat{\mathcal{I}}_3^{\mathrm{PP};1} \end{pmatrix} (R_0, s_{\mathrm{P}}) =$$
$$-\int_{R=0}^{\infty}\int_{\psi=0}^{\frac{\pi}{2}}\int_{\phi=0}^{\pi} \exp\left[i\omega\left(2s_{\mathrm{P}}R\right)\right] H\left[2s_{\mathrm{P}}\left(R\cos(\psi) - R_0\right)\right] \begin{pmatrix} \sin(\psi)\cos(\phi) \\ \sin(\psi)\sin(\phi) \\ \cos(\psi) \end{pmatrix} D_1^{\mathrm{P}}(\psi)\sin(\psi)\, dR\, d\psi\, d\phi \,, \tag{2.92}$$

$$\begin{pmatrix} \hat{\mathcal{I}}_1^{\mathrm{SVSV};1} \\ \hat{\mathcal{I}}_2^{\mathrm{SVSV};1} \\ \hat{\mathcal{I}}_3^{\mathrm{SVSV};1} \end{pmatrix} (R_0, s_{\mathrm{S}}) =$$
$$-\int_{R=0}^{\infty}\int_{\psi=0}^{\frac{\pi}{2}}\int_{\phi=0}^{\pi} \exp\left[i\omega\left(2s_{\mathrm{S}}R\right)\right] H\left[2s_{\mathrm{S}}\left(R\cos(\psi) - R_0\right)\right] \begin{pmatrix} \cos(\psi)\cos(\phi) \\ \cos(\psi)\sin(\phi) \\ -\sin(\psi) \end{pmatrix} D_1^{\mathrm{SV}}(\psi)\sin(\psi)\, dR\, d\psi\, d\phi \,. \tag{2.93}$$

The dependency of $\hat{\mathcal{I}}_1^{\mathrm{PP};1}, \hat{\mathcal{I}}_2^{\mathrm{PP};1}$ and $\hat{\mathcal{I}}_1^{\mathrm{SVSV};1}, \hat{\mathcal{I}}_2^{\mathrm{SVSV};1}$ on $\cos(\phi)$ and $\sin(\phi)$ linked to the integration over a full period of ϕ leads to the fact that these components vanish:

$$\hat{v}_1^{\mathrm{PP}} = \hat{v}_2^{\mathrm{PP}} = \hat{v}_1^{\mathrm{SVSV}} = \hat{v}_2^{\mathrm{SVSV}} = 0 \,. \tag{2.94}$$

Applying the substitution

$$\begin{aligned} t &= 2s_{\odot}R \quad \text{with} \quad t > 0 \,, \\ t_0 &= 2s_{\odot}R_0 \quad \text{with} \quad t_0 > 0 \,, \end{aligned} \tag{2.95}$$

with $\odot \in \{\mathrm{P,S}\}$ transforms the remaining components $\hat{\mathcal{I}}_3^{\mathrm{PP;1}}$ and $\hat{\mathcal{I}}_3^{\mathrm{SVSV;1}}$ of equations 2.92 and 2.93 to

$$\hat{\mathcal{I}}_3^{\mathrm{PP;1}}\left(R_0, s_{\mathrm{P}}\right) = -\frac{\pi}{s_{\mathrm{P}}} \int\limits_{\psi=0}^{\frac{\pi}{2}} \cos^2\left(\psi\right) \sin\left(\psi\right) d\psi \int\limits_{t=0}^{\infty} \exp\left[i\omega t\right] H\left[t\cos\left(\psi\right) - t_0^{\mathrm{P}}\right] dt \tag{2.96}$$

and

$$\hat{\mathcal{I}}_3^{\mathrm{SVSV;1}}\left(R_0, s_{\mathrm{S}}\right) = \frac{\pi}{s_{\mathrm{S}}} \int\limits_{\psi=0}^{\frac{\pi}{2}} \sin^3\left(\psi\right) d\psi \int\limits_{t=0}^{\infty} \exp\left[i\omega t\right] H\left[t\cos\left(\psi\right) - t_0^{\mathrm{S}}\right] dt\,. \tag{2.97}$$

The most right-hand side term in both equations (2.96, 2.97) represents a Fourier transform of $H\left[t\cos\left(\psi\right) - t_0^{\odot}\right]$, which can be evaluated completly analytically. By definition (Buttkus, 2000),

$$\int\limits_{t=0}^{\infty} \exp\left[i\omega t\right] H\left[t\cos\left(\psi\right) - t_0^{\odot}\right] dt = -\frac{1}{i\omega} \exp\left[i\omega \frac{t_0^{\odot}}{\cos\left(\psi\right)}\right]\,. \tag{2.98}$$

Substituting this result in equations 2.96 and 2.97 yields

$$\hat{\mathcal{I}}_3^{\mathrm{PP;1}}\left(R_0, s_{\mathrm{P}}\right) = \frac{1}{i\omega}\frac{\pi}{s_{\mathrm{P}}} \int\limits_{\psi=0}^{\frac{\pi}{2}} \exp\left[i\omega \frac{t_0^{\mathrm{P}}}{\cos\left(\psi\right)}\right] \cos^2\left(\psi\right) \sin\left(\psi\right) d\psi \tag{2.99}$$

and

$$\hat{\mathcal{I}}_3^{\mathrm{SVSV;1}}\left(R_0, s_{\mathrm{S}}\right) = -\frac{1}{i\omega}\frac{\pi}{s_{\mathrm{S}}} \int\limits_{\psi=0}^{\frac{\pi}{2}} \exp\left[i\omega \frac{t_0^{\mathrm{S}}}{\cos\left(\psi\right)}\right] \sin^3\left(\psi\right) d\psi\,. \tag{2.100}$$

With respect to an analytic solution of the resulting integrations the two following substitutions are applied

$$\begin{aligned} \frac{1}{\cos\left(\psi\right)} &= q\,, \\ t_0^{\odot} q &= t'\,. \end{aligned} \tag{2.101}$$

This yields

$$\hat{\mathcal{I}}_3^{\mathrm{PP;1}}\left(R_0, s_{\mathrm{P}}\right) = \frac{1}{i\omega}\frac{\pi}{s_{\mathrm{P}}}\frac{1}{t_0^{\mathrm{P}}} \int\limits_{t'=t_0^{\mathrm{P}}}^{\infty} \exp\left[i\omega t'\right] \left(\frac{t'}{t_0^{\mathrm{P}}}\right)^{-4} dt' \tag{2.102}$$

and

$$\hat{\mathcal{I}}_3^{\mathrm{SVSV;1}}\left(R_0, s_{\mathrm{S}}\right) = -\frac{1}{i\omega}\frac{\pi}{s_{\mathrm{S}}}\frac{1}{t_0^{\mathrm{S}}}\int\limits_{t'=t_0^{\mathrm{S}}}^{\infty} \exp\left[i\omega t'\right]\left[\left(\frac{t'}{t_0^{\mathrm{S}}}\right)^2 - 1\right]\left(\frac{t'}{t_0^{\mathrm{S}}}\right)^{-4} dt' \,, \tag{2.103}$$

where the most right hand-side terms in both equations represent Fourier transforms of $\left(\frac{t'}{t_0^{\mathrm{P}}}\right)^{-4}$ and $\left[\left(\frac{t'}{t_0^{\mathrm{S}}}\right)^2 - 1\right]\left(\frac{t'}{t_0^{\mathrm{S}}}\right)^{-4}$, respectively. Inserting equations 2.102 and 2.103 in equation 2.83 and applying the Fourier transforms finally yields explicit expressions for the spectral scattered wave particle velocities for a zero-offset configuration, resulting from a dipole excitation along $\mathbf{e}_3$ being perpendicular to a plane scatterer

$$\hat{v}_3^{\mathrm{PP}} = -\frac{\omega^2 s_{\mathrm{P}}^2}{16\pi\rho}\frac{1}{2R_0}\overline{\mathcal{R}}^{\mathrm{PP}}\hat{T}\left(\omega\right)\mathcal{F}_{t'}\left[H\left(t' - t_0^{\mathrm{P}}\right)\left(\frac{t'}{t_0^{\mathrm{P}}}\right)^{-4}\right](\omega) \tag{2.104}$$

and

$$\hat{v}_3^{\mathrm{SS}} = \hat{v}_3^{\mathrm{SVSV}} = -\frac{\omega^2 s_{\mathrm{S}}^2}{16\pi\rho}\frac{1}{2R_0}\overline{\mathcal{R}}^{\mathrm{SVSV}}\hat{T}\left(\omega\right)\mathcal{F}_{t'}\left[H\left(t' - t_0^{\mathrm{S}}\right)\left[\left(\frac{t'}{t_0^{\mathrm{S}}}\right)^2 - 1\right]\left(\frac{t'}{t_0^{\mathrm{S}}}\right)^{-4}\right](\omega) \tag{2.105}$$

since

$$\hat{v}_3^{\mathrm{SHSH}} = 0 \,, \tag{2.106}$$

where $\mathcal{F}\left(\omega\right)$ denotes the Fourier-transform operator, depending on ω. Remembering that the first two components $\hat{v}_1^{\odot\oplus}$ and $\hat{v}_2^{\odot\oplus}$ vanish completely, it can be concluded that the observed scattered wave field particle velocity is not only proportional to the occurring Fourier transforms, respectively, but with regard to equation 2.95 it is also inversely proportional to $2R_0$, i.e., the two way travel distance to the scatterer.

Dipole excitation parallel to the scatterer along $\mathbf{e}_2$

In this case, $\mathbf{e}_r = \mathbf{e}_2$ in equations 2.86 - 2.88. The transformation of the resulting dipole directivities for the incident wave to spherical coordinates yields

$$D_1^{\mathrm{P}}\left(\psi, \phi\right) = \sin\left(\psi\right)\sin\left(\phi\right) \,, \tag{2.107}$$

$$D_1^{\mathrm{SV}}\left(\psi\phi\right) = \cos\left(\psi\right)\sin\left(\phi\right) \,, \tag{2.108}$$

$$D_1^{\mathrm{SH}}\left(\psi\phi\right) = \cos\left(\phi\right) \,, \tag{2.109}$$

while the polarization vectors for the scattered waves are still given by equations 2.80 - 2.82. Including these expressions in equation 2.84 and following the evaluation procedure given for

a dipole excitation along $\mathbf{e}_3$ yields the following explicit expressions for the spectral scattered wave particle velocity for a zero-offset configuration, resulting from a dipole excitation along $\mathbf{e}_2$ being parallel to a plane scatterer

$$\hat{v}_2^{\mathrm{PP}} = -\frac{\omega^2 s_{\mathrm{P}}^2}{16\pi\rho}\frac{1}{2R_0}\overline{\mathcal{R}}^{\mathrm{PP}}\hat{T}\left(\omega\right)\mathcal{F}_{t'}\left[H\left(t'-t_0^{\mathrm{P}}\right)\left[\left(\frac{t'}{t_0^{\mathrm{P}}}\right)^2-1\right]\left(\frac{t'}{t_0^{\mathrm{P}}}\right)^{-4}\right](\omega) \tag{2.110}$$

and

$$\hat{v}_2^{\mathrm{SS}} = \hat{v}_2^{\mathrm{SVSV}} + \hat{v}_2^{\mathrm{SHSH}} = \frac{\omega^2 s_{\mathrm{S}}^2}{16\pi\rho}\frac{1}{2R_0}\overline{\mathcal{R}}^{\mathrm{SS}}\hat{T}\left(\omega\right)\mathcal{F}_{t'}\left[H\left(t'-t_0^{\mathrm{S}}\right)\left[\left(\frac{t'}{t_0^{\mathrm{S}}}\right)^{-4}+\left(\frac{t'}{t_0^{\mathrm{S}}}\right)^{-2}\right]\right](\omega) \tag{2.111}$$

with

$$\hat{v}_2^{\mathrm{SVSV}} = \frac{\omega^2 s_{\mathrm{S}}^2}{32\pi\rho}\frac{1}{2R_0}\overline{\mathcal{R}}^{\mathrm{SVSV}}\hat{T}\left(\omega\right)\mathcal{F}_{t'}\left[H\left(t'-t_0^{\mathrm{S}}\right)\left(\frac{t'}{t_0^{\mathrm{S}}}\right)^{-4}\right](\omega) \tag{2.112}$$

and

$$\hat{v}_2^{\mathrm{SHSH}} = -\frac{\omega^2 s_{\mathrm{S}}^2}{32\pi\rho}\frac{1}{2R_0}\overline{\mathcal{R}}^{\mathrm{SHSH}}\hat{T}\left(\omega\right)\mathcal{F}_{t'}\left[H\left(t'-t_0^{\mathrm{S}}\right)\left(\frac{t'}{t_0^{\mathrm{S}}}\right)^{-2}\right](\omega) \tag{2.113}$$

and $\overline{\mathcal{R}}^{\mathrm{SVSV}} = -\overline{\mathcal{R}}^{\mathrm{SHSH}} = \overline{\mathcal{R}}^{\mathrm{SS}}$ according to equation 2.73.

Obviously, in this case, the dependency of $\hat{\mathcal{I}}_1^{\mathrm{PP};1}$, $\hat{\mathcal{I}}_3^{\mathrm{PP};1}$, $\hat{\mathcal{I}}_1^{\mathrm{SVSV};1}$, $\hat{\mathcal{I}}_3^{\mathrm{SVSV};1}$ and $\hat{\mathcal{I}}_1^{\mathrm{SHSH};1}$, $\hat{\mathcal{I}}_3^{\mathrm{SHSH};1}$ on $\cos\left(\phi\right)$ and $\sin\left(\phi\right)$ linked to the integration over a full period of ϕ leads to the fact that the according components vanish:

$$\hat{v}_1^{\mathrm{PP}} = \hat{v}_3^{\mathrm{PP}} = \hat{v}_1^{\mathrm{SVSV}} = \hat{v}_3^{\mathrm{SVSV}} = \hat{v}_1^{\mathrm{SHSH}} = \hat{v}_3^{\mathrm{SHSH}} = 0\,. \tag{2.114}$$

Dipole excitation parallel to the scatterer along $\mathbf{e}_1$

In this case, $\mathbf{e}_r = \mathbf{e}_1$ in equations 2.86 - 2.88. The transformation of the resulting dipole directivities for the incident wave to spherical coordinates yields

$$D_1^{\mathrm{P}}\left(\psi,\phi\right) = \sin\left(\psi\right)\cos\left(\phi\right)\,, \tag{2.115}$$

$$D_1^{\mathrm{SV}}\left(\psi\phi\right) = \cos\left(\psi\right)\cos\left(\phi\right)\,, \tag{2.116}$$

$$D_1^{\mathrm{SH}}\left(\psi\phi\right) = -\sin\left(\phi\right)\,, \tag{2.117}$$

while the polarization vectors for the scattered waves are again given by equations 2.80 - 2.82. Including these expressions in equation 2.84 and following the evaluation procedure given for

a dipole excitation along $\mathbf{e}_3$ yields the following explicit expressions for the spectral scattered wave particle velocity for a zero-offset configuration, resulting from a dipole excitation along $\mathbf{e}_1$ being parallel to a plane scatterer

$$\hat{v}_1^{\mathrm{PP}} = -\frac{\omega^2 s_{\mathrm{P}}^2}{16\pi\rho}\frac{1}{2R_0}\overline{\mathcal{R}}^{\mathrm{PP}}\hat{T}\left(\omega\right)\mathcal{F}_{t'}\left[H\left(t'-t_0^{\mathrm{P}}\right)\left[\left(\frac{t'}{t_0^{\mathrm{P}}}\right)^2-1\right]\left(\frac{t'}{t_0^{\mathrm{P}}}\right)^{-4}\right](\omega) \tag{2.118}$$

and

$$\hat{v}_1^{\mathrm{SS}} = \hat{v}_1^{\mathrm{SVSV}} + \hat{v}_1^{\mathrm{SHSH}} = \frac{\omega^2 s_{\mathrm{S}}^2}{16\pi\rho}\frac{1}{2R_0}\overline{\mathcal{R}}^{\mathrm{SS}}\hat{T}\left(\omega\right)\mathcal{F}_{t'}\left[H\left(t'-t_0^{\mathrm{S}}\right)\left[\left(\frac{t'}{t_0^{\mathrm{S}}}\right)^{-4}+\left(\frac{t'}{t_0^{\mathrm{S}}}\right)^{-2}\right]\right](\omega) \tag{2.119}$$

with

$$\hat{v}_1^{\mathrm{SVSV}} = \frac{\omega^2 s_{\mathrm{S}}^2}{32\pi\rho}\frac{1}{2R_0}\overline{\mathcal{R}}^{\mathrm{SVSV}}\hat{T}\left(\omega\right)\mathcal{F}_{t'}\left[H\left(t'-t_0^{\mathrm{S}}\right)\left(\frac{t'}{t_0^{\mathrm{S}}}\right)^{-4}\right](\omega) \tag{2.120}$$

and

$$\hat{v}_1^{\mathrm{SHSH}} = -\frac{\omega^2 s_{\mathrm{S}}^2}{32\pi\rho}\frac{1}{2R_0}\overline{\mathcal{R}}^{\mathrm{SHSH}}\hat{T}\left(\omega\right)\mathcal{F}_{t'}\left[H\left(t'-t_0^{\mathrm{S}}\right)\left(\frac{t'}{t_0^{\mathrm{S}}}\right)^{-2}\right](\omega) \tag{2.121}$$

and $\overline{\mathcal{R}}^{\mathrm{SS}} = \overline{\mathcal{R}}^{\mathrm{SVSV}} = -\overline{\mathcal{R}}^{\mathrm{SHSH}}$ according to equation 2.73.

Obviously, in this case, the dependency of $\hat{\mathcal{I}}_2^{\mathrm{PP};1}$, $\hat{\mathcal{I}}_3^{\mathrm{PP};1}$, $\hat{\mathcal{I}}_2^{\mathrm{SVSV};1}$, $\hat{\mathcal{I}}_3^{\mathrm{SVSV};1}$ and $\hat{\mathcal{I}}_2^{\mathrm{SHSH};1}$, $\hat{\mathcal{I}}_3^{\mathrm{SHSH};1}$ on $\cos\left(\phi\right)$ and $\sin\left(\phi\right)$ linked to the integration over a full period of ϕ leads to the fact that the according components vanish:

$$\hat{v}_2^{\mathrm{PP}} = \hat{v}_3^{\mathrm{PP}} = \hat{v}_2^{\mathrm{SVSV}} = \hat{v}_3^{\mathrm{SVSV}} = \hat{v}_2^{\mathrm{SHSH}} = \hat{v}_3^{\mathrm{SHSH}} = 0\,. \tag{2.122}$$

Due to symmetry reasons the final results for the scattered wave particle velocity due to a dipole excitation along $\mathbf{e}_1$ and a dipole excitation along $\mathbf{e}_2$ are equal. As equations 2.110, 2.111 and 2.118, 2.119 reveal, they only differ in terms of the component, on which the scattered wave particle velocity occurs.

To finally arrive at an explicit expression for the spectral scattered wave particle velocity due to an arbitrary oriented dipole excitation, the superposition principle is applied according to equation 2.85 and yields

$$\hat{\mathbf{v}}^{\mathrm{total}} = \sin\left(\psi_0\right)\cos\left(\phi_0\right)\begin{pmatrix}\hat{v}_1^{\mathrm{scat}}\\0\\0\end{pmatrix} + \sin\left(\psi_0\right)\sin\left(\phi_0\right)\begin{pmatrix}0\\\hat{v}_2^{\mathrm{scat}}\\0\end{pmatrix} + \cos\left(\psi_0\right)\begin{pmatrix}0\\0\\\hat{v}_3^{\mathrm{scat}}\end{pmatrix}, \tag{2.123}$$

where

$$\hat{v}_r^{\mathrm{scat}} = \hat{v}_r^{\mathrm{PP}} + \hat{v}_r^{\mathrm{SVSV}} + \hat{v}_r^{\mathrm{SHSH}} \quad \text{with} \quad r \in \{1,2,3\}\,. \tag{2.124}$$

2.4.3 Physical interpretation

The comparison of all derived zero-offset results for the scattered wave particle velocity in the presence of a plane scatterer due to a dipole excitation (cf. equations 2.104 - 2.105, 2.110 - 2.111, 2.118 - 2.119) shows, that these results can be summarized as

$$\hat{v}_r^{\text{scat},\otimes} \propto -\frac{\overline{\mathcal{R}}^{\otimes}}{2R_0}\,\omega^2\,\hat{T}\,(\omega)\,\mathcal{F}_{t'}\left[H\left(t'-t_0^{\otimes}\right)\mathcal{G}_r^{\otimes}\left(\frac{t'}{t_0^{\otimes}}\right)\right](\omega) \quad \text{with} \quad \otimes \in \{\text{PP, SS}\}\ , \tag{2.125}$$

where $\propto$ indicates proportionality. The function $\mathcal{G}_r^{\otimes}$ depends only on the considered wave type and is a function of the argument $\left(\frac{t'}{t_0^{\otimes}}\right)$. Hence, the function $\mathcal{G}_r^{\otimes}$ directly follows from the comparison between equation 2.125 and the according excitation specific result (cf. equations 2.104 - 2.105, 2.110 - 2.111, 2.118 - 2.119).

In order to arrive at a physical interpretation of equation 2.125, an analysis of the scattered wave field particle displacement $\hat{u}_r^{\text{scat},\otimes}$ is performed in the time domain. According to Buttkus (2000) $\hat{v}_r^{\text{scat},\otimes} = -i\omega\,\hat{u}_r^{\text{scat},\otimes}$. Thus, the time domain scattered wave field particle displacement follows from equation 2.125 as

$$u_r^{\text{scat},\otimes} \propto \frac{\overline{\mathcal{R}}^{\otimes}}{2R_0}\left[T\,(t') * \frac{d}{dt'}\left[H\left(t'-t_0^{\otimes}\right)\mathcal{G}_r^{\otimes}\left(\frac{t'}{t_0^{\otimes}}\right)\right]\right](\omega) \quad \text{with} \quad \otimes \in \{\text{PP, SS}\}\ , \tag{2.126}$$

where $*$ indicates the convolution operator. Performing the differentiation with respect to t' and evaluating the resulting two convolutions, yields

$$u_r^{\text{scat},\otimes}\,(t) = u_r^{\text{scat},\otimes,\text{A}}\,(t) + u_r^{\text{scat},\otimes,\text{B}}\,(t)\ , \tag{2.127}$$

where

$$u_r^{\text{scat},\otimes,\text{A}}\,(t) \propto \frac{\overline{\mathcal{R}}^{\otimes}}{2R_0} T\left(t-t_0^{\otimes}\right)\mathcal{G}_r^{\otimes}\,(1) \tag{2.128}$$

and

$$u_r^{\text{scat},\otimes,\text{B}}\,(t) \propto \frac{\overline{\mathcal{R}}^{\otimes}}{2R_0}\left[\frac{1}{t_0^{\otimes}}\int\limits_{t'=t_0^{\otimes}}^{\infty} T\,(t-t')\,\frac{d}{d\left(\frac{t'}{t_0^{\otimes}}\right)}\left[\mathcal{G}_r^{\otimes}\left(\frac{t'}{t_0^{\otimes}}\right)\right]dt'\right]\ . \tag{2.129}$$

Equations 2.127 - 2.129 reveal that the total scattered particle displacement is composed of two parts. The first one, specified in equation 2.128, clearly presents the dominant part and is denoted as the specular part of the wave field (Geerits et al., 2013; Comninos, 2006). In principle, it presents a by $\frac{t'}{t_0^{\otimes}}$ time-delayed and in the amplitude decreased reproduction of the source pulse. The amplitude-decrease is proportional to the contrast parameter $\overline{\mathcal{R}}^{\otimes}$ and inversely proportional to $2R_0$, denoting the sum of the incident and scattered ray path (cf. Figure 2.5). The second part,

specified in equation 2.129, is denoted as the diffuse part of the wave field. It is also time-delayed by $\frac{t'}{t_0^{\otimes}}$ relative to the source pulse and its decreased amplitude is also proportional to the contrast parameter $\overline{\mathcal{R}}^{\otimes}$ and inversely proportional to $2R_0$. However, the diffuse part of the wave field does not present a reproduction of the source pulse.

For all considered cases in this work, the function $\mathcal{G}_r^{\otimes}$ in equation 2.128 yields either ± 1 or 0, while the latter only occurs in case the source directivity vanishes at the image point associated with $2R_0$, i.e., the sum of the incident and scattered ray path. In this case, the total scattered wave particle displacement only consists of $u_r^{\text{scat},\otimes,\text{B}}(t)$ (cf. equation 2.129), i.e., the diffuse part of the wave field, which is present in any case. For the sake of completeness the concrete expressions for $\mathcal{G}_r^{\otimes}\left(\frac{t'}{t_0^{\otimes}}\right)$ are summarized in appendix C together with the according differentiations, occurring in equation 2.129.

Chapter 3

Validation of the approach: sensitivity and accuracy analysis

In order to verify the validation of the derived approach, in this chapter I compare the zero-offset analytic Born results for the scattered wave particle displacement due to a dipole excitation (cf. equations 2.127, 2.128, 2.129) with the quasi-analytic results of a benchmark code, named *qseis*. The latter is a reflectivity method (Kennett, 1983) based *FORTRAN* code using the wavenumber integration technique. Wang (1999) describes the principles of the implementation which are based on a horizontally layered, homogeneous and isotropic elastic medium.

The following sensitivity and accuracy analysis was performed for the two setups shown in Figure 3.1. In a first study I investigated the results for a plane scatterer over a half-space, where the scatterer is parallel to the borehole axis (cf. Figure 3.1, left). In a second study I then investigated the results for a dipped scatterer over a half-space (cf. Figure 3.1, right). While the elastic parameters of the background medium Λ, M and ρ were fixed in all tests, the elastic parameters of the scatterer $\Lambda(\mathbf{x}), \mathrm{M}(\mathbf{x})$ and $\rho(\mathbf{x})$ were calculated using perturbations in the range $-0.3 \leq \delta\mathrm{M} \leq 0.3$ (cf. equation 2.75), $-0.3 \leq \delta\Lambda \leq 0.3$ (cf. equation 2.76) and $-0.3 \leq \delta\rho \leq 0.3$ (cf. equation 2.77). According to equations 2.22 and 2.23 the resulting slownesses for both the P- and S-wave were calculated. The corresponding P- and S-wave velocities arise from the reciprocal values, respectively. They are presented together with the background parameters (highlighted in gray) in Table 3.1.

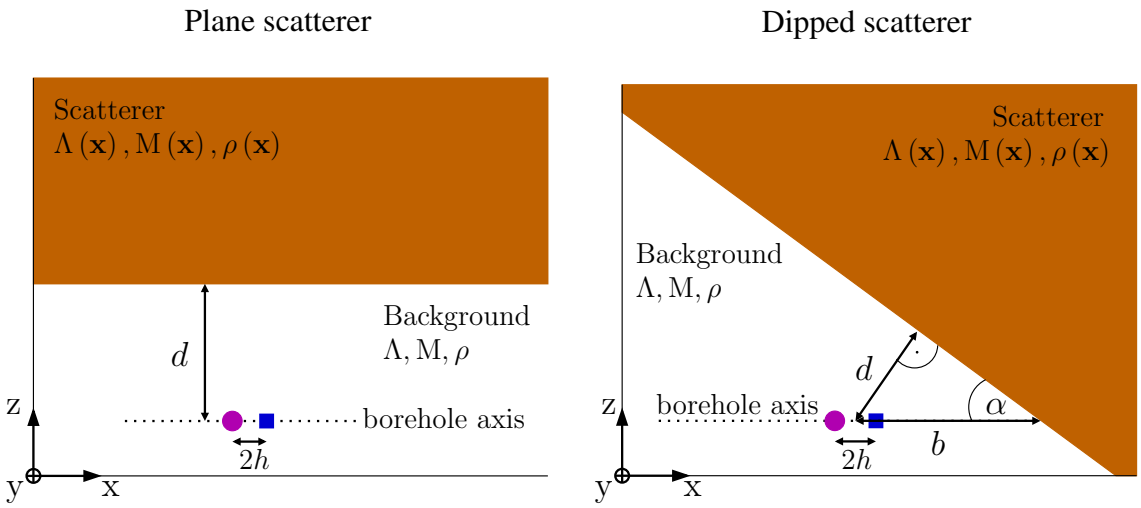

Figure 3.1: The two setups used for the sensitivity and accuracy analysis to verify the validation of the developed approach. Left: the plane scatterer is parallel to the borehole axis and has a distance d to source and receiver that offset by $2h$. Right: source and receiver offset by $2h$. Their midpoint has an horizontal offset b and a distance d to the dipped scatterer that intersects the borehole axis with the angle α. In both setups as source a single force source was used, realized by a Ricker wavelet with $f_c = 1\,\text{kHz}$ and a maximum amplitude of 1 N.

Table 3.1: Elastic properties $v_{\mathrm{P}}, v_{\mathrm{S}}$ and ρ for the background medium (highlighted in gray) and the scatterer used in the sensitivity and accuracy analysis. The corresponding slowness values are given in µs/ft for perspicuity reasons for the American readers. According to equations 2.22 and 2.23 the listed parameters for the scatterer result from perturbations of the fixed background parameters between -30% and $+30\%$, i.e., $\{\delta\mathrm{M}, \delta\Lambda, \delta\rho\} = (-0.3, -0.2, -0.1, 0.1, 0.2, 0.3)$ (cf. equations 2.75 - 2.77).

δM	v_{P} (in m/s) s_{P} (in µs/ft)	v_{S} (in m/s) s_{S} (in µs/ft)	ρ (in kg/m^3)
0.3	3678 82.9	2226 136	2100
0.2	3925 77.7	2317 131	2100
0.1	4244 71.8	2420 125	2100
0	4688 65	2538 120	2100
-0.1	5385 56.6	2675 113	2100
-0.2	6805 44.8	2838 107	2100
-0.3	14810 20.6	3033 100	2100

$\delta\mathbf{\Lambda}$	v_{P} (in m/s) s_{P} (in µs/ft)	v_{S} (in m/s) s_{S} (in µs/ft)	ρ (in kg/m^3)
0.3	6731 45.3	2538 120	2100
0.2	5640 54.0	2538 120	2100
0.1	5057 60.3	2538 120	2100
0	4688 65	2538 120	2100
-0.1	4431 68.8	2538 120	2100
-0.2	4242 71.9	2538 120	2100
-0.3	4096 74.4	2538 120	2100

$\delta\rho$	v_{P} (in m/s) s_{P} (in µs/ft)	v_{S} (in m/s) s_{S} (in µs/ft))	ρ (in kg/m^3)
0.3	4112 74.1	2226 136	2730
0.2	4280 71.2	2317 131	2520
0.1	4470 68.2	2420 125	2310
0	4688 65	2538 120	2100
-0.1	4942 61.7	2675 114	1890
-0.2	5241 58.2	2838 107	1680
-0.3	5603 54.4	3033 101	1470

Table 3.2: Setup-parameters used in the sensitivity and accuracy analysis: d denotes the distance from the borehole axis to the plane scatterer and h denotes half of the source-receiver offset.

	Configuration 1	Configuration 2	Configuration 3
d (in m)	4.8	17.68	30.48
h (in m)	0.48	1.77	3.05

3.1 Plane scatterer (parallel to the borehole axis) over a half-space

Firstly, the results for a model, where the plane scatterer is parallel to the borehole axis are investigated. The detailed setup is sketched in Figure 3.1 (left) and is described in the introduction of this chapter. Based on the explained setup, three quasi zero-offset configurations were built with typical distances d between the borehole axis and the plane scatterer. Table 3.2 gives an overview of the investigated configurations. Due to implementation-limitations, it is not possible to evaluate a true zero-offset case in *qseis*. Therefore, I applied a far-field criterion, ensuring that half the source-receiver offset is considerably smaller than firstly the smallest occurring dominant wavelength and, secondly the distance from source-receiver midpoint to the scatterer (i.e., $h \ll d$), which enables a comparison of the two results. Appendix D shows that in case $h \ll d$ the source-receiver offset does not influence the result significantly. All tests were performed for two different dipole excitations:

- a dipole excitation perpendicular to the scatterer (i.e., in $\mathbf{z}$-direction): $\mathbf{F}_z$
- a dipole excitation parallel to the scatterer (i.e., in $\mathbf{x}$-direction): $\mathbf{F}_x$.

As derived and discussed in Subsection 2.4.2, in zero-offset cases with a dipole excitation perpendicular to the scatterer, i.e., $\mathbf{F}_z$, the scattered wave field occurs only on the $\mathbf{z}$-component (cf. equations 2.104, 2.105). The other components vanish (cf. equation 2.94). Hence, regarding these investigations, only the results on the $\mathbf{z}$-component are shown. Subsection 2.4.2 also discusses that in zero-offset cases with a dipole excitation parallel to the scatterer, i.e., $\mathbf{F}_x$, the scattered wave field occurs only on the $\mathbf{x}$-component (cf. equations 2.118, 2.119). The other components vanish (cf. equation 2.122). Hence, regarding these investigations, only the results on the $\mathbf{x}$-component are shown. In all cases, the dipole excitation generated a Ricker wavelet with $f_c = 1$ kHz and a maximum amplitude of 1 N (cf. appendix F).

3.1.1 Configuration 1: 4.8 m from the borehole axis to the scatterer

In the first configuration the distance from the borehole axis to the scatterer is 4.8 m which corresponds to a situation, where the bore tool is quite close to the scatterer. Generally, shorter distances are not subject of investigations.

Figure 3.2, 3.3 and 3.4 present the results for the time domain scattered wave particle displacement for the respective perturbations $\delta\mathrm{M} = 0.2, \delta\Lambda = 0.2$ and $\delta\rho = 0.2$. The corresponding

(a)-Figures show the results in case of a single force soure excitation parallel to the scatterer, while the corresponding (b)-Figures show the results in case of a single force soure excitation perpendicular to the scatterer. In all Figures, from top to bottom, the results are presented according to equation 2.128, i.e., the specular wave field (green), equation 2.129, i.e., the diffuse wave field (blue) and equation 2.127, i.e., the sum of both (red). The latter is compared withthe quasi-analytic reference result of *qseis*, plotted in black. Furthermore, Figure 3.5 shows the weighting factors $\mathcal{G}_r^{\otimes}$ (cf. equation 2.129 and appendix C) used to calculate the diffuse part of the scattered wave particle displacements.

In both cases of a dipole excitation (i.e., $\mathbf{F}_x$ and $\mathbf{F}_z$) the two main reflections (i.e. the PP-reflection in case of $\mathbf{F}_z$ and the SS-reflection in case of $\mathbf{F}_x$) are clearly visible. Furthermore, in most cases also a minor reflection is visible, i.e., the SS-reflection in case of $\mathbf{F}_z$ and the PP-reflection in case of $\mathbf{F}_x$. As discussed in subsection 2.4.3, in the presented setup, these reflections represent the diffuse part of the wave field (cf. equation 2.129). It can be observed that this part is generally about one order of magnitude smaller than the specular wave field (cf. equation 2.128). Hence, its contribution to the total scattered wave field (cf. equation 2.127) is not more than about 10%. To verify the accuracy of the calculated diffuse scattered wave particle displacement, a comparison between the Born-based results and the quasi-analytic reference result of *qseis* with respect to these minor reflections (i.e., cases, where no specular contribution exists) would be useful. Unfortunatley, the numerical noise level of the *qseis*-results is due to implementation-limitations for the simulated zero-offset configuration in some cases of the same order of magnitude as the diffuse scattered wave particle displacement. Hence, a quantitative comparison could not be carried out. However, in the cases where the total scattered wave particle displacement consists of both, a specular and a diffuse part (i.e., the PP-reflection in case of $\mathbf{F}_z$ and the SS-reflection in case of $\mathbf{F}_x$) the Born-based results show good agreement with the quasi-analytic reference result of *qseis*. For the sake of completeness, Figures E.1 - E.5 in appendix E show the comparison of the total scattered wave particle displacement for all 18 investigated perturbations (cf. Table 3.1) in case of a dipole excitation perpendicular to the scatterer and a dipole excitation parallel to the scatterer, respectively.

In general, the obtained results show that the analytic Born approach is able to reconstruct the single scattered wave field. However, the results indicate that the higher the contrast between the background medium and the scatterer gets the more the two results differ. As discussed in Chapter 2, this is due to the limited validation of the Born approximation for increasing contrasts. A qualitative study of Figures E.1 - E.5 leads to the following investigations:

- In general, the misfit between the *qseis*-result and the analytic Born result is considerably smaller for SS-reflections than for PP-reflections.

- Regarding perturbations in M and ρ the misfit between the *qseis*-result and the analytic Born result is generally smaller for positive contrasts (i.e., $\{\delta\mathrm{M}, \delta\rho\} = 0.1, 0.2, 0.3$) than for negative contrasts (i.e., $\{\delta\mathrm{M}, \delta\rho\} = -0.1, -0.2, -0.3$). Regarding perturbations in Λ it is just the other way round: the misfit between the two results is generally higher for positive contrasts (i.e., $\delta\Lambda = 0.1, 0.2, 0.3$) than for negative contrasts (i.e., $\delta\Lambda = -0.1, -0.2, -0.3$).

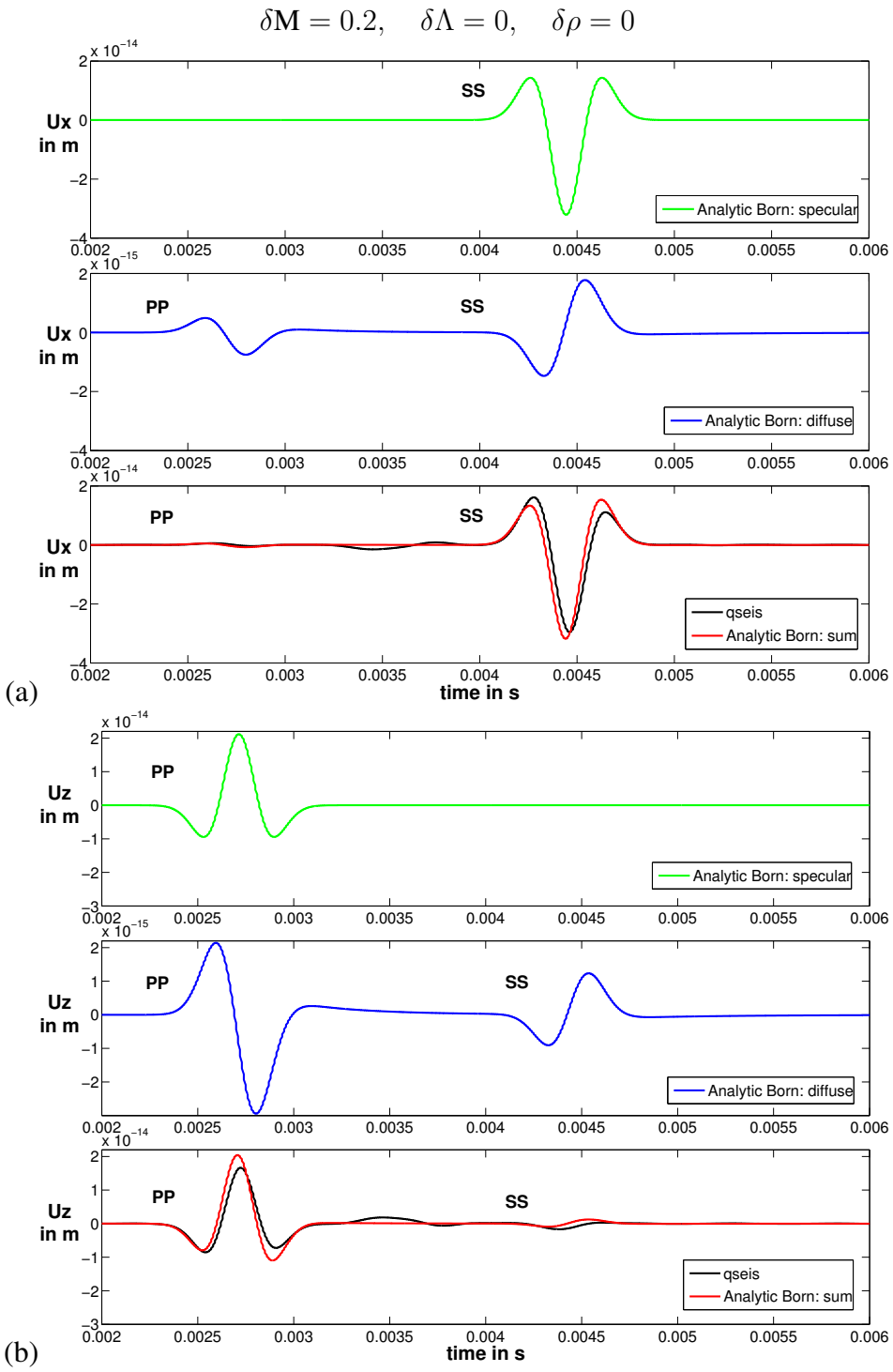

Figure 3.2: Sensitivity and accuracy analysis for Configuration 1 in case $\delta\mathrm{M} = 0.2$: comparison of the zero-offset results for the scattered wave particle displacement between *qseis* (black) and the analytic Born solution. The results of the latter are presented in terms of the specular wave field (green), the diffuse wave field (blue) and the sum of both (red). (a) The results pertain to a dipole excitation parallel to the scatterer. Hence, only the $\mathbf{x}$-component is shown. (b) The results pertain to a dipole excitation perpendicular to the scatterer. Hence, only the $\mathbf{z}$-component is shown.

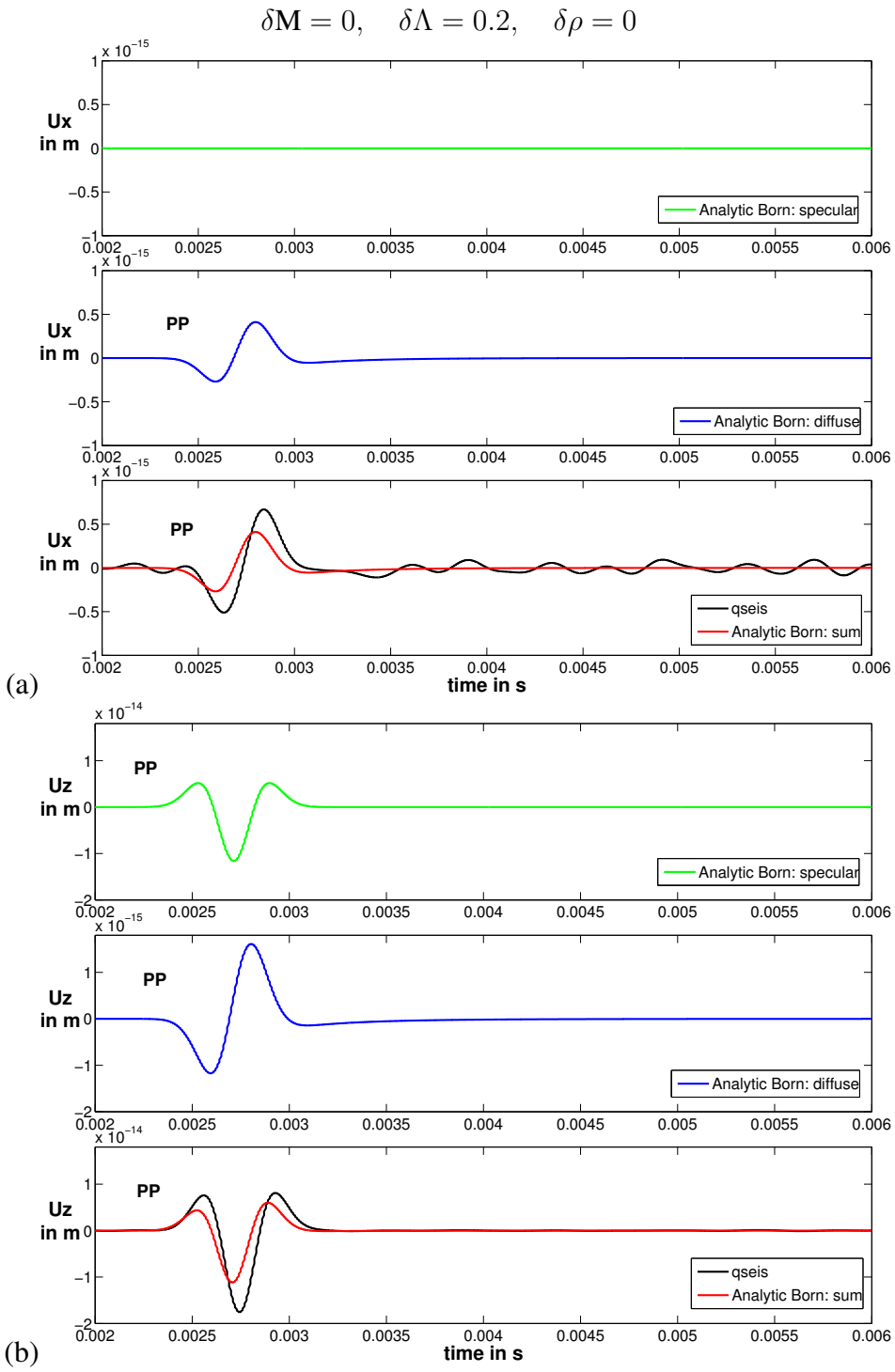

Figure 3.3: Sensitivity and accuracy analysis for Configuration 1 in case $\delta\Lambda = 0.2$: comparison of the zero-offset results for the scattered wave particle displacement between *qseis* (black) and the analytic Born solution. The results of the latter are presented in terms of the specular wave field (green), the diffuse wave field (blue) and the sum of both (red). (a) The results pertain to a dipole excitation parallel to the scatterer. Hence, only the x-component is shown. (b) The results pertain to a dipole excitation perpendicular to the scatterer. Hence, only the z-component is shown.

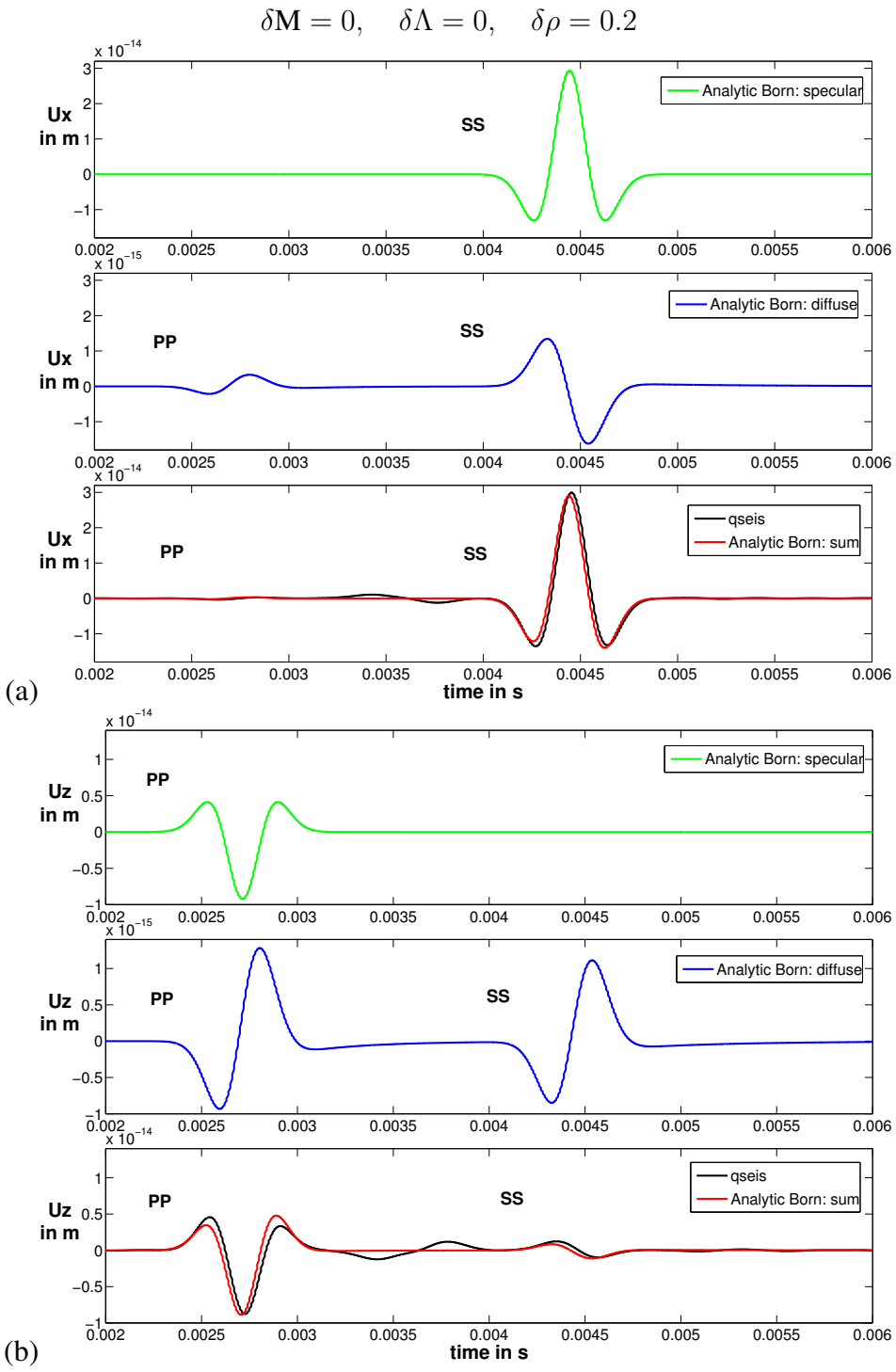

Figure 3.4: Sensitivity and accuracy analysis for Configuration 1 in case $\delta\rho = 0.2$: comparison of the zero-offset results for the scattered wave particle displacement between *qseis* (black) and the analytic Born solution. The results of the latter are presented in terms of the specular wave field (green), the diffuse wave field (blue) and the sum of both (red). (a) The results pertain to a dipole excitation parallel to the scatterer. Hence, only the x-component is shown. (b) The results pertain to a dipole excitation perpendicular to the scatterer. Hence, only the z-component is shown.

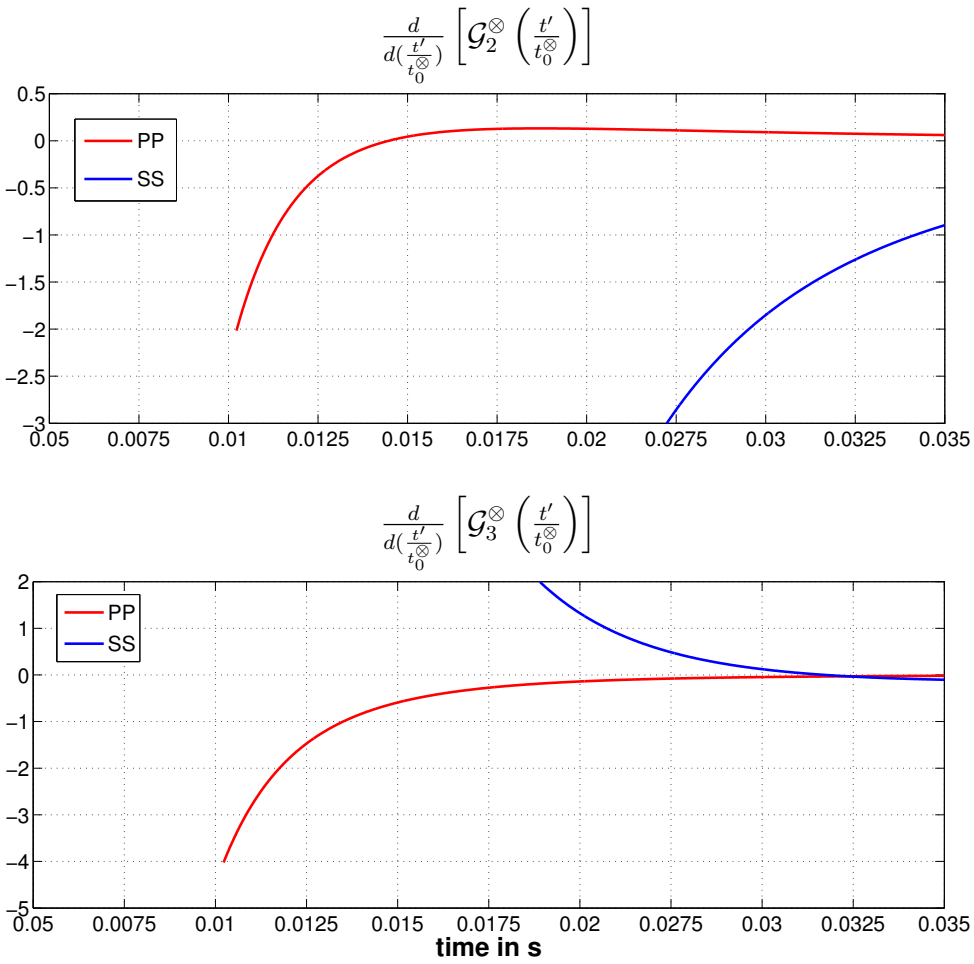

Figure 3.5: Geometrical time domain weighting factors $\mathcal{G}_r^{\otimes}$ used in the calculation of the diffuse part of the scattered wave particle displacement (cf. equation 2.129 and appendix C). Top: weighting factors in case of a dipole excitation parallel to the scatterer. Bottom: weighting factors in case of a dipole excitation perpendicular to the scatterer.

- Regarding perturbations in M and ρ the misfit between the *qseis*-result and the analytic Born result is increasing faster with increasing negative contrast (i.e., $\{\delta\mathrm{M}, \delta\rho\} = -0.1, -0.2, -0.3$) than with increasing positive contrast (i.e., $\{\delta\mathrm{M}, \delta\rho\} = 0.1, 0.2, 0.3$). This holds for both reflection types. However, with respect to the PP-reflection the effect is much stronger than with respect to the SS-reflection.
  Regarding perturbations in Λ it is just the other way round: the misfit between the *qseis*-result and the analytic Born result is increasing faster with increasing positive contrast (i.e., $\delta\Lambda = 0.1, 0.2, 0.3$) than with increasing negative contrast (i.e., $\delta\Lambda = -0.1, -0.2, -0.3$).

In order to systematically investigate the observed aspects, the relative misfits between the maximum amplitudes of the *qseis*-results $u_r^{\odot\oplus,\,qseis}$ (serving as analytic reference) and the Born-based results $u_r^{\odot\oplus,\,Born}$ are calculated (Geerits et al., 2013) according to

Table 3.3: Relative misfit $\delta u_r^{\odot\oplus}$ between the results of *qseis* and the Born-based approach for the PP-reflection in case of $\mathbf{F}_z$ and the SS-reflection in case of $\mathbf{F}_x$ for Configuration 1 resulting from perturbations in M.

δM	0.3	0.2	0.1	-0.1	-0.2	-0.3
δu_2^{SS}	-0.080	-0.076	-0.014	0.137	0.148	0.207
δu_3^{PP}	0.322	0.226	0.091	-0.272	-0.428	-0.680

Table 3.4: Relative misfit $\delta u_r^{\odot\oplus}$ between the results of *qseis* and the Born-based approach for the PP-reflection in case of $\mathbf{F}_z$ for Configuration 1 resulting from perturbations in Λ. Since there is no contrast in v_{S} (cf. Table 3.1) no SS-reflection is observed in case of $\mathbf{F}_x$.

$\delta\Lambda$	0.3	0.2	0.1	-0.1	-0.2	-0.3
δu_3^{PP}	-0.508	-0.369	-0.204	0.093	0.187	0.210

$$\delta u_r^{\odot\oplus} = \frac{|u_r^{\odot\oplus,\,qseis} - u_r^{\odot\oplus,\,Born}|}{u_r^{\odot\oplus,\,qseis}} \quad \text{with} \quad \begin{matrix} \odot, \oplus \in \{\text{P,S}\} \\ r \in \{1,2,3\} \end{matrix}. \tag{3.1}$$

The resulting values for the relative misfits are specified in Tables 3.3, 3.4 and 3.5, pertaining to the perturbations in M, Λ and ρ respectively. Figure 3.6 presents an overview of the calculated misfits for Configuration 1 as a function of the perturbation parameters δM, $\delta\Lambda$ and $\delta\rho$ from left to right, respectively. The green dots represent the relative misfits between the *qseis*- and the Born-based result with respect to the PP-reflection on the **z**-component in case of a dipole excitation perpendicular to the scatterer. The blue diamonds represent the relative misfits between the *qseis*- and the Born-based result with respect to the SS-reflection on the **x**-component in case of a dipole excitation parallel to the scatterer.

The obtained misfit results confirm the investigations based on the graphs in Figures E.1 - E.5. Figure 3.7 provides clear evidence of the following investigations:

- Regarding perturbations in M the relative misfit between the *qseis*-result and the analytic

Table 3.5: Relative misfit $\delta u_r^{\odot\oplus}$ between the results of *qseis* and the Born-based approach for the PP-reflection in case of $\mathbf{F}_z$ and the SS-reflection in case of $\mathbf{F}_x$ for Configuration 1 resulting from perturbations in ρ.

$\delta\rho$	0.3	0.2	0.1	-0.1	-0.2	-0.3
δu_2^{SS}	0.042	0.030	0.062	-0.109	-0.198	-0.244
δu_3^{PP}	-0.036	-0.014	-0.017	0.078	0.210	0.285

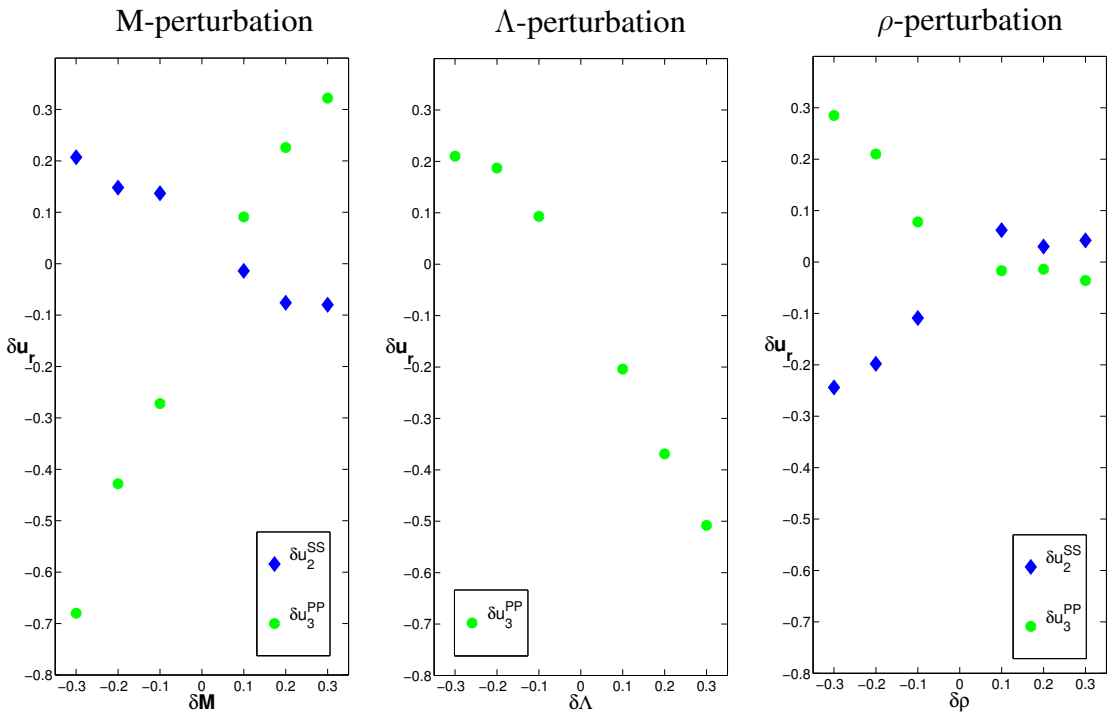

Figure 3.6: Sensitivity and accuracy analysis for Configuration 1: results for the relative misfit concerning the maximum displacement amplitudes between the *qseis*-results and the Born-based results for the PP-reflection in case of $\mathbf{F}_z$ and the SS-reflection in case of $\mathbf{F}_x$ as a function of the three perturbation parameters δM, $\delta\Lambda$ and $\delta\rho$ from left to right, respectively.

Born result is twice as high for PP-reflections than for SS-reflections.

- Regarding perturbations in ρ the relative misfit between the *qseis*-result and the analytic Born result for both reflection types is generally less than 0.3. In cases of positive contrasts the relative misfit is even less than 0.1, which is favorable.
- The rapid increase of the relative misfit between the *qseis*-result and the analytic Born result for δM and $\delta\rho$ with increasing negative contrast and for $\delta\Lambda$ with increasing positive contrast is confirmed. However, the effect for $\delta\rho$ is much less pronounced. This reveals that especially the scattering-coefficient for PP is sensitive to high contrasts in the compliance parameters, which is approved by equations 2.72 - 2.76.

3.1.2 Configuration 2: 17.68 m from the borehole axis to the scatterer

In the second configuration the distance from the borehole axis to the scatterer is 17.68 m which corresponds to an ordinary borehole setup. Figures E.6 - E.10 in appendix E show the comparison between the total scattered wave particle displacement of *qseis* and the Born-based approach, respectively, for all 18 investigated perturbations (cf. Table 3.1) in case of a dipole excitation perpendicular to the scatterer and a force source excitation parallel to the scatterer, respectively.

Table 3.6: Relative misfit $\delta u_r^{\odot\oplus}$ between the results of *qseis* and the Born-based approach for the PP-reflection in case of $\mathbf{F}_z$ and the SS-reflection in case of $\mathbf{F}_x$ for Configuration 2 resulting from perturbations in M.

δM	0.3	0.2	0.1	-0.1	-0.2	-0.3
δu_2^{SS}	-0.079	-0.094	-0.019	0.152	0.142	0.204
δu_3^{PP}	0.329	0.231	0.095	-0.269	-0.427	-0.691

Table 3.7: Relative misfit $\delta u_r^{\odot\oplus}$ between the results of *qseis* and the Born-based approach for the PP-reflection in case of $\mathbf{F}_z$ for Configuration 2 resulting from perturbations in Λ. Since there is no contrast in v_{S} (cf. Table 3.1) no SS-reflection is observed in case of $\mathbf{F}_x$.

$\delta\Lambda$	0.3	0.2	0.1	-0.1	-0.2	-0.3
δu_3^{PP}	-0.496	-0.351	-0.173	0.136	0.224	0.251

In general, the results obtained for Configuration 2 confirm the observations made for Configuration 1: the analytic-Born approach is also in this case, representing an intermediate distance from the borehole axis to the scatterer, able to reconstruct the single scattered wave field with a good accuracy. In addition, all further investigations concerning Configuration 1, such as the (rapid) increase of the relative misfit for δM and $\delta\rho$ with increasing negative contrast and for $\delta\Lambda$ with increasing positive contrast are similarly observed for Configuration 2 and therefore confirmed.

In order to systematically investigate the observed results for Configuration 2, again, the relative misfit $\delta u_r^{\odot\oplus}$ between the *qseis*-results (i.e., the analytic reference) and the Born-based results is computed according to equation 3.1. The resulting values for the misfit are specified in Tables 3.6, 3.7 and 3.8, pertaining to perturbations in M, Λ and ρ, respectively.

Figure 3.7 presents an overview of the calculated misfits for Configuration 2 as a function of the perturbation parameters δM, $\delta\Lambda$ and $\delta\rho$ from left to right, respectively. The green dots represent the relative misfits between the *qseis*- and the Born-based result with respect to the PP-reflection on the **z**-component in case of a single force source excitation perpendicular to the scatterer. The blue diamonds represent the relative misfits between the *qseis*- and the Born-based result with

Table 3.8: Relative misfit $\delta u_r^{\odot\oplus}$ between the results of *qseis* and the Born-based approach for the PP-reflection in case of $\mathbf{F}_z$ and the SS-reflection in case of $\mathbf{F}_x$ for Configuration 2 resulting from perturbations in ρ.

$\delta\rho$	0.3	0.2	0.1	-0.1	-0.2	-0.3
δu_2^{SS}	0.046	0.021	0.065	-0.119	-0.215	-0.252
δu_3^{PP}	-0.069	-0.041	-0.014	0.035	0.196	0.259

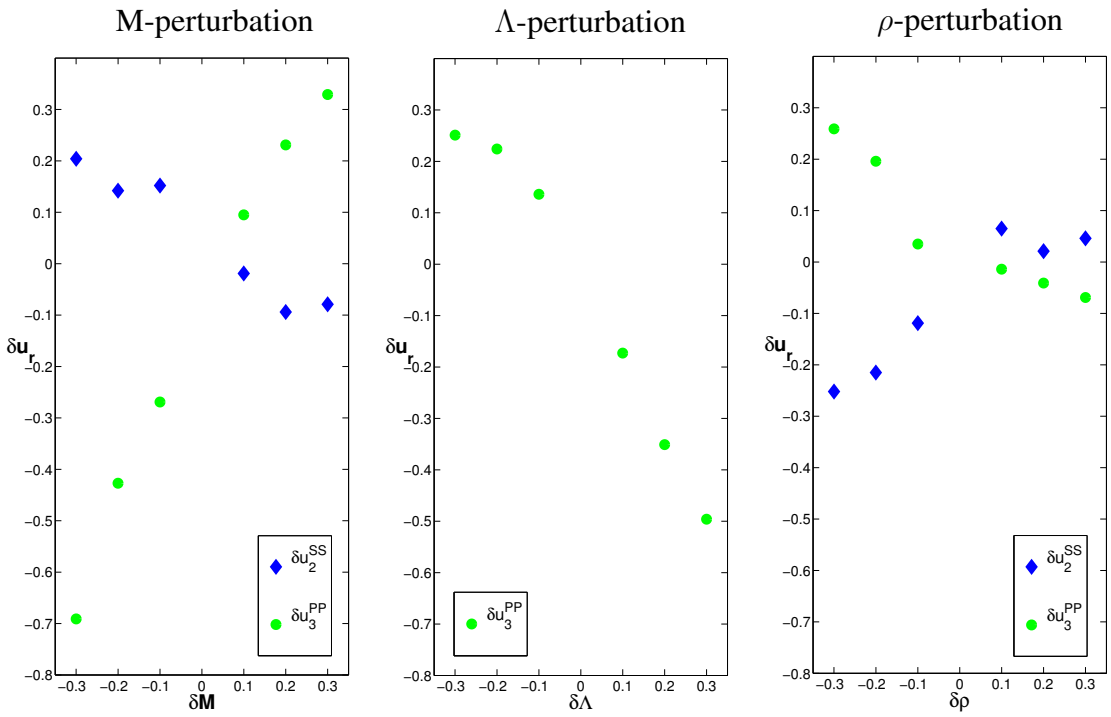

Figure 3.7: Sensitivity and accuracy analysis for Configuration 2: results for the relative misfit concerning the maximum displacement amplitudes between the *qseis*-results and the Born-based results as a function of the perturbation parameters δM, $\delta\Lambda$ and $\delta\rho$ from left to right, respectively.

respect to the SS-reflection on the x-component in case of a dipole excitation parallel to the scatterer.

The obtained misfit results clearly confirm the investigations made for Configuration 1. Furthermore it is obvious that the misfit values for this configuration do not considerably differ from the ones obtained for Configuration 1. This indicates that the occurring (small) differences can be traced back to the differences between the approximated Born-scattering coefficients and the true reflection coefficients. Furthermore, this indicates that the geometrical spreading is correctly handled by the implemented Born based approach, where it is assumed to be inversely proportional to the two way distance from the borehole axis to the scatterer.

3.1.3 Configuration 3: 30.48 m from the borehole axis to the scatterer

To further prove the correct handling of the geometrical spreading in the Borb-based approach, a third configuration is investigated, where the distance from the borehole axis to the scatterer is 30.48 m. This case corresponds to a limiting case in borehole applications. Generally, larger distances are not subject of investigations. Figures E.11 - E.15 in appendix E show the comparison between the total scattered wave particle displacement of *qseis* and the Born-based approach, respectively, for all 18 investigated perturbations (cf. Table 3.1) in case of a dipole excitation perpendicular to the scatterer and a force source excitation parallel to the scatterer, respectively.

Table 3.9: Relative misfit $\delta u_r^{\odot\oplus}$ between the results of *qseis* and the Born-based approach for the PP-reflection in case of $\mathbf{F}_z$ and the SS-reflection in case of $\mathbf{F}_x$ for Configuration 3 resulting from perturbations in M.

δM	0.3	0.2	0.1	-0.1	-0.2	-0.3
δu_2^{SS}	-0.101	-0.104	-0.015	0.126	0.126	0.187
δu_3^{PP}	0.369	0.256	0.115	-0.249	-0.413	-0.685

Table 3.10: Relative misfit $\delta u_r^{\odot\oplus}$ between the results of *qseis* and the Born-based approach for the PP-reflection in case of $\mathbf{F}_z$ for Configuration 3 resulting from perturbations in Λ. Since there is no contrast in v_{S} (cf. Table 3.1) no SS-reflection is observed in case of $\mathbf{F}_x$.

$\delta\Lambda$	0.3	0.2	0.1	-0.1	-0.2	-0.3
δu_3^{PP}	-0.484	-0.339	-0.150	0.166	0.250	0.275

In general, the results obtained for Configuration 2 confirm the observations made for Configuration 1: the analytic-Born approach is also in this case, representing an intermediate distance from the borehole axis to the scatterer, able to reconstruct the single scattered wave field with a good accuracy. In addition, all further investigations concerning Configuration 1, such as the (rapid) increase of the relative misfit for δM and $\delta\rho$ with increasing negative contrast and for $\delta\Lambda$ with increasing positive contrast are similarly observed for Configuration 2 and therefore confirmed.

In general, the results obtained for Configuration 3 confirm the observations made for Configuration 1 and Configuration 2. The analytic-Born approach is also in this case, representing a limiting case in borehole applications, able to reconstruct the single scattered wave field with a good accuracy. In addition, all further investigations concerning Configuration 1 and Configuration 2, such as the (rapid) increase of the relative misfit for δM and $\delta\rho$ with increasing negative contrast and for $\delta\Lambda$ with increasing positive contrast are similarly observed for Configuration 3 and therefore confirmed.

In order to systematically investigate the observed results for Configuration 3, again, the relative misfit $\delta u_r^{\odot\oplus}$ between the *qseis*-results (i.e., the analytic reference) and the Born-based results is computed according to equation 3.1. The resulting values for the misfit are specified in Tables 3.9, 3.10 and 3.11, pertaining to perturbations in M, Λ and ρ respectively.

Figure 3.8 presents an overview of the calculated misfits for Configuration 3 as a function of the perturbation parameters δM, $\delta\Lambda$ and $\delta\rho$ from left to right, respectively. The green dots represent the relative misfits between the *qseis*- and the Born-based result with respect to the PP-reflection on the **z**-component in case of a single force source excitation perpendicular to the scatterer. The blue diamonds represent the relative misfits between the *qseis*- and the Born-based result with respect to the SS-reflection on the **x**-component in case of a dipole excitation parallel to the scatterer.

Table 3.11: Relative misfit $\delta u_r^{\odot\oplus}$ between the results of *qseis* and the Born-based approach for the PP-reflection in case of $\mathbf{F}_z$ and the SS-reflection in case of $\mathbf{F}_x$ for Configuration 3 resulting from perturbations in ρ.

$\delta\rho$	0.3	0.2	0.1	-0.1	-0.2	-0.3
δu_2^{SS}	0.077	0.002	0.008	-0.059	-0.180	-0.223
δu_3^{PP}	-0.092	-0.064	-0.026	0.007	0.167	0.243

The obtained misfit results for this configuration clearly confirm the investigations made for Configuration 1 and Configuration 2. Again, the misfit values for this configuration do not considerably differ from the ones obtained for the other two configurations. This confirms the already stated assumption that the occurring (small) differences in the relative misfit can be traced back to the differences between the approximated Born scattering coefficients and the true reflection coefficients. Hence, this again indicates that the geometrical spreading is correctly handled by the implemented Born-based approach, where the geometrical spreading is assumed to be inversely proportional to the two way distance from the borehole axis to the scatterer.

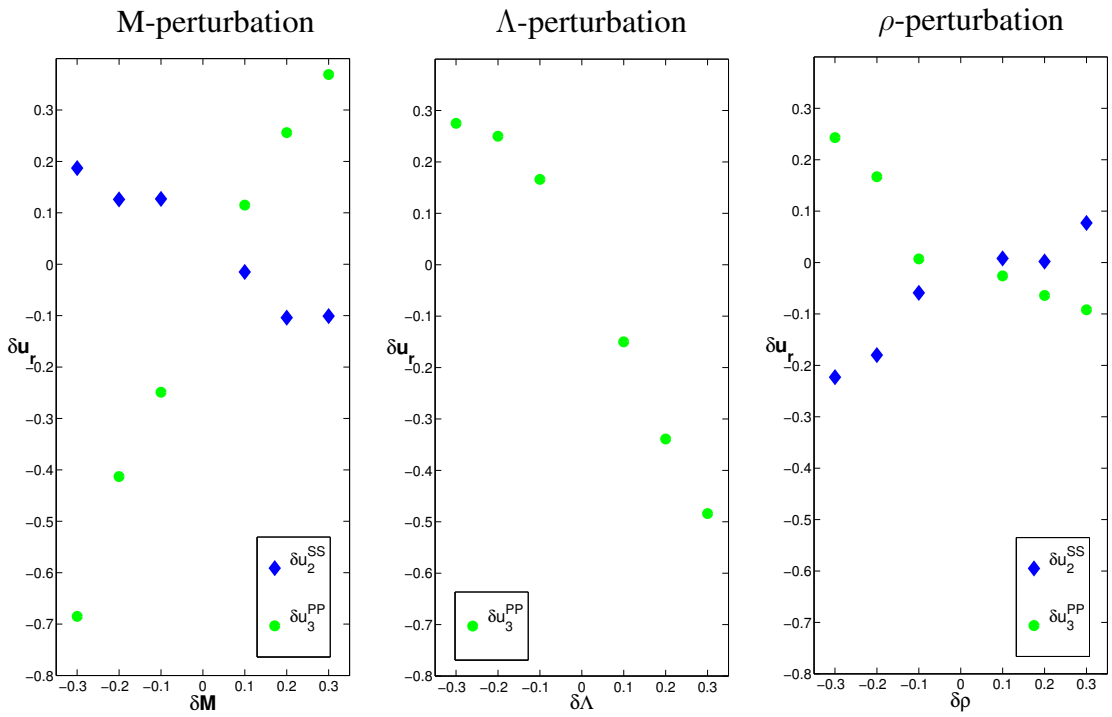

Figure 3.8: Sensitivity and accuracy analysis for Configuration 3: results for the relative misfit concerning the maximum displacement amplitudes between the *qseis*-results and the Born-based results as a function of the three perturbation parameters $\delta\mathrm{M}, \delta\Lambda$ and $\delta\rho$ from left to right, respectively.

3.1.4 Comparison of the Born scattering coefficients with the Zoeppritz reflection coefficients

In order to underpin the conclusion concerning the correct handling of the geometrical spreading in the Born-based approach, in the following the Born scattering coefficients $\overline{\mathcal{R}}^{\mathrm{PP}}, \overline{\mathcal{R}}^{\mathrm{SS}}$ (cf. equations 2.72, 2.73) are compared with the corresponding Zoeppritz reflection coefficients for zero-offset $R_{\mathrm{Z}}^{\mathrm{PP}}, R_{\mathrm{Z}}^{\mathrm{SS}}$ (Zoeppritz (1919), Aki and Richards (1980)). Although the latter pertain to plane waves, the comparison with the Born scattering coefficients is feasible since they result from the derived first order Born approximation, which is a far-field approximation. In this case the local wavefront curvature can be assumed to be plane. Tables 3.12 and 3.13 list the absolute values of the Born scattering coefficients and the Zoeppritz reflection coefficients, respectively, for all tested perturbations $\delta\mathrm{M}, \delta\Lambda$ and $\delta\rho$. Furthermore, Figures 3.9 and 3.10 visualize the comparison of the absolute values of the obtained PP- and SS-coefficients, respectively, as a function of the three perturbation parameters $\delta\mathrm{M}, \delta\Lambda$ and $\delta\rho$ from left to right, respectively. In addition to an expected constant factor, separating the first order Born scattering coefficients from the Zoeppritz reflection coefficients, a further discrepancy is observed. This discrepancy is increasing with increasing positive and negative contrast. To further investigate this observation, in a first step the Born scattering coefficients are expressed as a function of the perturbation parameters $\delta\mathrm{M}, \delta\Lambda$ and $\delta\rho$

$$\overline{\mathcal{R}}^{\odot\oplus} = \gamma_{\mathrm{B}}^{\odot\oplus}\delta\mathrm{B} \quad \text{with} \quad \begin{array}{c} \odot\oplus \in \{\mathrm{PP}, \mathrm{SS}\} \\ \mathrm{B} \in \{\mathrm{M}, \Lambda, \rho\} \end{array}, \tag{3.2}$$

where $\gamma_{\mathrm{B}}^{\odot\oplus}$ denotes a constant varying with the according perturbation type B. Based on this, the following relation between the Zoeppritz reflection coefficients and the Born scattering coefficients is derived

$$R_{\mathrm{Z}}^{\odot\oplus} = C_0^{\odot\oplus}\overline{\mathcal{R}}^{\odot\oplus} + F^{\odot\oplus}(\delta\mathrm{B}) \quad \text{with} \quad \odot \oplus \in \{\mathrm{PP}, \mathrm{SS}\}\ . \tag{3.3}$$

$C_0^{\odot\oplus}$ represents the observed constant shift between the two coefficients and $F^{\odot\oplus}(\delta\mathrm{B})$ denotes an error correction function depending on the perturbation type B. In case of no contrast, this correction vanishes, i.e., $F^{\odot\oplus}(0) = 0$. A devision of equation 3.3 by the Born scattering coefficients (equation 3.2) yields

$$\frac{R_{\mathrm{Z}}^{\odot\oplus}}{\overline{\mathcal{R}}^{\odot\oplus}} = C_0^{\odot\oplus} + \frac{F^{\odot\oplus}(\delta\mathrm{B})}{\gamma_{\mathrm{B}}^{\odot\oplus}\delta\mathrm{B}}\,. \tag{3.4}$$

Figures 3.11 and 3.12 visualize this ratio for the observed PP- and SS-reflection, respectively, as a function of the three perturbation parameters $\delta\mathrm{M}, \delta\Lambda$ and $\delta\rho$ from left to right, respectively and indicate $C_0^{\odot\oplus}$ in equation 3.4 to be ≈ 0.25. Furthermore, all graphs of Figure 3.12 and the most right hand side graph in Figure 3.11 indicate a linear relationship between the ratio of the two coefficients and the perturbation parameters $\delta\rho$ in case of the PP- and the SS-reflection, and $\delta\mathrm{M}$ in case of the SS-reflection. Assuming this to be true, the introduced correction function $F^{\odot\oplus}(\delta\mathrm{B})$ is of linear shape for the mentioned cases, i.e.,

$$F^{\odot\oplus}(\delta\mathrm{B}) = C_1^{\odot\oplus}(\delta\mathrm{B})^2\ , \tag{3.5}$$

Table 3.12: Absolute values of the Born scattering coefficients $\bar{\mathcal{R}}^{\odot\oplus}$ for PP- and SS-reflections, resulting from perturbations in M, Λ and ρ. Since in case of $\delta\Lambda$ there is no contrast in v_{S} (cf. Table 3.1) the corresponding SS-coefficients in case of $\mathbf{F}_x$ are zero.

$\delta\mathrm{M}$	0.3	0.2	0.1	-0.1	-0.2	-0.3
$\bar{\mathcal{R}}^{\mathrm{PP}}$	0.6934	0.4720	0.2367	0.2194	0.4565	0.6872
$\bar{\mathcal{R}}^{\mathrm{SS}}$	0.3034	0.2100	0.1025	0.0975	0.2049	0.3056

$\delta\Lambda$	0.3	0.2	0.1	-0.1	-0.2	-0.3
$\bar{\mathcal{R}}^{\mathrm{PP}}$	0.3902	0.2584	0.1351	0.1381	0.2657	0.3657
$\bar{\mathcal{R}}^{\mathrm{SS}}$	0	0	0	0	0	0

$\delta\rho$	0.3	0.2	0.1	-0.1	-0.2	-0.3
$\bar{\mathcal{R}}^{\mathrm{PP}}$	0.3030	0.2056	0.1050	0.1110	0.1953	0.2860
$\bar{\mathcal{R}}^{\mathrm{SS}}$	0.2974	0.1917	0.0977	0.1028	0.1938	0.2921

Table 3.13: Absolute values of the Zoeppritz reflection coefficients $R_{\mathrm{Z}}^{\odot\oplus}$ for PP- and SS-reflections, resulting from perturbations in M, Λ and ρ. Since in case of $\delta\Lambda$ there is no contrast in v_{S} (cf. Table 3.1) the corresponding SS-coefficients in case of $\mathbf{F}_x$ are zero.

$\delta\mathrm{M}$	0.3	0.2	0.1	-0.1	-0.2	-0.3
$R_{\mathrm{Z}}^{\mathrm{PP}}$	0.1290	0.0886	0.0497	0.0692	0.1842	0.5191
$R_{\mathrm{Z}}^{\mathrm{SS}}$	0.0655	0.0455	0.0238	0.0263	0.0556	0.0889

$\delta\Lambda$	0.3	0.2	0.1	-0.1	-0.2	-0.3
$R_{\mathrm{Z}}^{\mathrm{PP}}$	0.1789	0.0922	0.0379	0.0282	0.0499	0.0674
$R_{\mathrm{Z}}^{\mathrm{SS}}$	0	0	0	0	0	0

$\delta\rho$	0.3	0.2	0.1	-0.1	-0.2	-0.3
$R_{\mathrm{Z}}^{\mathrm{PP}}$	0.0655	0.0456	0.0238	0.0263	0.0558	0.0890
$R_{\mathrm{Z}}^{\mathrm{SS}}$	0.0655	0.0456	0.0238	0.0264	0.0557	0.0890

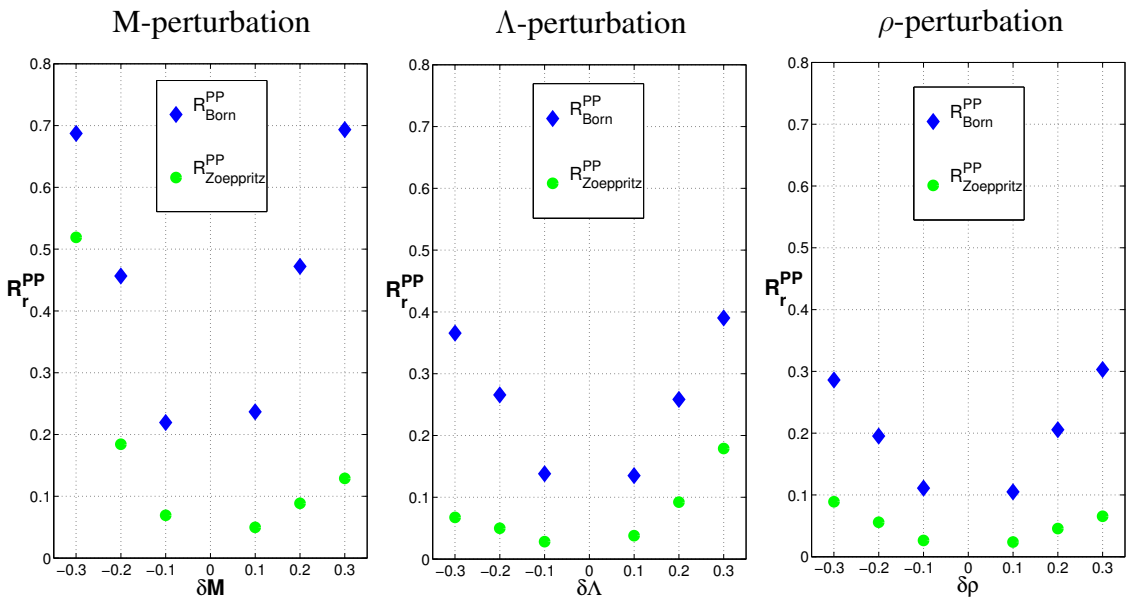

Figure 3.9: Comparison of the Born scattering coefficients and the Zoeppritz reflection coefficients for the PP-reflection as a function of the three perturbation parameters δM, $\delta\Lambda$ and $\delta\rho$ from left to right, respectively.

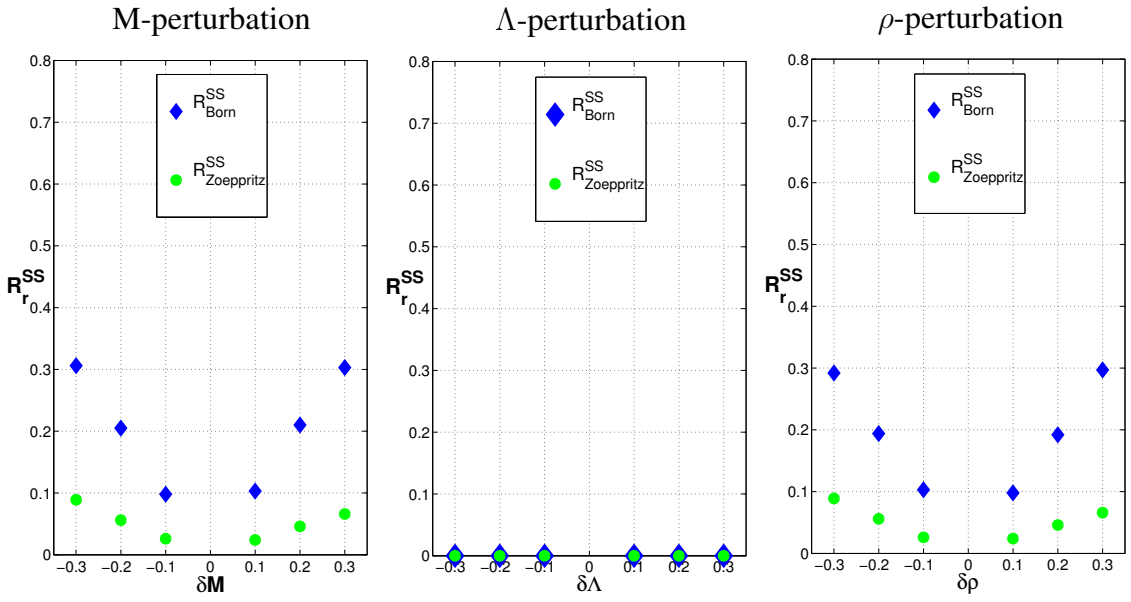

Figure 3.10: Comparison of the Born scattering coefficients and the Zoeppritz reflection coefficients for the SS-reflection as a function of the three perturbation parameters δM, $\delta\Lambda$ and $\delta\rho$ from left to right, respectively. Since there is no contrast in v_S in case of $\delta\Lambda$ (cf. Table 3.1) the corresponding SS-coefficients are truly zero.

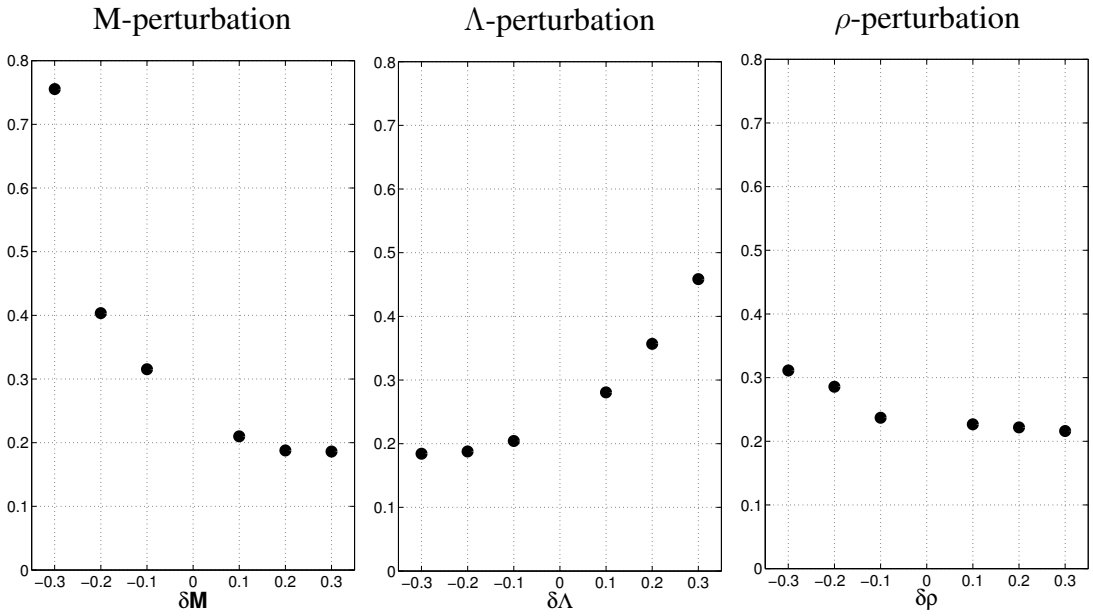

Figure 3.11: Ratio of the Zoeppritz reflection coefficients and the Born scattering coefficients according to equation 3.4 for the PP-reflection as a function of δM, $\delta\Lambda$ and $\delta\rho$ from left to right, respectively.

with $C_1^{\odot\oplus}$ being a new constant. Incorporating this in equation 3.4 leads to a linear relationship for the ratio of the two coefficients with respect to the perturbation parameters δM and $\delta\rho$

$$\frac{R_{\mathrm{Z}}^{\odot\oplus}}{\mathcal{R}^{\odot\oplus}} = C_2^{\odot\oplus}\delta\mathrm{B}\,, \tag{3.6}$$

with

$$C_2^{\odot\oplus} = \frac{C_1^{\odot\oplus}}{\gamma_{\mathrm{B}}^{\odot\oplus}}\,. \tag{3.7}$$

Therefrom it can be concluded that a second order correction in δM with respect to the SS-reflection and in $\delta\rho$ with respect to the PP- and the SS-reflection has to be applied to match the Born scattering coefficients with the Zoeppritz reflection coefficients. However, especially in case of the SS-reflection, the amount of the needed correction is very small. Furthermore, with regard to the observed small relative misfits for the SS-reflections in general (cf. Figures E.1 - E.15 and Tables 3.12 - 3.13) the application of the correction is not essential to properly model the reflection. Concerning the perturbations in δM and $\delta\Lambda$ with respect to the PP-reflection, the discussed second order correction is not suitable but a higher order correction is needed. However, in case of $\delta\mathrm{M} < -0.2$ and $\delta\Lambda > 0.2$, where the mismatch between the Born scattering coefficients and the Zoeppritz reflection coefficients gets quite high, it has to be mentioned that the corresponding material parameters rarely occur under any practical circumstances. Hence, the linear dependency of the first order Born scattering coefficients on the perturbations parameters δM, $\delta\Lambda$ and $\delta\rho$ (cf. equations 2.72 - 2.77, 3.2) seems to be acceptable.

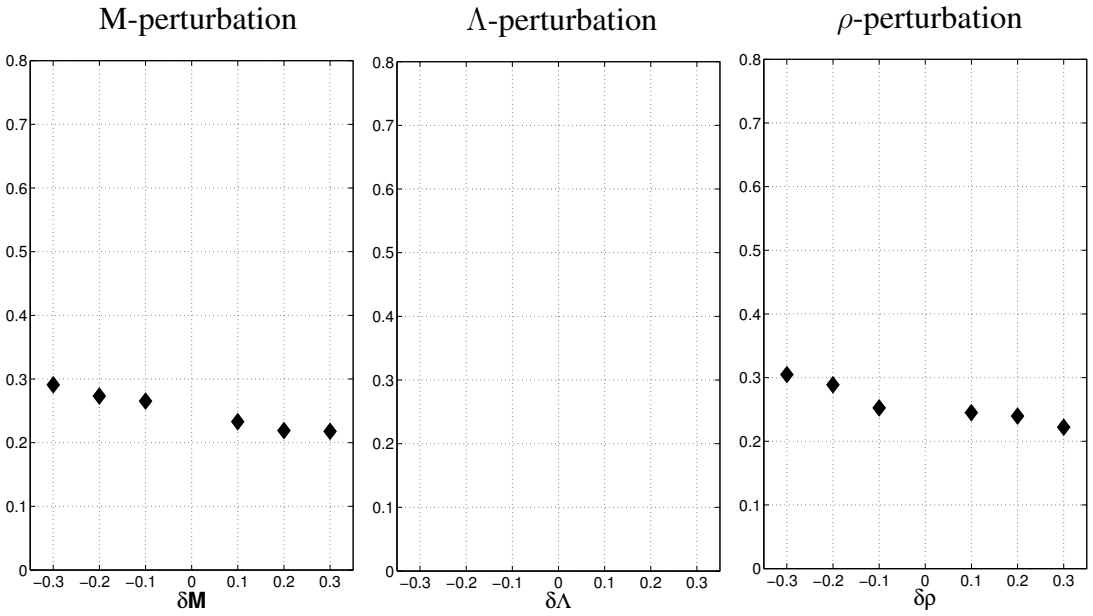

Figure 3.12: Ratio of the Zoeppritz reflection coefficients and the Born scattering coefficients according to equation 3.4 for the SS-reflection as a function of δM, $\delta\Lambda$ and $\delta\rho$ from left to right, respectively. Since both coefficients are truly zero in case of $\delta\Lambda$ (cf. Figure 3.10) the corresponding ratios are not evaluated.

3.2 Dipped scatterer (relative to the borehole axis) over a half-space

Secondly, the results for a model, where the scatterer is dipped relative to the borehole axis are investigated. The setup is sketched in Figure 3.1 (right) and has been described in the introduction of this chapter. Regarding the modelings with *qseis*, again, the developed far-field criterion was applied (cf. appendix D), ensuring that source and receiver offset by 10% of the two way distance from source-receiver midpoint to the scatterer. This implies that the source-receiver offset is smaller than the smallest occurring dominant wavelength and can still be seen as a zero-offset case. Based on the explained setup for Configuration 1 and perturbations in M (cf. Table 3.1), four quasi zero-offset cases were built with different dip-angles α between the scatterer and the borehole axis. Table 3.14 gives an overview of the investigated configurations. In addition, it lists the investigated cases for a plane scatterer parallel to the borehole axis and a dipole excitation perpendicular (i.e., $\alpha = 0°$) and parallel (i.e., $\alpha = 90°$) to the latter. All tests were performed for a dipole excitation in $\mathbf{z}$-direction (i.e., $\mathbf{F}_z$). In all cases, the dipole excitation was realized by a Ricker wavelet with $f_c = 1\,\text{kHz}$ and a maximum amplitude of 1 N (cf. appendix F).

With respect to further apply the explicit derived analytic Born solutions for a plane scatterer in $\mathbf{e}_3$-direction in case of a dipole excitation (cf. equations 2.104 - 2.105, 2.110 - 2.111, 2.118 - 2.119), the following principle is applied: regarding the investigated configuration there is no difference concerning the resulting scattered particle displacements whether the scatterer is dipped relative to the dipole excitation or the dipole excitation is dipped relative to the scatterer.

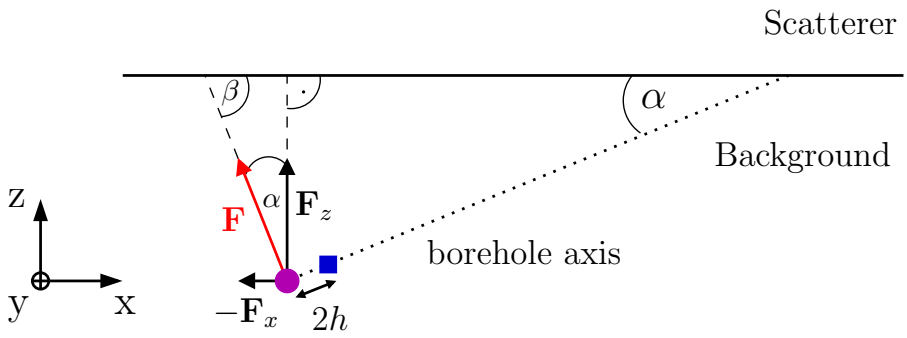

Figure 3.13: Superposition principle: the desired single force $\mathbf{F}$ (red) can be build by an angle-weighted summation of the two single forces $-\mathbf{F}_x$ and $\mathbf{F}_z$ being perpendicular to each other (cf. equation 3.8).

Accordingly, to receive the particle displacement due to a dipole excitation, striking the scatterer with the angle $\beta = 90° - \alpha$, the Born-based results due to a dipole excitation $\mathbf{F}_x$ parallel to the scatterer and due to a dipole excitation $\mathbf{F}_z$ perpendicular to the scatterer, respectively, are superposed according to Figure 3.13

$$\mathbf{F} = -\mathbf{F}_x \cdot \sin\alpha + \mathbf{F}_z \cdot \cos\alpha \,. \tag{3.8}$$

As derived and discussed in Chapter 2, Section 2.4, Subsection 2.4.2, the resulting force source excitation $\mathbf{F}$ (marked in red in Figure 3.13) is then arbitrarily oriented in the $\mathbf{x}-\mathbf{z}$-plane with an angle $\beta = 90° - \alpha$ relative to the scatterer. Due to the rotation of the dipole excitation, the obtained results on the $\mathbf{z}$- and $\mathbf{x}$-component are then no longer oriented along the direction of the dipole excitation and perpendicular to it (i.e., along the borehole axis), respectively, as Figure 3.13 indicates. Hence, the coordinate system for the resulting scattered particle displacements $\mathrm{u_x}$ and $\mathrm{u_z}$ has to be rotated by applying the rotational matrix

$$\begin{pmatrix} \mathrm{u}'_\mathrm{x} \\ \mathrm{u}'_\mathrm{z} \end{pmatrix} = \begin{pmatrix} \cos\alpha & \sin\alpha \\ -\sin\alpha & \cos\alpha \end{pmatrix} \cdot \begin{pmatrix} \mathrm{u_x} \\ \mathrm{u_z} \end{pmatrix} \tag{3.9}$$

to finally examine the same component-directions as for the reference results.

Figures 3.14 - 3.19 show the results on the $\mathbf{z}$-component due to a dipole excitation in $\mathbf{z}$-direction as a function of the dip-angle α for six different perturbations in the compliance parameter M between the background medium and the scatterer. The applied values for $v_\mathrm{P}, v_\mathrm{S}$ and ρ are listed in Table 3.1. In all figures the analytic Born results are plotted in red and the *qseis*-results, representing a quasi analytic reference, are plotted in black.

In Chapter 2, Section 2.4, Subsection 2.4.2 I have explicitly derived the scattered wave field for zero-offset configurations with a plane scatterer in $\mathbf{z}$-direction over a half-space due to a dipole excitation. In addition, I have shown that in case of a dipole excitation perpendicular to the scatterer (i.e., $\mathbf{F}_z$) the scattered wave field occurs only on the $\mathbf{z}$-component (i.e., the component pointing in the direction of the dipole excitation). In this case, the PP-reflection represents the main signal, whereas the minor SS-reflection is very small. Furthermore, I have

Table 3.14: Setup-parameters used in the sensitivity and accuracy analysis: d denotes the distance from the source-receiver midpoint to the scatterer, h denotes half the source-receiver offset, b denotes the distance (along the borehole axis) from the source to the point of intersection with the dipped scatterer and α denotes the angle of intersection. The cases $\alpha = \{0°, 90°\}$ correspond to the investigated cases Chapter 3, Section 3.1 with a dipole excitation perpendicular and parallel to the scatterer, respectively.

		Dip 1	Dip 2	Dip 3	Dip 4	
d (in m)	4.8	4.8	4.8	4.8	4.8	4.8
h (in m)	0.48	0.48	0.48	0.48	0.48	0.48
b (in m)	-	9.6	6.7	5.54	4.9	-
α	0°	30°	45°	60°	75°	90°

derived that in case of a dipole excitation parallel to the scatterer (i.e., $\mathbf{F}_x$) the reflected wave field occurs only on the $\mathbf{x}$-component (i.e., again the component pointing in the direction of the dipole excitation). In this case, the SS-reflection represents the main signal, whereas the minor PP-reflection is very small. The investigations shown in Section 3.1 prove this relation. Hence, in case of a dipped scatterer and a dipole excitation in $\mathbf{z}$-direction it is to be expected that the amplitude of the PP-reflection on the component pointing in the direction of the dipole excitation (i.e., the $\mathbf{z}$-component) decreases with increasing dip-angle, while the amplitude of the SS-reflection on the same component increases with increasing dip-angle. Intuitively explained, this corresponds to the case, where the dipole excitation perpendicular to the scatterer turns into a dipole excitation parallel to the scatterer while always the component pointing towards the dipole excitation is examined. Figures 3.14 - 3.19 exemplarily prove this expectation for all investigated perturbations δM. Furthermore, the results show the same characteristics as the study for a plane scatterer parallel to the borehole axis revealed. The relative misfits for the SS-reflection are significantly smaller than the ones obtained for the PP-reflection. In addition, the relative misfit for both reflections increases faster with negative than with positive contrast. Similar investigations were made concerning perturbations in Λ and ρ. Since the according results do not present new aspects they are not shown.

According to the discussed observations, it can be assumed that the dip-angle of the scatterer has no significant influence on the relative misfit between the *qseis*-results and the Born-based results. To quantify this misfit, again, the relative misfits $\delta u_r^{\odot\oplus}$ are calculated according to equation 3.1. The resulting values are specified in Tables 3.15 and 3.16, referring to the PP- and the SS-reflection, respectively. For the sake of completeness Table 3.15 presents also the misfit results for a dipole excitation perpendicular to the scatterer (i.e., $\alpha = 0°$) and Table 3.16 presents the misfit results for a dipole excitation parallel to the scatterer (i.e. $\alpha = 90°$). Obviously, the results widely meet the expectations. In most cases the relative misfit differs only slightly with increasing dip-angle. However, regarding negative contrasts, a systematic light increase of the misfit for an increasing dip-angle regarding the PP-reflection and a decreasing dip-angle regarding the SS-reflection can be observed. In addition, regarding positive contrast, a systematic light decrease of the misfitfor an increasing dip-angle regarding the PP-reflection and a decreasing dip-angle regarding the SS-reflection can be observed, respectively. This phenomenon corresponds to the

Table 3.15: Relative misfit δu_3^{PP} between the results of *qseis* and the Born-based approach in case of a dipole excitation in z-direction resulting from perturbations in M for the investigated dip-angles $\alpha = \{0°, 30°, 45°, 60°, 75°\}$ of the scatterer.

α	δM	0.3	0.2	0.1	-0.1	-0.2	-0.3
0°	δu_3^{PP}	0.322	0.226	0.091	-0.272	-0.428	-0.680
30°	δu_3^{PP}	0.313	0.222	0.085	-0.273	-0.430	-0.681
45°	δu_3^{PP}	0.296	0.201	0.072	-0.275	-0.434	-0.682
60°	δu_3^{PP}	0.251	0.156	0.039	-0.282	-0.442	-0.685
75°	δu_3^{PP}	0.041	0.113	0.047	-0.332	-0.487	-0.699

Table 3.16: Relative misfit δu_2^{SS} between the results of *qseis* and the Born-based approach in case of a dipole excitation in z-direction resulting from perturbations in M for the investigated dip-angles $\alpha = \{30°, 45°, 60°, 75°, 90°\}$ of the scatterer.

α	δM	0.3	0.2	0.1	-0.1	-0.2	-0.3
30°	δu_2^{SS}	-0.052	-0.049	-0.124	0.241	0.256	0.309
45°	δu_2^{SS}	-0.034	-0.032	-0.045	0.174	0.187	0.244
60°	δu_2^{SS}	-0.064	-0.061	-0.016	0.149	0.161	0.220
75°	δu_2^{SS}	-0.076	-0.073	-0.004	0.139	0.151	0.210
90°	δu_2^{SS}	-0.080	-0.076	-0.014	0.137	0.148	0.207

observed fact, that the relative misfit in all investigations is bigger for the scattered particle displacements in case of a dipole excitation perpendicular to the scatterer as for a dipole excitation parallel to the scatterer. Similar investigations were made concerning perturbations in Λ and ρ. Since the results do not present new aspects they are not shown.

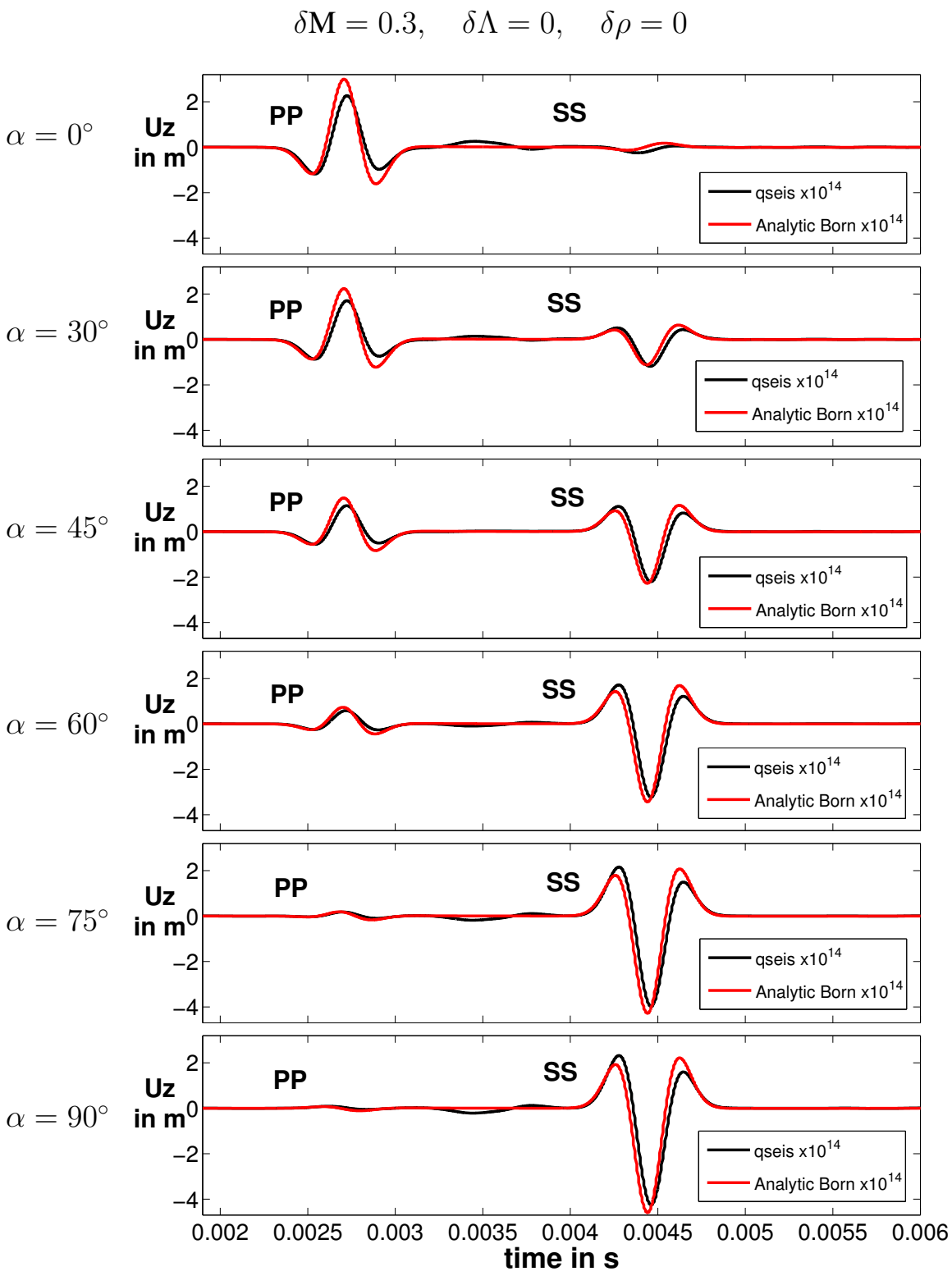

Figure 3.14: Sensitivity and accuracy analysis for $\delta \mathrm{M} = 0.3$: results for a dipole excitation in **z**-direction as a function of the varying dip-angle α of the scatterer. The resulting values for $v_\mathrm{P}, v_\mathrm{S}$ and ρ are given in Table 3.1. The displayed graphs show the comparisons of the resulting particle displacements on the **z**-component, pointing in the direction of the force source excitation, between the analytic Born result (red) and the *qseis*-result (black).

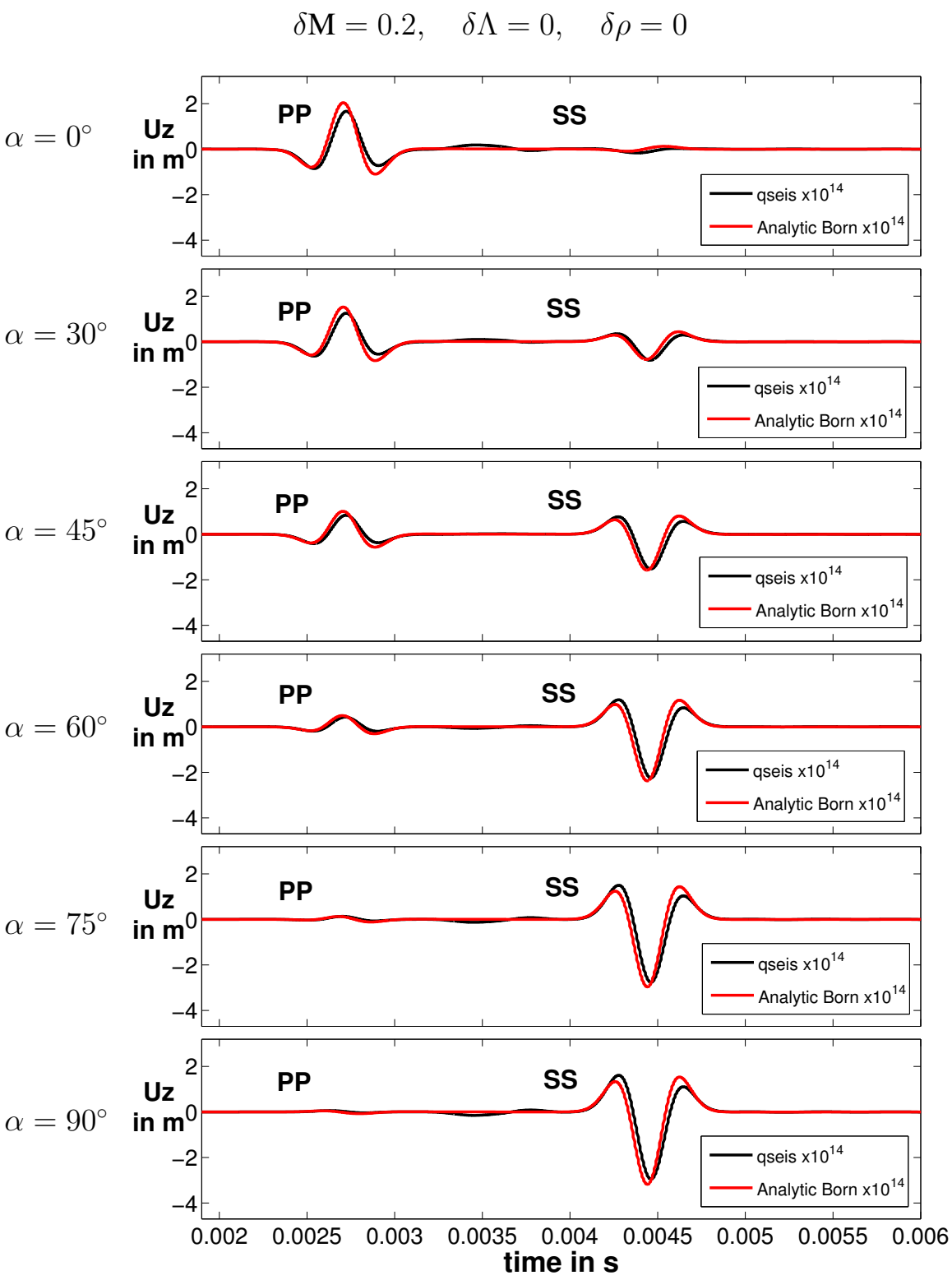

Figure 3.15: Sensitivity and accuracy analysis for $\delta \mathbf{M} = 0.2$: results for a dipole excitation in **z**-direction as a function of the varying dip-angle α of the scatterer. The resulting values for $v_{\mathrm{P}}, v_{\mathrm{S}}$ and ρ are given in Table 3.1. The displayed graphs show the comparisons of the resulting particle displacements on the **z**-component, pointing in the direction of the force source excitation, between the analytic Born result (red) and the *qseis*-result (black).

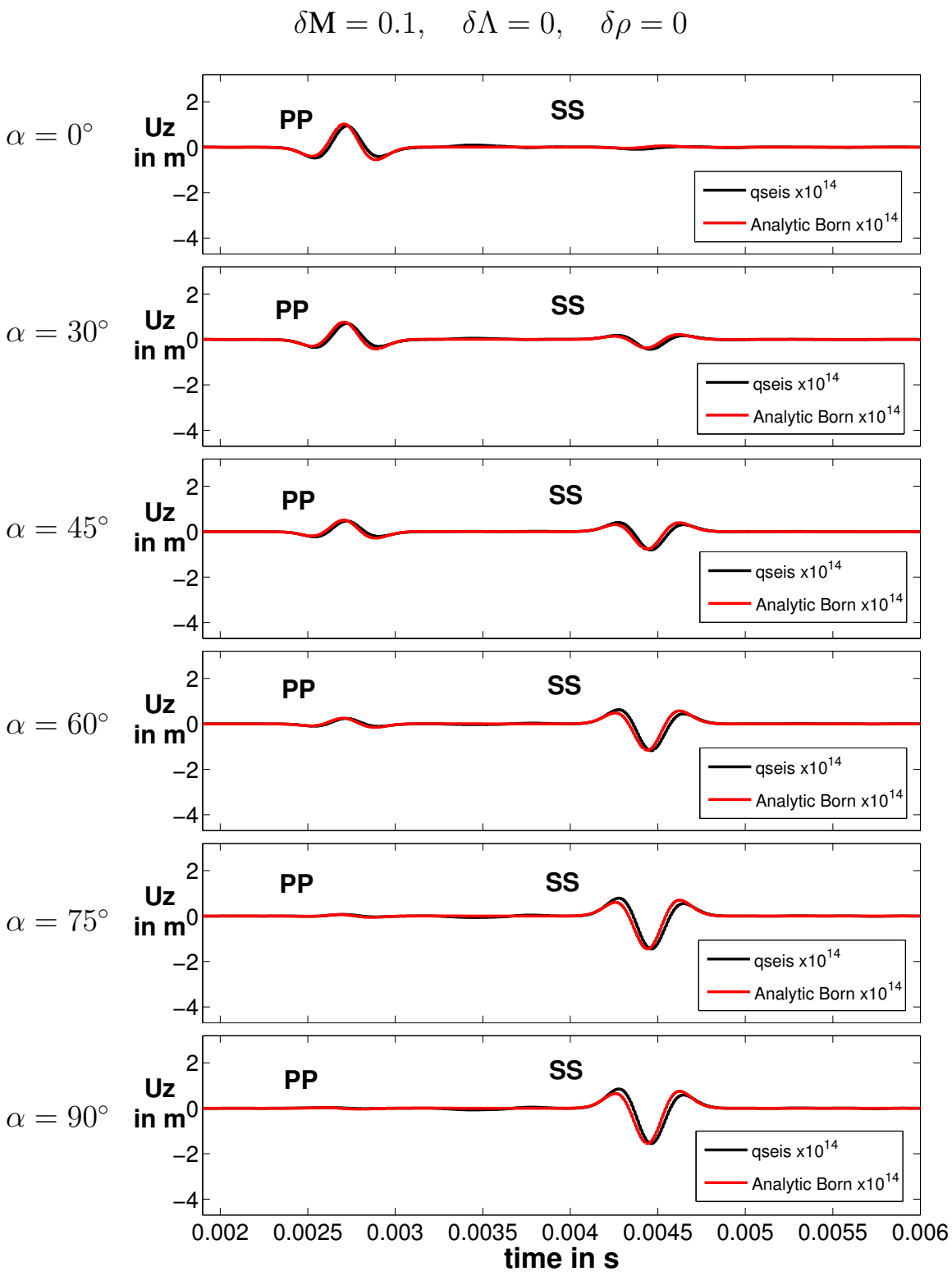

Figure 3.16: Sensitivity and accuracy analysis for $\delta \mathrm{M} = 0.1$: results for a dipole excitation in **z**-direction as a function of the varying dip-angle α of the scatterer. The resulting values for $v_\mathrm{P}, v_\mathrm{S}$ and ρ are given in Table 3.1. The displayed graphs show the comparisons of the resulting particle displacements on the **z**-component, pointing in the direction of the force source excitation, between the analytic Born result (red) and the *qseis*-result (black).

$$\delta \mathrm{M} = -0.1, \quad \delta\Lambda = 0, \quad \delta\rho = 0$$

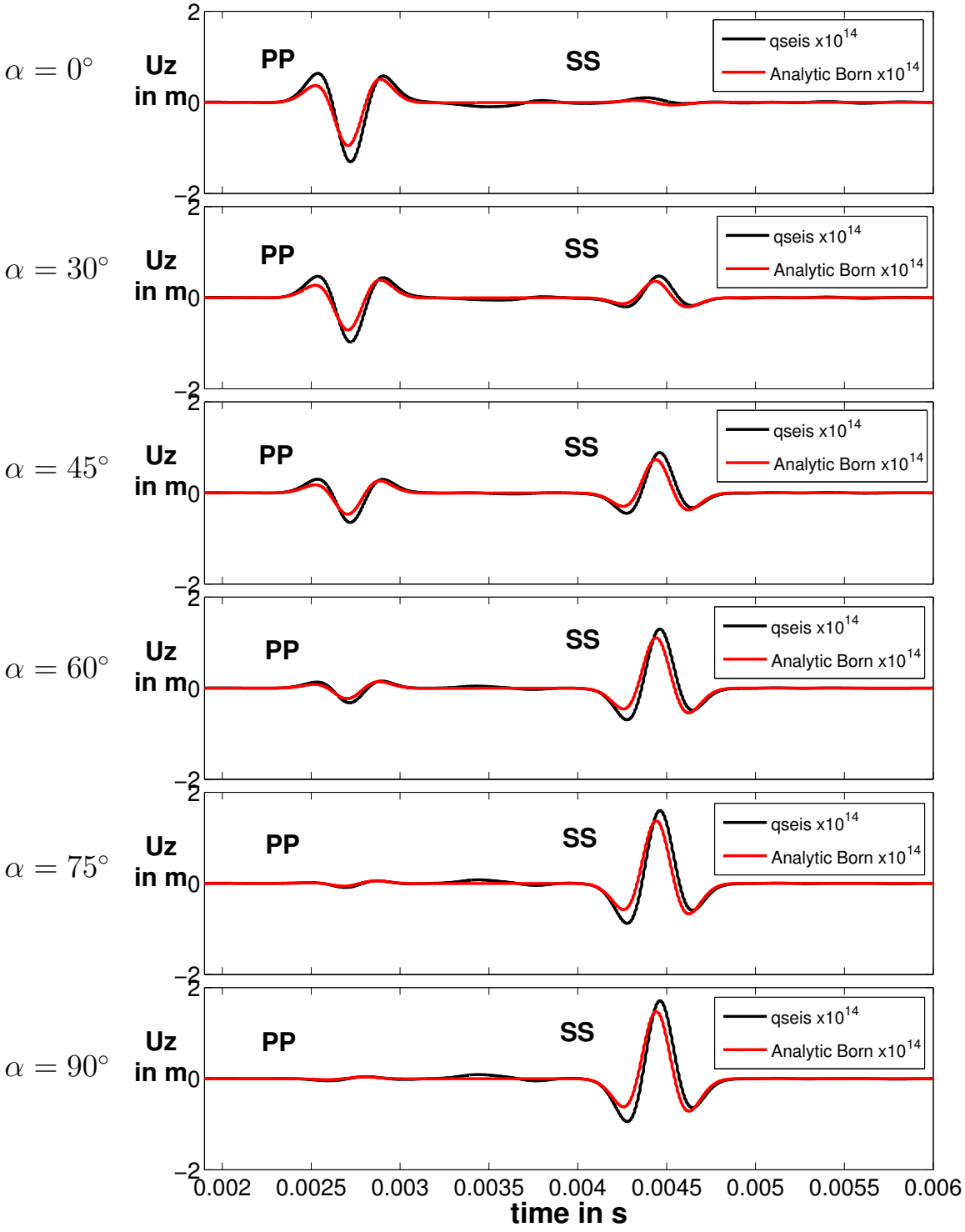

Figure 3.17: Sensitivity and accuracy analysis for $\delta \mathrm{M} = -0.1$: results for a dipole excitation in **z**-direction as a function of the varying dip-angle α of the scatterer. The resulting values for $v_{\mathrm{P}}, v_{\mathrm{S}}$ and ρ are given in Table 3.1. The displayed graphs show the comparisons of the resulting particle displacements on the **z**-component, pointing in the direction of the dipole excitation, between the analytic Born result (red) and the *qseis*-result (black).

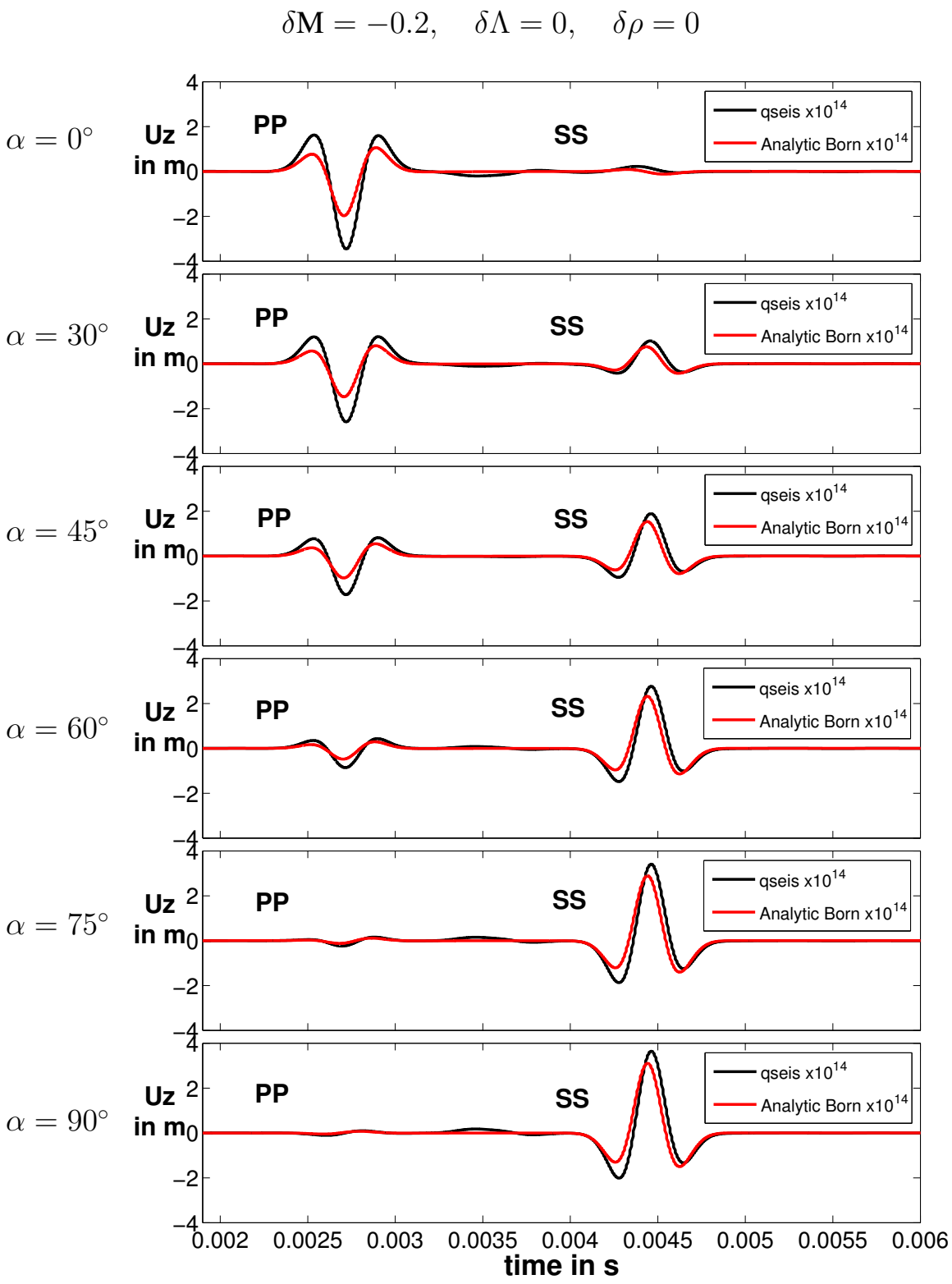

Figure 3.18: Sensitivity and accuracy analysis for $\delta \mathrm{M} = -0.2$: results for a dipole excitation in **z**-direction as a function of the varying dip-angle α of the scatterer. The resulting values for $v_{\mathrm{P}}, v_{\mathrm{S}}$ and ρ are given in Table 3.1. The displayed graphs show the comparisons of the resulting particle displacements on the **z**-component, pointing in the direction of the dipole excitation, between the analytic Born result (red) and the *qseis*-result (black).

$$\delta \mathrm{M} = -0.3, \quad \delta\Lambda = 0, \quad \delta\rho = 0$$

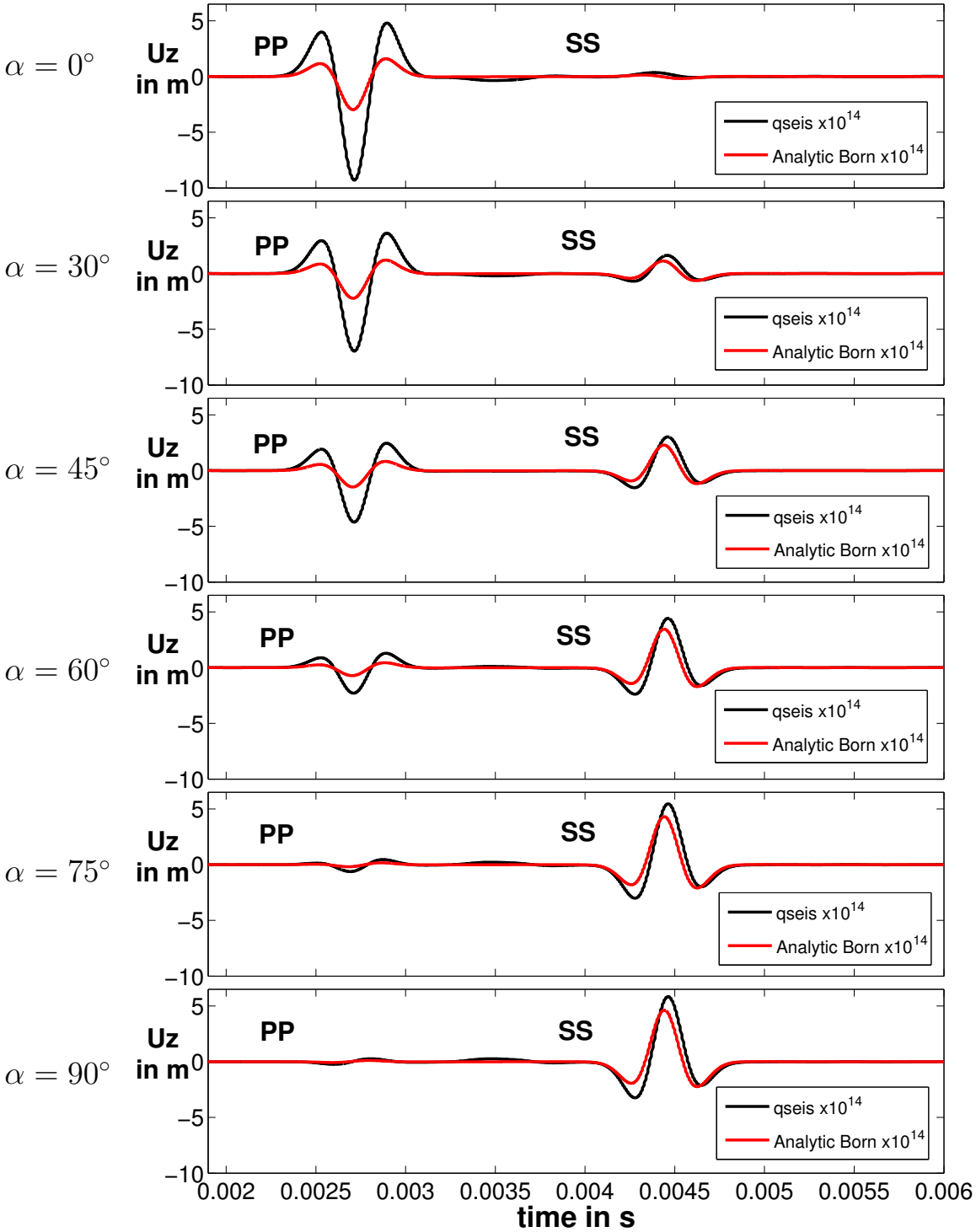

Figure 3.19: Sensitivity and accuracy analysis for $\delta \mathrm{M} = -0.3$: results for a dipole excitation in **z**-direction as a function of the varying dip-angle α of the scatterer. The resulting values for $v_{\mathrm{P}}, v_{\mathrm{S}}$ and ρ are given in Table 3.1. The displayed graphs show the comparisons of the resulting particle displacements on the **z**-component, pointing in the direction of the dipole, between the analytic Born result (red) and the *qseis*-result (black).

3.3 Summary

In general, the presented sensitivity and accuracy analysis shows that the derived first-order Born-based approach is able to reconstruct the single scattered wave field in terms of phase and amplitude. The accuracy of the results is sufficient to properly model single scattered waves in configurations, where the contrast between the background medium and the scatterer is up to 20% in the compliance parameters M and Λ and even up to 30% in the density. The evaluation of the relative misfits between the Born-based results and the quasi-analytic reference result shows that for perturbations up to 20% the misfit is at the very most less than 0.2 - 0.25, which is a good result based on a first order approximation. The investigations also show that, in general, the misfit between the *qseis*-result and the analytic Born result is considerably smaller for SS-reflections than for PP-reflections. Furthermore, the misfit for perturbations in M and ρ is increasing faster with increasing negative contrast (i.e., $\{\delta\mathrm{M}, \delta\rho\} = -0.1, -0.2, -0.3$) than with increasing positive contrast (i.e., $\{\delta\mathrm{M}, \delta\rho\} = 0.1, 0.2, 0.3$) and the misfit for perturbations in Λ is increasing faster with increasing positive contrast (i.e., $\delta\Lambda = 0.1, 0.2, 0.3$) than with increasing negative contrast (i.e., $\delta\Lambda = -0.1, -0.2, -0.3$). Altogether, the effect for $\delta\rho$ is much less pronounced than for the other perturbations. The analysis further showed, that a dip of the plane scatterer relative to the borehole axis has no significant influence on the accuracy.

The mentioned systematic misfit-effects reveal that especially the scattering-coefficient for PP is sensitive to high contrasts in the compliance parameters M and Λ, which is also reflected in the equations for the scattering coefficients (cf. equations 2.72 - 2.77). The analysis further showed that the misfit values for configurations with varying distances between the borehole axis and the scatterer do not considerably differ from each other. This indicates that the occurring (small) differences in the misfit can be traced back to the differences between the approximated Born scattering coefficients and the true reflection coefficients. In turn, this leads to the conclusion that the geometrical spreading is correctly handled by the implemented Born-based approach, where it is assumed to be inversely proportional to the two way distance from the borehole axis to the scatterer.
In this regard, the comparison of the Born scattering coefficients with the Zoeppritz reflection coefficients shows that the application of a small second order correction in the perturbation parameters M (for the SS-reflection) and ρ (for the PP- and SS-reflection) would lead to a match of the two coefficients (apart from an expected constant factor). For the other cases a higher order correction is needed. However, since the mismatch between the coefficients is really small, the implemented linear dependency of the first-order Born scattering coefficients on the perturbations parameters $\delta\mathrm{M}, \delta\Lambda$ and $\delta\rho$ (cf. equations 2.72 - 2.77, 3.2) seems to be acceptable.

Chapter 4

Numerical implementation of the approach

Based on the explicit expression for the far-field first-order scattered wave field due to an arbitrarily oriented dipole excitation, derived in chapter 2, I developed the program *FMBORN*. This numerical implementation allows an efficient modeling of the 3D elastodynamic scattered wave field in a moving source-receiver experiment (e.g., borehole acoustics, VSP, surface seismics) as shown in Veile et al. (2012). In this chapter, the details of the implementation are discussed and its performance is analyzed.

4.1 The numerical implementation *FMBORN*

FMBORN is based on the separation between the background medium and the scatterer. Therefore, the implementation uses two grids with the same grid spacing as shown in Figure 4.1. The perturbation grid (illustrated with dashed lines) where all grid points act as potential scattering points represents the geological structure. In case the elastic properties of the geological structure differ from those of the background medium, perturbations arise (cf. equations 2.50 - 2.52) which are exemplarily indicated by brown dots in Figure 4.1, left. The background grid (illustrated with continuous lines) represents the unbounded, homogeneous, isotropic and elastic background medium where the wave propagation takes place. Hence, source and receiver positions are fixed on this grid.

The separation between the two grids allows an independent computation of the scattering coefficients and the terms related to the wave propagation. Thus, the unitary ray vectors (cf. equation 2.27, 2.43, 2.45 - 2.47) of all possible incident and scattered waves, respectively, and the directivities of all possible incident waves (cf. equation 2.86 - 2.88) are calculated on the background grid and are then stored. Furthermore, the Green's functions $\hat{G}_{\odot}(\mathbf{x}, \mathbf{x}'')$ and $\hat{G}_{\oplus}(\mathbf{x}', \mathbf{x})$ (cf. equation 2.15, 2.16), representing the incident and scattered wave propagation, are calculated on the background grid for all possible incident and scattered ray paths and are also stored. Figure 4.1 (right) illustrates one of these possible ray paths from the source location $\mathbf{x}''$ to a

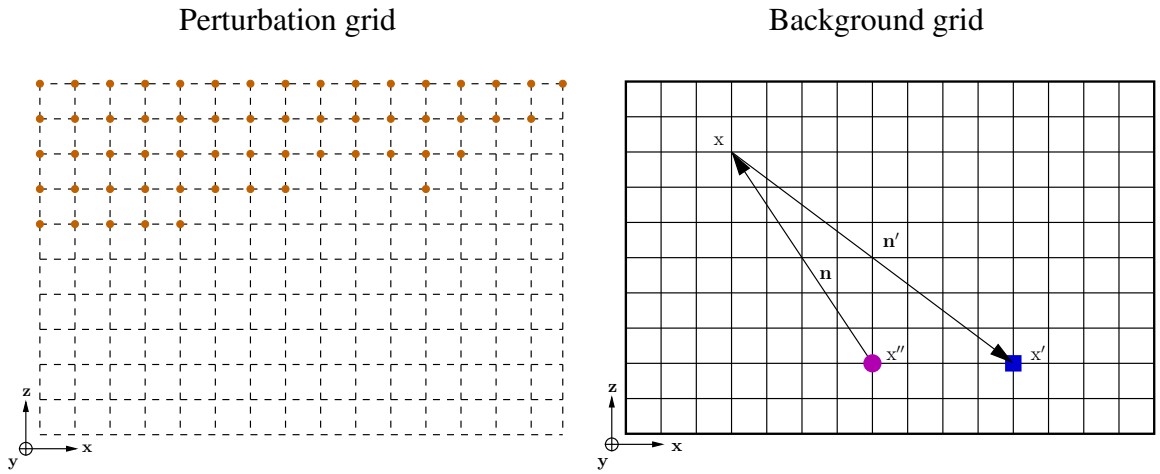

Figure 4.1: Visualization of the two grids used in *FMBORN* on which the calculations are performed. Left: the perturbation grid represents the geological structure. The brown dots indicate a perturbation of the background medium. Right: the background grid represents the unbounded, homogeneous, isotropic and elastic background medium where the wave propagation takes place. Source (pink) and receiver (blue) are fixed on this grid at $\mathbf{x}''$ and $\mathbf{x}'$, respectively. Here, $\mathbf{n}$ and $\mathbf{n}'$ denote a ray path from the source location $\mathbf{x}''$ to a potential scattering point $\mathbf{x}$ and then to the receiver location $\mathbf{x}'$.

potential scattering point $\mathbf{x}$ and then to the receiver location $\mathbf{x}'$. In contrast, the scattering coefficients $R_r^{\odot\oplus}(\mathbf{x})$ (cf. equations 2.54 - 2.58) are evaluated for all possible reflected and converted waves (PP, PSV, SVP, SVSV, SHSH) on each grid point of the perturbation grid and they are stored, too. In case the perturbation is zero (i.e., if no contrast to the background medium exists, cf. equations 2.50 - 2.52), the scattering coefficients vanish at this grid point.

In order to calculate the scattered wave field, the integrand of the spectral scattered wave particle velocity (cf. equation 2.59) can then be evaluated by a simple multiplication of the afore mentioned factors at each grid point, according to equation 2.59. This step can be visualized by superposing the two grids shown in Figure 4.1 and combining the wave propagation related terms with the scattering coefficients at the corresponding grid points. In the next step, a summation over the perturbation grid which represents the potential scattering volume and a multiplication with the spectral source signature is performed. Finally, an inverse Fourier transform into the time domain is applied, using the freely available subroutine library *FFTW* (Frigo and Johnson, 2005). The different stages of the computations are illustrated in Figure 4.2.

To account for the drilling process (i.e., the movement of the fixed source-receiver geometry relative to the geology), the background grid (including source and receiver) is shifted relative to the perturbation grid by a user-defined distance in $\mathbf{x}$-direction (i.e., the direction of the borehole axis). This process is visualized in Figure 4.3, where, for reasons of visualization, the two grids are displayed slightly out of alignment. The already mentioned separate computation and storage of both the Green's functions and the scattering coefficients finally allows for an efficient simulation of the drilling process by this simple shift of the background grid relative to the perturbation grid. Because they are precalculated and stored, neither scattering coefficients nor Green's functions have to be evaluated again. Only a different combination of both is necessary to

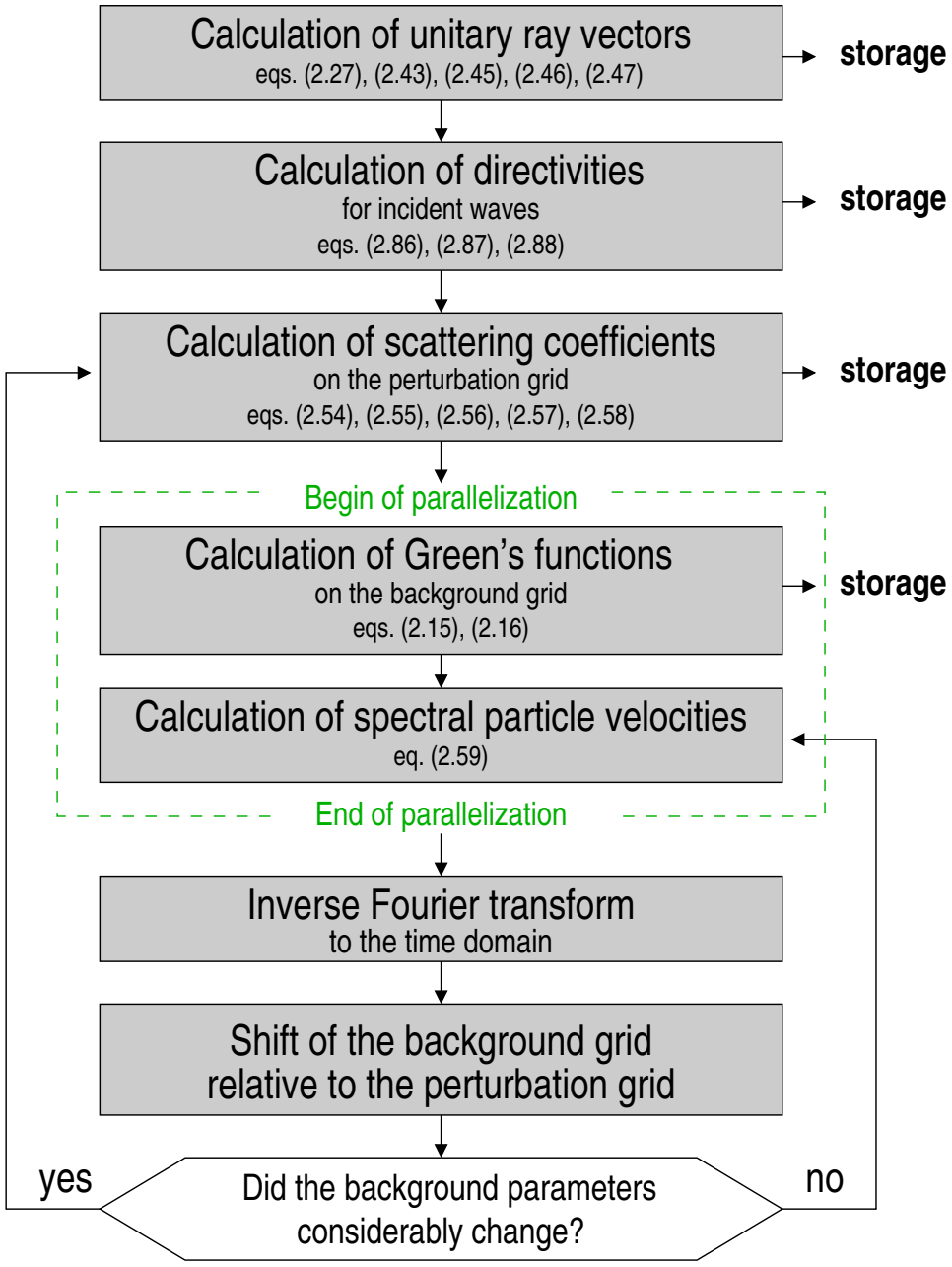

Figure 4.2: Schematic process of the numerical implementation *FMBORN*. All required factors for the evaluation of the spectral scattered particle velocities are independently calculated and stored. Afterwards, the latter are evaluated in a parallel environment by a simple multiplication of the stored factors on each grid point and a summation over the perturbation area. Applying an inverse Fourier transform to the time domain delivers the desired corresponding time series. The drilling process is then realized by a shift of the two superposed grids relative to each other. As long as the background parameters do not change considerably, the scattered wave field resulting from the next source-receiver position is obtained by a different combination of the stored factors.

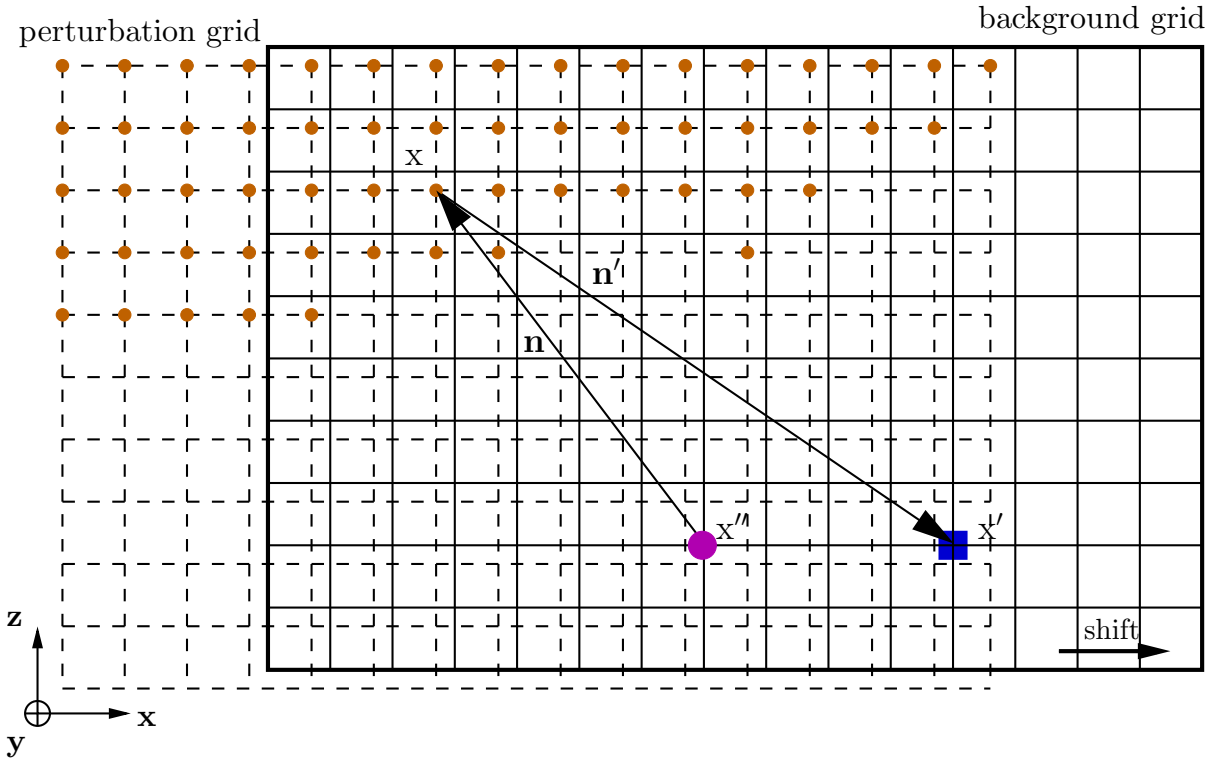

Figure 4.3: Visualized interpretation of the numerical implementation *FMBORN*. The dashed lines represent the perturbation grid, whereas the continuous lines represent the background grid on which a source (pink) and a receiver (blue) are placed. For better visualization the two grids are displayed slightly out of alignment. Grid points marked with brown dots indicate a perturbation to the homogeneous background medium and lead to a finite scattering coefficient. The tool movement is realized by a shift of the fixed source-receiver combination on the background grid relative to the perturbation grid.

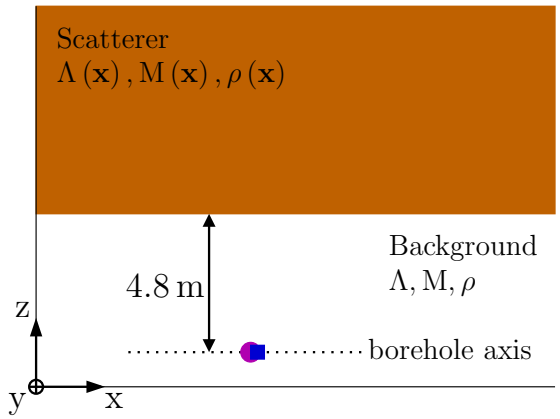

Figure 4.4: Setup for the convergence study: the plane scatterer has a distance of 4.8 m to the borehole axis. Source (pink) and receiver (blue) coincide and are located in the middle of the $\mathbf{x}$- and $\mathbf{y}$-dimension of the model, respectively, and close to $\mathbf{z} = 0$ m. As source a dipole excitation was used, which generates a Ricker wavelet with $f_c = 1$ kHz and a maximum amplitude of 1 N.

compute the spectral scattered particle velocity of the next tool position, i.e., the next position of the fixed source-receiver geometry relative to the geology. This procedure is justified as long as the elastodynamic properties of the background medium do not change considerably. Otherwise, the Green's functions and the scattering coefficients have to be recalculated and almost the entire process has to be run again. Figure 4.2 visualizes the corresponding workflow.

4.2 Convergence study for the scattering integral

In this section, the convergence of the scattering integral (cf. equation 2.59) is investigated with respect to the summation region. For this purpose, results of *FMBORN* are compared with results of the zero-offset analytic Born solution (cf. equations 2.104 - 2.105, 2.118 - 2.119) for an exemplary setup shown in Figure 4.4. The plane scatterer has a distance of 4.8 m to the borehole axis, which represents a realistic borehole setup. Source (pink) and receiver (blue) coincide and are located in the middle of the $\mathbf{x}$- and $\mathbf{y}$-dimension of the model, respectively, and close to $\mathbf{z} = 0$ m. As source a dipole excitation perpendicular to the scatterer was used, which generates a Ricker wavelet with a center-frequency $f_c = 1$ kHz and a maximum amplitude of 1 N (cf. appendix F). In this case the reflections do only occur on the $\mathbf{z}$-component as shown in chapter 2, section 2.4. Hence, only this component is actually investigated.

The chosen parameters $v_{\mathrm{P}}, v_{\mathrm{S}}$ and ρ for the background medium are specified in Table 4.1 and correspond to a medium containing salt. Based on a density perturbation of 20% to the background medium and no perturbation in the elastodynamic parameters Λ and M, the parameters $v_{\mathrm{P}}(\mathbf{x}), v_{\mathrm{S}}(\mathbf{x})$ and $\rho(\mathbf{x})$ for the scatterer were calculated according to equations 2.22 and 2.23 and are also listed in Table 4.1.

Using the background medium velocity of 4688 m/s for the P-wave and the center-frequency $f_c = 1$ kHz of the Ricker wavelet, the largest occurring dominant wavelength is $\lambda_{\mathrm{P,dom}} = 4.69$ m.

The convergence study was performed with a spatial discretization DH = 0.1 m in all three dimensions. Initially, for the model a spatial extension of 10 m in all three dimensions was chosen. For the scatterer this implies a spatial extension of 10 m × 10 m × 5 m in $\mathbf{x}$-, $\mathbf{y}$- and $\mathbf{z}$-direction, respectively. For the summation region of the scattering volume this corresponds to twice $\lambda_{\mathrm{P,dom}}$ in $\mathbf{x}$- and $\mathbf{y}$-direction and $\lambda_{\mathrm{P,dom}}$ in $\mathbf{z}$-direction and covers approximately the area of the first Fresnel zone (Yilmaz, 1987) which has in this case a radius of about 4 m. Table 4.2 lists the different sizes of the tested scattering volumes and the corresponding relation between its spatial extension in $\mathbf{x}$-, $\mathbf{y}$- and $\mathbf{z}$-direction, respectively, and the dominant P-wavelength. Figure 4.5 shows the scattered particle displacement on the $\mathbf{z}$-component computed with the analytic Born solution (black) and *FMBORN* for different spatial extensions of the scattering volume (other colors). According to equation 2.127, the scattered particle displacement is composed of a specular part (cf. equation 2.128) and a diffuse part (cf. equation 2.129). Only the latter is responsible for the occurring SS-reflection.

The results show that a convergence of the scattering integral in equation 2.59 is only ensured if the largest occurring dominant wavelength fits at least four times into the horizontal and three times into the vertical spatial extension of the scattering volume. This case leads to a total scattering volume of 20 m × 20 m × 15 m and a total model size of 20 m × 20 m × 20 m. Although the PP-reflection itself is already properly modeled for smaller spatial extensions of the scattering region, the effect of the non-converging integral is clearly visible in the coda. In Test 1 the SS-reflection is not even clearly distinguishable from the occurring truncation errors (cf. Figure 4.5, blue curve). If the scattering volume is gradually enlarged in all three dimensions (cf. Tests 2 - 5), these errors vanish. However, the SS-reflection is not properly modeled when the largest occurring dominant wavelength does not fit at least four times into the horizontal and three times into the vertical spatial dimension of the scattering volume, respectively. The necessary summation area then corresponds to approximately twice the (first) Fresnel zone which has in this case a radius of about 4 m. Thus, this result reflects common practice in other approaches.

4.3 Discretization study

In order to establish a criterion for the spatial discretization, a second convergence test was performed for the same scenario. This test was carried out for a dipole excitation perpendicular

Table 4.1: Parameters for the homogeneous background medium and the scatterer used in the convergence study for *FMBORN*.

	v_{P} (in m/s) s_{P} (in μs/ft)	v_{S} (in m/s) s_{S} (in μs/ft)	ρ (in kg/m^3)
background	4688 65	2538 120	2100
scatterer	4279 71	2316 132	2520

Table 4.2: Convergence study for the scattering integral calculated in *FMBORN*: overview of the tested scattering volumes and the resulting relation between its spatial dimensions and the largest dominant wavelength which occurs.

	Test 1			Test 2			Test 3		
scattering volume	x	y	z	x	y	z	x	y	z
in grid points	100	100	50	150	150	100	150	150	150
in m	10	10	5	15	15	10	15	15	15
$\frac{\text{dimension in m}}{\lambda_{P,\text{dom}} \text{ in m}}$	2.13	2.13	1.07	3.20	3.20	2.13	3.20	3.20	3.20

	Test 4			Test 5		
scattering volume	x	y	z	x	y	z
in grid points	200	150	150	200	200	150
in m	20	15	15	20	20	15
$\frac{\text{dimension in m}}{\lambda_{P,\text{dom}} \text{ in m}}$	4.27	3.20	3.20	4.27	4.27	3.20

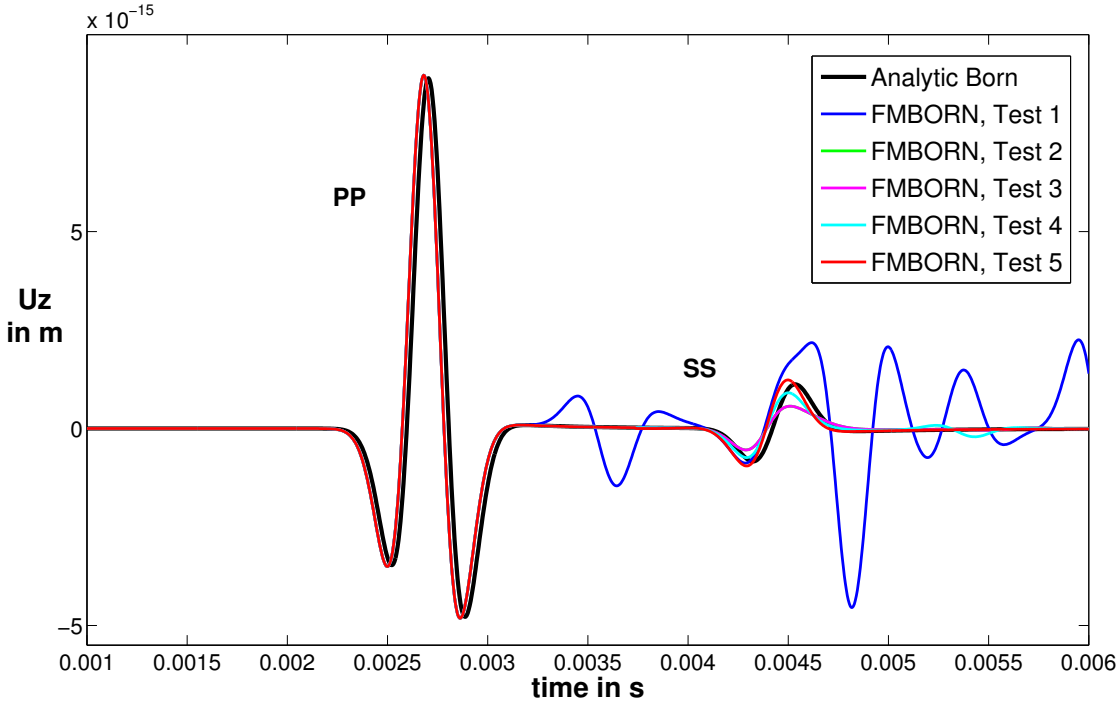

Figure 4.5: Convergence study for the scattering integral calculated in *FMBORN*: the Born approximation based analytic solution of the particle displacement is plotted in black and clearly shows the PP- and the SS-reflection, respectively. The curves in other colors show the corresponding results of the numerical implementation *FMBORN* for different scattering volumes. The related grid sizes and scattering volumes are listed in Table 4.2.

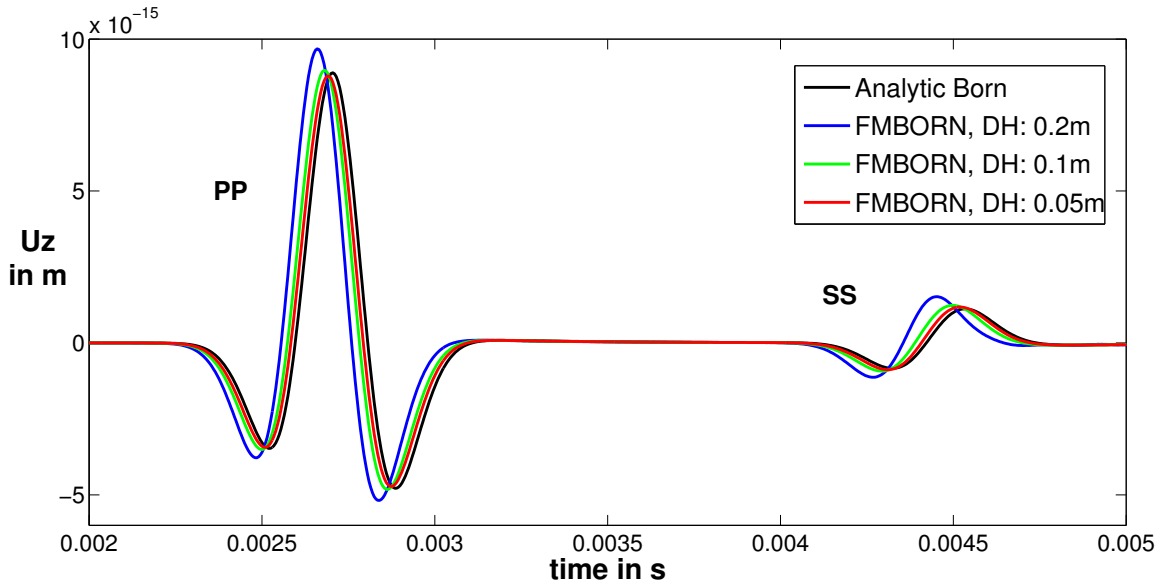

Figure 4.6: Convergence study for *FMBORN* for the spatial discretization using a dipole excitation in z-direction: the result of the zero-offset analytic Born solution for the particle displacement is plotted in black. The curves in other colors show the results of the numerical implementation *FMBORN* for different grid spacings. As in this case reflections occur only on the vertical component (cf. subsection 2.4.2), only this component is actually shown.

(i.e., along the z-direction) and parallel to the scatterer (i.e., along the x-direction).

Dipole excitation perpendicular to the scatterer, i.e., in z-direction

Figure 4.6 shows the result of the convergence test for the spatial discretization (DH) in case of a dipole excitation perpendicular to the scatterer, i.e., in z-direction. The plot shows the scattered particle displacement on the z-component for a zero-offset configuration computed with the analytic Born solution (black) and *FMBORN* with different DHs (other colors).

The convergence test was performed for three different grid spacings. To ensure a convergence of the integral in equation 2.59 in all four cases a model size of 20 m × 20 m × 20 m was used (cf. Section 4.2), leading to a rapid growth of grid points with decreasing grid spacing. In the investigated case here, the PP-reflection represents the main reflection; the dominant P-wavelength is 4.69 m. Table 4.3 lists the different spatial discretizations, the resulting sampling per dominant P-wavelength, the total grid size and the least-squares-misfit between the analytic and the corresponding numerical solution. A definition of the used least-squares-misfit function is given in appendix F.

The results indicate that a sampling of the dominant P-wavelength by 23 grid points is not sufficient, as the corresponding curve (blue) for the scattered particle displacement in Figure 4.6 differs in phase and amplitude significantly from the analytic Born result (black). A coherent summation in equation 2.59 does not seem to be ensured. Furthermore, it can be observed that the smaller the spatial discretization gets, the closer the numerical result gets to the analytic

Table 4.3: Discretization study for *FMBORN* using a dipole excitation perpendicular to the scatterer: overview of the tested spatial discretizations (DH), the resulting dominant P-wavelengths $\lambda_{\text{P,dom}}$, the total grid size, and the least-squares misfit between the analytic and the corresponding numerical result.

	DH (in m)	grid points per $\lambda_{\text{P,dom}}$	grid points in x,y,z-direction	ℓ^2-misfit	color in Figure 4.6
1	0.2	23	$100 \times 100 \times 100$	0.684	blue
2	0.1	46	$200 \times 200 \times 200$	0.350	green
3	0.05	93	$400 \times 400 \times 400$	0.191	red

result (in phase as well as in amplitude). Although the two curves do not coincide, the ℓ^2-misfit between the analytic and the numerical results decreases significantly with decreasing DH as shown in Table 4.3. Thus, in a next step the results for the same setup but a dipole excitation parallel to the scatterer are investigated. In this case, the SS-reflection represents the main signal (cf. section 3.1). As its wavelength is considerably smaller than the P-wavelength, it is to be expected that the corresponding results lead to a clear conclusion regarding the spatial discretization.

Dipole excitation parallel to the scatterer, i.e., in $\mathbf{x}$-direction

Figure 4.7 shows the result of the convergence test for the spatial discretization in case of a dipole excitation parallel to the scatterer, i.e., in $\mathbf{x}$-direction. The plot shows the scattered particle displacement on the $\mathbf{x}$-component for a zero-offset configuration computed with the analytic Born solution (black) and *FMBORN* with different DHs (other colors).

In this context, the same parameters were applied as in the case with a dipole excitation in $\mathbf{z}$-direction. This time, the SS-reflection represents the main reflection; the dominant S-wavelength is 2.54 m. Table 4.4 lists the different spatial discretizations, the resulting sampling per dominant S-wavelength, the total grid size and the least-squares misfit between the analytic and the corresponding numerical solution.

The results confirm the observations made for the dipole excitation in $\mathbf{z}$-direction. In case the dominant S-wavelength is sampled by twelve grid points, individual scatterers and their responses are observed and the signal develops a coda as the blue curve in Figure 4.7 clearly shows. In this case it can also be observed that the smaller the spatial discretization gets, the closer the numerical result gets to the analytic result (in phase as well as in amplitude). Although the two curves do not coincide, the least-squares misfit between the analytic and the numerical results decreases significantly when the grid spacing is diveded in half as shown in Table 4.4. Based on the shown results, I conclude that a spatial discretization of at least 25 grid points per dominant wavelength is sufficient to properly sample the scattering region. In comparison to other numerical modeling techniques this is a relatively dense discretization. Finite-difference methods which (in contrast to the presented scattering approach) sample the wave field require a

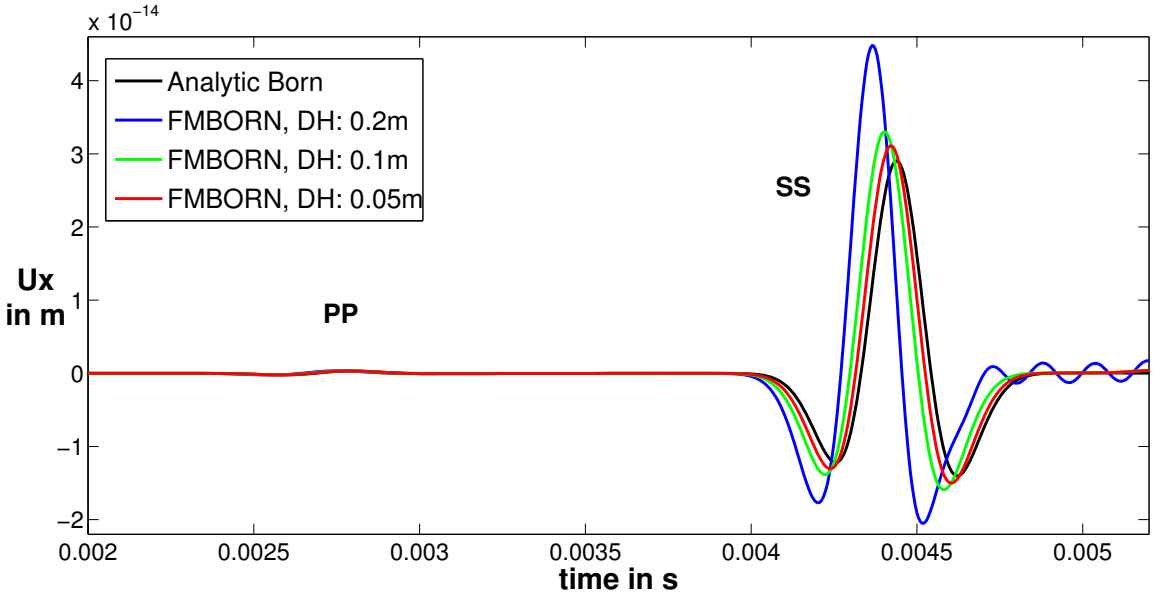

Figure 4.7: Convergence study for *FMBORN* for the spatial discretization using a dipole excitation in x-direction: the results of the zero-offset analytic Born solution for the particle displacement is plotted in black. The curves in other colors show the results of the numerical implementation *FMBORN* for different grid spacings. As in this case reflections occur only on the x-component (cf. subsection 2.4.2), only this component is actually shown.

Table 4.4: Convergence study for *FMBORN* using a dipole excitation parallel to the scatterer: overview of the tested spatial discretizations (DH), the resulting dominant S-wavelengths $\lambda_{S,dom}$, the total grid size and the least-squares misfit between the analytic result and the corresponding numerical result.

	DH (in m)	grid points per $\lambda_{S,dom}$	grid points in x,y,z-direction	ℓ^2-misfit	color in Figure 4.7
1	0.2	12	$100 \times 100 \times 100$	-	blue
2	0.1	25	$200 \times 200 \times 200$	0.589	green
3	0.05	50	$400 \times 400 \times 400$	0.272	red

spatial discretization of only six to ten grid points per dominant wavelength (Robertsson et al., 1994). Comparable spectral methods actually need a discretization of only two to three grid points per dominant wavelength (Červený, 2001).

4.4 Performance

For the simulation of a realistic borehole configuration with *FMBORN*, a model with at least $200 \times 200 \times 200$ grid points in $\mathbf{x}$-, $\mathbf{y}$- and $\mathbf{z}$-direction, respectively, is needed due to the requirement for the spatial discretization. The associated total computation time for the evaluation of the scattered wave field is about 143 min and the total memory requirement accumulates to approximately 490 GB.

Due to these constraints, a parallel implementation is required to reduce the calculation time and to distribute the overall memory requirement over different domains. In the following, the implemented parallelization is discussed and performance results for the static case (i.e., without a moving tool) and the dynamic case (i.e., with a moving tool) are shown. Furthermore, the total memory requirement is discussed in detail.

Parallelization

Most of the incurred computational efforts can be traced back to the evaluation of the Green's functions for the incident and the scattered wave. In addition to the discussed dense spatial discretization leading to small grid spacings (i.e., 5-10 cm), particularly frequencies between 1 kHz and 10 kHz cause the large computation time and memory requirement of *FMBORN*. Meeting the Nyquist-criterion (Nyquist, 1928) these high-frequency data lead to small time samplings (i.e., 0.5 ms - 10 µs). Thus, given a typical length for a time series a large number of frequencies results, for which the Green's functions in the presented approach do not only have to be evaluated but also have to be stored. Thus, the large memory requirement results. As a consequence, I decided to parallelize the implementation by a decomposition of the model (in the following referred to as 'domain decomposition') using the Message Passing Interface (MPI) specification (Gropp et al., 1999).

With respect to the 'while drilling' approach (i.e., a real-time simulation of the moving source-receiver combination relative to the geology), not only the computation of the Green's functions but also the evaluation of the spectral scattered particle velocity (cf. equation 2.59) has to be efficient. Therefore, in addition to the computation of the Green's functions, I parallelized their computation as indicated in Figure 4.2. As the computations of the Green's functions as well as of the spectral scattered wave particle velocities are the same for each grid point, it is reasonable to divide the model into several equally sized sub-domains which can then be distributed over different cores. With respect to the calculations on these sub-domains, only an initial communication is required, to distribute the results of the precursory calculations (i.e., the computation of the unitary ray vectors, the directivities, etc.) from the master core over the other cores. A communication between the sub-domains is not necessary. For each of these sub-domains, the Green's functions and then the resulting spectral scattered wave particle velocity

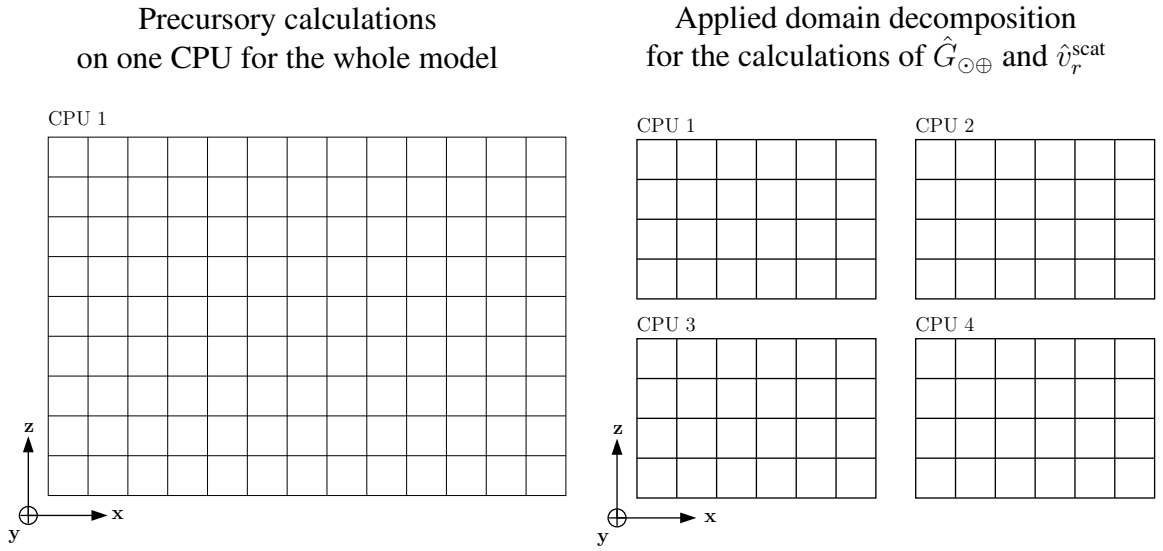

Figure 4.8: Exemple of domain decomposition on a computer consisting of four cores. Left: precursory calculations are performed for the whole model on one core. Right: for the calculation of the Green's functions and the spectral scattered particle velocities, the model is divided into four sub-domains and distributed over four cores, while no information exchange between the sub-domains is required.

are evaluated on a different core. Afterwards, the local results for the spectral scattered wave particle velocity are communicated to the master process which finally adds up all local results and applies the inverse Fourier transform (cf. appendix F). Hence, the exchange of information requires communication only between the master process and the other cores and is realized by corresponding MPI routines. The advantage of the implemented domain decomposition is the reduction of memory use and computation time per core. Figure 4.8 illustrates the implemented domain decomposition on a quad-core computer.

4.4.1 Static case

Firstly, the performance of the static case, i.e., without a moving source-receiver geometry, is discussed. Therefore, Table 4.5 shows total computation times on one and on 64 cores, respectively, for a model with $200 \times 200 \times 200$ grid points. The improvement of the performance based on the applied domain decomposition is clearly visible: using 64 cores the total computation time is approximately 60 times faster than using one core and the resulting turnaround time definitely matches the requirements of a real-time application. Hence, in the following the required computation time is investigated in more detail.

Figure 4.9 shows computation times as a function of the number of cores for a model with $100 \times 100 \times 100$ grid points in $\mathbf{x}$-, $\mathbf{y}$- and $\mathbf{z}$- direction, respectively, and a spatial discretization DH = 0.2 m. An overview of the corresponding distribution of cores in $\mathbf{x}$-, $\mathbf{y}$- and $\mathbf{z}$-direction and the resulting grid sizes of the sub-domains are listed in Table 4.6. At this point it should be noted that whenever computation times are specified in the following, the values represent

Table 4.5: Computation times of *FMBORN* for a static case for a total grid size of $200 \times 200 \times 200$ points in $\mathbf{x}$-, $\mathbf{y}$,- and $\mathbf{z}$-direction, respectively, and the corresponding number of cores (NC).

NC	grid points in x,y,z-direction	total computation time
1	$200 \times 200 \times 200$	143 min
64	$200 \times 200 \times 200$	2 min 25 s

an arithmetic mean of multiple code runs. Figure 4.9 (left) displays the total computation time and the fraction used for the parallel part of the code as a function of the number of cores (NC). Obviously, the major part of the computation time is needed for the parallelized part of the code which corresponds to the fact that the most time-consuming computations are performed there. Therefore, the required time for the non-parallel precursory calculations is quite short. Furthermore, it is clearly visible that with an increasing number of cores the difference between the total computation time and the computation time needed for the parallel part remains more or less constant which meets the expectations: the model size remains the same and therefore the non-parallel computations should not increase. In addition, the plot shows that with an increasing number of cores the computation time generally decreases. However, when using more than 64 cores the total computation time slightly increases. To further investigate this effect Figure 4.9 (right) shows again the computation time for the parallel part but also the fraction used for the computation of the Green's functions and the necessary communication time between the master core an the other cores. Here, it is visible that the computation time needed for the evaluation of the Green's functions still decreases with an increasing number of cores although the saving in time considerably reduces. However, at the same time, the communication cost rises linearly due to the doubling of the number of used cores. Hence, the saving in time gained by the faster calculation of the Green's functions is over-compensated by the time loss due to the larger communication cost. Thus, the total computation time gently increases. The required rising communication cost is due to the fact that the size of the sub-domain for each core continuously decreases (as the total model size remains the same), resulting in a reduced number of grid points as Table 4.6 indicates. This leads to a decreasing number of computations per core but an increasing communication cost due to the increasing number of cores. Thus, the total saving in time minimizes at the point where the time needed for the communication exceeds the reduction of computation time for the Green's functions.

In addition, the behaviour of the computation time for a fixed size of the sub-domains but an increasing total grid size (TGS) and a corresponding increasing number of cores are investigated. In the following investigations, the size of the sub-domains is fixed at 50 grid points in each direction, and the total grid size is gradually increased. Figure 4.10 shows the resulting computation time as a function of the number of cores. An overview of the corresponding total grid sizes and the number of cores and their distribution over the three dimensions are listed in Table 4.7.

Figure 4.10 displays the total computation time and the fraction spent in the parallel part of the code as a function of the number of used cores. Additionally, the computation time for the

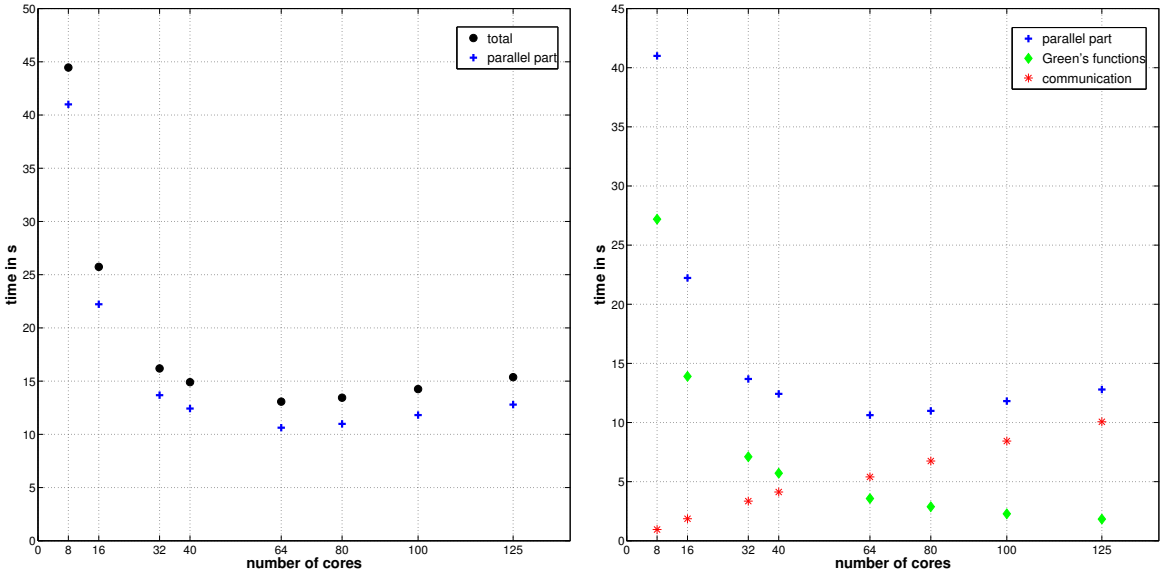

Figure 4.9: Visualization of the computation time of *FMBORN* for a model with $100 \times 100 \times 100$ grid points in x-, y- and z-direction, respectively. Left: the total computation time and the fraction for the parallel part of the code are displayed as a function of the number of cores. Right: the parallel computation time the computation time for the Green's functions and the time required for the communication between the master core and the other cores are displayed as a function of the number of cores.

Table 4.6: Domain decomposition: distribution of the discussed model over an increasing number of cores (NC) resulting in an increasing number but a decreasing size of the sub-domains.

NC (total)	NC in x,y,z-direction	grid points on each sub-domain in x,y,z-direction
8	$2 \times 2 \times 2$	$50 \times 50 \times 50$
16	$2 \times 2 \times 4$	$50 \times 50 \times 25$
32	$2 \times 4 \times 4$	$50 \times 25 \times 25$
40	$2 \times 5 \times 4$	$50 \times 20 \times 25$
64	$4 \times 4 \times 4$	$25 \times 25 \times 25$
80	$4 \times 4 \times 5$	$25 \times 25 \times 20$
100	$4 \times 5 \times 5$	$25 \times 20 \times 20$
125	$5 \times 5 \times 5$	$20 \times 20 \times 20$

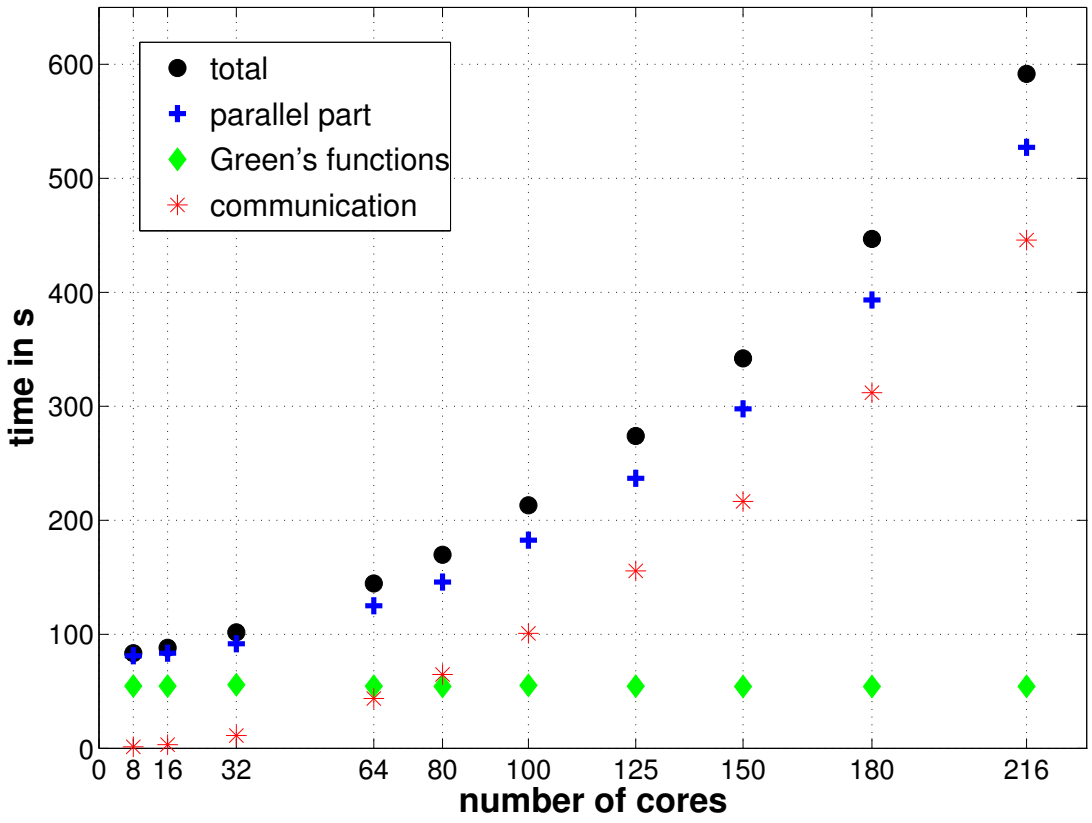

Figure 4.10: Visualization of the computation time of *FMBORN* for a fixed size of the sub-domains but an increasing total grid size. The plot shows the total computation time and the fraction spent in the parallel part of the code as a function of the number of used cores. Furthermore, the computation time for the Green's functions and the time needed for the communication between the master core and the other cores are displayed. The corresponding total grid sizes are listed in Table 4.7.

Green's functions and the time required for the communication are plotted (cf. Table 4.7 for the corresponding total grid sizes). It is clearly visible that the computation time required for the Green's functions stays approximately constant. As they are evaluated in the parallel environment on the sub-domains (which are fixed in their size) this meets the expectations. In contrast, the computation time for the parallel part of the code increases almost quadratic. Hence, also the total computation time increases. However, the increase of the latter is also caused by another factor. As Figure 4.10 clearly shows, the difference between the total computation time and the computation time for the parallel part is getting bigger with an increasing total grid size. This can be explained by the fact that with an increasing total number of grid points also the necessary precursory calculations in the non-parallelized part of the code (i.e., generation of the model, unitary ray vectors, directivities, etc.) increase and thereby the total computation time increases.

Already at the beginning of this section I stated that the memory requirement (MR) of *FMBORN* is relatively large. The following discussion will analyze the memory requirement and reveal that it is by far due to the storage of the Green's functions on each grid point for each frequency

sample. The (peak) memory requirement for the non-parallel calculations (cf. Figure 4.2) can be evaluated (in Bytes) according to

$$\mathrm{MR}_{\mathrm{head}} = 27 \cdot \mathrm{NGP}_{\mathbf{x}} \cdot \mathrm{NGP}_{\mathbf{y}} \cdot \mathrm{NGP}_{\mathbf{z}} \cdot 4\,\mathrm{Bytes}\,, \tag{4.1}$$

where $\mathrm{NGP}_{\mathbf{x}}, \mathrm{NGP}_{\mathbf{y}}, \mathrm{NGP}_{\mathbf{z}}$ denotes the total number of grid points in $\mathbf{x}$-, $\mathbf{y}$-, and $\mathbf{z}$-direction, respectively. Moreover, 27 indicates the number of 3D (floating-point)arrays, that need to be stored at the same time and 4 Bytes corresponds to the size of a 'float' on the used systems (cf. appendix G). The memory requirement for one (complex) Green's function $\hat{G}_{\odot\oplus}$ with $\odot\oplus \in \{\mathrm{P,S}\}$ can be evaluated (in Byte) according to

$$\mathrm{MR}_{\mathrm{Green}} = \mathrm{NGP}_{\mathbf{x}} \cdot \mathrm{NGP}_{\mathbf{y}} \cdot \mathrm{NGP}_{\mathbf{z}} \cdot \mathrm{n}_f \cdot 2 \cdot 4\,\mathrm{Bytes}\,, \tag{4.2}$$

where $\mathrm{NGP}_{\mathbf{x}}, \mathrm{NGP}_{\mathbf{y}}, \mathrm{NGP}_{\mathbf{z}}$ again denotes the total number of grid points in $\mathbf{x}$-, $\mathbf{y}$-, and $\mathbf{z}$-direction, respectively, n_f indicates the number of frequency samples and $2 \cdot 4$ Bytes corresponds to the size of a 'complex float' on the used systems. Table 4.8 gives an overview of the total memory requirement for a zero-offset case (i.e., without converted waves) and a non-zero-offset case (i.e., with converted waves). The total memory requirement is split into the part needed for each type of Green's function $\hat{G}_{\odot\oplus}$ with $\odot\oplus \in \{\mathrm{P,S}\}$ (cf. equation 4.2) and the part that the rest of the code needs (cf. equation 4.1). The specified memory requirement corresponds to 2048 frequency samples used in this example. This number results from the discretization in time and the desired length of the seismogram in the time-domain. In general, the final inverse Fourier transform requires a power of two for the number of frequency samples and therefore zero-padding might be required, leading to an additional increase of the number of frequencies.

Obviously, the total memory requirement is really large; much larger than it is for most common techniques. This is mainly due to the storage of the Green's functions, which accounts for over

Table 4.7: Domain decomposition: a fixed size of the sub-domains but an increase of the total grid size leads to a corresponding increasing number of cores.

NC (total)	NC in x,y,z-direction	total number of grid points in x,y,z-direction
8	$2 \times 2 \times 2$	$100 \times 100 \times 100$
16	$4 \times 2 \times 2$	$200 \times 100 \times 100$
32	$4 \times 4 \times 2$	$200 \times 200 \times 100$
64	$4 \times 4 \times 4$	$200 \times 200 \times 200$
80	$5 \times 4 \times 4$	$250 \times 200 \times 200$
100	$5 \times 5 \times 4$	$250 \times 250 \times 200$
125	$5 \times 5 \times 5$	$250 \times 250 \times 250$
150	$6 \times 5 \times 5$	$300 \times 250 \times 250$
180	$6 \times 6 \times 5$	$300 \times 300 \times 250$
216	$6 \times 6 \times 6$	$300 \times 300 \times 300$

Table 4.8: Total memory requirement (MR) of *FMBORN* for different grid sizes, split in the part required to store each type of Green's function $\hat{G}_{\odot\oplus}$ (cf. equation 4.2) and the part required for the rest of the code (cf. equation 4.1).

grid points in x,y,z-direction	MR for one Green's function	head MR (peak value)	total MR for ZO	total MR for non-ZO
$50 \times 50 \times 50$	1.91 GB	15.3 MB	3.83 GB	7.64 GB
$100 \times 100 \times 100$	15.3 GB	112 MB	30.6 GB	61.1 GB
$200 \times 200 \times 200$	122 GB	886 MB	245 GB	489 GB
$400 \times 400 \times 400$	977 GB	6.92 GB	1.91 TB	3.82 TB

99.6% of the required total memory. For rather small models in borehole applications this will normally not be any obstacle though, especially if computations are performed on large compute cluster. However, it is clearly visible that an increase of the total grid size rapidly leads to a significant increase of the memory requirement. As this is a 3D approach, a doubling of the model in each spatial dimension involves an eightfold increase of the total memory requirement as shown in Table 4.8. In the static case where the fixed source-receiver geometry is not shifted relative to the perturbation grid, this is, of course, not really required. However, the real advantage of storing the Green's functions becomes obvious when the moving source-receiver geometry is considered, as described in the next subsection.

The nodes available on high-performance clusters used in this study have up to 16 cores and 20 GB accessible memory. With respect to the memory requirement listed in Table 4.8, it is obviously not possible to compute models that have significantly more than 50 grid points in each direction, on one node. Therefore, for larger models the sub-domains are distributed over several nodes involving inter-node communication. Therfore, it was tested whether the number of used nodes affects the communication time. As Figure 4.11 indicates, this is not the case. Even a doubling of the used nodes has no significant effect on the computation time. Hence, it can be concluded that the large memory requirement does not lead to an additional time loss.

4.4.2 Dynamic case

In this subsection, the performance of the dynamic case, i.e., with a moving source-receiver geometry, is discussed. Initially, it has to be mentioned that, basically, the memory requirement does not differ in case the scattered wave field is evaluated for one or for multiple source-receiver positions. Therefore, the memory requirement corresponds to the static case. In addition, the computation time for the calculation of the scattered wave field resulting from the first source-receiver position corresponds exactly to the static case. Assuming that the elastic background parameters do not change considerably the scattered wave field resulting from other source-receiver positions can simply be evaluated by combining the previously stored factors, as explained in section 4.1 in detail and indicated in Figure 4.2. Therefore, the total computation time for the scattered wave field of all other source-receiver positions reduces significantly.

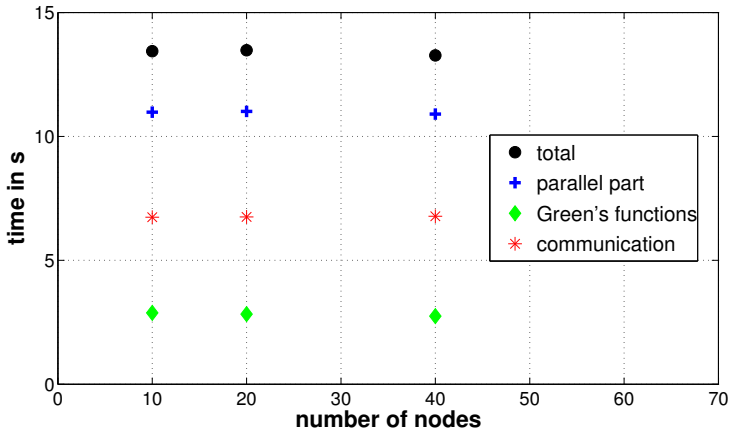

Figure 4.11: Visualization of the computation time of *FMBORN* for a fixed number of 80 cores distributed over an increasing number of nodes.

Table 4.9: Computation time of *FMBORN* for the dynamic case, i.e., with a moving source-receiver geometry from position 1 to position 4 for different grid sizes and the corresponding number of cores (NC).

	NC	number of grid points in x-, y,- and z-direction	total computation time at position			
			1	2	3	4
Test 1	64	$200 \times 200 \times 200$	144 s	31 s	32 s	30 s
Test 2	125	$250 \times 250 \times 250$	274 s	42 s	43 s	39 s
Test 3	250	$300 \times 300 \times 200$	801 s	93 s	90 s	89 s

Table 4.9 shows the total computation time for different positions of a moving source-receiver geometry using different grid sizes and the corresponding number of used cores. It is clearly visible that the saving of computation time for other positions of the source-receiver geometry is remarkable in comparison to the computation time for the first position. At this point, the large memory requirement for the storage of the Green's functions pays off and allows for an efficient simulation of the scattered wave field in a moving source-receiver geometry.

With regard to the listed total computation time of *FMBORN* for position 1 in case of Test 2 and Test 3, it has to be mentioned that the used number of cores (NC) for the modeling does not present an optimal choice as shown in section 4.4 because the required communication time between the large number of cores exceeds the saving in pure computation time by orders of magnitude. In case of Test 3, 11 min 54 s are needed for the communication only, i.e., more than 89% of the total computation time. Obviously, the large number of cores dominates the total computation time. However, the large memory requirement due to the storage of the Green's functions on each grid point for each frequency (cf. Table 4.8) does not allow for a clear reduction of the number of cores for the tested model size. This is due to the maximum accessible memory of 20 GB per node on high-performance clusters used in this study. The use of so-called fat nodes

with more than 256 GB memory surely presents an alternative. However, they are not available on all common high-performance clusters.

As mentioned before, in principle the total memory requirement of *FMBORN* does not increase if the scattered wave field is evaluated for more than one position of the fixed source-receiver geometry. However, the total grid size has to be chosen, dependent on the distance that the moving source-receiver geometry shall cover. As for each position of the moving source-receiver geometry the remaining overlap of the two grids reduces and this overlap has to be large enough to ensure a convergence of the scattering integral (cf. section 4.2), the total grid size might increase significantly compared to the presented examples (cf. Table 4.9). Hence, it is clear that for the simulation of large distances covered by the moving source-receiver geometry the memory requirement increases accordingly. For such configurations, the large memory requirement of *FMBORN* might pose a problem.

In this respect, the question arises, how efficient an implementation of the derived approach is if the Green's functions are not stored for each frequency on each grid point but computed 'on the fly', i.e., during the evaluation of the integrand of the scattered particle velocity (cf. equation 2.59). In this case for each position of the moving source-receiver geometry, a new run of the modified code version has to be performed to evaluate the scattered wave field. In order to investigate this approach, a modified version of *FMBORN* was built which has, of course, a significantly smaller memory requirement than the version where the Green's functions are stored and held in memory. The (peak) memory requirement for this modified code version can be evaluated (in Bytes) according to

$$\mathrm{MR}_{\mathrm{head}}^{\mathrm{modified}} = 31 \cdot \mathrm{NGP}_{\mathbf{x}} \cdot \mathrm{NGP}_{\mathbf{y}} \cdot \mathrm{NGP}_{\mathbf{z}} \cdot 4\,\mathrm{Bytes}\,, \tag{4.3}$$

and

$$\mathrm{MR}_{\mathrm{Green}}^{\mathrm{modified}} = 0\,\mathrm{Bytes}\,, \tag{4.4}$$

where $\mathrm{NGP}_{\mathbf{x}}, \mathrm{NGP}_{\mathbf{y}}, \mathrm{NGP}_{\mathbf{z}}$ denotes the total number of grid points in $\mathbf{x}$-, $\mathbf{y}$-, and $\mathbf{z}$-direction, respectively. Moreover, 31 indicates the number of 3D (floating-point)arrays, that need to be stored at the same time and 4 Bytes corresponds to the size of a 'float' on the used systems (cf. appendix G). Table 4.10 gives an overview of the total memory requirement of the modified code version for the same setups as presented in Table 4.8 for *FMBORN*. Table 4.11 presents computation times of the modified code version for a model with 200 grid points in each direction. It is clearly visible that the memory requirement of the modified version of *FMBORN* will not cause any problems, even for large 3D models. However, its total computation time rises significantly. The required turnaround time (cf. Table 4.5) cannot be achieved, even with a large number of cores. Hence, at this point it becomes obvious that the modified approach where the Green's functions are not stored does not present an alternative to *FMBORN* for a real-time application.

4.5 Summary

This chapter discussed the explicit modeling scheme and the parallelization of the numerical implementation *FMBORN*, which is based on the presented theoretical approach in chapter 2.

Table 4.10: Total memory requirement (MR) of a modified version of *FMBORN* where the Green's functions are not stored for different grid sizes.

grid points in x,y,z-direction	total MR
$50 \times 50 \times 50$	14.8 MB
$100 \times 100 \times 100$	118 MB
$200 \times 200 \times 200$	946 MB
$400 \times 400 \times 400$	7.4 GB
$800 \times 800 \times 800$	59 GB

Table 4.11: Computation times of a modified version of *FMBORN* where the Green's functions are not stored, for a model with 200 grid points in each direction.

NC	total computation time
64	11 min 38 s
128	7 min 08 s
256	5 min 50 s
512	6 min 42 s

A convergence study for the scattering integral (equation 2.59) revealed that a coherent summation of the integral is only ensured if the largest occurring dominant wavelength fits at least four times into each horizontal and three times into the vertical spatial dimension of the scattering volume, respectively. This area corresponds then to approximately twice the (first) Fresnel zone.
Furthermore, a discretization study showed that a spatial discretization of 25 grid points per smallest dominant wavelength is sufficient to properly sample the scattering region. In comparison to other numerical modeling techniques this is a relatively dense discretization.

Finally, the performance of *FMBORN* was discussed. In order to evaluate the scattered wave field for the first position of a moving source-receiver combination, total computation times between 2 and 15 minutes were achieved for models describing typical borehole configurations (i.e., model sizes of 10 m $\times$ 10 m $\times$ 10 m to 30 m $\times$ 30 m $\times$ 30 m). In these cases, between 64 and 250 CPU cores were used to process the data. For the evaluation of the scattered wave field for other positions of the fixed source-receiver geometry, *FMBORN* only needs 20 - 40 seconds. These efficient computation times definitely allow for a real-time simulation of the drilling process with *FMBORN*.

However, due to the storage of the Green's functions on each grid point for each frequency sample, the memory requirement of *FMBORN* is quite large. Regarding the mentioned (relatively small) model sizes, between 60 GB and 1.6 TB memory are allocated. For small borehole configurations this does not pose a problem, at least not on common cluster computers. But with respect to large 3D models, as needed e.g., when the moving source-receiver geometry shall cover large distances, the memory requirement rises significantly and might pose problems at the moment. However, it is expected that with respect to the rapid progress in the development of computer hardware, in the future, problems due to the high memory consumption of *FMBORN* will continuously decrease.
In addition, not storing the Green's functions does not present an alternative. Investigations of a modified version of *FMBORN*, where the Green's functions are not stored but calculated 'on the fly', revealed that even for small models and in case the computations are distributed over a large number of cores (i.e., NC$>$250), the total computation time for each source-receiver position lies in a range from 6 to 7 minutes and is thus, too high to allow for a real-time application.

Chapter 5

Forward modeling with *FMBORN*

In order to investigate the potential of *FMBORN* in this chapter the implemented modeling algorithm is tested with regard to the following aspects:

- In section 5.1 the accuracy of *FMBORN* is analyzed in near-field configurations. For this purpose, a case study was performed where the fixed source-receiver geometry approaches a dipped scatterer.
- In section 5.2 the accuracy of *FMBORN* is analyzed in multiple-layer cases. For this purpose the results for two horizontal two-layer cases are presented. One of these cases represents a half-space perturbed by a low-velocity zone and the other case represents a half-space perturbed by a high-velocity zone.
- In order to classify *FMBORN* among existing approaches in terms of accuracy and efficiency, in section 5.3 results of *FMBORN* are compared to results of an established finite-difference (FD) based method. The comparison is performed for two configurations: subsection 5.3.1 shows results for a model with a plane scatterer over a half-space and a static source-receiver geometry. Subsection 5.3.2 shows results for a moving source-receiver geometry that approaches a dipped scatterer (relative to the borehole axis) over a half-space.

5.1 Forward modeling with *FMBORN* while drilling: case study

In this section I present results of *FMBORN* for a case study where the fixed source-receiver geometry moves towards a dipped scatterer. As a far-field approximation was applied to the implemented Green's functions (cf. equations 2.15, 2.16), it is of special interest what influence near-field effects have on the modeled wave field as the source-receiver combination approaches the scatterer. As to this, according results of *FMBORN* are compared to results of *qseis*, serving as quasi-analytic reference.

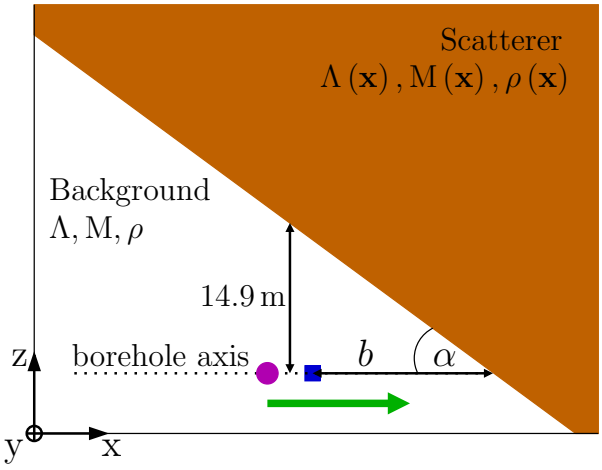

Figure 5.1: Setup for the case study of *FMBORN* regarding the tool movement: the moving source-receiver geometry (green arrow) approaches the dipped scatterer. Source (pink) and receiver (blue) offset by 3 m. At the starting point the midpoint of source and receiver has a (vertical) distance of 14.9 m to the scatterer. The receiver has a horizontal offset b to the dipped scatterer that intersects the borehole axis with an angle $\alpha = 52.4°$. The P- and S-wave velocity as well as the density for both the background medium and the scatterer are given in Table 5.1.

The following case study was performed for the setup shown in Figure 5.1 and two exemplary contrasts that are specified in Table 5.1 while a moving source-receiver geometry approaches the dipped scatterer in discrete steps. The chosen parameters v_P, v_S and ρ for the background medium correspond to a medium containing salt. Based on a density perturbation of 20% to the background medium and no perturbation in the compliance parameters Λ and M, the parameters $v_P(\mathbf{x}), v_S(\mathbf{x})$ and $\rho(\mathbf{x})$ for the scatterer in case 1 were calculated according to equations 2.22 and 2.23. Based on a perturbation in the compliance parameter M of 20% to the background medium and no perturbation in Λ and ρ, the parameters $v_P(\mathbf{x}), v_S(\mathbf{x})$ and $\rho(\mathbf{x})$ for the scatterer in case 2 were calculated according to equations 2.22 and 2.23. The source-receiver offset was 3 m and as source a dipole excitation in **z**-direction was used, generating a Ricker wavelet with $f_c = 1$ kHz and a maximum amplitude of 1 N (cf. appendix F). At the starting point the source-receiver midpoint had a (vertical) distance of 14.9 m to the scatterer. Moreover, the receiver had a horizontal offset of 10 m to the dipped scatterer that intersects the borehole axis with the angle $\alpha = 52.4°$. In the course of the simulated drilling process (indicated by the green arrow in Figure 5.1), this distance decreased gradually.

Case 1

Figure 5.2 shows the modeled wave fields on the **z**-component for case 1 (cf. Table 5.1) for four selected stationary positions of the moving source-receiver geometry. The axes of the plots for the results of all positions are scaled identically according to the amplitude of the SS-reflection. The results of *FMBORN* are plotted in green and the results of *qseis* are plotted in black. From top to bottom the source-receiver geometry approaches the scatterer in discrete

Table 5.1: Parameters for the homogeneous background medium and the scatterer in case 1 and case 2, respectively, used in the case study for *FMBORN* concerning the tool movement.

	v_P (in m/s) s_P (in μs/ft)	v_S (in m/s) s_S (in μs/ft)	ρ (in kg/m^3)
background	4688 65	2538 120	2100
scatterer - case 1	4279 71	2316 132	2520
scatterer - case 2	3925 78	2317 131	2100

Table 5.2: Case study of *FMBORN* regarding the tool movement: least-squares misfits of the *FMBORN*-result to the quasi-analytic reference result of *qseis* for the PP- and SS-reflection, respectively, in case 1 as a function of the horizontal distance b between the receiver and the dipped scatterer.

position	1	2	3	4
b	10 m	7 m	4 m	1 m
ℓ^2-misfit (PP)	0.297	0.442	-	-
ℓ^2-misfit (SS)	0.181	0.198	0.445	-

steps of 3 m. The corresponding horizontal distances between the receiver and the scatterer are listed in Table 5.2 together with the least-squares misfits (cf. appendix F) of the *FMBORN* result to the quasi-analytic reference result of *qseis*. The least-squares misfits for the PP-reflections were calculated over 140 time samples, which corresponds to a time window of 0.00126 s. The misfits for the SS-reflections were calculated for 180 time samples, which corresponds to a time window of 0.00162 s. Converted waves are not investigated in this case, as they are very small. Furthermore, direct waves are not subject of that investigation, as *FMBORN* models only the scattered wave field.

Generally, the results of *FMBORN* for the reflected waves are in line with the results of *qseis*. Regarding the *qseis*-results, it is clearly visible that with decreasing distance to the scatterer, firstly the PP-reflection (i.e., for $b < 4$ m) and then the SS-reflection (i.e., for $b < 1$ m) interferes with the direct wave field (i.e., P- and S-wave are not separated yet) and is no longer independently visible. As *FMBORN* does not model the direct wave field, the according results still show the reflected wave field independently. As a consequence, in the following analysis only those near-field situations are investigated where the scattered wave field is clearly separated from the direct wave field. Figure 5.2 reveals, that with decreasing distance to the scatterer, the misfit between the *FMBORN*-result and the *qseis*-result increases. Especially for distances between the source-receiver geometry and the scatterer that are equal to or smaller than the source-receiver

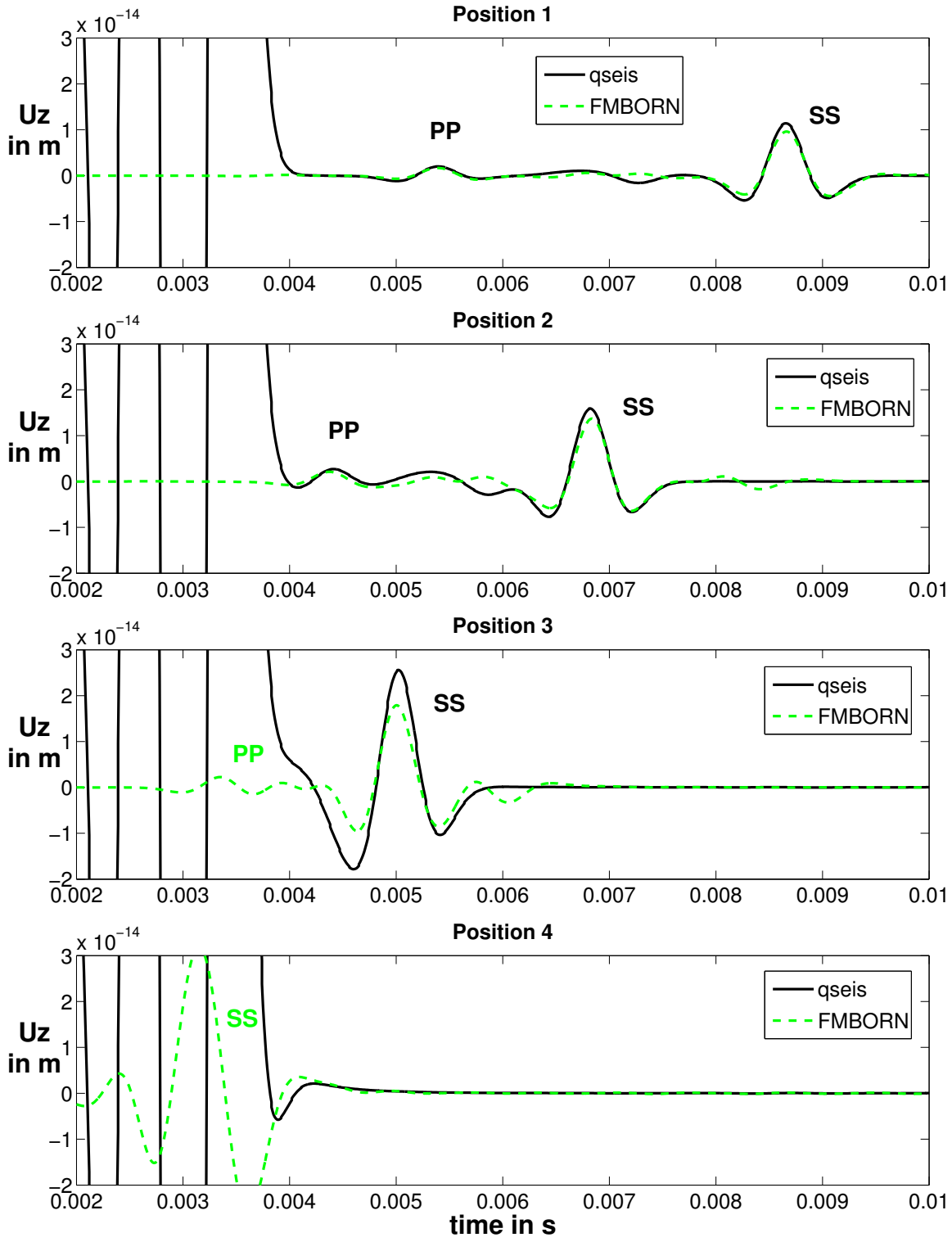

Figure 5.2: Case study regarding the tool movement: particle displacements of *FMBORN* (green) and *qseis* (black) on the z-component for case 1. At position 1 the receiver has a horizontal distances of 10 m to the scatterer. From top to bottom the source-receiver geometry approaches the scatterer in discrete steps of 3 m. Hence, at position 4 the remaining horizontal distance between receiver and scatterer is 1 m (cf. Table 5.2). The axes for the results of all positions are scaled identically according to the amplitude of the SS-reflection.

offset, the misfit suddenly increases. The corresponding calculated least-squares misfit of the *FMBORN*-result to the quasi-analytic reference result of *qseis* for both the PP- and SS-reflection (listed in Table 5.2) confirm this observation and match the expectations. Considering the used dominant wavelengths (i.e., $\lambda_{\text{P,dom}} = 4.69\,m and \lambda_{\text{S,dom}} = 2.54\,m$), this is due to the fact that for distances between the source-receiver geometry and the scatterer that are equal to or smaller than the source-receiver offset, the assumed far-field approximation is no longer valid. Hence, near-field effects contribute to the scattered wave field. As these effects are not included in the modeling approach of *FMBORN*, it is to be expected that the misfit to the quasi-analytic reference result increases. However, up to the time when the scattered wave field completely interferes with the direct wave field, the least-squares misfit for both the PP- and SS-reflection is still less than 0.5. This is also due to the fact, that the near-field effects mainly influence the amplitudes of the scattered wave field. The phases of both the PP- and SS-reflection are still properly modeled.

Case 2

For the second case a contrast between the background medium and the scatter of $\delta\text{M} = 0.2$ (cf. Table 3.1) was chosen because in the frame of the sensitivity and accuracy study, discussed in Chapter 3, the calculated relative misfits based on perturbations in M were generally slightly worse than the ones based on perturbations in ρ. Particularly the PP-reflection is poorly visible on the **z**-component in case of $\delta\text{M} = 0.2$, a dipole excitation in **z**-direction and a dipped scatterer (cf. Figure 3.15). Therefore, the question arises whether the observed near-field effects (cf. case 1) have a higher impact on the scattered wave field resulting from perturbations in M.

Figure 5.3 shows the modeled wave fields on the **z**-component for case 2 (cf. Table 5.1) for the same four selected stationary positions of the moving source-receiver geometry as in case 1. The axes of plots for the results of all positions are again identically scaled according to the amplitude of the SS-reflection. The results of *FMBORN* are plotted in green and the results of *qseis* are plotted in black. From top to bottom the source-receiver geometry approaches the dipped scatterer in discrete steps of 3 m. The corresponding horizontal distances between the receiver and the scatterer are listed in Table 5.3 together with the least-squares misfits of the *FMBORN* result to the quasi analytic reference result of *qseis*. The least-squares misfits for the PP-reflections were calculated over 140 time samples, which corresponds to a time window of 0.00126 s. The misfits for the SS-reflections were calculated for 180 time samples, which corresponds to a time window of 0.00162 s. Again, converted waves are not investigated. The same applies to direct waves.

In principle, the results meet the expectations and confirm the observations made in case 1. As the PP-reflection is in this case almost not visible (which was expected due to observations made in the scope of the sensitivity and accuracy analysis, discussed in chapter 3), the corresponding least-squares misfit is not further discussed. However, the calculated least-squares misfits for the SS-reflection exactly reflect the near-field effects observed in case 1. For distances between the source-receiver geometry and the scatterer that are equal to or smaller than the source-receiver offset, the least-squares misfit suddenly increases. However, again mainly the amplitudes of the scattered wave field are affected. The phases for the SS-reflection are still properly modeled.

As already mentioned, these investigations correspond only to those near-field situations where

Table 5.3: Case study of *FMBORN* regarding the tool movement: least-squares misfits of the *FMBORN*-result to the quasi-analytic reference result of *qseis* for the PP- and SS-reflection, respectively, in case 2 as a function of the horizontal distance b between the receiver and the dipped scatterer.

position	1	2	3	4
b	10 m	7 m	4 m	1 m
ℓ^2-misfit (PP)	0.785	0.827	-	-
ℓ^2-misfit (SS)	0.266	0.297	0.593	-

the scattered wave field is clearly separated from the direct wave field. However, as near-field effects contribute mainly to the wave field for arrival times, when direct waves and scattered waves are not separated yet, a general conclusion regarding the accuracy of *FMBORN* in the near-field cannot be drawn yet. Thus, for further analysis it is necessary to add a modeling algorithm for the direct wave field to the implementation.

5.2 Forward modeling with *FMBORN*: multiple scattering interfaces

The aim of this section is to discuss the accuracy of *FMBORN* in cases with more than one scattering interface. As in the developed approach, incident and scattered waves exclusively propagate with the velocities of the homogeneous background medium, it is to be expected that the phases of reflected waves generated by other scattering interfaces than the first one are not properly modeled. As to this, results of *FMBORN* for a model with two scattering interfaces are compared to according results of *qseis*, serving as quasi-analytic reference. In the first investigated case the model represents a half-space including a low-velocity zone and in the second case the model represents a half-space including a high-velocity zone.

The results in this section arise from the setup shown in Figure 5.4, representing a plane two-layer case, where the borehole axis has a distance $d_1 = 7.8$ m to the first scattering interface and a distance $d_2 = 19.8$ m to the second scattering interface. As source a dipole excitation in $\mathbf{z}$-direction (i.e., perpendicular to the scattering interfaces) was used, generating a Ricker wavelet with $f_c = 1$ kHz and a maximum amplitude of 1 N (cf. appendix F). Regarding *FMBORN*, source and receiver coincide but for *qseis* the discussed far-field criterion (cf. appendix D) was applied. Table 5.4 lists the elastic parameters used for the model in the two investigated cases. The first one represents a half-space perturbed by a low-velocity zone and the second one represents a half-space perturbed by a high-velocity zone. Again, the chosen parameters $v_\mathrm{P}, v_\mathrm{S}$ and ρ for the background medium correspond to a medium containing salt. Based on a density perturbation of 20% and -20% to the background medium, respectively, and no perturbation in the compliance parameters Λ and M, the parameters $v_\mathrm{P}(\mathbf{x}), v_\mathrm{S}(\mathbf{x})$ and $\rho(\mathbf{x})$ for the scatterers were calculated according to equations 2.22 and 2.23.

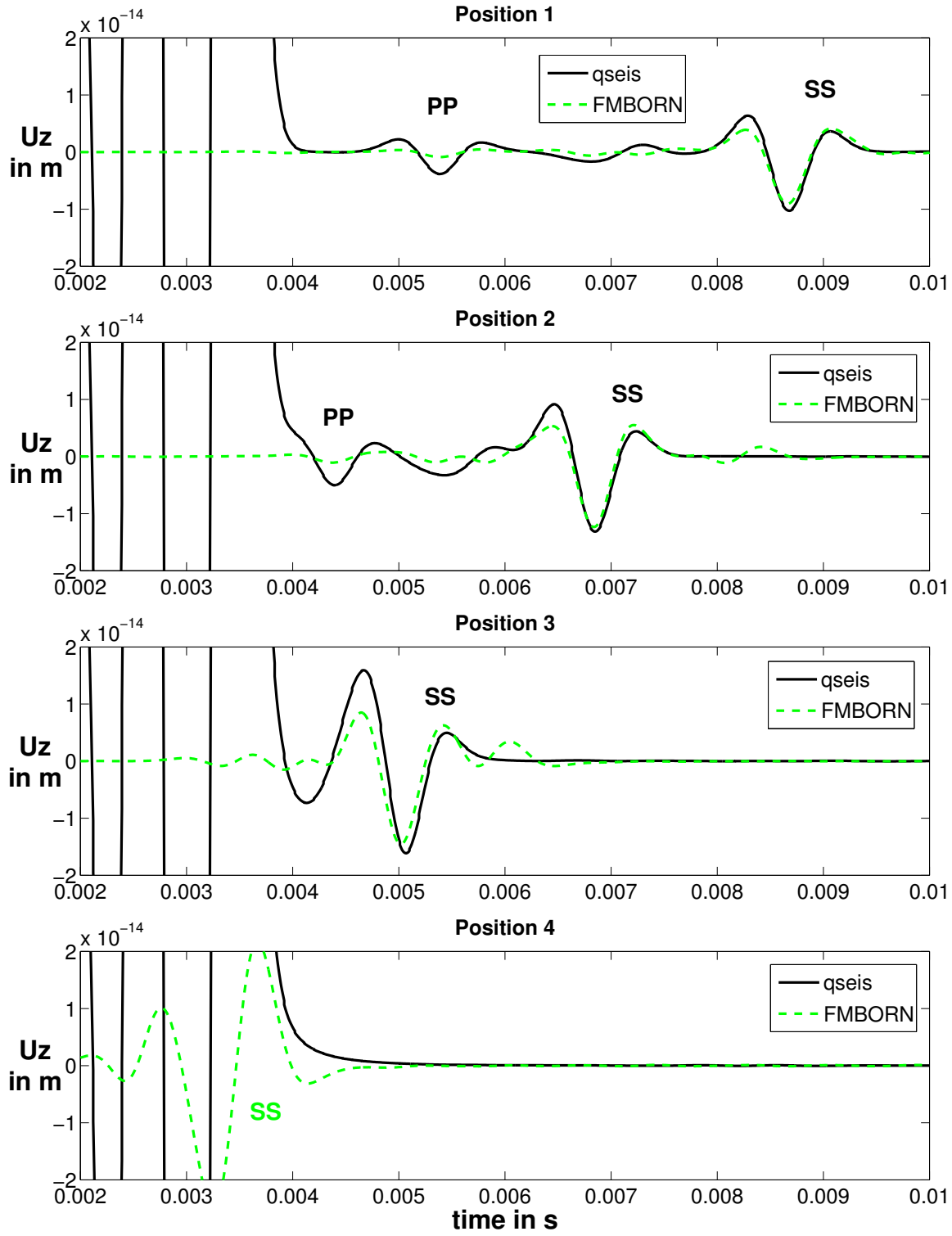

Figure 5.3: Case study regarding the tool movement: particle displacements of *FMBORN* (green) and *qseis* (black) on the z-component for case 2. At position 1 the receiver has a horizontal distances of 10 m to the scatterer. From top to bottom the source-receiver geometry approaches the scatterer in discrete steps of 3 m. Hence, at position 4 the remaining horizontal distance between receiver and scatterer is 1 m (cf. Table 5.2). The axes for the results of all positions are scaled identically according to the amplitude of the SS-reflection.

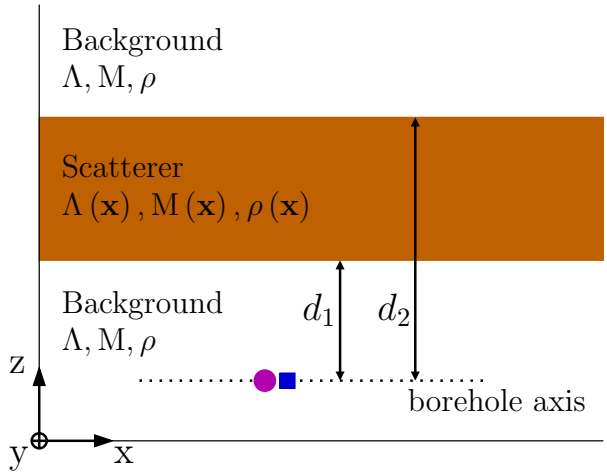

Figure 5.4: Setup for the zero-offset two-layer case study: the homogeneous background medium is perturbed by two scattering interfaces. Source (pink) and receiver (blue) have a distance $d_1 = 7.8$ m to the first scattering interface and a distance $d_2 = 19.8$ m to the second scattering interface. The values for the used elastic parameters for both the background medium and the scatterer are listed in Table 5.4.

Table 5.4: Parameters for both the homogeneous background medium and the scatterer in case 1 and case 2, respectively, used in the zero-offset two-layer case study.

	v_P (in m/s) s_P (in μs/ft)	v_S (in m/s) s_S (in μs/ft)	ρ (in kg/m^3)
background	4688 65	2538 120	2100
scatterer - case 1	4279 71	2316 132	2520
scatterer - case 2	5240 58	2840 107	1680

For case 1, representing a low-velocity zone within a homogeneous half-space, the results on the z-component are shown in Figure 5.5. All expected reflections are clearly visible, i.e., both the PP- and SS- reflection resulting from the first scattering interface (denoted as PP_1 and SS_1) and both, the PP- and SS-reflection resulting from the second scattering interface (denoted as PP_2 and SS_2). The amplitudes and phases of PP_1 and SS_1 are properly modeled. This is not surprising as the modeling process for the scattered wave field resulting from the first scattering interface corresponds to the modeling process in the comprehensive single-scattering interface investigations (cf. section 5.1 and chapter 3). The occurring (small) phase shifts $\delta t_{\odot\oplus}$ and relative misfits (cf. equation 3.1) between the maximum amplitudes of both the PP- and SS-reflections modeled by *FMBORN* and *qseis*, respectively, are listed in Table 5.5. They are in line with the calculated misfits in the single-scattering interface cases investigated in chapter 3. Hence, these reflections are not further investigated. However, the scattered wave field resulting from the second scattering interface needs special attention. Obviously, the amplitudes are properly modeled. The according relative misfits (cf. equation 3.1) between the maximum amplitudes of both the PP- and SS-reflection modeled by *FMBORN* and *qseis*, respectively, are listed in Table 5.5. In fact, these misfits are even smaller than the ones obtained for the reflections resulting from the first scattering interface. However, regarding the arrival times, a clear phase shift between the *qseis*-result and the *FMBORN*-result arised. This phase shift is due to the fact that the wave propagation in *FMBORN* is modeled exclusively in the background medium with the according wave velocities. Regarding the second scattering interface, that means that the incident waves propagate not only through the half-space but also through the low-velocity zone with the (faster) wave velocities of the background medium. Hence, the *FMBORN*-modeled reflections resulting from the second scattering interface occur too early in the time series. To quantitatively confirm this explanation, the phase shift $\delta t_{\odot\oplus,i}$ with $\odot,\oplus \in \{\text{P,S}\}$ between the arrival time of the scattered wave field modeled with *qseis* $t^{qseis}_{\odot\oplus,i}$ and modeled with *FMBORN* $t^{FMBORN}_{\odot\oplus,i}$, respectively, is calculated according to

$$\delta t_{\odot\oplus,i} = t^{qseis}_{\odot\oplus,i} - t^{FMBORN}_{\odot\oplus,i} \quad \text{with} \quad \begin{array}{r} \odot,\oplus \in \{\text{P, S}\} \\ i \in \{1,2\} \end{array}, \tag{5.1}$$

where $i \in \{1,2\}$ indicates due to which scattering interface the reflection appears. In a next step, the calcualted phase shifts for reflections of the second scattering interface $\delta t_{\odot\oplus,2}$ are corrected by $\delta t_{\odot\oplus,1}$, representing the phase shifts that are observed for reflections from the first scattering interface:

$$\delta t^{\text{corr}}_{\odot\oplus} = \delta t_{\odot\oplus,2} - \delta t_{\odot\oplus,1} \quad \text{with} \quad \odot,\oplus \in \{\text{P, S}\}\ . \tag{5.2}$$

In order to analyze if the corrected phase-shifts for reflections resulting from the second scattering interface $\delta t^{\text{corr}}_{\odot\oplus}$ can be explained by the presented theory, the theoretical time delay $t^{\text{delay}}_{\odot\oplus}$ is evaluated which the wave experiences while propagating with a wrong velocity from the first to the second scattering interface and back:

$$t^{\text{delay}}_{\odot\oplus} = \left(\frac{d_{\text{scat}}}{v^{\text{bg}}_{\odot}} + \frac{d_{\text{scat}}}{v^{\text{bg}}_{\oplus}}\right) - \left(\frac{d_{\text{scat}}}{v^{\text{scat}}_{\odot}} + \frac{d_{\text{scat}}}{v^{\text{scat}}_{\oplus}}\right) \quad \text{with} \quad \odot,\oplus \in \{\text{P, S}\}\ , \tag{5.3}$$

where d_{scat} denotes the distance between the two scattering interfaces, $v^{\text{scat}}_{\odot}$ and $v^{\text{scat}}_{\oplus}$ the wave-velocities of the incident and scattered waves within the scatterer as well as $v^{\text{bg}}_{\odot}$ and $v^{\text{bg}}_{\oplus}$ the

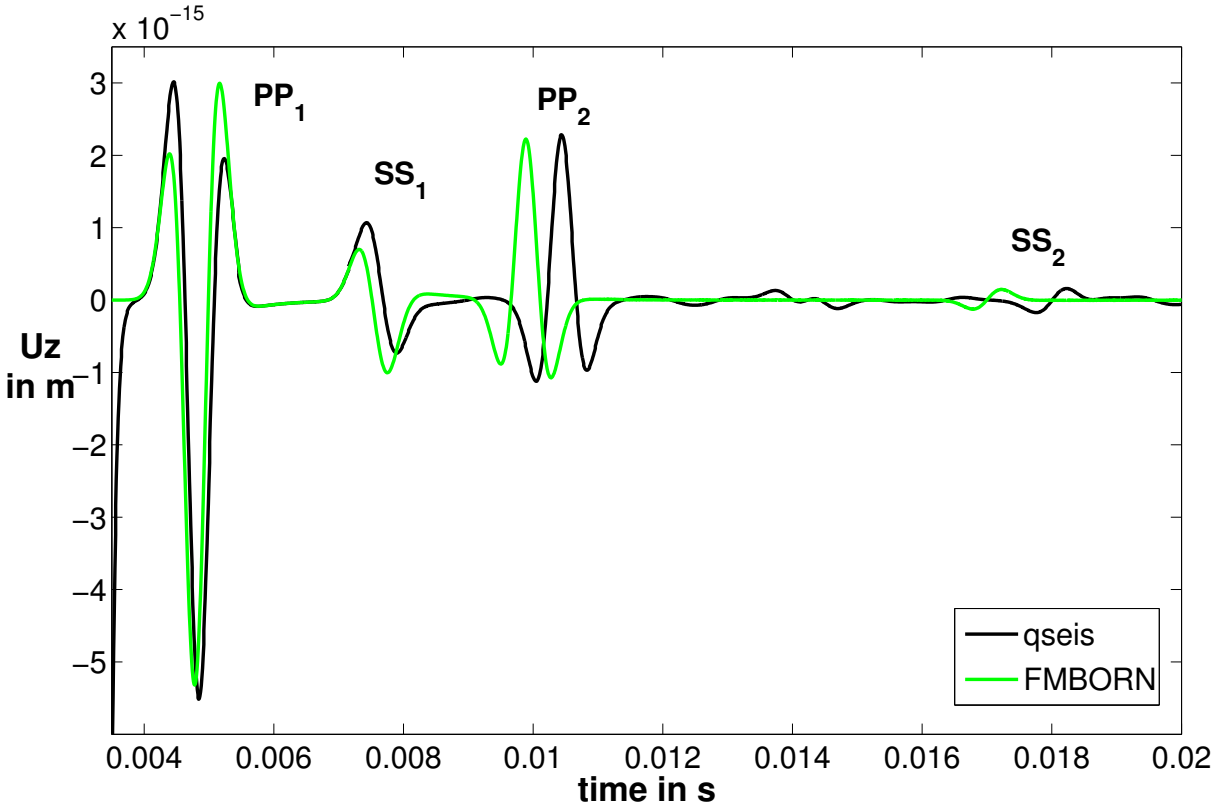

Figure 5.5: Two-layer case study: results on the z-component for a dipole excitation perpendicular to a low-velocity zone within a homogeneous half-space (case 1). The scattered particle displacements calculated by *FMBORN* are plotted in green and the ones computed by *qseis* are plotted in black, while the latter serves as quasi-analytic reference. The scattered wave modes resulting from the first scattering interface are denoted as PP_1 and SS_1, while the scattered wave modes resulting from the second scattering interface are denoted as PP_2 and SS_2.

wave-velocities of incident and scattered waves within the background medium. The computed values for the (corrected) phase shifts and the time delays in case 1 are listed in Table 5.5. It is clearly visible that the corrected phase shifts exactly correspond to the theoretically evaluated time delays. Thus, the results for a model with a half-space including a low-velocity zone meet the expectations: the scattered-wave modes resulting from the second scattering interface suffer from a phase shift due to the incorrect phase modeling within the low-velocity zone, while their amplitudes are properly modeled.

In a second step, the results for case 2 representing a high-velocity zone within a homogeneous half-space are investigated. The resulting particle displacements on the z-component are shown in Figure 5.6. Again, all expected reflections are clearly visible, i.e., both the PP- and SS-reflection resulting from the first scattering interface (denoted as PP_1 and SS_1) and both the PP- and SS-reflection resulting from the second scattering interface (denoted as PP_2 and SS_2). As expected, the amplitudes and phases of PP_1 and SS_1 are properly modeled. The occurring (small) phase shifts $\delta t_{\odot\oplus,1}$ and relative misfits between the maximum amplitudes of PP_1 and SS_1 modeled with *FMBORN* and *qseis*, respectively, are listed in Table 5.5. With regard to the reflected wave field

Table 5.5: Comparison of the observed phase shift $\delta t_{\odot\oplus,i}$, the corrected phase shift $\delta t^{\text{corr}}_{\odot\oplus}$ and the theoretically calcualted time delay $t^{\text{delay}}_{\odot\oplus}$ for reflections caused by the second scattering interface in case 1 modeled with *FMBORN* and *qseis*, respectively. Furthermore, the relative misfit $\delta u^{\odot\oplus}$ between the maximum amplitudes of both results are listed.

	$\delta t_{\odot\oplus,i}$ (in s)	$\delta t^{\text{corr}}_{\odot\oplus}$ (in s)	$t^{\text{delay}}_{\odot\oplus}$ (in s)	$\delta u^{\odot\oplus}$
PP_1	-0.000061	-	-	0.036
SS_1	-0.000113	-	-	-0.345
PP_2	-0.00055	-0.00049	-0.00049	-0.027
SS_2	-0.00100	-0.00089	-0.00090	0.282

Table 5.6: Comparison of the observed phase shift $\delta t_{\odot\oplus,i}$, the corrected phase shift $\delta t^{\text{corr}}_{\odot\oplus}$ and the theoretically calcualted time delay $t^{\text{delay}}_{\odot\oplus}$ for reflections caused by the second scattering interface in case 2 modeled with *FMBORN* and *qseis*, respectively. Furthermore, the relative misfit $\delta u^{\odot\oplus}$ between the maximum amplitudes of both results are listed.

	$\delta t_{\odot\oplus,i}$ (in s)	$\delta t^{\text{corr}}_{\odot\oplus}$ (in s)	$t^{\text{delay}}_{\odot\oplus}$ (in s)	$\delta u^{\odot\oplus}$
PP_1	0.000079	-	-	-0.201
SS_1	0.000141	-	-	-0.383
PP_2	0.000471	0.00055	0.00054	0.128
SS_2	0.000870	0.00101	0.00100	0.174

resulting from the second scattering interface, observations according to case 1 are made. The amplitudes of PP_2 and SS_2 evaluated with *FMBORN* are properly modeled but the phases are delayed. Here, the phase shift is positive as the background medium velocities are slower than the velocities of the scatterer. For reflections from the second scattering interface that means, that incident and scattered waves propagate not only through the half-space but also through the high-velocity zone with the (lower) wave velocities of the background medium. Hence, reflections caused by the second scattering interface appear too late in the time series. To quantitatively confirm this explanation, again, the corrected phase shift and theoretical time delay for both PP_2 and SS_2 are evaluated according to equations 5.2, 5.3 and listed in Table 5.6. Obviously, these phase shifts exactly correspond to the calcualted time delays. Additionally, Table 5.6 gives the relative misfits between the maximum amplitudes of both PP_2 and SS_2, modeled with *FMBORN* and *qseis*, respectively. Qualitatively they are in line with the relative misfits observed in the sensitivity and accuracy analysis discussed in chapter 3. Thus, also the results for a model with a half-space including a high-velocity zone meet the expectations: the scattered-wave modes resulting from the second scattering interface suffer from a phase shift due to the incorrect phase modeling within the high-velocity zone while their amplitudes are properly modeled.

Certainly, the observed incorrect modeling of phases for reflections from the second scattering

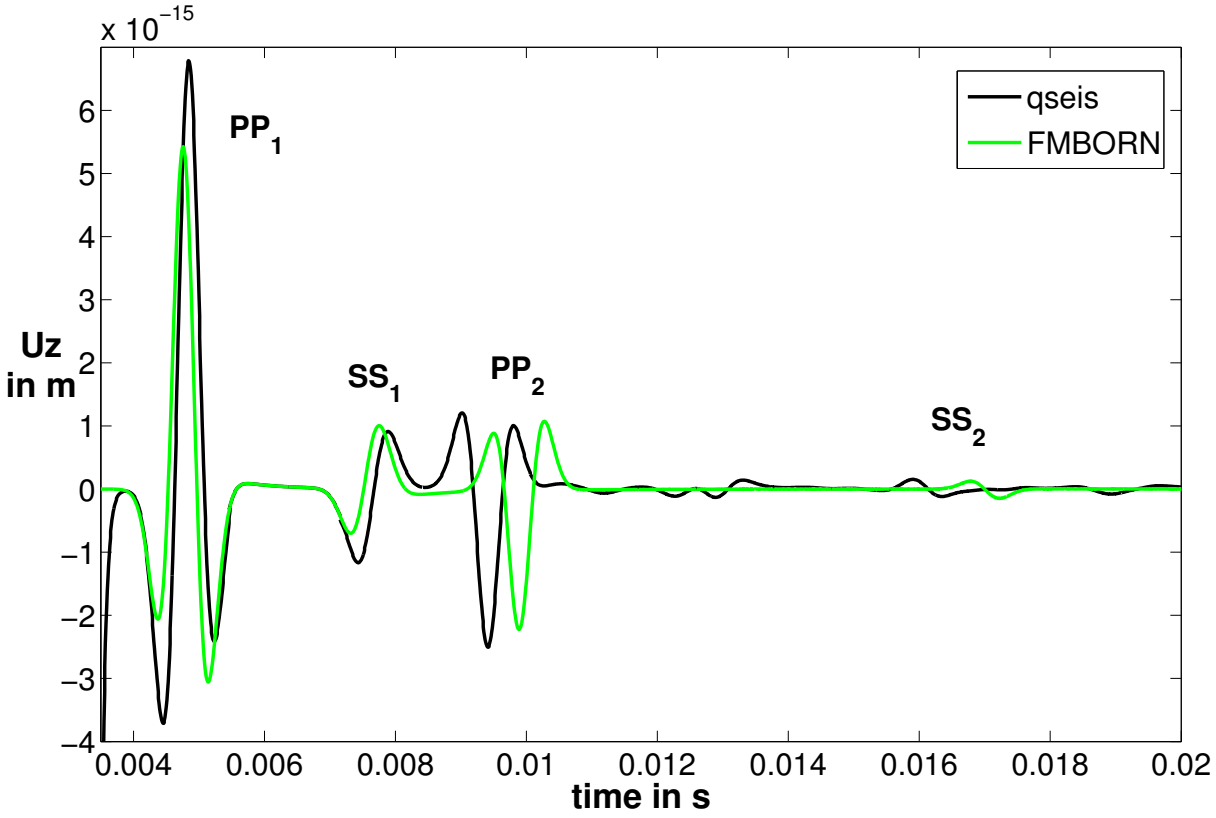

Figure 5.6: Two-layer case study: results on the z-component for a dipole excitation perpendicular to a high-velocity zone within a homogeneous half-space (case 2). The scattered particle displacements calculated by *FMBORN* are plotted in green and the ones computed by *qseis* are plotted in black, while the latter serves as quasi-analytic reference. The scattered wave modes resulting from the first scattering interface are denoted as PP_1 and SS_1, while the scattered wave modes resulting from the second scattering interface are denoted as PP_2 and SS_2.

interface will occur for reflections from all other scattering interfaces than the first one in cases with more than one scattering interface. Regarding synthetic applications, this does not pose a problem as the expected phase-shifts can be calculated and an according correction can be applied. However, considering real-data applications the direct interpretation of seismograms in terms of phases received with *FMBORN* is problematic. Hence, before interpreting the data, the application of a suitable migration scheme accounting for several characteristics of the implemented modeling-algorithm (e.g., first-order approximation, wave propagation in the background medium, etc.) is indispensable. Thus, with respect to the application of *FMBORN* in multiple-layer cases further developments are necessary and recommended. However, they are not part of this thesis.

Table 5.7: Parameters for the homogeneous background medium and the scatterer, respectively, used in the accuracy and efficiency analysis between *FMBORN* and *SOFI3D*.

	v_P (in m/s) s_P (in μs/ft)	v_S (in m/s) s_S (in μs/ft)	ρ (in kg/m^3) ρ (in kg/m^3)
background	4688 65	2538 120	2100 2100
scatterer	4279 71	2316 132	2520 2520

5.3 *FMBORN*-results in comparison with *FD*-based results: accuracy and efficiency analysis

In order to investigate the accuracy and efficiency of the developed numerical implementation in comparison with an already established numerical method, in this section results of *FMBORN* are compared with results of *SOFI3D* (Bohlen, 2002; Bohlen et al., 2012). The latter represents a 3D time-domain finite-difference based numerical forward modeling program, freely available under the *GNU* General Public License as published by the Free Software Foundation. *SOFI3D* provides the possibility to simulate viscoelastic, elastic and acoustic wave fields due to a variety of source types. Furthermore, the implemented domain-decomposition (MPI-based) allows to use modern cluster technology while the program shows good performance on massive parallel supercomputers. Thus, *SOFI3D* presents a suitable numerical program to classify *FMBORN* with respect to its accuracy and efficiency. The according *FD*-results presented in the following were calculated with the elastic version of *SOFI3D* in the frame of a BSc-thesis (Pontius, 2013).

The following accuracy and efficiency analysis was performed for the two setups shown in Figure 5.7. Regarding the accuracy, in a first step I show results of both codes for a plane scatterer over a half-space, where the scatterer is parallel to the borehole axis (cf. Figure 5.7, left). Regarding accuracy and efficiency, in a second step I investigate the results of both codes for a dipped scatterer over a half-space (cf. Figure 5.7, right) while the fixed source-receiver geometry moves towards the scatterer in discrete steps of 3 m. In all cases as source a dipole excitation in $\mathbf{z}$-direction was used, generating a Ricker wavelet with $f_c = 1$ kHz and a maximum amplitude of 1 N (cf. appendix F). Moreover, in all investigated cases, the according *qseis*-results serve as quasi-analytic reference.

The chosen parameters v_P, v_S and ρ for the background medium are specified in Table 5.7 and correspond to a medium containing salt. Based on a density perturbation of 20% to the background medium and no perturbation in the compliance parameters Λ and M, the parameters $v_P(\mathbf{x}), v_S(\mathbf{x})$ and $\rho(\mathbf{x})$ for the scatterer were calculated according to equations 2.22 and 2.23 and are also listed in Table 5.7.

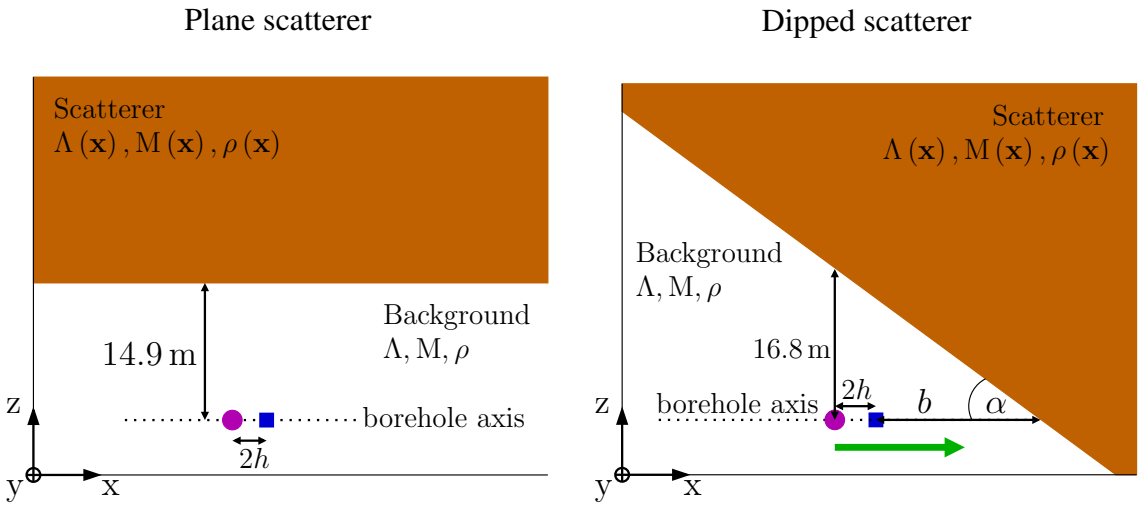

Figure 5.7: The two setups used for the accuracy and efficiency analysis to classify *FMBORN*. Left: the plane scatterer is parallel to the borehole axis and has a distance of 14.9 m to source (pink) and receiver (blue) that offset by $2h$. Right: the moving source-receiver geometry approaches the dipped scatterer (indicated by the green arrow). Source and receiver offset by $2h$ and at the starting point the source has a (vertical) distance of 16.8 m to the scatterer. The receiver has a horizontal offset b to the dipped scatterer that intersects the borehole axis with the angle $\alpha = 52.4°$. In both setups a dipole excitation in **z**-direction was used, generating a Ricker wavelet with $f_c = 1$ kHz and a maximum amplitude of 1 N.

5.3.1 Plane scatterer (parallel to the borehole axis) over a half-space

Firstly, the results for a model where the plane scatterer is parallel to the borehole axis are investigated. The detailed setup is sketched in Figure 5.7 (left) and is described in the introduction of this section. Based on the explained setup, a configuration was built with a distance of 14.9 m between the borehole axis and the plane scatterer. As offset to the source, 0 m, 3 m and 6 m were chosen for the first, second and third receiver, respectively. The first offset represents a true zero-offset case while the two other distances correspond to common borehole setups, where the first receiver typically offsets by approximately 3 m and the last receiver by approximately 6 m to the source, respectively. As source a dipole excitation in **z**-direction was used, generating a Ricker wavelet with $f_c = 1$ kHz and a maximum amplitude of 1 N. As derived and discussed in Chapter 2, Section 2.4, Subsection 2.4.2, in zero-offset cases with a dipole excitation perpendicular to the scatterer, the scattered wave field occurs only on the **z**-component. The other components vanish. Hence, only this component is shown.

Figure 5.8 shows the according results for the first (top), the second (middle) and the third receiver (bottom), respectively, on the **z**-component. The *FMBORN*-result is plotted in green, the *SOFI3D*-result is plotted in red and the *qseis*-result is plotted in black, serving as quasi-analytic reference. Based on the physical theory, in the presented zero-offset case with a dipole excitation perpendicular to the scatterer, I expect the single scattered wave field to consist of both a PP- and an SS-reflection while the PP-reflection represents the main reflected signal. Converted waves do not occur in this case. Once, the offset between source and receiver starts to increase,

Table 5.8: Accuracy and efficiency analysis: least-squares misfit of the *FMBORN*- and *SOFI3D*-results, respectively, to the quasi analytic reference result of *qseis*.

ℓ^2-misfit	PP			SS		
offset	0 m	3 m	6 m	0 m	3 m	6 m
SOFI3D	0.394	0.278	0.276	0.443	0.423	0.470
FMBORN	0.123	0.233	0.252	0.341	0.301	0.342

the amplitude of the PP-reflection gradually decreases while the amplitude of the SS-reflection gradually increases. Moreover, with existing source-receiver offset a converted wave appears and its amplitude increases with increasing offset.

As Figure 5.8 illustrates, all three programs show a good correlation regarding both the PP- and SS-reflection, especially in terms of their phases. But also the amplitudes match well. Quantitatively, this is shown by the calculated least-squares misfits (cf. appendix F) listed in Table 5.8. The given values present the least-squares misfit of the numerical results of *SOFI3D* and *FMBORN*, respectively, to the according quasi-analytic reference result of *qseis*. The misfits for both the PP- and the SS-reflections were calculated over 250 time samples, which corresponds to a time window of 0.00225 s. The calculated misfits are generally smaller for *FMBORN* than for *SOFI3D*. Hence, the Born approximation based numerical solution is closer to the quasi-analytic reference result than the FD-based solution; at least for the investigated (relatively small) source-receiver offsets. Apart from that, it can be observed that with increasing source-receiver offset the least-squares misfit (PP) of the *FD*-based results slightly decreases while the one of *FMBORN* slightly increases. This poses the question whether the implemented FD-algorithm suffers from (small) numerical inaccuracies for small source-receiver offsets.

Next, the converted waves are investigated. Firstly, it has to be mentioned that in the true zero-offset case (regarding the investigated setup) no converted waves are expected. This is based on the directivity patterns of the used dipole excitation and the resulting scattering coefficients for PSV and SVP, respectively, being zero (cf. equation 2.69). Apart from this true zero-offset case, in the investigated setup with a plane scatterer being parallel to the borehole axis, the occurring converted wave is expected to present a superposition of the PSV- and SVP-wave, respectively. Hence, for the investigated source-receiver offsets of 3 m and 6 m, respectively, only one converted wave train is expected. The results in Figure 5.8 clearly show that only the result of *FMBORN* meets this expectation. Both, *SOFI3D* and *qseis* do not properly model the converted wave field according to the current theoretical understanding as there is a clear converted wave already in the true zero-offset case. Regarding *qseis*, the applied far-field criterion (cf. appendix D) might be an explanation for the unexpected result. Potentially, the criterion works properly for the PP- and SS-reflections but has an influence on the converted wave field. This impression is further indicated by the fact that the *qseis*-result does not present one clearly formed wave train for the converted wave, but rather looks like two interfering wave trains. As to the results of *SOFI3D*, the supposition is intensified that the implemented FD-algorithm is inaccurate for small source-receiver offsets regarding converted waves (raised in the last paragraph). This supposition is not only due to the fact that there is a clear converted wave field

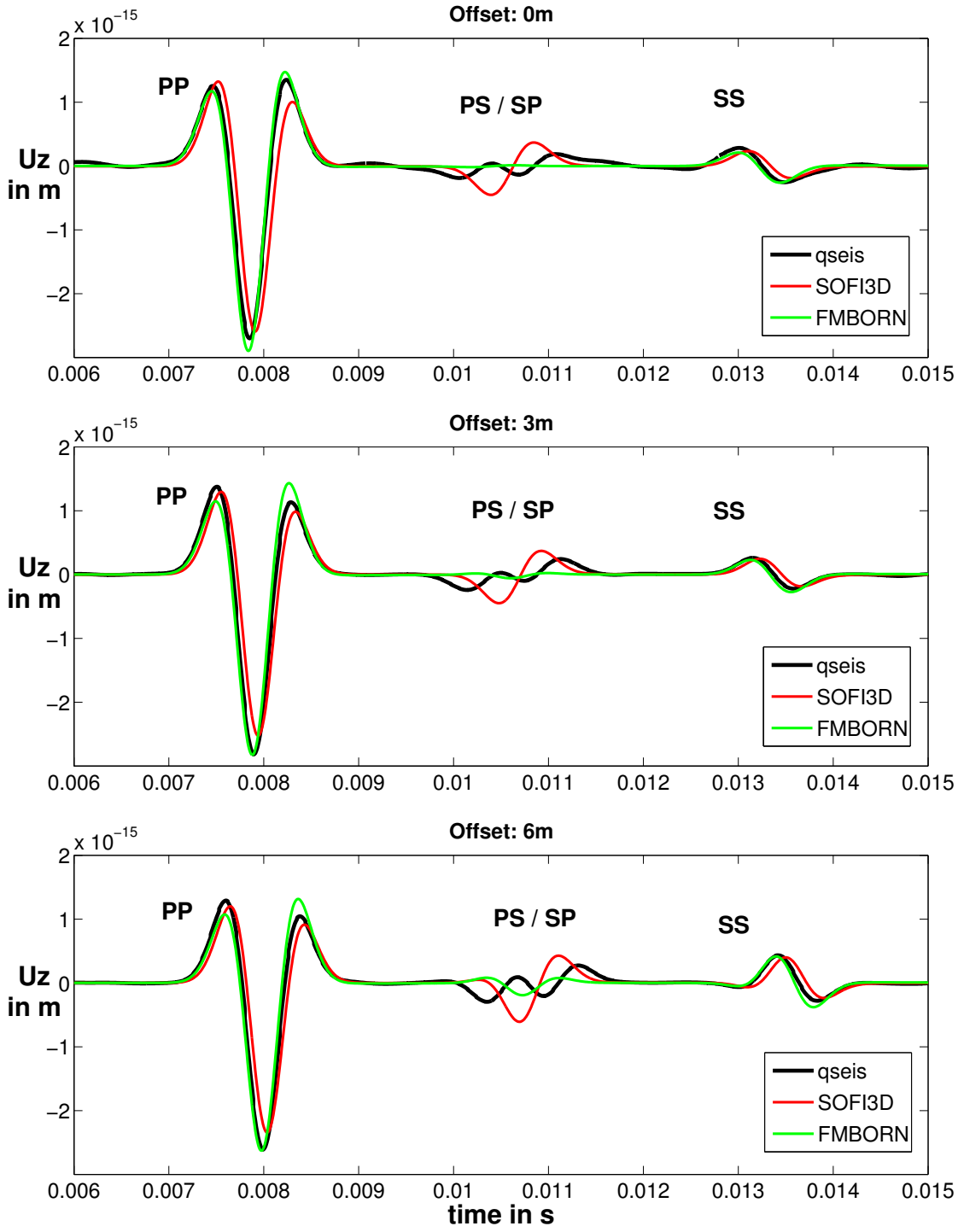

Figure 5.8: Accuracy and efficiency analysis: comparison between the results of *FMBORN* (green), *SOFI3D* (red) and *qseis* (black), respectively, for a plane scatterer over a half-space and a dipole excitation in z-direction. Accordingly, only the particle displacements on the z-component are shown. Top: results for a source-receiver offset of 0 m. Middle: results for a source-receiver offset of 3 m. Bottom: results for a source-receiver offset of 6 m.

in the zero-offset case but also due to the fact, that this converted wave is already well-formed for the smallest shown source-receiver offset and does not gradually develop with an increasing source-receiver offset.

In summary, the presented comparison of the results of *FMBORN*, *SOFI3D* and *qseis*, respectively, for a plane scatterer over a half-space and a dipole excitation perpendicular to it, shows good agreement with respect to both the PP- and SS-reflection. Their phases as well as their amplitudes modeled with the three mentioned programs only show small differences to each other. The least-squares misfits of the *FMBORN*-results are even smaller than the ones of *SOFI3D* (cf. Table 5.8). In particular, it is positive, that *FMBORN*, representing a first-order far-field scattering approach, is able to achieve the same order of precision in the far-field as the FD-based modeling does. However, regarding converted waves, a quantitative comparison between the three results was not possible as they show totally different wave trains in this respect. So far, the shown results indicate that *FMBORN* is able to properly model the converted wave field for the shown setup in contrast to *qseis* and *SOFI3D*, at least regarding the investigated relatively small source-receiver offsets. An according detailed study to further investigate this phenomenon is necessary and recommended. However, this study is not included in this thesis.

5.3.2 Dipped scatterer (relative to the borehole axis) over a half-space

Secondly, the results for a model, where the scatterer is dipped relative to the borehole axis are investigated. The following case study was performed for the setup shown in Figure 5.7 (right) while the fixed source-receiver geometry moves towards the scatterer in discrete steps of 3 m. As offset to the source, 0 m and 3 m were chosen for the first and second receiver, respectively. As source a dipole excitation in $\mathbf{z}$-direction was used generating a Ricker wavelet with $f_c = 1\,\text{kHz}$ and a maximum amplitude of 1 N. At the starting point the source had a (vertical) distance of 16.8 m to the scatterer. Moreover, the dipped scatterer intersects the borehole axis with the angle $\alpha = 52.4°$. In the course of the simulated drilling process (indicated by the green arrow in Figure 5.7 (right)) the (horizontal) distance b between the receiver and the scatterer decreased gradually.

Figures 5.9 and 5.10 show the resulting particle velocities on the $\mathbf{z}$-component at the first and second receiver, respectively. Again, only the reflected wave field is investigated as *FMBORN* does not model direct waves. Furthermore, a comparison of converted waves is not carried out due to the observed according fundamental discrepancy discussed in subsection 5.3.1. Generally, the results of all three programs show good agreement in relation to both the phases and the amplitudes of the PP- and SS-reflection. Quantitatively, this is shown by the calculated least-squares misfits, listed in Table 5.9 for the zero-offset case and in Table 5.10 for the source-receiver offset of 3 m. The given values present the least-squares misfits of the numerical results of *SOFI3D* and *FMBORN*, respectively, to the according quasi-analytic reference result of *qseis*. The misfits for the PP-reflections were calcualted over 120 time samples, which corresponds to a time window of 0.00108 s. The least-squares misfits for the SS-reflections were calculated over 170 time samples, which corresponds to a time window of 0.00153 s. Regarding the zero-offset case, no least-squares misfit is evaluated at position 4 for both the PP- and SS-reflection due to the total (PP) or partial (SS) superposition of these reflections with the direct wave field.

Table 5.9: Accuracy and efficiency analysis regarding the tool movement: least-squares misfits of the *FMBORN*- and *SOFI3D*-results, respectively, to the quasi analytic reference results of *qseis* for the PP- and SS-reflection, respectively, in a zero-offset configuration as a function of the horizontal distance b between the receiver and the dipped scatterer.

position	1	2	3	4
b	13 m	10 m	7 m	4 m
ℓ^2-misfit (PP)				
SOFI3D	0.387	0.291	0.482	-
FMBORN	0.360	0.402	0.482	-
ℓ^2-misfit (SS)				
SOFI3D	0.329	0.342	0.358	-
FMBORN	0.205	0.190	0.233	-

Accordingly, in case of a source-receiver offset of 3 m, no least-squares misfit is evaluated at position 3 for the PP-reflection and at position 4 for both, the PP- and SS-reflection, due to the superposition of these reflections with the direct wave field.

Generally, the results of both codes for the reflected wave field show that the closer the source-receiver combination gets to the dipped scatterer, the higher the calculated least-squares misfits get. This holds for both the PP- and SS-reflection. Regarding the results of *FMBORN* this trend is due to the fact that near-field effects are not included in the modeling scheme as discussed in section 5.1. A closer look at the least-squares misfits reveals furthermore, that in relation to the SS-reflection, the misfits for *FMBORN* are significantly smaller than for *SOFI3D*, regardless of the source-receiver offset. With respect to the PP-reflection this is just the other way round. The misfits for *SOFI3D* are clearly smaller than for *FMBORN* (source-receiver offset = 3 m) or similar to them (zero-offset). This is consistent with the results of the accuracy and sensitivity analysis, discussed in chapter 3. There, the presented results indicate that compared to the Zoeppritz reflection coefficients, the Born scattering coefficient for the SS-reflection is slightly more accurate than the one for the PP-reflection.

Altogether, the presented results for the scattered wave field reveal that the accuracy achieved by *FMBORN* compares very well with the accuracy achieved by *SOFI3D*; not only in case of a plane scatterer being parallel to the borehole axis but also in case of a dipped scatterer relative to the borehole axis. Even when the source-receiver geometry approaches the dipped scatterer and near-field effects arise, the *FMBORN*-results show good agreement with the *SOFI3D*-results. This is particularly surprising as *FMBORN* represents a first-order far-field scattering approach, that does not include near-field terms in the implemented modeling algorithm.

Exemplary computation times of *SOFI3D* and *FMBORN* are compared for the presented model with a dipped scatterer relative to the borehole axis, while the fixed source-receiver geoemtry with 3 m offset approaches the scatterer. It is clear, that only a qualitative comparison is possible as the implemented algorithms are very different. Therefore, the computation-related requirements differ significantly. Moreover, it has to be mentioned that the FD-based algorithm delivers the total

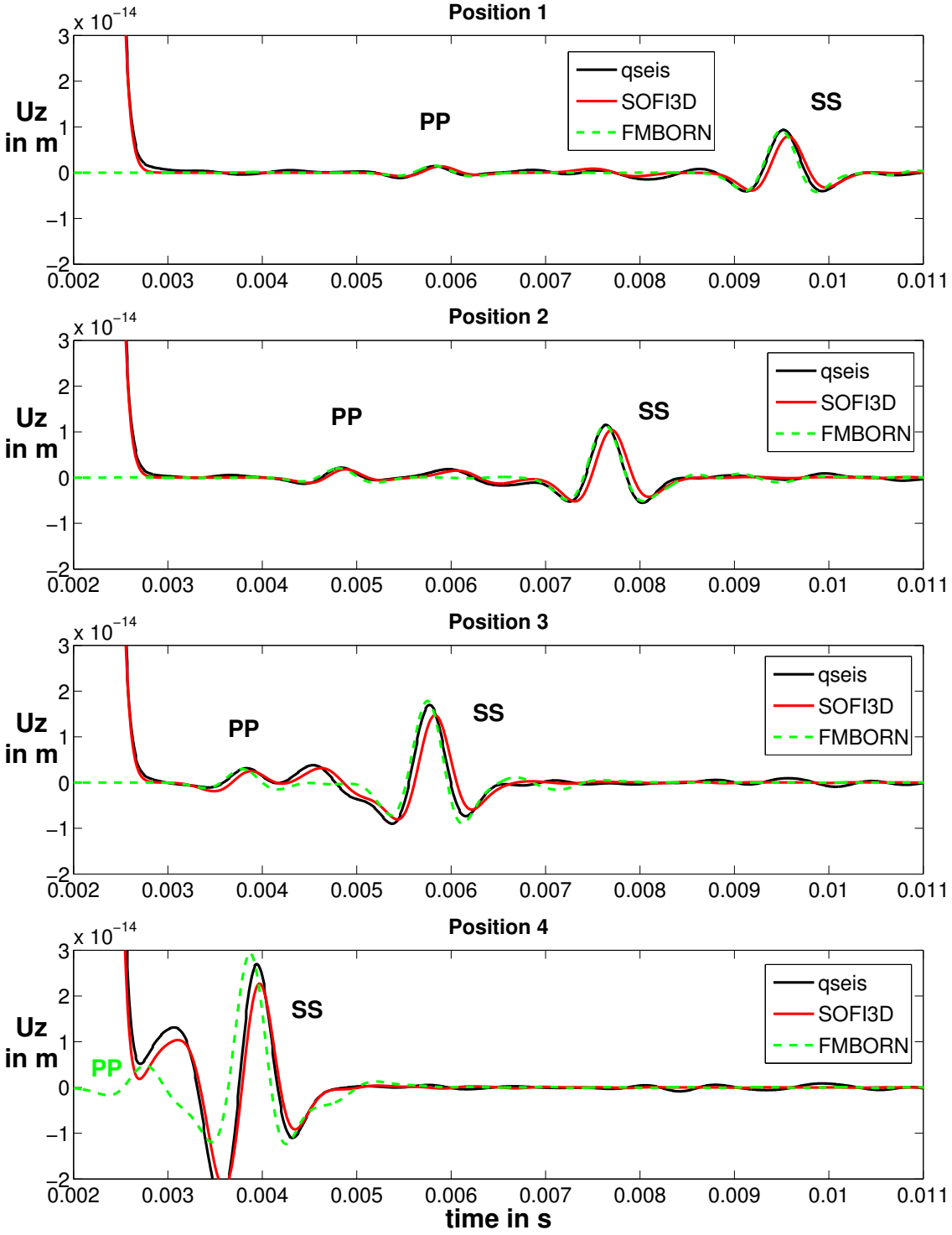

Figure 5.9: Accuracy and efficiency analysis: comparison between the particle displacements on the z-component of *FMBORN* (green), *SOFI3D* (red) and *qseis* (black) for a dipped scatterer relative to the borehole axis over a half-space and no source-receiver offset. From top to bottom the source-receiver combination approaches the scatterer in discrete steps of 3 m. The corresponding horizontal distances between the receiver and the scatterer are listed in Table 5.9. The axes for the results of all positions are identically scaled according to the amplitude of the SS-reflection.

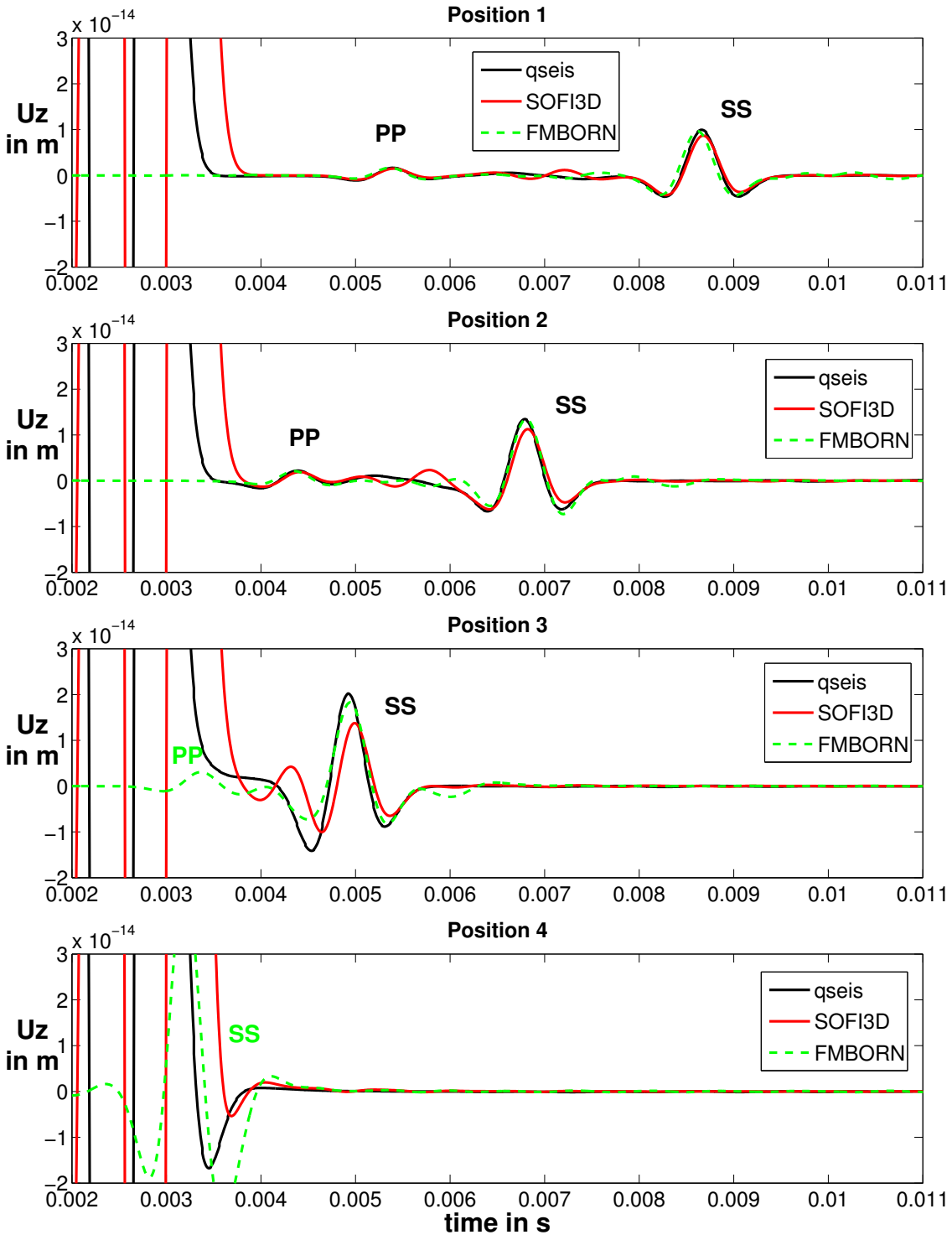

Figure 5.10: Accuracy and efficiency analysis: comparison between the particle displacements on the z-component of *FMBORN* (green), *SOFI3D* (red) and *qseis* (black) for a dipped scatterer relative to the borehole axis over a half-space. The source-receiver offset is 3 m. From top to bottom the source-receiver combination approaches the scatterer in discrete steps of 3 m. The corresponding horizontal distances between the receiver and the scatterer are listed in Table 5.10. The axes for the results of all positions are identically scaled according to the amplitude of the SS-reflection.

Table 5.10: Accuracy and efficiency analysis concerning the tool movement: least-squares misfits of the *FMBORN*- and *SOFI3D*-results, respectively, to the quasi analytic reference results of *qseis* for the PP- and SS-reflection, respectively. Source and receiver offset by 3 m and the horizontal distance b between the receiver and the dipped scatterer decreases in discrete steps.

position	1	2	3	4
b	10 m	7 m	4 m	1 m
ℓ^2-misfit (PP)				
SOFI3D	0.182	0.252	-	-
FMBORN	0.330	0.415	-	-
ℓ^2-misfit (SS)				
SOFI3D	0.153	0.231	0.636	-
FMBORN	0.073	0.162	0.317	-

wave field and further wave field quantities (e.g., the dynamic stress) while *FMBORN* calculates only the single-scattered wave field in terms of the particle velocity or the particle displacement. However, in the scope of this thesis the aim was to develop a suitable modeling approach with respect to borehole applications. Therefore, the following qualitative comparison of the total computation times is also done in this respect. Table 5.11 lists the according specifications chosen for the modelings with both codes in the presented case.

The main difference between the two modeling schemes lies, of course, in the simulation of the movement of the fixed source-reveiver geometry. In case of *SOFI3D*, for each position of the fixed source-receiver combination relative to the geology a new code run has to be performed. This cannot be changed, as the implemented FD-algorithm does not allow a separation between the wave propagation and the scattering-related terms. Hence, the total computation time for each evaluated position of the source-receiver geometry remains equal as shown in Table 5.12. In contrast, using *FMBORN* only the computations for the first source-receiver position are 'expensive'. As discussed in chapter 4, all needed factors (i.e., Green's functions, scattering coefficients, etc.) to evaluate the scattered particle velocity are calculated and stored only once. The scattered wave field for further source-receiver positions can then be evaluated by a simple combination of these stored factors. Therefore, the total computation time for all other source-receiver positions reduces considerably, relative to the computation time needed for the first position as shown in Table 5.12.

With regard to the listed total computation time of *FMBORN* for position 1 it has to be mentioned that the used number of cores (NC) for the modeling (cf. Table 5.11) does not present an optimal choice as discussed in chapter 4, section 4.4 as the needed communication time between the high number of involved cores exceeds the saving in pure computation time by orders of magnitude. However, the high memory-requirement due to the storage of the Green's functions on each grid point for each frequency (cf. Table 4.8) does not allow a clear reduction of the used number of cores for the tested model size on the available cluster-computers in this work.

Table 5.11: Accuracy and efficiency analysis regarding the movement of the fixed source-receiver geometry: juxtapose of the relevant modeling specifications needed for *FMBORN* and *SOFI3D*, respectively.

	SOFI3D	*FMBORN*
total grid size (x × y × z) (in grid points)	680 × 680 × 1080	300 × 300 × 200
grid spacing DH (in m)	0.1	0.2
time sampling	9 µs	9 µs
boundary condition	PerfectlyMatchedLayers	-
spatial FD-order	4	-
NC	64	250
time steps	2778	-
total memory	55 GB	1100 GB

Table 5.12: Accuracy and efficiency analysis regarding the movement of the fixed source-receiver geometry: comparison of the total computation times of *FMBORN* and *SOFI3D*, respectively.

position	1	2	3	4
SOFI3D	51 min 30 s	52 min 30 s	50 min 50 s	50 min 58 s
FMBORN	13 min 20 s	1 min 33 s	1 min 30 s	1 min 29 s

5.4 Summary

In this chapter the potential of *FMBORN* was discussed rearding different aspects, such as the accuracy in near-field configurations, the applicability in multiple-layer cases as well as the accuracy and efficiency compared to a finite-difference based approach.

Regarding the accuracy in near-field configurations, a case study was presented, where the fixed source-receiver geometry approaches a dipped scatterer (relative to the borehole axis) in discrete steps of 3 m. These results show, that with decreasing distance of the source-receiver combination to the scatterer, the accuracy of the *FMBORN*-result decreases. Especially for distances between the source-receiver combination and the scatterer that are equal to or smaller than the source-receiver offset (i.e., the near-field), the misfit to the quasi-analytic reference result suddenly increases. This is due to the applied far-field approximation in *FMBORN*, regarding the implemented Green's functions (cf. equations 2.15, 2.16). As a consequence, near-field effects are not included in the modeling approach of *FMBORN*. Even so, the case study reveals that these effects mainly influence the amplitudes of the scattered wave field. The phases of both the PP- and SS-reflection are not affected and also in the near-field properly modeled. However, it has to be mentioned that these investigations correspond only to those near-field situations where the scattered wave field is clearly separated from the direct wave field. For further accuracy analysis involving a superposition of both wave fields an appropriate extension to model the direct wave field has to be added to the implementation.

Regarding the accuracy of *FMBORN* in multiple-layer cases, the results for two horizontal two-layer cases were analyzed and compared to quasi-analytic reference results of *qseis*. The two investigated cases represent firstly, a half-space perturbed by a low-velocity zone and secondly, a half-space perturbed by a high-velocity zone. As in the developed modeling algorithm, incident and scattered waves exclusively propagate with the velocities of the homogeneous background medium, I expected that the amplitudes of the reflected waves generated by the second scattering interface are properly modeled while the waveforms suffer from a phase shift. The presented results cleary meet this expectation. Furthermore, they show that the occurring phase shift exactly corresponds to the theoretical time delay that the wave experiences by propagating too fast or too slow through the perturbed area. Regarding synthetic applications, this does not pose a problem, as the expected phase shifts can be calculated and an according correction can be applied. However, regarding real-data applications a direct interpretation of seismograms in terms of phases received with *FMBORN* is problematic for reflections from other scattering interfaces than the first one. Hence, for the application in multiple-layer cases further development is necessary and recommended.

Finally, in order to classify *FMBORN* in terms of accuracy and efficiency among existing numerical approaches, I compared results of *FMBORN* with results of the finite-difference based numerical forward modeling program *SOFI3D* for a model with a plane scatterer over a half-space and a dipped scatterer over a half-space (relative to the borehole axis) while the fixed source-receiver geometry approaches the dipped scatterer. The comparisons revealed that the accuracy regarding both the PP- and SS-reflection, (in terms of phase and amplitude) achieved by *FMBORN* compares very well with the accuracy achieved by *SOFI3D*, even when the fixed source-receiver geometry approaches the dipped scatterer and near-field effects arise. This is particularly surprising, as *FMBORN* represents a first-order far-field scattering approach, that

does not include near-field terms in the implemented modeling approach.
A quantitative comparision of the converted wave field was not possible, as the results of the two codes and the quasi-analytic reference result show three totally different wave trains in this respect. So far, the presented results indicate that *FMBORN* is able to properly model the converted wave field in contrast to *qseis* and *SOFI3D*, at least in case of the presented setups and the investigated relatively small source-receiver offsets. However, an according detailed study to further investigate this phenomenon is necessary and recommended.
Regarding efficiency in simulating a moving source-receiver geometry, *FMBORN* provides clear advantages due to its ability of reusing all factors contributing to the scattered wave field. Using the FD-based algorithm, firstly, the total computation time for the evaluation of the scattered wave field for a single source-receiver position is significantly higher than using *FMBORN*. Secondly, in order to simulate the scattered wave field in a moving source-receiver geometry with the FD-based algorithm, for each source-receiver position a complete new code run has to be performed. Hence, considering the presented codes, a real-time simulation in borehole setups is only feasible with *FMBORN*.

Chapter 6

Summary and conclusions

Based on the elastodynamic forward scattering theory, in this thesis I **derived a closed form explicit expression** for the far-field first-order 3D scattered elastic wave field resulting from an arbitrary multipole excitation in an unbounded, homogeneous and isotropic elastic medium. To **verify the validity of the approach** based on the full elastodynamic Born approximation, the zero-offset analytic Born results were compared with results of the quasi-analytic benchmark code *qseis*. On the basis of the derived approach and with focus on borehole measurements, I **developed a new 3D forward modeling code**, called *FMBORN*. The performance of its parallel numerical implementation was analyzed and specific features of the modeling approach were discussed. Furthermore, **results of *FMBORN* were investigated** for different models in order to analyze the accuracy of the scattered wave field in near-field configurations and in the presence of multiple scattering interfaces. Finally, **results of *FMBORN* were compared** with results of an established FD-based method to classify *FMBORN* in terms of accuracy and efficiency among another numerical approach.

Derivation of a suitable theoretical approach In the scope of this thesis, the main issue was the development of a new fast and efficient 3D elastodynamic forward modeling technique with focus on borehole measurements. In this respect, the elastodynamic forward scattering formulation of De Hoop (1995) was revisited and a closed form explicit expression for the single scattered wave particle velocity due to a multipole source was derived. The mathematical elaborations revealed that the scattered wave field can be decomposed into two parts, i.e., the specular part and the diffuse part of the wave field. However, only the diffuse part is always present, while the specular part vanishes for vanishing source directivity.

Validation of the derived approach In general, the first-order Born approximation represents a well-established approach in forward scattering methods. However, the validity of the derived elastic first-order approach for borehole configurations had to be verified. In this respect, the zero-offset analytic Born results were compared to results of the quasi-analytic benchmark code *qseis* for a model with a plane scatterer over a half-space. A detailed sensitivity and accuracy study showed that the derived first-order Born-based approach is able to model the single scattered wave field in terms of phase and amplitude. For contrasts between the background medium and

the scatterer up to 20% in the compliance parameters M and Λ and up to 30% in the density, the Born-based results show a high correlation with the quasi-analytic reference results. The investigations also showed that the Born scattering coefficient for PP is more sensitive to high contrasts in the compliance parameters M and Λ than the Born scattering coefficient for SS, which is in accordance with the theory. This observation implies that generally *FMBORN* models SS-reflections more accurately than PP-reflections. Moreover, an analysis for configurations with varying distances between the borehole axis and the plane scatterer showed that the geometrical spreading is correctly handled by the implemented Born-based approach.

Development of a numerical implementation for the derived approach The newly developed 3D forward modeling code *FMBORN* was introduced. A discretization study revealed that a spatial discretization of at least 25 grid points per smallest dominant wavelength is needed to properly sample the scattering region and ensure a coherent summation of the scattering integral. Moreover, the study showed that the scattering region has to cover about twice the first Fresnel zone to avoid truncation errors when the scattering integral is evaluated.
Furthermore, the algorithm scheme of *FMBORN* was described and its parallel numerical implementation was presented in detail. Additionally, the performance of the algorithm was analyzed. The achieved total computation time to evaluate the scattered wave field for typical borehole setups is very fast, especially with respect to a moving source-receiver experiment. The scattered wave field for the first simulated source-receiver position can be evaluated in 2 - 10 minutes, depending on the model size. As the Green's functions and the scattering coefficients required for the evaluation of the scattered wave field are precalculated on each grid point and are held in memory, the evaluation of the scattered wave field for other positions of the fixed source-receiver geometry takes then only 30 to 40 seconds. These times definitely allow a real-time simulation of the drilling process. However, the memory requirement of *FMBORN* is quite large due to the storage of the Green's functions for each frequency sample at each grid point. For typical borehole setups and depending on the model size as well as the distance that the moving source-receiver geometry shall cover, at least 490 GB - 3.8 TB memory are needed. However, I expect that with respect to the substantial progress in the development of computer hardware, in the near future this potential problem will decrease rapidly.
Above all, a low-cost modeling without storing the Green's functions to save memory does not represent an alternative. Corresponding investigations, involving an 'on the fly' calculation of the Green's functions revealed that even for small models and in case the necessary computations are distributed over a large number of cores, the total computation time for each source-receiver position lies in a range from 6 to 7 minutes and is, thus, too high to allow for a real-time application.

Forward modeling with the developed approach In order to investigate the potential of *FMBORN*, various tests were performed:
A case study, where the fixed source-receiver geometry approaches a dipped scatterer (relative to the borehole axis) revealed that the accuracy of the scattered wave field modeled with *FMBORN* is also satisfying when near-field effects arise. In these cases, the phases of the scattered wave field are not affected at all, but the amplitudes suffer slightly due to the implemented far-field approximation. However, these investigations correspond only to those near-field situations

where the scattered wave field is already separated from the direct wave field. As within the scope of this thesis, first of all, the accuracy of the scattered wave field and the efficiency of the approach was of interest, an algorithm for the direct wave field is not implemented in *FMBORN* so far. Of course, for further accuracy analysis involving a superposition of both wave fields an appropriate extension has to be added to the implementation.
A study about the applicability of *FMBORN* in multiple-layer cases showed that only reflections from the first scattering interface are correctly modeled in terms of their phase. Reflections resulting from other scattering interfaces are properly modeled in terms of their amplitude but suffer from a phase shift as in the presented approach waves propagate exclusively with the velocities of the homogeneous background medium. Hence, the occurring phase shifts exactly correspond to the theoretical time delays that the waves experience by propagating with the too fast or too slow background velocity through perturbed areas. Regarding synthetic applications, this does not pose a problem as the expected phase shifts can be calculated and an according correction can be applied. However, regarding real-data applications a direct interpretation of seismograms in terms of phases received with *FMBORN* is problematic for reflections from other scattering interfaces than the first one. Hence, for the application in multiple-layer cases further development is necessary.
In order to classify *FMBORN* in terms of accuracy and efficiency among other numerical approaches, results for a moving source-receiver experiment were compared to corresponding results of an established FD-based code called *SOFI3D*. Again, results of *qseis* served as quasi-analytic reference solution. The comparisons for models with a plane scatterer and a dipped scatterer relative to the borehole axis over a half-space revealed that the accuracy in terms of phase and amplitude of the scattered wave field obtained by *FMBORN* compares very well with the accuracy obtained by *SOFI3D*. Unfortunately, a quantitative verification was only possible for the PP- and SS-reflection. A verification of the converted wave field was not possible, as the results of *FMBORN*, *SOFI3D* and *qseis* show totally different wave trains in this respect. So far, the presented results indicate that *FMBORN* is able to properly model the converted wave field in contrast to *SOFI3D*, at least in case of the presented setups and the investigated relatively small source-receiver offsets. However, an according detailed study to further investigate this phenomenon is recommended.
Regarding efficiency, the comparison showed that with respect to the simulation of the moving source-receiver geometry, *FMBORN* provides clear advantages due to its implemented modeling scheme over the FD-based algorithm. Using the latter, firstly, the total computation time for the evaluation of the scattered wave field for a single source-receiver position is significantly higher than using *FMBORN*. But even more important is the fact that in order to simulate the scattered wave field in a moving source-receiver geometry, in contrast to *FMBORN*, the FD-based algorithm requires a complete new code run for the simulation of each source-receiver position.

Conclusion Altogether, the presented results indicate that the developed modeling code *FMBORN* based on the first-order Born approximation is able to model the scattered wave field fast and efficient enough to allow a real-time simulation. Furthermore, the achieved accuracy is remarkable good considering the implemented first-order and far-field approximation. Hence, this conclusion provides the basis for further developments of *FMBORN*, such as the implementation of an algorithm to model the direct wave field and an extension of the algorithm to account for

the fluid-filled borehole. Aside from that, case studies for more complex geological models and analysis for noisy synthetic data are of high interest.

Bibliography

Aki, K. and Richards, P. G. (1980). *Quantitative seismology – theory and methods*, volume 1. W. H. Freeman & Co., San Fransisco.

Beylkin, G. (1985). Imaging of discontinuities in the inverse scattering problem by inversion of a causal generalized radon transform. *J. Math. Phys.*, 26:99–108.

Beylkin, G. and Burridge, R. (1990). Linearized inverse scattering problems in acoustics and elasticity. *Wave Motion*, 12:15–52.

Bohlen, T. (2002). Parallel 3D viscoelastic finite difference seismic modelling. *Computers & Geosciences*, 28:887–899.

Bohlen, T. (2004). *Analysis of Seismic Waves in the Presence of Small-Scale Strong Material Discontinuities*. Christian-Albrechts-Universität zu Kiel. Professorial dissertation.

Bohlen, T., De Nil, D., Köhn, D., and Jetschny, S. (2012). *SOFI 3D - Seismic modeling with finite differences, 3D - acoustic and elastic version*. Geophysical Institute, KIT.

Buttkus, B. (2000). *Spectral analysis and filter theory in Applied Geophysics*. Springer Verlag, Berlin.

Carcione, J. M., Herman, G. C., and ten Kroode, A. P. E. (2002). Seismic modeling. *Geophysics*, 67(4):1304–1325.

Červený, V. (2001). *Seismic ray theory*. Cambridge University Press, Cambridge.

Claerbout, J. F. and Muir, F. (1973). Robust modeling with erratic data. *Geophysics*, 38(5):826–844.

Colton, D. and Kress, R. (1998). *Inverse Acoustic and Electromagnetic Scattering Theory - Second Edition*. Springer Verlag, Berlin.

Comninos, P. (2006). *Mathematical and Computer Programming Techniques for Computer Graphics*. Springer Verlag, London.

De Hoop, A. T. (1990). Reciprocity theorems for acoustic wave fields in fluid/solid configurations. *J. Acoust. Soc. of Am.*, 87(5):1932–1937.

De Hoop, A. T. (1991). Convergence criterion for the time-domain iterative Born approximation to scattering by an inhomogeneous, dispersive object. *J. Opt. Soc. Am. A*, 8(8):1256–1260.

De Hoop, A. T. (1995). *Handbook of Radiation and Scattering of Waves*. Academic Press, London.

Eaton, D. W. (1999). Weak elastic-wave scattering from massive sulfide orebodies. *Geophysics*, 64(1):289–299.

Einstein, A. (1916). Die Grundlage der allgemeinen Relativitätstheorie. *Annalen der Physik*, 354(7):769–822.

Frigo, M. and Johnson, S. G. (2005). The Design and Implementation of FFTW3. In *Proceedings of the IEEE 93, Special Issue on Program Generation, Optimization, and Platform Adaptation*.

Geerits, T., Tang, X., Hellwig, O., and Bohlen, T. (2010). Multipole borehole acoustic theory: Source imbalances and the effect of an elastic logging tool. *J. Appl. Geophys.*, 70(2):113–143.

Geerits, T., Veile, I., and Hellwig, O. (2013). Far field elastodynamic Born scattering revisited. *J. Appl. Geophys.*, 89(2):141–163.

Gritto, R., Korneev, V., and Johnson, L. (1995). Low-frequency elastic-wave scattering by an inclusion: limits of application. *Geophys. J. Intern.*, 120(3):677–692.

Gropp, W., Lusk, E., and Skjellum, A. (1999). *Using MPI - Portable Parallel Programming with the Message-Passing Interface, second edition*. The MIT press, Cambridge, Massachusetts.

Gubernatis, J., Domany, E., Krumhansl, J., and Huberman, M. (1977). The Born approximation in the theory of the scattering of elastic waves by flaws. *J. Appl. Phys.*, 48:2812–2819.

Hornby, B. E. (1989). Imaging near-borehole of formation structure using full-waveform sonic data. *Geophysics*, 54:7475–757.

Hudson, J. and Heritage, J. (1981). The use of the Born Approximation in seismic scattering problems. *Geophys. J. R. Astr. Soc.*, 66(1):221–240.

Huygens, C. (1996). *Abhandlung über das Licht (Deutsche Übersetzung von E. Lommel von Traité de la lumiére, 1690)*. Thun, Frankfurt am Main.

Kennett, B. L. (1983). *Seismic wave propagation in stratified media*. Cambridge University Press, Cambridge.

Knuth, D. E. (1991). *Computers & typesetting, vol. A: the TEXbook*. Addison-Wesley, Reading.

Korneev, V. and Johnson, L. (1993a). Scattering of elastic waves by a spherical inclusion: Limitations of asymptotic solutions. *Geophys. J. Intern.*, 115(1):251–263.

Korneev, V. and Johnson, L. (1993b). Scattering of elastic waves by a spherical inclusion: Theory and numerical results. *Geophys. J. Intern.*, 115(1):230–250.

Kurkjian, A. and Chang, S. (1986). Acoustic multipole sources in fluid-filled boreholes. *Geophysics*, 51:148–163.

Kurkjian, A. L. (1985). Numerical computation of individual far-field arrivals excited by an acoustic source in a borehole. *Geophysics*, 50:852–866.

Lamport, L. (1986). *LaTeX: A document preparation system*. Addison-Wesley, Reading.

Miller, D., Oristaglio, M., and Beylkin, G. (1987). A new slant on seismic imaging: Migration and integral geometry. *Geophysics*, 52:943–964.

Moradi Tehrani, A. and Slob, E. (2009). Iterative extended Born approximation based on CG-FFT integral equation method for low-frequency 3D modeling. In *CWP Annual Project Review Book*, pages 73–80. Colorado School of Mines.

Murch, R. D. (1992). An extended Born approximation. *Inverse Problems*, 8:L5–L11.

Nyquist, H. (1928). Certain topics in telegraph transmission theory. *Transactions of the American Institute of Electrical Engineers*, 47(2):617–644.

Panning, M. P., Capdeville, Y., and Romanowicz, B. A. (2009). Seismic waveform modelling in a 3-D Earth using the Born approximation: potential shortcomings and a remedy. *Geophys. J. Intern.*, 177(1):161–178.

Pontius, M. (2013). Genauigkeit der Finiten Differenzen Methode von Reflexionen bei einer Bohrlochkonfiguration. Bsc-thesis, University of Karlsruhe.

Ravaut, C., Alerini, M., Pannetier-Lescoffit, S., and Thomassen, E. (2008). Sub-salt imaging by full-waveform inversion: a parameter analysis. In *Expanded abstracts, 70th Conf.* Eur. Assn. Geosci. Eng.

Robertsson, J., Blanch, J. O., and Symes, W. W. (1994). Viscoelastic finite-difference modeling. *Geophysics*, 59(9):1444–1456.

Sato, T. and Smith, B. V. (2009). *Xfig User Manual, Version 3.2.5b*. `http://xfig.org/userman`.

Schmitt, D. (1988). Shear wave logging in elastic formations. *J. Acoust. Soc. of Am.*, 84:2215–2229.

Schmitt, D. (1993). Dipole logging in cased boreholes. *J. Acoust. Soc. of Am.*, 93:640–657.

Stockwell, Jr., J. W. (1997). Free software in education: a case study of CWP/SU: Seismic Un*x. *The Leading Edge*, 16(7):1045–1049.

Stockwell, Jr., J. W. (1999). The CWP/SU: Seismic Un*x package. *Computers and Geosciences*, 25(4):415–419.

Tang, X. M. (2004). Imaging near-borehole structure using directional acoustic-wave measurements. *Geophysics*, 69(6):1378–1386.

Tang, X. M. and Cheng, C. H. A. (2004). *Quantitative Borehole Acoustic Methods*. Elsevier, Oxford, 1st edition.

Tang, X. M., Glassman, H., and Patterson, D. J. (2008). Single-well acoustic imaging in anisotropic formations. *Geophysics*, 73(4):11–16.

Tang, X. M. and Patterson, D. J. (2009). Single-well S-Wave imaging using multicomponent dipole acoustic-log data. *Geophysics*, 74(6):211–223.

Tang, X. M., Zheng, Y., and Patterson, D. J. (2007). Processing array acoustic-logging data to image near-borehole geologic structures. *Geophysics*, 72(2):87–97.

Tsang, L. and Radar, D. (1979). Numerical evaluation of the transient acoustic waveform due to a point source in the fluid-filled borehole. *Geophysics*, 44:1706–1720.

Veile, I., Geerits, T., and Bohlen, T. (2012). Efficient 3D borehole forward modeling of the reflected wave field while drilling. In *Extended abstracts, 74th Conf.* Eur. Assn. Geosci. Eng. Session P076.

Wang, R. (1999). A simple orthonormalization method for stable and efficient computation of green's functions. *Bull. Seismol. Soc. Am.*, 89:733–741.

Yilmaz, Ö. (1987). *Seismic data processing*. Soc. Expl. Geophys., Tulsa.

Zoeppritz, K. (1919). *Erdbebenwellen VII. VIIb. Über Reflexion und Durchgang seismischer Wellen durch Unstetigkeitsflächen.* Nachrichten von der Königlichen Gesellschaft der Wissenschaften zu Göttingen, Mathematische-Physikalische Klasse, Göttingen.

List of Figures

List of Tables

Appendix A

Spatial derivatives of scalar Green's function

In the following, I list the first four spatial derivatives of the scalar Green's function

$$\hat{G}_{\odot}\left(\mathbf{x}', \mathbf{x}\right) = \frac{\exp\left[i\omega s_{\odot}\left|\mathbf{x}' - \mathbf{x}\right|\right]}{4\pi\left|\mathbf{x}' - \mathbf{x}\right|}, \quad \text{with} \quad \odot \in \{\text{P, S}\}\ , \tag{A.1}$$

with respect to the observation coordinate $\mathbf{x}'$. The multiple spatial differentiation of equation A.1 introduces one more singularity (of one order higher) with each spatial differentiation. The highest order singularity occurring during in the derivatives is of order 5 in equation A.5. It can be assumed that the first order term (i.e. the least singular term) contributes the leading part to the incident and scattered wave amplitude. Hence, only this term is incorporated when the scattered wave field particle velocity $\hat{v}_r^{\text{scat}}$ (equation 2.59) is derived. This is referred to as as the far-field approximation (Geerits et al., 2013).

$$\partial_r \hat{G}_{\odot}\left(\mathbf{x}', \mathbf{x}\right) = \left[-\frac{n_r}{\left|\mathbf{x}' - \mathbf{x}\right|^2} + i\omega s_{\odot}\frac{n_r}{\left|\mathbf{x}' - \mathbf{x}\right|}\right]\frac{\exp\left[i\omega s_{\odot}\left|\mathbf{x}' - \mathbf{x}\right|\right]}{4\pi} \tag{A.2}$$

$$\partial_k\partial_r \hat{G}_{\odot}\left(\mathbf{x}', \mathbf{x}\right) = \left[\frac{3n_k n_r - \delta_{k,r}}{\left|\mathbf{x}' - \mathbf{x}\right|^3} - i\omega s_{\odot}\frac{3n_k n_r - \delta_{k,r}}{\left|\mathbf{x}' - \mathbf{x}\right|^2} - \omega^2 s_{\odot}^2\frac{n_k n_r}{\left|\mathbf{x}' - \mathbf{x}\right|}\right]\frac{\exp\left[i\omega s_{\odot}\left|\mathbf{x}' - \mathbf{x}\right|\right]}{4\pi} \tag{A.3}$$

$$\begin{aligned}\partial_m\partial_k\partial_r \hat{G}_{\odot}\left(\mathbf{x}', \mathbf{x}\right) = \Bigg[&\frac{3\left(\delta_{m,k}n_r + \delta_{m,r}n_k + \delta_{k,r}n_m\right) - 15n_m n_k n_r}{\left|\mathbf{x}' - \mathbf{x}\right|^4} \\ &- i\omega s_{\odot}\frac{3\left(\delta_{m,k}n_r + \delta_{m,r}n_k + \delta_{k,r}n_m\right) - 15n_m n_k n_r}{\left|\mathbf{x}' - \mathbf{x}\right|^3} \\ &- \omega^2 s_{\odot}^2\frac{\delta_{m,k}n_r + \delta_{m,r}n_k + \delta_{k,r}n_m - 6n_m n_k n_r}{\left|\mathbf{x}' - \mathbf{x}\right|^2} \\ &+ i\omega^3 s_{\odot}^3\frac{n_m n_k n_r}{\left|\mathbf{x}' - \mathbf{x}\right|}\Bigg]\frac{\exp\left[i\omega s_{\odot}\left|\mathbf{x}' - \mathbf{x}\right|\right]}{4\pi}\end{aligned} \tag{A.4}$$

$$
\begin{aligned}
&\partial_n\partial_m\partial_k\partial_r\hat{G}_{\odot}\left(\mathbf{x}',\mathbf{x}\right) = \\
&\left[\left[\frac{3\left(\delta_{m,k}\delta_{n,r}+\delta_{m,r}\delta_{n,k}+\delta_{k,r}\delta_{n,m}\right)}{\left|\mathbf{x}'-\mathbf{x}\right|^5}-\frac{15\left(\delta_{n,m}n_kn_r+\delta_{n,k}n_mn_r+\delta_{n,r}n_mn_k+\delta_{m,k}n_nn_r+\delta_{m,r}n_nn_k+\delta_{k,r}n_nn_m\right)}{\left|\mathbf{x}'-\mathbf{x}\right|^5}+\frac{105n_nn_mn_kn_r}{\left|\mathbf{x}'-\mathbf{x}\right|^5}\right]\right. \\
&-i\omega s_{\odot}\left[\frac{3\left(\delta_{m,k}\delta_{n,r}+\delta_{m,r}\delta_{n,k}+\delta_{k,r}\delta_{n,m}\right)}{\left|\mathbf{x}'-\mathbf{x}\right|^4}-\frac{15\left(\delta_{n,m}n_kn_r+\delta_{n,k}n_mn_r+\delta_{n,r}n_mn_k+\delta_{m,k}n_nn_r+\delta_{m,r}n_nn_k+\delta_{k,r}n_nn_m\right)}{\left|\mathbf{x}'-\mathbf{x}\right|^4}+\frac{105n_nn_mn_kn_r}{\left|\mathbf{x}'-\mathbf{x}\right|^4}\right] \\
&-\omega^2s_{\odot}^2\left[\frac{\delta_{m,k}\delta_{n,r}+\delta_{m,r}\delta_{n,k}+\delta_{k,r}\delta_{n,m}}{\left|\mathbf{x}'-\mathbf{x}\right|^3}-\frac{6\left(\delta_{n,m}n_kn_r+\delta_{n,k}n_mn_r+\delta_{n,r}n_mn_k+\delta_{m,k}n_nn_r+\delta_{m,r}n_nn_k+\delta_{k,r}n_nn_m\right)}{\left|\mathbf{x}'-\mathbf{x}\right|^3}+\frac{45n_nn_mn_kn_r}{\left|\mathbf{x}'-\mathbf{x}\right|^3}\right] \\
&+i\omega^3s_{\odot}^3\left[\frac{-\left(\delta_{n,m}n_kn_r+\delta_{n,k}n_mn_r+\delta_{n,r}n_mn_k+\delta_{m,k}n_nn_r+\delta_{m,r}n_nn_k+\delta_{k,r}n_nn_m\right)+10n_nn_mn_kn_r}{\left|\mathbf{x}'-\mathbf{x}\right|^2}\right] \\
&\left.+\omega^4s_{\odot}^4\left[\frac{n_nn_mn_kn_r}{\left|\mathbf{x}'-\mathbf{x}\right|}\right]\right]\frac{\exp\left[i\omega s_{\odot}\left|\mathbf{x}'-\mathbf{x}\right|\right]}{4\pi}
\end{aligned}
\tag{A.5}
$$

with

$$
n_r=\frac{\mathrm{x}_r'-\mathrm{x}_r}{\left|\mathbf{x}'-\mathbf{x}\right|} \tag{A.6}
$$

being the unit vector pointing from the source coordinate $\mathbf{x}$ to the observation coordinate $\mathbf{x}'$.

Appendix B

The multipole force source

With respect to borehole applications in this appendix the mathematical formulation of a multipole force source of order n is presented as given in Geerits et al. (2010) and Geerits et al. (2013). By definition, the source consists of $2n$ point force sources that are arranged in a circle with radius R. The single sources separate from each other by $\frac{\pi}{n}$ radians and point alternately radially outward and inward as indicated in Figure B.1. These specifications yield

$$\hat{f}_k\left(\mathbf{x}''; \omega\right) = \frac{\hat{T}\left(\omega\right)}{2n} \sum_{j=1}^{2n} \sigma^j e_k^j \delta\left[\mathrm{x}_k'' - R e_k^j\right]. \tag{B.1}$$

Provided that there are no source imbalances resulting in equal source signatures, $\hat{T}\left(\omega\right)$ denotes the spectral domain source signature of the j-th force source with polarity σ^j (i.e., $\sigma^j = (-1)^j$) and $\mathbf{e}^j$ being the corresponding radially outward pointing unitary direction vector.

In the following, I derive an explicit expression for an exemplary dipole excitation (where the force source vector $\mathbf{f}^{\odot}$ is parallel to $\mathbf{e}_3$), since all results presented in this work correspond to dipole excitations. Hence, the chosen parameters are

$$n = 1, \quad \sigma^j = (-1)^j, \quad \mathbf{e}^1 = \mathbf{e}_3 \quad \mathbf{e}^2 = -\mathbf{e}_3 .$$

Inserting those in equation B.1 and incorporating the result in equation 2.26 yields

$$\mathbf{f}^{\odot}\left(\mathbf{k}^{\odot}\right) = -\hat{T}\left(\omega\right)\mathbf{e}_3 \cos\left[R\left(\mathbf{k}^{\odot}\cdot\mathbf{e}_3\right)\right] \quad \text{with} \quad \odot \in \{\mathrm{P,S}\}. \tag{B.2}$$

Evaluated at the P- and S-wavenumber $\mathbf{k}^{\mathrm{P}}$ and $\mathbf{k}^{\mathrm{S}}$, respectively, the corresponding directional pattern for the incident wave results in

$$n_l f_l^{\mathrm{P}} = \mathbf{n}\cdot\mathbf{f}^{\mathrm{P}} = -\hat{T}\left(\omega\right)\left(\mathbf{n}\cdot\mathbf{e}_3\right)\cos\left[R\left(\mathbf{k}^{\mathrm{P}}\cdot\mathbf{e}_3\right)\right] \tag{B.3}$$

and

$$p_l^{\mathrm{S}}\left(\mathbf{p}^{\mathrm{S}}\right) = \mathbf{n}\times\left(\mathbf{f}^{\mathrm{S}}\times\mathbf{n}\right) = -\hat{T}\left(\omega\right)\left[\mathbf{n}\times\left(\mathbf{e}_3\times\mathbf{n}\right)\right]\cos\left[R\left(\mathbf{k}^{\mathrm{S}}\cdot\mathbf{e}_3\right)\right]. \tag{B.4}$$

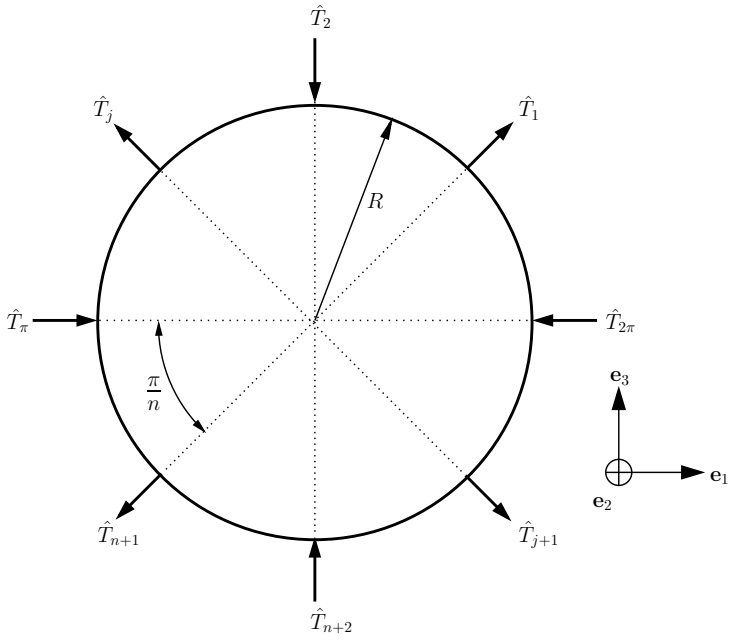

Figure B.1: Schematic cross section of a multipole force source of order n. The source consists of $2n$ point force sources that are arranged in a circle with radius R and offset from each other by $\frac{\pi}{n}$ radians. The Figure was made after Geerits et al. (2013).

Obviously, the argument of the $\cos$-function in both directional patterns describes the ratio between the radius of the multipole ring and the wavelength of the P- and S-wave, respectively. Clearly, if the wavelength is considerably larger than the radius of the multipole source ring the argument of the cosine becomes very small and the factor can be neglected, since $\cos(0) = 1$. In borehole applications this condition is certainly complied. Hence, equations B.3 and B.4 reduce to

$$n_l f_l^{\mathrm{P}} = \mathbf{n} \cdot \mathbf{f}^{\mathrm{P}} = -\hat{T}(\omega)(\mathbf{n} \cdot \mathbf{e}_3) = -\hat{T}(\omega) D_1^{\mathrm{P}} \tag{B.5}$$

and

$$p_l^{\mathrm{S}}\left(\mathbf{p}^{\mathrm{S}}\right) = \mathbf{n} \times \left(\mathbf{f}^{\mathrm{S}} \times \mathbf{n}\right) = -\hat{T}(\omega)[\mathbf{n} \times (\mathbf{e}_3 \times \mathbf{n})] = -\hat{T}(\omega)\mathbf{D}_1^{\mathrm{S}}, \tag{B.6}$$

with D_1^{P} representing the P-wave dipole directivity and $\mathbf{D}_1^{\mathrm{S}}$ representing the S-wave dipole directivity vector. From this, I derive the general relation for a multipole force source excitation of order n

$$f_l^{\odot} = -\hat{T}(\omega) D_n^{\odot}(\mathbf{x}) \quad \text{with} \quad \odot \in \{\mathrm{P,S}\} \tag{B.7}$$

where $\hat{T}(\omega)$ is the spectral domain source signature and $D_n^{\odot}(\mathbf{x})$ is the multipole directivity of the incident wave.

Appendix C

Explicit expressions for $\mathcal{G}_r^{\otimes}$

In the following, the explicit expressions for $\mathcal{G}_r^{\otimes}\left(\frac{t'}{t_0^{\otimes}}\right)$ with $\otimes \in \{\text{PP, SS}\}$ and the according differentiations with respect to $\left(\frac{t'}{t_0^{\otimes}}\right)$, occurring in chapter 2, equation 2.129, are summarized.

Dipole excitation perpendicular to the scatterer, i.e., along e_3:

$$\mathcal{G}_3^{\text{PP}}\left(\frac{t'}{t_0^{\text{P}}}\right) = \left(\frac{t'}{t_0^{\text{P}}}\right)^{-4} \tag{C.1}$$

$$\frac{d}{d\left(\frac{t'}{t_0^{\text{P}}}\right)}\left[\mathcal{G}_3^{\text{PP}}\left(\frac{t'}{t_0^{\text{P}}}\right)\right] = -4\left(\frac{t'}{t_0^{\text{P}}}\right)^{-5} \tag{C.2}$$

$$\mathcal{G}_3^{\text{SS}}\left(\frac{t'}{t_0^{\text{S}}}\right) = \left[\left(\frac{t'}{t_0^{\text{S}}}\right)^2 - 1\right]\left(\frac{t'}{t_0^{\text{S}}}\right)^{-4} \tag{C.3}$$

$$\frac{d}{d\left(\frac{t'}{t_0^{\text{S}}}\right)}\left[\mathcal{G}_3^{\text{SS}}\left(\frac{t'}{t_0^{\text{S}}}\right)\right] = 2\left[2 - \left(\frac{t'}{t_0^{\text{S}}}\right)^2\right]\left(\frac{t'}{t_0^{\text{S}}}\right)^{-5} \tag{C.4}$$

Dipole excitation parallel to the scatterer, i.e., along e_2:

$$\mathcal{G}_2^{\text{PP}}\left(\frac{t'}{t_0^{\text{P}}}\right) = \left[\left(\frac{t'}{t_0^{\text{P}}}\right)^2 - 1\right]\left(\frac{t'}{t_0^{\text{P}}}\right)^{-4} \tag{C.5}$$

$$\frac{d}{d\left(\frac{t'}{t_0^{\mathrm{P}}}\right)}\left[\mathcal{G}_2^{\mathrm{PP}}\left(\frac{t'}{t_0^{\mathrm{P}}}\right)\right] = -2\left[2-\left(\frac{t'}{t_0^{\mathrm{P}}}\right)^2\right]\left(\frac{t'}{t_0^{\mathrm{P}}}\right)^{-5} \tag{C.6}$$

$$\mathcal{G}_2^{\mathrm{SS}}\left(\frac{t'}{t_0^{\mathrm{S}}}\right) = \frac{1}{2}\left[\left(\frac{t'}{t_0^{\mathrm{S}}}\right)^2+1\right]\left(\frac{t'}{t_0^{\mathrm{S}}}\right)^{-4} \tag{C.7}$$

$$\frac{d}{d\left(\frac{t'}{t_0^{\mathrm{S}}}\right)}\left[\mathcal{G}_2^{\mathrm{SS}}\left(\frac{t'}{t_0^{\mathrm{S}}}\right)\right] = -\left[2+\left(\frac{t'}{t_0^{\mathrm{S}}}\right)^2\right]\left(\frac{t'}{t_0^{\mathrm{S}}}\right)^{-5} \tag{C.8}$$

Dipole excitation parallel to the scatterer, i.e., along $\mathbf{e}_1$:

$$\mathcal{G}_1^{\mathrm{PP}}\left(\frac{t'}{t_0^{\mathrm{P}}}\right) = \left[\left(\frac{t'}{t_0^{\mathrm{P}}}\right)^2-1\right]\left(\frac{t'}{t_0^{\mathrm{P}}}\right)^{-4} \tag{C.9}$$

$$\frac{d}{d\left(\frac{t'}{t_0^{\mathrm{P}}}\right)}\left[\mathcal{G}_1^{\mathrm{PP}}\left(\frac{t'}{t_0^{\mathrm{P}}}\right)\right] = -2\left[2-\left(\frac{t'}{t_0^{\mathrm{P}}}\right)^2\right]\left(\frac{t'}{t_0^{\mathrm{P}}}\right)^{-5} \tag{C.10}$$

$$\mathcal{G}_1^{\mathrm{SS}}\left(\frac{t'}{t_0^{\mathrm{S}}}\right) = \frac{1}{2}\left[\left(\frac{t'}{t_0^{\mathrm{S}}}\right)^2+1\right]\left(\frac{t'}{t_0^{\mathrm{S}}}\right)^{-4} \tag{C.11}$$

$$\frac{d}{d\left(\frac{t'}{t_0^{\mathrm{S}}}\right)}\left[\mathcal{G}_1^{\mathrm{SS}}\left(\frac{t'}{t_0^{\mathrm{S}}}\right)\right] = -\left[2+\left(\frac{t'}{t_0^{\mathrm{S}}}\right)^2\right]\left(\frac{t'}{t_0^{\mathrm{S}}}\right)^{-5} \tag{C.12}$$

Appendix D

Establishing a zero-offset approximation for *qseis*

As mentioned in section 3.1, it is not possible to evaluate true zero-offset cases in *qseis* due to implementation limitations. In order to be able to compare the analytic Born result (which is only evaluable for true zero-offset cases) with the qseis result (serving as analytic reference), I investigated the influence of the source-receiver distance for small offsets, i.e., where $h << d$, on the scattered particle displacement calculated by *qseis*. To systematically study this influence different source-receiver offsets were tested for configuration 1 with $\delta\rho = 0.2$ (cf. Table 3.1), described in chapter 3, section 3.1. Table D.1 gives an overview of the investigated (half) source-receiver offsets varying from 5% to 20% of the distance from the borehole axis to the scatterer. The listed percentages Q are given by the quotient

$$Q = \frac{h}{d} \cdot 100\,. \tag{D.1}$$

In all cases the source-receiver offset was smaller than one and a half times of the smallest occurring dominant wavelength, pertaining to the dominant S-wavelength being 2.538 m. Table D.1 also lists the ratio p between the source-receiver offset (i.e., $2h$) and the dominant S-wavelength.

Figure D.1 (top) exemplarily shows the resulting particle displacements for the PP-reflection for all investigated source-receiver offsets. Already at first sight it is obvious that the results do not differ significantly. However, to quantify the misfit, the difference between the results for the closest (half) source receiver offset, i.e., $Q = 5\%$ and the two other (half) source-receiver offsets are computed and plotted in Figure D.1 (bottom). In both cases the difference is of order $1 \cdot 10^{-17}$ which is at least two orders of magnitude smaller than the signal of the PP-reflection itself. Hence, it can be concluded that in cases where firstly, the source receiver offset is less than one smallest dominant wavelength and secondly, the source-receiver offset is smaller than 20% of the distance from the borehole axis to the scatterer (i.e., $h < 0.2 \cdot d$), the influence of the source-receiver offset can be neglected. Accordingly, for all zero-offset cases, investigated with *qseis*, the following criterion was established and applied

$$h = 0.1 \cdot d\,. \tag{D.2}$$

The adherence to this criterion leads to a far-field approximation which enables a quantitative comparison of the zero-offset analytic Born solution with the 'quasi zero-offset' *qseis* result.

Table D.1: Setup-parameters used for the investigation of the influence of the source-receiver offset to establish a zero-offset approximation for *qseis*: d denotes the distance from the borehole axis to the plane scatterer, h denotes half the source-receiver distance and Q gives the ratio of both as defined in equation D.1, while p denotes the relation between the smallest occurring dominant (S-)wavelength and the source-receiver offset.

	Test 1	Test 2	Test 3
d (in m)	4.8	4.8	4.8
h (in m)	1.92	0.96	0.48
Q (in%)	20	10	5
p	1.51	0.76	0.38

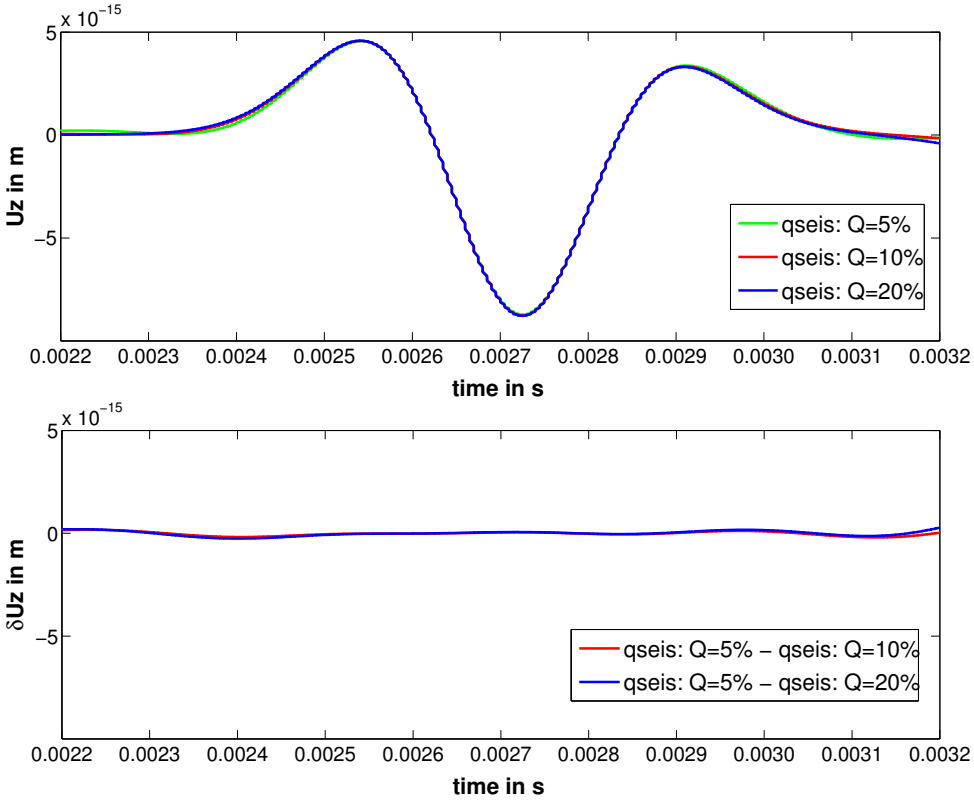

Figure D.1: Investigation of the influence of the source-receiver offset in *qseis* to establish a zero-offset approximation for the modelings performed with the latter. Top: the resulting particle displacements for the PP-reflection for all investigated source-receiver offsets. Bottom: the difference between the results for the closest (half) source-receiver offset, i.e., $Q = 5\%$ and the two other (half) source-receiver offsets is of order 10^{-17}.

Appendix E

Sensitivity and accuracy analysis: results

In the following, results of the sensitivity and accuracy analysis (cf. chapter 3) are presented:

- Figures E.1 - E.5 show the comparison of the single scattered particle displacement for configuration 1 between the analytic Born result and the *qseis*-result, while the latter serves as quasi-analytic reference. In this configuration the distance between the borehole axis and the scatterer is 4.8 m.
- Figures E.6 - E.10 show the comparison of the single scattered particle displacement for configuration 2 between the analytic Born result and the *qseis*-result, while the latter serves as quasi-analytic reference. In this configuration the distance between the borehole axis and the scatterer is 17.68 m.
- Figures E.11 - E.15 show the comparison of the single scattered particle displacement for configuration 3 between the analytic Born result and the *qseis*-result, while the latter serves as quasi-analytic reference. In this configuration the distance between the borehole axis and the scatterer is 30.48 m.

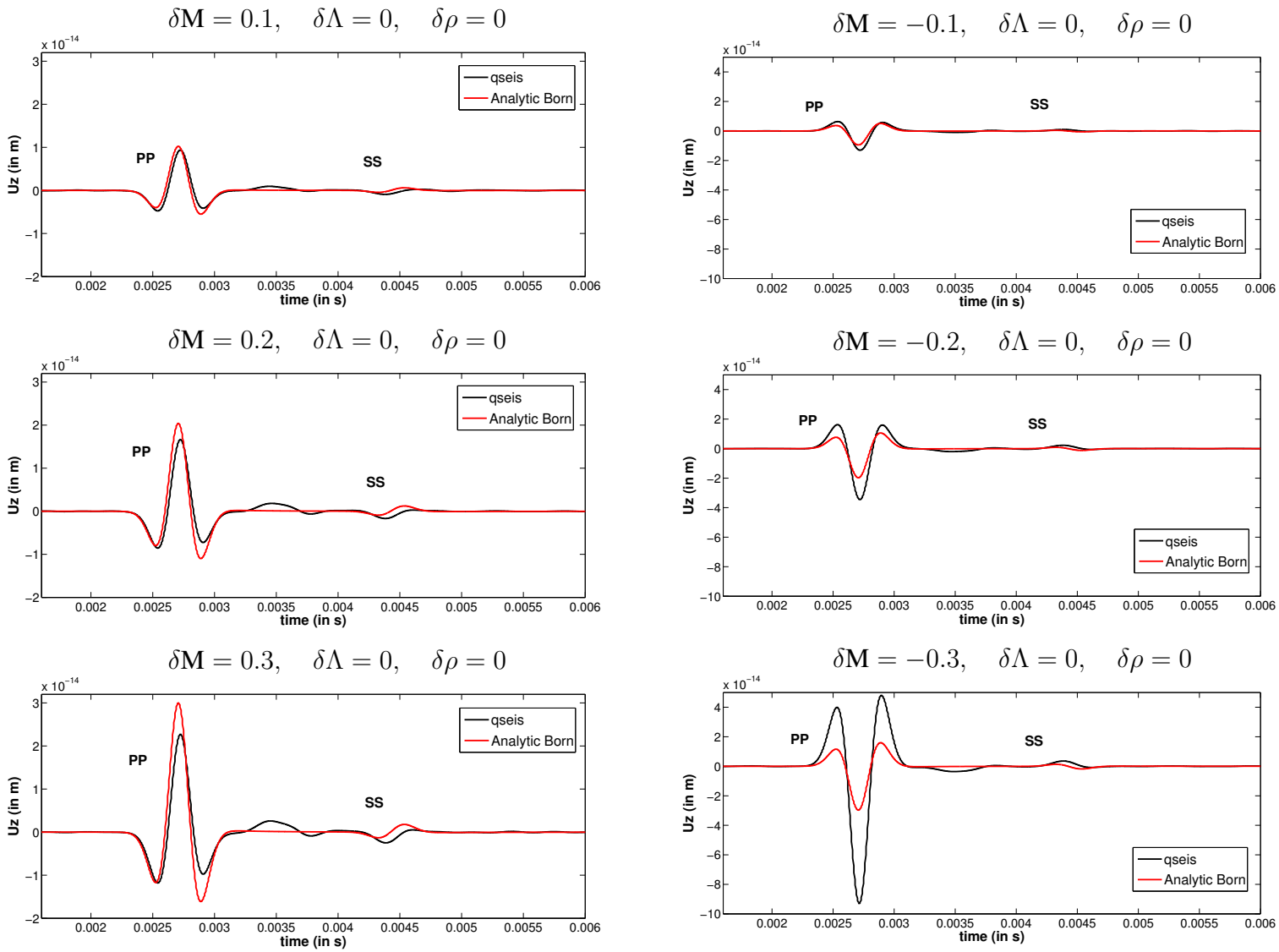

Figure E.1: Sensitivity and accuracy analysis for Configuration 1 with a dipole excitation in z-direction and different perturbations in M. The resulting values for v_P, v_S and ρ are given in Table 3.1. The displayed graphs show the comparisons of the particle displacements on the z-component for the PP- and SS-reflection between the analytic Born result (red) and the *qseis*-result (black). As in this case (cf. equation 2.94) the other components vanish, they are not shown.

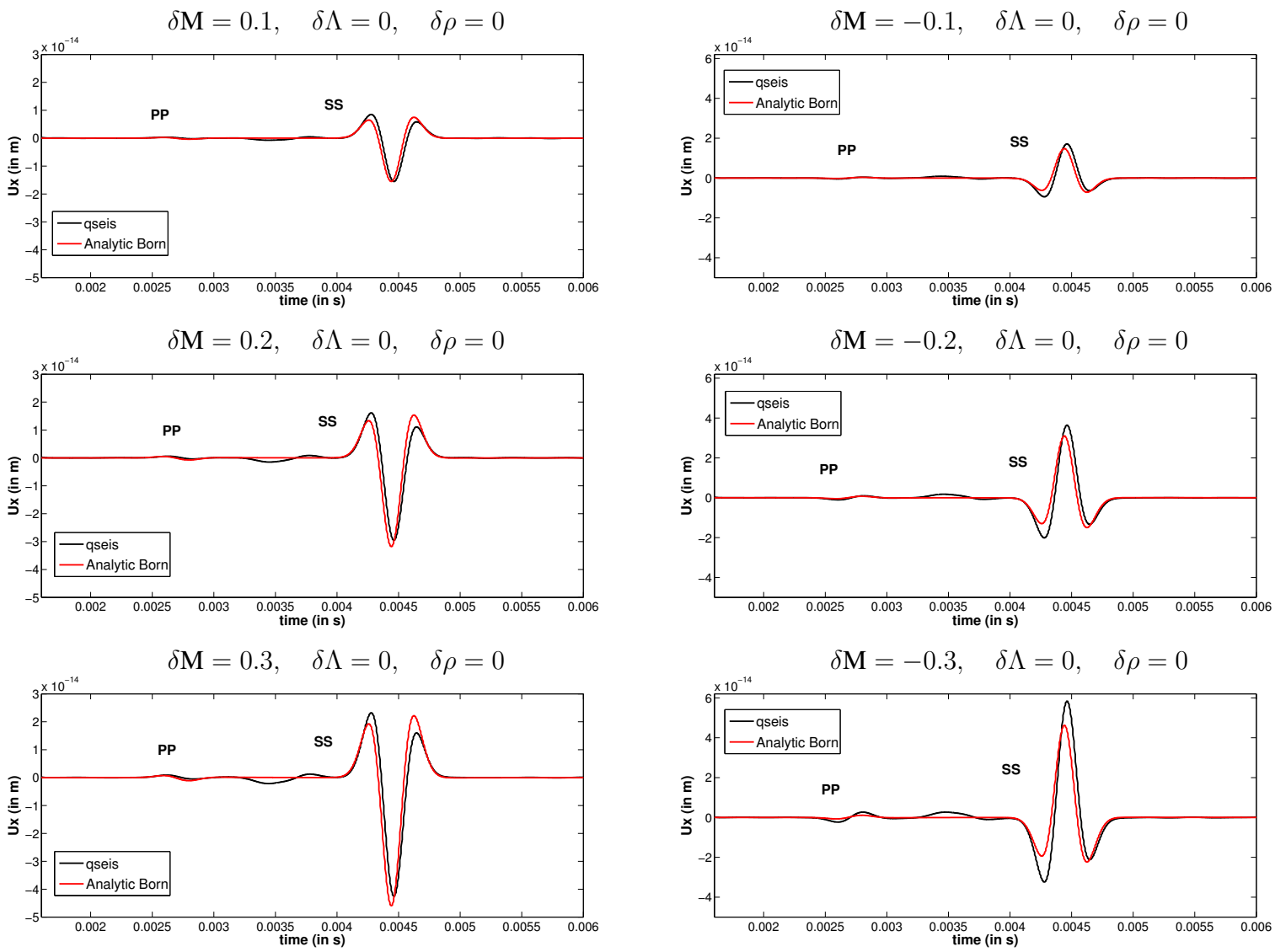

Figure E.2: Sensitivity and accuracy analysis for Configuration 1 with a dipole excitation in $\mathbf{x}$-direction and different perturbations in M. The resulting values for v_{P}, v_{S} and ρ are given in Table 3.1. The displayed graphs show the comparisons of the particle displacements on the $\mathbf{x}$-component for the SS-reflection between the analytic Born result (red) and the *qseis*-result (black). As in this case (cf. equation 2.122) the other components vanish, they are not shown.

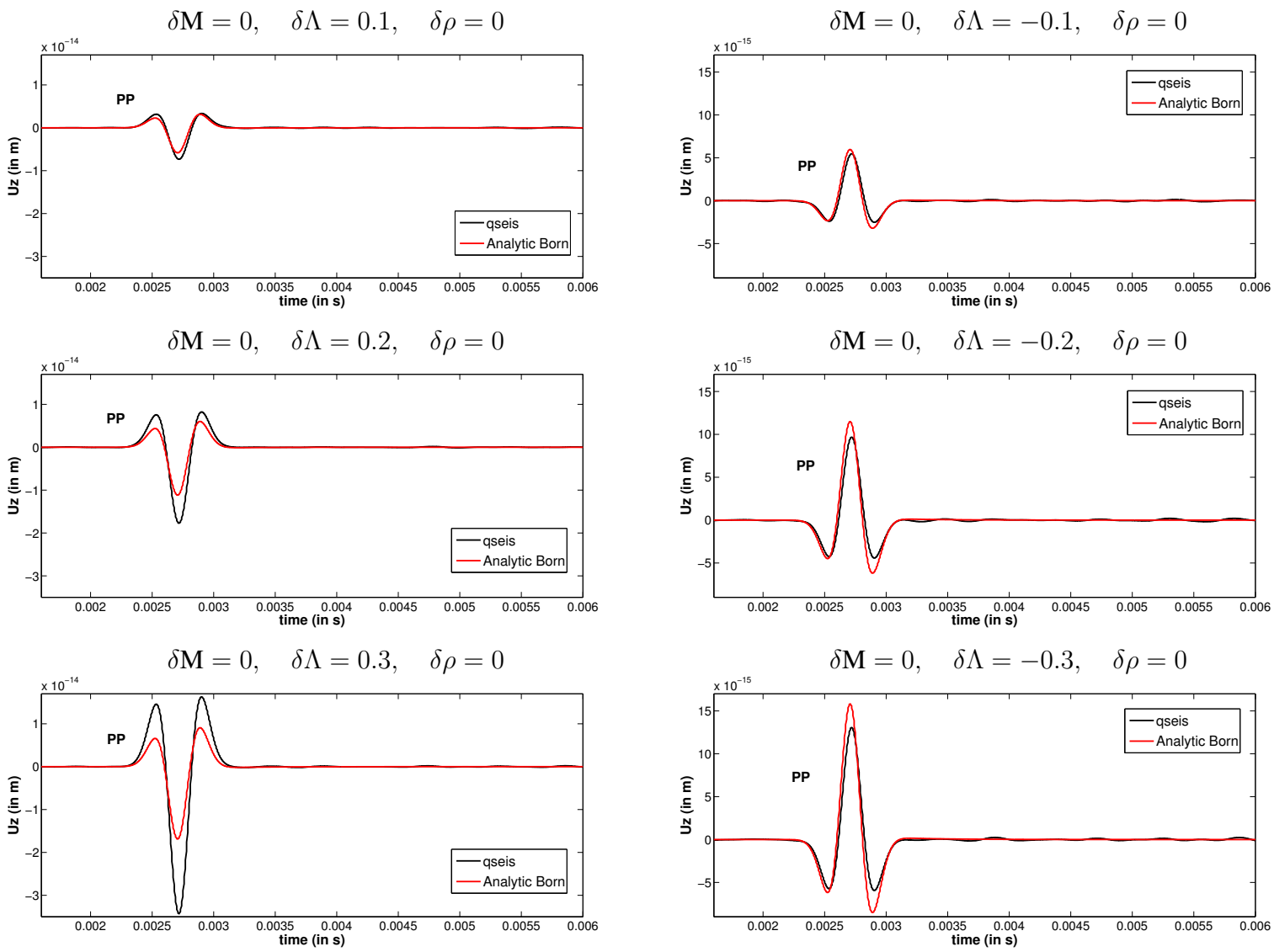

Figure E.3: Sensitivity and accuracy analysis for Configuration 1 with a dipole excitation in **z**-direction and different perturbations in Λ. The resulting values for v_P, v_S and ρ are given in Table 3.1. The displayed graphs show the comparisons of the particle displacements on the **z**-component for the PP-reflection between the analytic Born result (red) and the *qseis*-result (black). As in this case (cf. equation 2.94) the other components vanish, they are not shown.

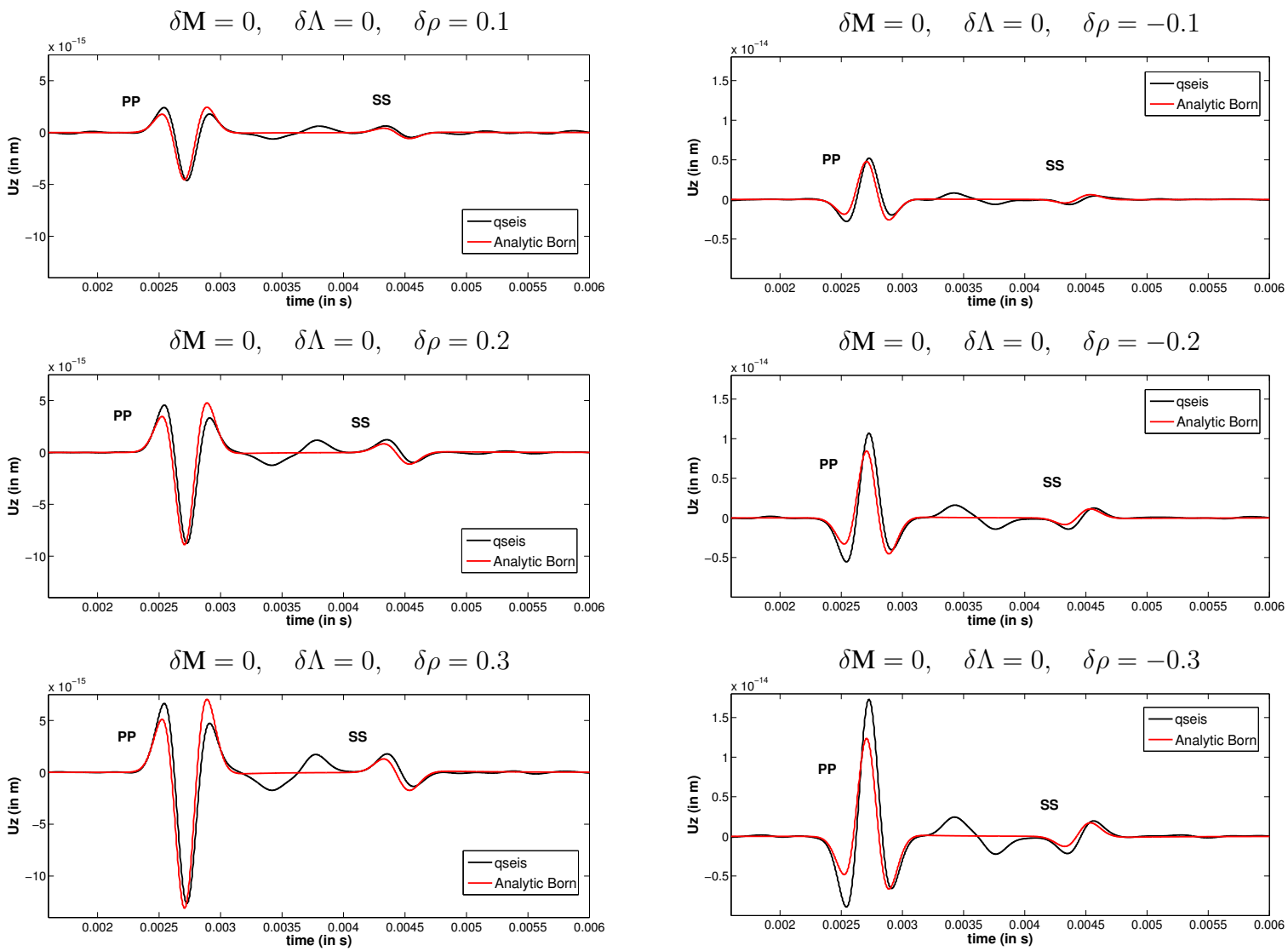

Figure E.4: Sensitivity and accuracy analysis for Configuration 1 with a dipole excitation in **z**-direction and different perturbations in ρ. The resulting values for v_P, v_S and ρ are given in Table 3.1. The displayed graphs show the comparisons of the particle displacements on the **z**-component for the PP- and SS-reflection between the analytic Born result (red) and the *qseis*-result (black). As in this case (cf. equation 2.94) the other components vanish, they are not shown.

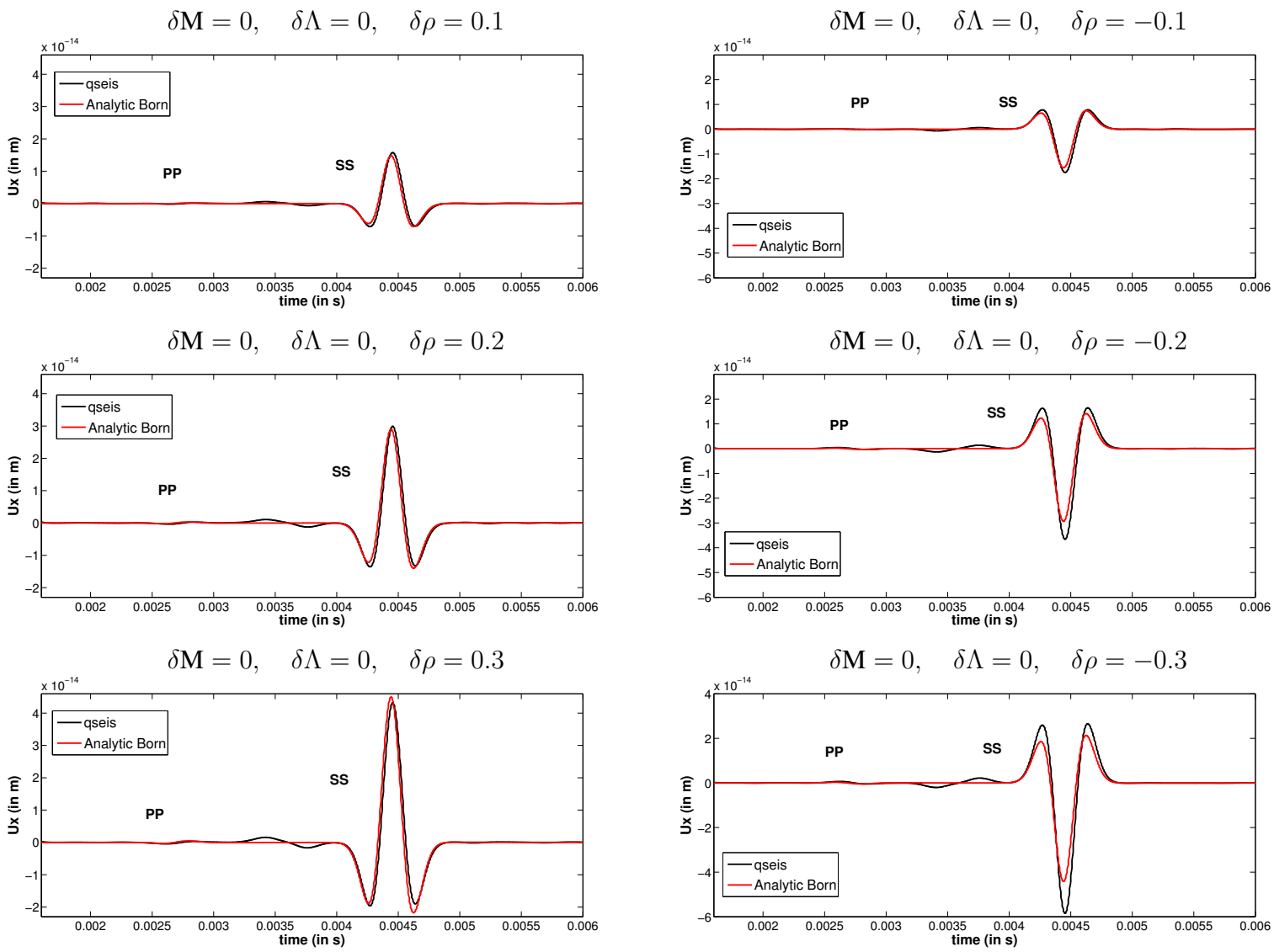

Figure E.5: Sensitivity and accuracy analysis for Configuration 1 with a dipole excitation in x-direction and different perturbations in ρ. The resulting values for v_P, v_S and ρ are given in Table 3.1. The displayed graphs show the comparisons of the particle displacements on the x-component for the SS-reflection between the analytic Born result (red) and the *qseis*-result (black). As in this case (cf. equation 2.122) the other components vanish, they are not shown.

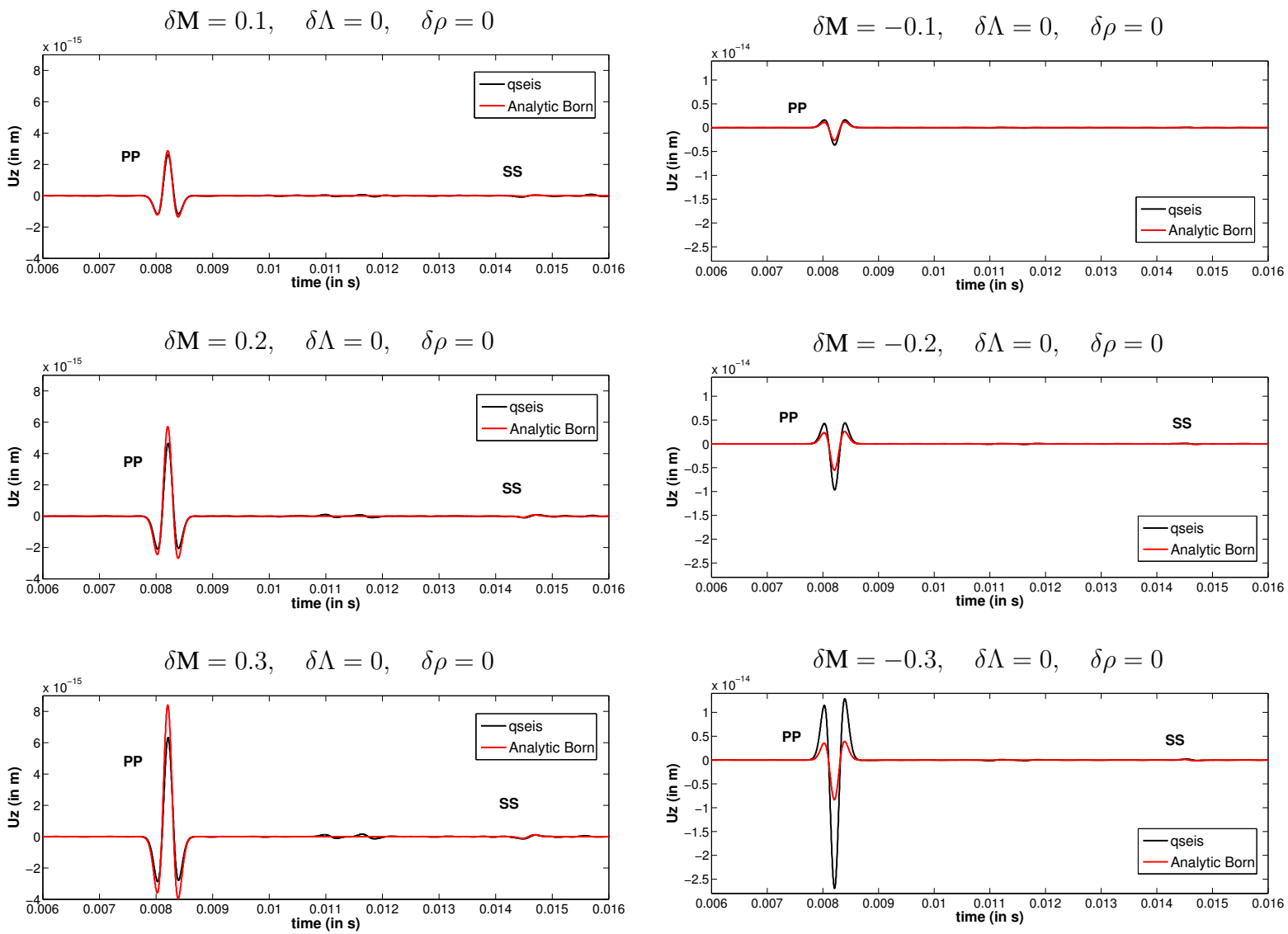

Figure E.6: Sensitivity and accuracy analysis for Configuration 2 with a dipole excitation in z-direction and different perturbations in M. The resulting values for v_P, v_S and ρ are given in Table 3.1. The displayed graphs show the comparisons of the particle displacements on the z-component for the PP- and SS-reflection between the analytic Born result (red) and the *qseis*-result (black). As in this case (cf. equation 2.94) the other components vanish, they are not shown.

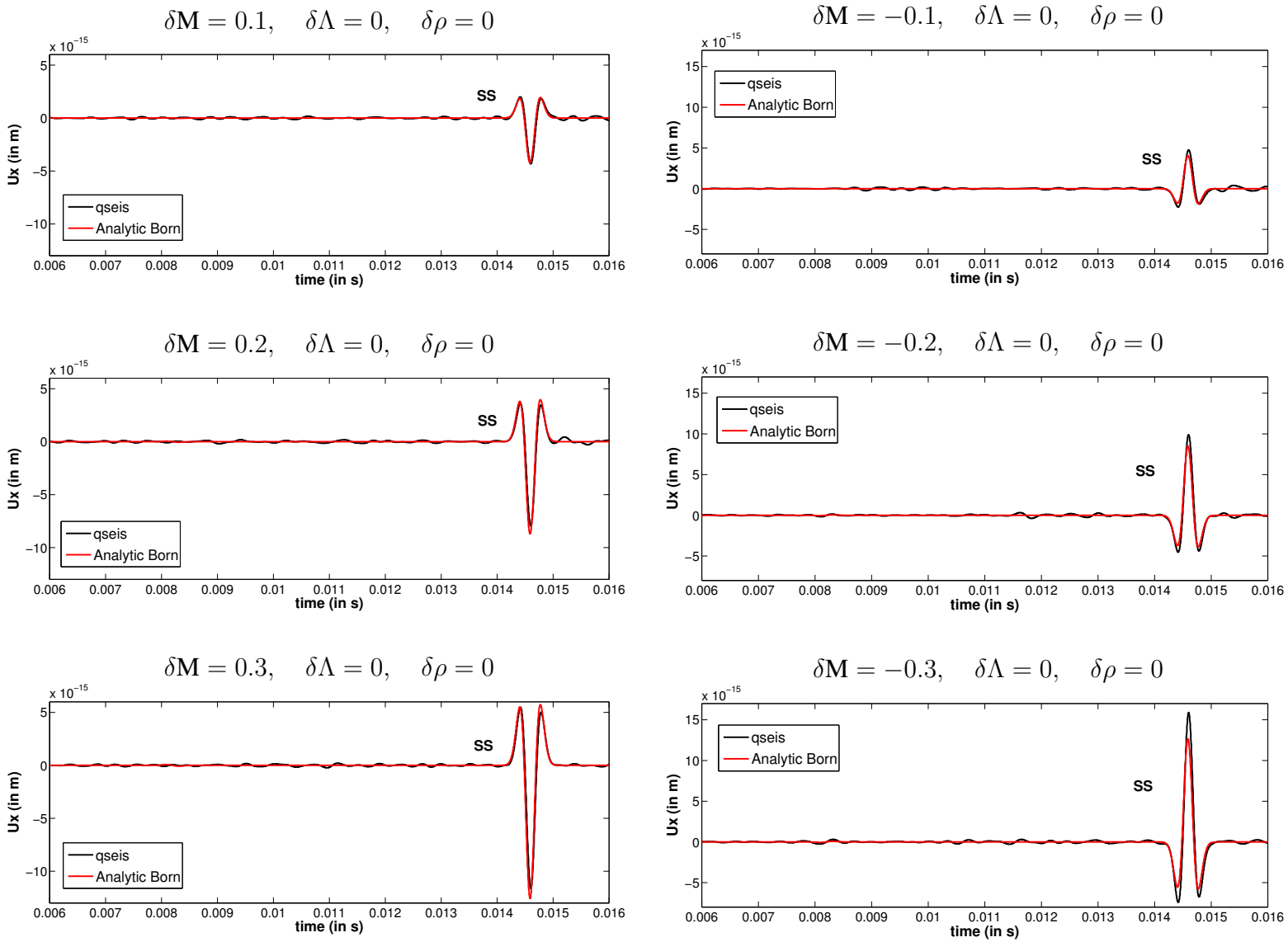

Figure E.7: Sensitivity and accuracy analysis for Configuration 2 with a dipole excitation in x-direction and different perturbations in M. The resulting values for v_P, v_S and ρ are given in Table 3.1. The displayed graphs show the comparisons of the particle displacements on the x-component for the SS-reflection between the analytic Born result (red) and the *qseis*-result (black). As in this case (cf. equation 2.122) the other components vanish, they are not shown.

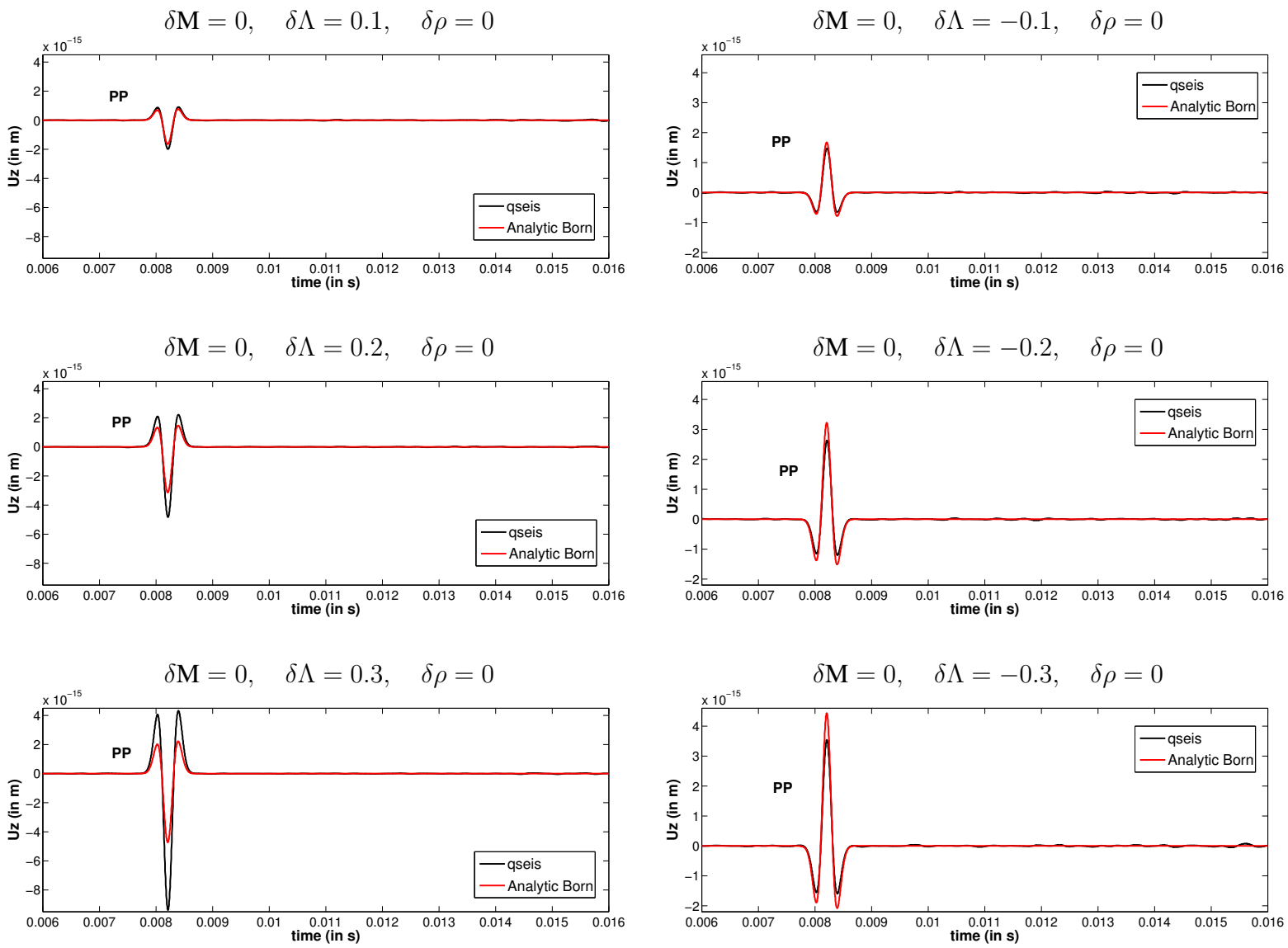

Figure E.8: Sensitivity and accuracy analysis for Configuration 2 with a dipole excitation in z-direction and different perturbations in Λ. The resulting values for $v_{\mathrm{P}}, v_{\mathrm{S}}$ and ρ are given in Table 3.1. The displayed graphs show the comparisons of the particle displacements on the z-component for the PP-reflection between the analytic Born result (red) and the *qseis*-result (black). As in this case (cf. equation 2.94) the other components vanish, they are not shown.

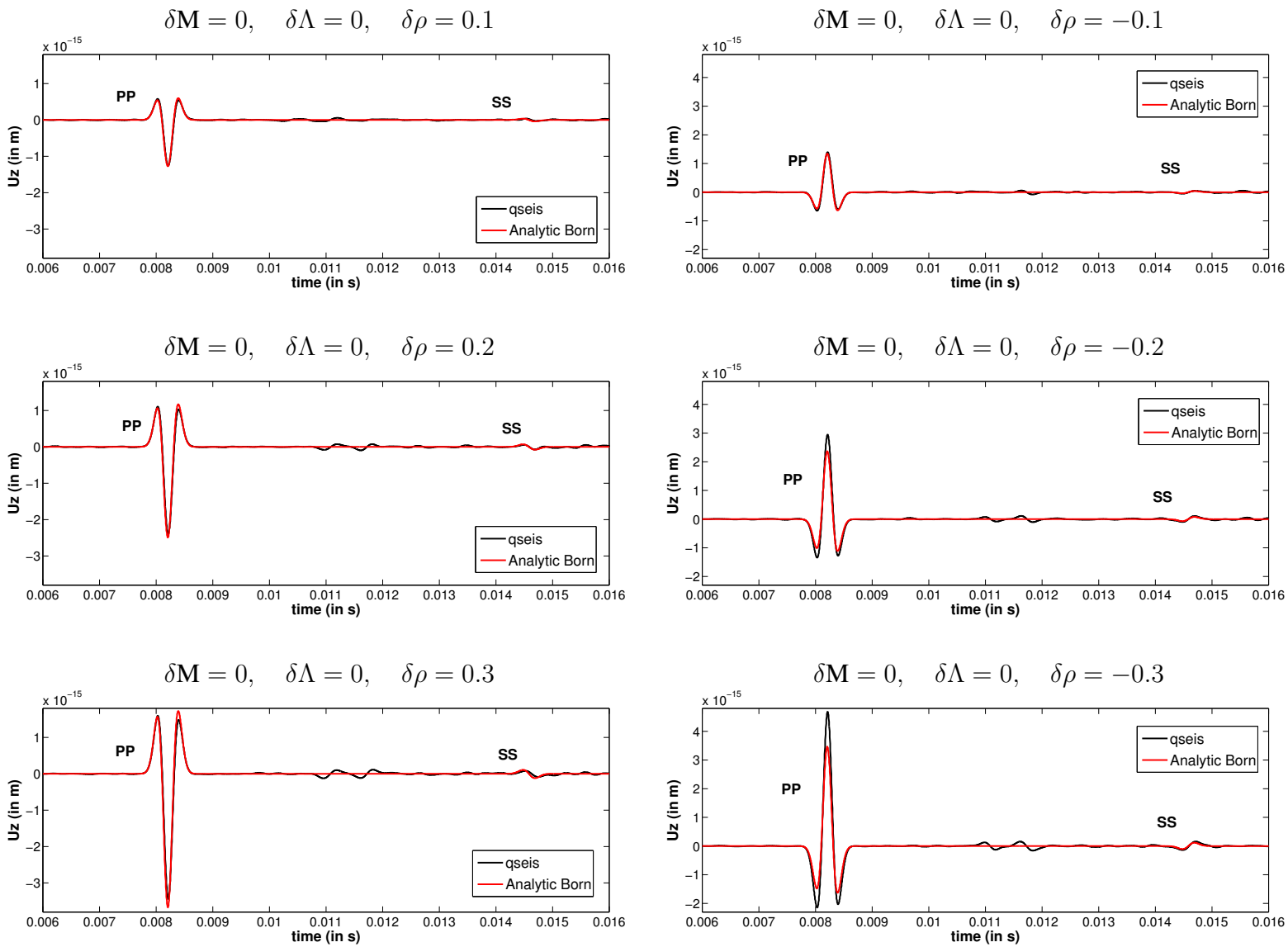

Figure E.9: Sensitivity and accuracy analysis for Configuration 2 with a dipole excitation in z-direction and different perturbations in ρ. The resulting values for v_P, v_S and ρ are given in Table 3.1. The displayed graphs show the comparisons of the particle displacements on the z-component for the PP- and SS-reflection between the analytic Born result (red) and the *qseis*-result (black). As in this case (cf. equation 2.94) the other components vanish, they are not shown.

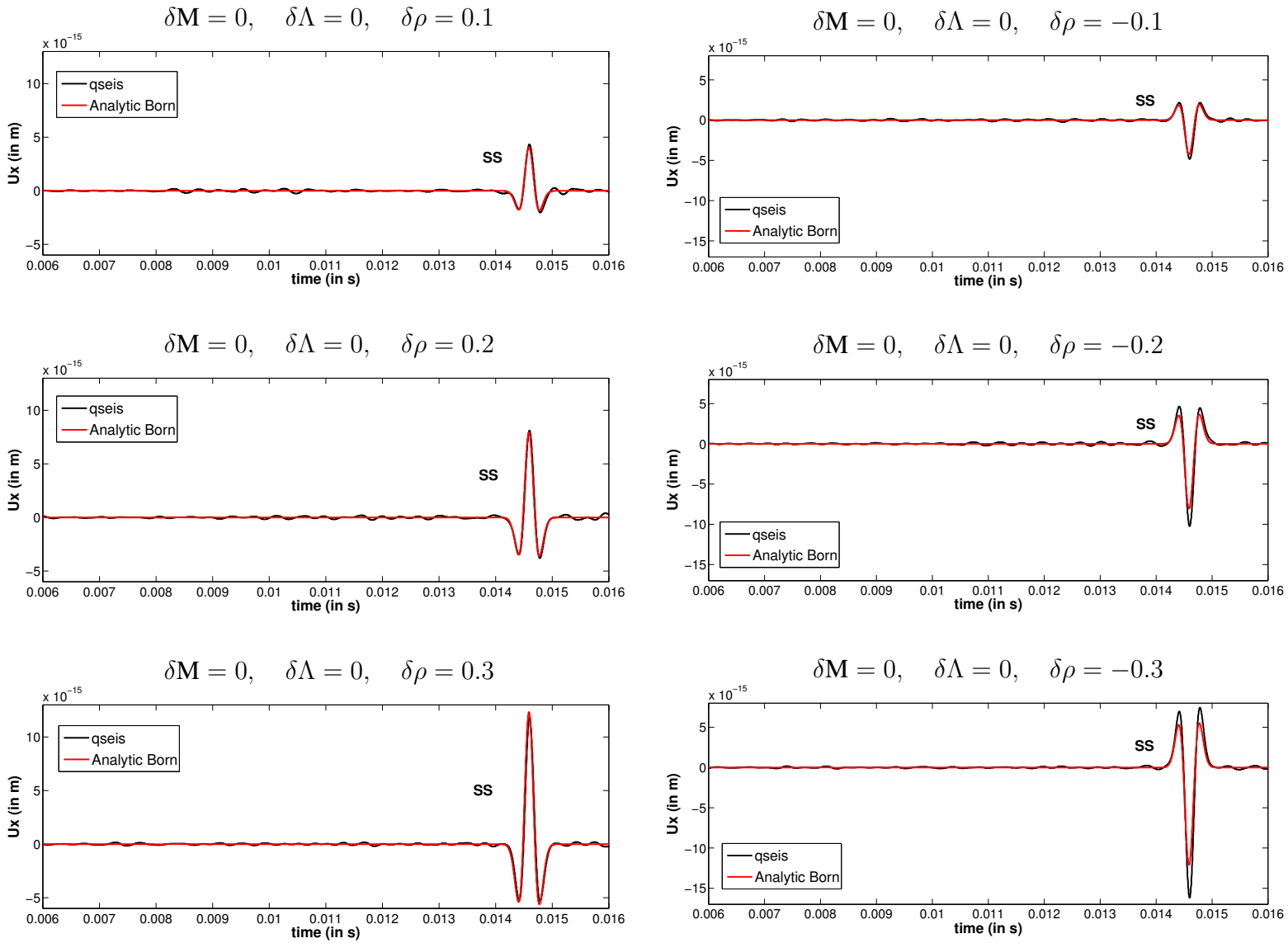

Figure E.10: Sensitivity and accuracy analysis for Configuration 2 with a dipole excitation in $\mathbf{x}$-direction and different perturbations in ρ. The resulting values for $v_{\mathrm{P}}, v_{\mathrm{S}}$ and ρ are given in Table 3.1. The displayed graphs show the comparisons of the particle displacements on the $\mathbf{x}$-component for the SS-reflection between the analytic Born result (red) and the *qseis*-result (black). As in this case (cf. equation 2.122) the other components vanish, they are not shown.

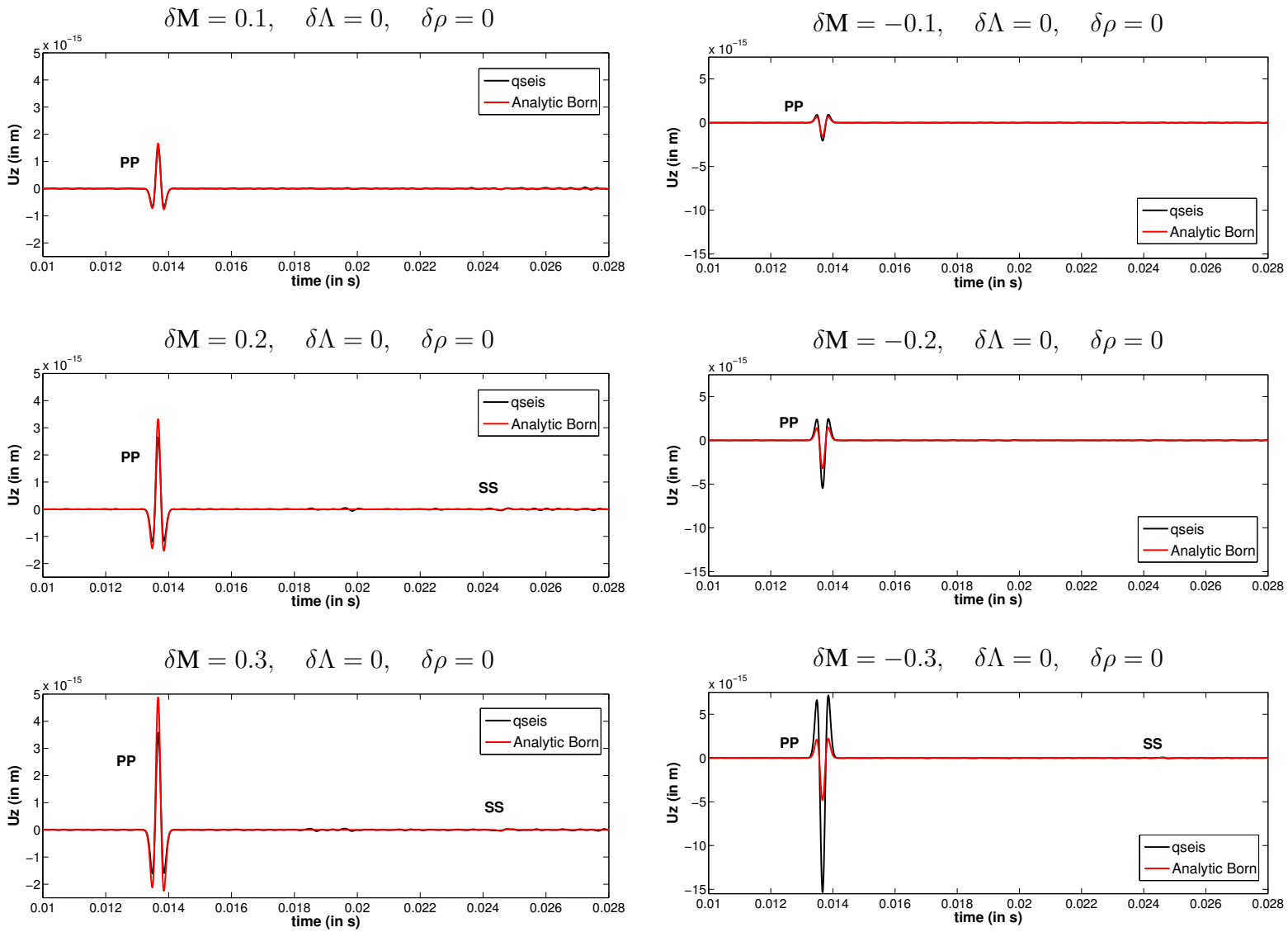

Figure E.11: Sensitivity and accuracy analysis for Configuration 3 with a dipole excitation in z-direction and different perturbations in M. The resulting values for v_P, v_S and ρ are given in Table 3.1. The displayed graphs show the comparisons of the particle displacements on the z-component for the PP- and SS-reflection between the analytic Born result (red) and the *qseis*-result (black). As in this case (cf. equation 2.94) the other components vanish, they are not shown.

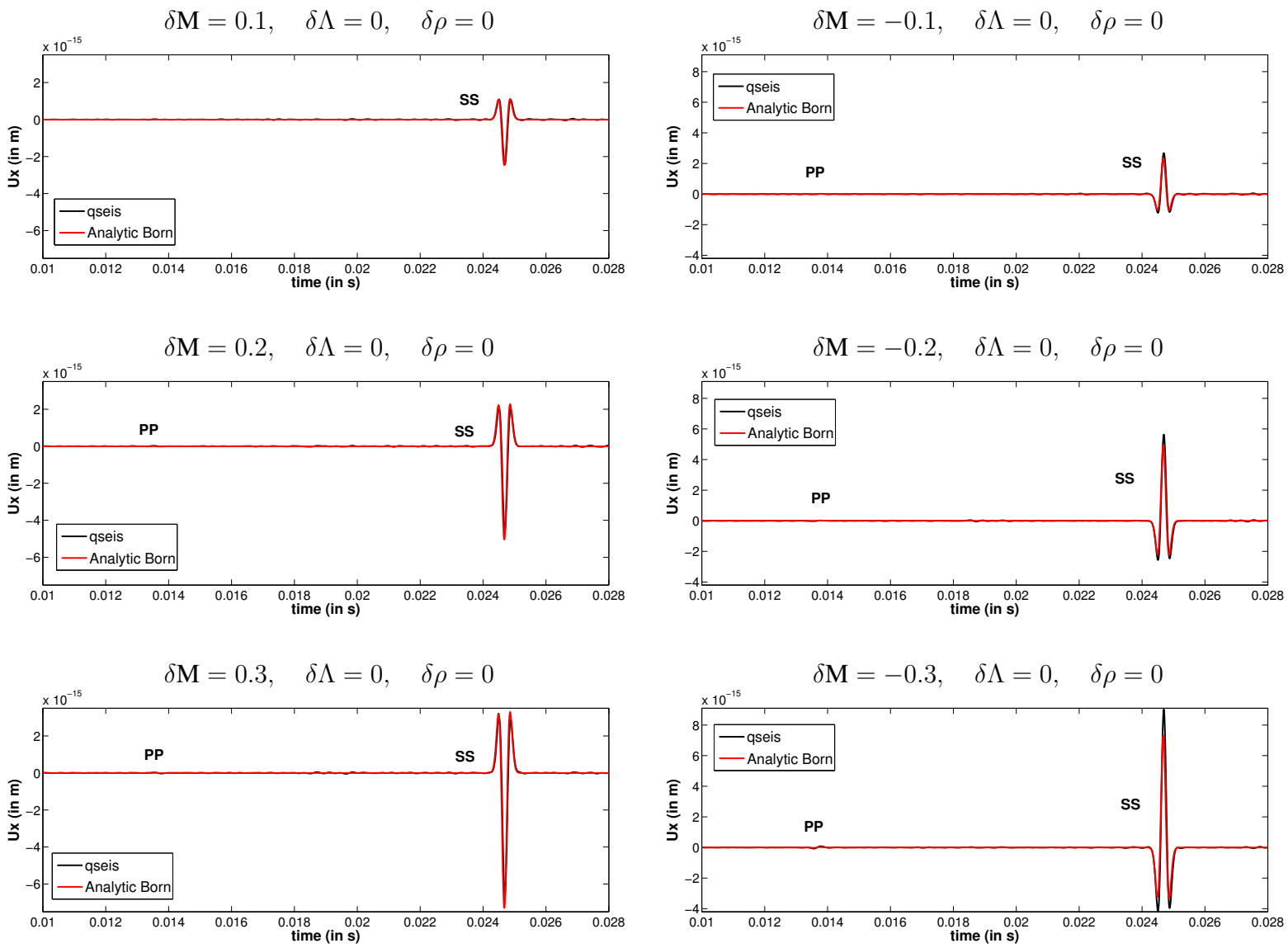

Figure E.12: Sensitivity and accuracy analysis for Configuration 3 with a dipole excitation in x-direction and different perturbations in M. The resulting values for v_P, v_S and ρ are given in Table 3.1. The displayed graphs show the comparisons of the particle displacements on the x-component for the SS-reflection between the analytic Born result (red) and the *qseis*-result (black). As in this case (cf. equation 2.122) the other components vanish, they are not shown.

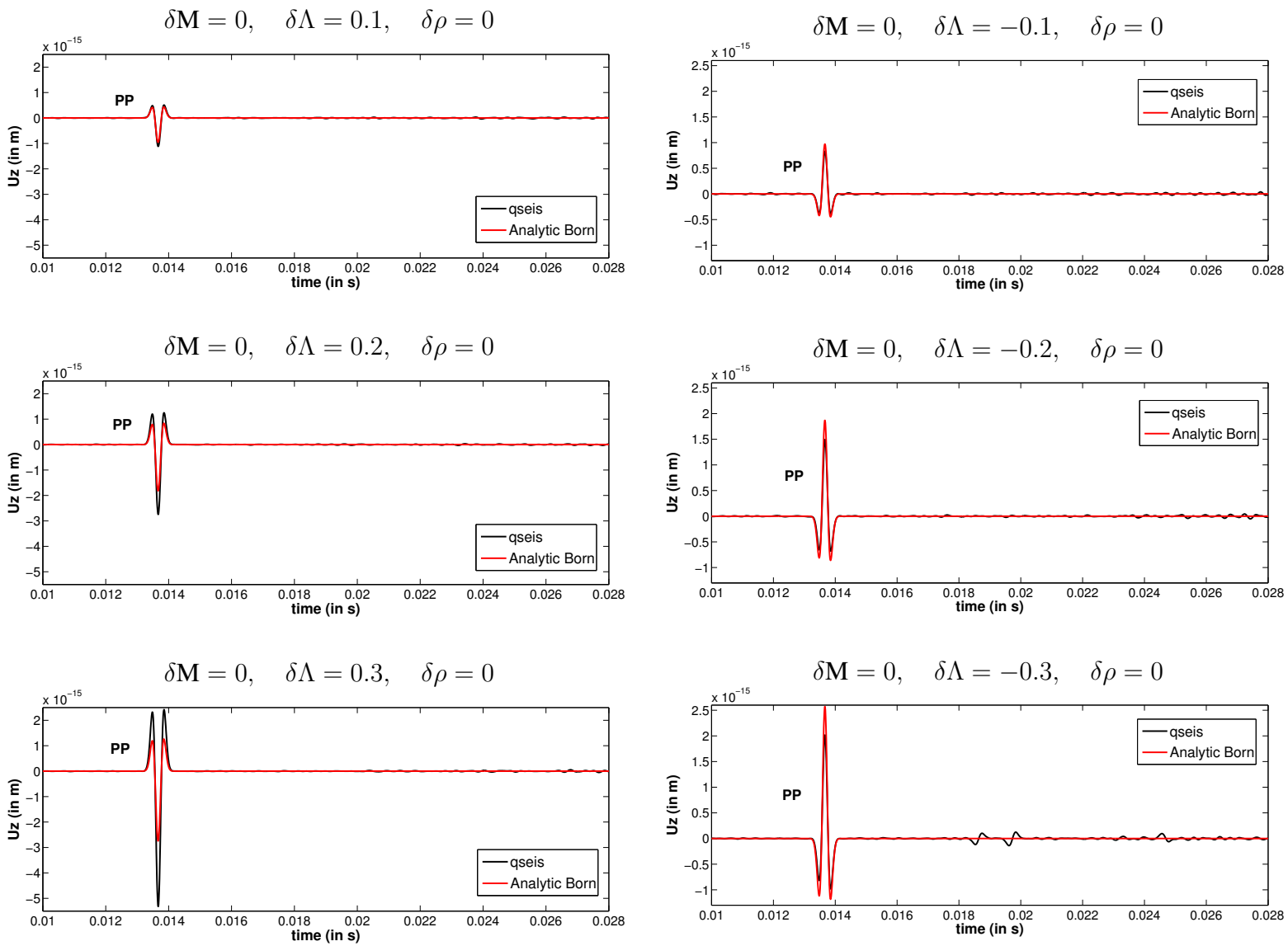

Figure E.13: Sensitivity and accuracy analysis for Configuration 3 with a dipole excitation in **z**-direction and different perturbations in Λ. The resulting values for $v_{\mathrm{P}}, v_{\mathrm{S}}$ and ρ are given in Table 3.1. The displayed graphs show the comparisons of the particle displacements on the **z**-component for the PP-reflection between the analytic Born result (red) and the *qseis*-result (black). As in this case (cf. equation 2.94) the other components vanish, they are not shown.

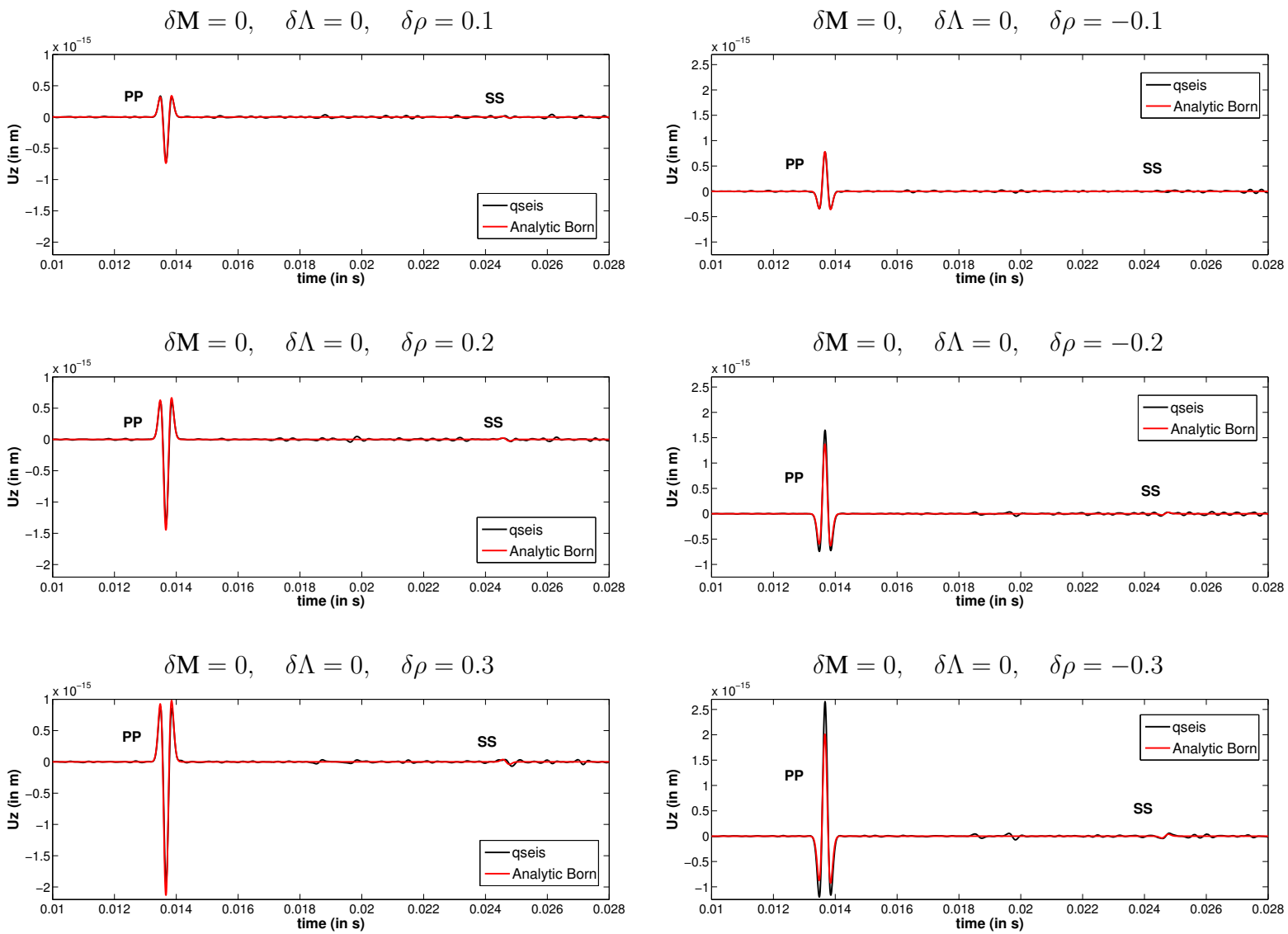

Figure E.14: Sensitivity and accuracy analysis for Configuration 3 with a dipole excitation in **z**-direction and different perturbations in ρ. The resulting values for v_P, v_S and ρ are given in Table 3.1. The displayed graphs show the comparisons of the particle displacements on the **z**-component for the PP- and SS-reflection between the analytic Born result (red) and the *qseis*-result (black). As in this case (cf. equation 2.94) the other components vanish, they are not shown.

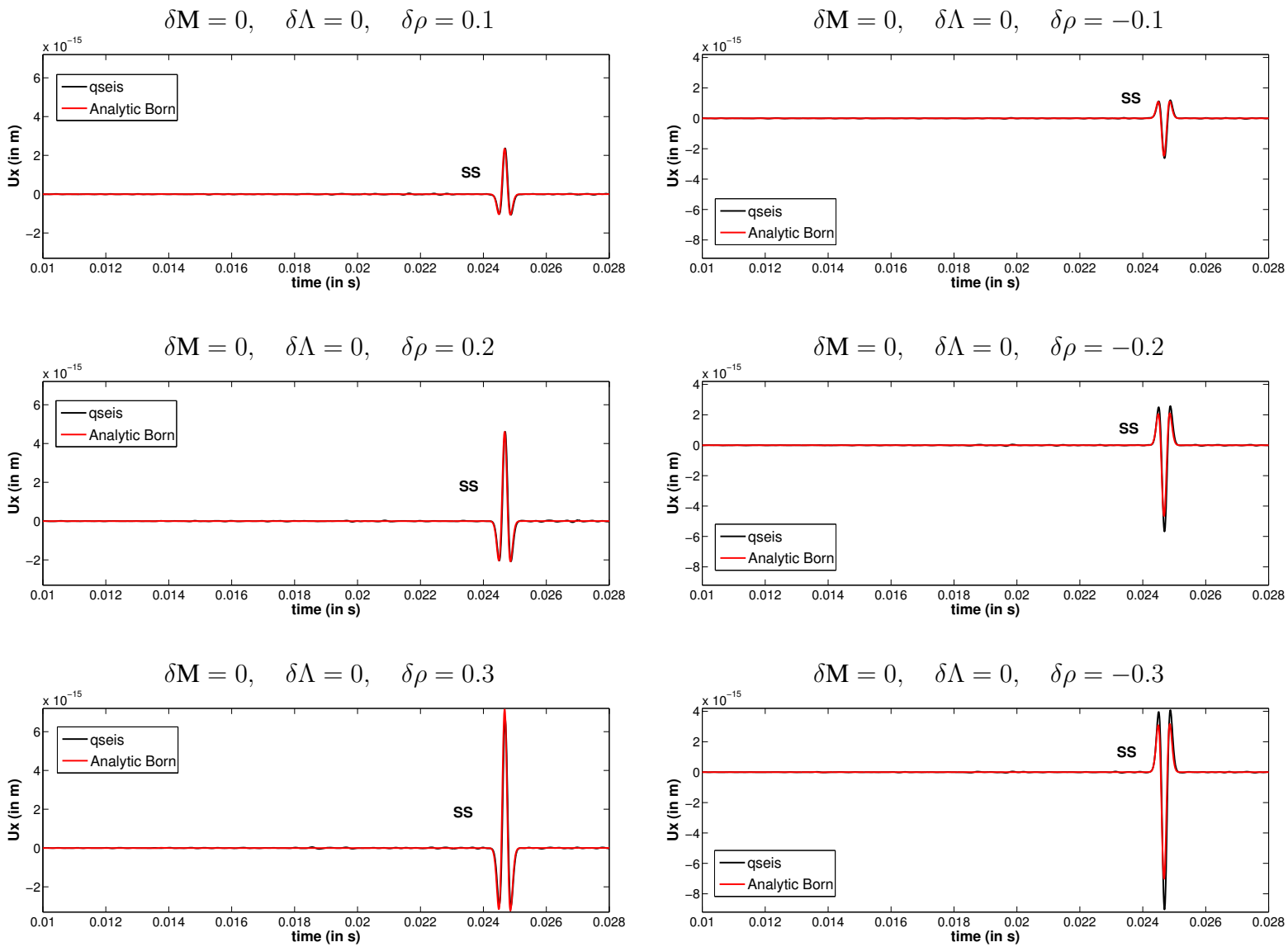

Figure E.15: Sensitivity and accuracy analysis for Configuration 3 with a dipole excitation in $\mathbf{x}$-direction and different perturbations in ρ. The resulting values for $v_{\mathrm{P}}, v_{\mathrm{S}}$ and ρ are given in Table 3.1. The displayed graphs show the comparisons of the particle displacements on the $\mathbf{x}$-component for the SS-reflection between the analytic Born result (red) and the *qseis*-result (black). As in this case (cf. equation 2.122) the other components vanish, they are not shown.

Appendix F

Definitions

Definition of the used Fourier transform pair

The definition of the used Fourier transform pair $X(\omega)$ and $x(t)$ is as follows:

$$X(\omega) = \mathcal{F}(x(t)) = \int_{-\infty}^{\infty} x(t) \exp[i\omega t]\, dt\,, \tag{F.1}$$

$$x(t) = \mathcal{F}^{-1}(X(\omega)) = \int_{-\infty}^{\infty} X(\omega) \exp[-i\omega t]\, d\omega\,, \tag{F.2}$$

where $\mathcal{F}(x(t))$ denotes the Fourier transform of $x(t)$ and $\mathcal{F}^{-1}(X(\omega))$ denotes the inverse Fourier transform of $X(\omega)$.

Definition of the used least-squares-misfit

To quantify the error between two time series I use the so-called ℓ^2-norm (Claerbout and Muir, 1973) as misfit function. It is defined as follows:

$$\delta d = \frac{\sqrt{\sum_{i=1}^{N} \left(d_i^{\text{ref}} - d_i^{\text{obs}}\right)^2}}{\sqrt{\sum_{i=1}^{N} \left(d_i^{\text{ref}}\right)^2}}\,, \tag{F.3}$$

where d^{ref} represents the reference and d^{obs} the observed data. The misfit is calculated by a summation over all individual misfits for all samples i of the two time series with N samples.

Definition of the used Ricker wavelet

The definition of the used time-domain Ricker wavelet $u(t)$ is given by:

$$u(t) = \left(1 - 2\tau^2\right) e^{-\tau^2} \tag{F.4}$$

with

$$\tau = \pi \left(t\, f_c - \frac{3}{2} \right) , \tag{F.5}$$

where f_c denotes the center-frequency and t the time.

Appendix G

Used software and hardware

Software

Within the scope of this work, several software packages were used to compute, process and visualize results:

- The numerical implementation *FMBORN* (Veile et al., 2012) was used to compute most of the shown Born-based results. In this program the "freely available subroutine library *FFTW* for computing the discrete Fourier transform in one or more dimensions, of arbitrary input size, and of both real and complex data [...]" is used (Frigo and Johnson, 2005). Furthermore, an *MPI*-based (Gropp et al., 1999) domain decomposition is implemented to improve the efficiency of the program.
- The program *qseis* (Wang, 1999) was used to compute quasi-analytic reference results for the validation of my new approach.
- The program *SOFI3D* (Bohlen, 2002; Bohlen et al., 2012) was used to compute FD-based results to compare the new approach with an established method in terms of efficiency and accuracy.
- The *MathWorks MATLAB*[1] environment was used to perform additional scientific computations and to visualize the computed results.
- The program *xfig* (Sato and Smith, 2009) was used to create all other sketches and figures.
- The conversion of seismic file formats was done with *Seismic Un*x* (Stockwell, 1997, 1999).
- For the visualization of data and creation of documents several small shell scripts (developed within the workgroup of applied geophysics at the Geophysical Institute) and public domain programs were used.

[1] MATLAB® is a high-level language and interactive environment for numerical computation, visualization, and programming. It is a registered trademark of The MathWorks, Inc.

Finally, this thesis was written using the freely available word processing package TEX (Knuth, 1991), the macro package LATEX (Lamport, 1986), and several extensions. The bibliography was generated with BibTEX.

Hardware

Within the scope of this work, the following workstations and high-performance computers were used to develop and test the discussed numerical approach *FMBORN*. These resources were also used to compute the presented results:

- A high-end workstation with i7 8-core CPUs and 8 GB main memory running openSUSE at the Geophysical Institute, Karlsruhe Institute of Technology (KIT);
- An SGI Altix 350 shared memory system with 12 Intel-Itanium CPUs and 64 GB main memory operated by SUSE Enterprise Server 10 at the Geophysical Institute, Karlsruhe Institute of Technology (KIT);
- The high-performance cluster system *InstitutsCluster 2* (IC2) of the Steinbuch Center for Computing at the KIT. The cluster is partly funded by the Geophysical Institute at KIT;
- The high-performance supercomputer *Jülich Research on Petaflop Architectures* (JuRoPA) of the Jülich Supercomputing Center.

Danksagung

Zu Beginn meiner Promotion dachte ich, die mir bevorstehenden drei bis vier Jahre seien eine kleine Ewigkeit. Natürlich war mir auch damals schon bewusst, dass diese Zeit sicherlich viel schneller vergehen würde als ich mir das zunächst ausgemalt hatte. Und nun ist es tatsächlich so gekommen: ich blicke auf so vieles zurück und habe dennoch den Eindruck, es sei erst einige Wochen her, dass ich mich für eine Promotion entschieden habe. Für die Begleitung und Unterstützung durch die zahlreichen Höhen und Tiefen der spannenden und lehrreichen aber auch anstrengenden letzten vier Jahre möchte ich mich im Folgenden bei einigen Menschen bedanken; meine Promotionszeit werde ich immer auch mit ihnen in Verbindung bringen.

Prof. Dr. Thomas Bohlen danke ich für die Übernahme des Referats und die kritische Begleitung meiner Arbeit. Den fachlichen sowie räumlichen Freiraum, den du mir während meiner Promotion gegeben hast, habe ich sehr genossen.

PD Dr. Joachim Ritter danke ich dafür, dass er ohne zu zögern das Korreferat meiner Arbeit übernommen hat.

Besonderer Dank gilt meinem Betreuer **Dr. Tim Geerits** bei Baker Hughes Inc. Dein stets offenes Ohr, insbesondere für bohrlochspezifische und theoriebezogene Fragen haben wesentlich zum Erfolg dieser Arbeit beigetragen. Dass du zu keinem Zeitpunkt müde wurdest, mir die abstrakt-theoretischen Formulierungen und Herleitungen von Prof. De Hoop näherzubringen, rechne ich dir hoch an. Außerdem möchte ich Baker Hughes Inc. für die Finanzierung meines Promotionsprojektes danken. Abgesehen von der eigentlichen Promotion war es mir dadurch möglich, an nationalen sowie internationalen Tagungen und Konferenzen teilzunehmen und einen Kurs zur parallelen Programmierung am Höchstleistungsrechenzentrum in Stuttgart zu besuchen. Ebenso bedanke ich mich beim WIT-Konsortium für die Finanzierung zu Beginn meiner Promotion.

Danken möchte ich auch **Dr. Rongjang Wang**, da er mir sein Programm *qseis* zur Verfügung gestellt hat und für Fragen zu dessen Handhabung immer ein offenes Ohr hatte.

Ein besonderer Dank gilt an dieser Stelle **André Kurzmann**, der mir insbesondere im Hinblick auf Fragestellungen, die im Rahmen der numerischen Implementierung auftraten, hilfreich zur Seite stand. Ohne deine universell einsetzbaren Gutscheine zur Unterstützung bei der Fehlersuche wäre ich manches Mal sicherlich verzweifelt. Des Weiteren möchte ich mich bei **Lisa Groos** bedanken, die immer ein offenes Ohr sowohl für promotionsrelevante als auch für private Probleme hatte. Die letzten vier Jahre haben uns definitiv unzählige Stunden beschert, über die wir in zehn Jahren gemeinsam schmunzeln werden. Ohne dich wäre es um ein Vielfaches schwerer gewesen.

An dieser Stelle möchte ich auch **Thomas Hertweck** erwähnen. Du bist ein besonderer Mensch und ich danke dir für so Vieles; insbesondere jedoch für die Male, in denen du mir bewusst gemacht hast, dass Aufgeben keine Option ist.

Des Weiteren gilt mein großer Dank natürlich meinen Kollegen aus der Arbeitsgruppe der Angewandten Geophysik am Geophysikalischen Institut in Karlsruhe. Trotz oder gerade aufgrund der thematischen Vielfalt unter den einzelnen Kollegen wurden aktuelle Fragestellungen nicht nur bereitwillig diskutiert, sondern auch diversifiziert betrachtet. Darüber hinaus kam der Spaß in den Mittagspausen und während des einen oder anderen Flurplauschs nie zu kurz, sodass auch in den auftretenden Motivationslöchern immer wieder Land in Sicht war. Ohne euch – **Lisa, Martin, Simone, Sven, Anja** und **André** – sowie den tollen Diplomanden, Master- und Bachelorstudenten wäre es sicherlich viel schwerer gewesen, den Promotionsalltag zu überstehen. Dieser Dank geht selbstverständlich auch an euch – **Stefan, Anna** und **Jürgen** – auch wenn ihr seit Kurzem oder Längerem nicht mehr am GPI seid. Und auch **Jörn** soll an dieser Stelle nicht vergessen werden. Formal gehörst du zwar zu einer anderen Arbeitsgruppe; wir hatten dich dennoch immer gerne in unseren Reihen und ich konnte oft von deinen Ratschlägen profitieren.

Ein ebenso herzlicher und aufrichtiger Dank gilt **Thomas Forbriger**. Dein Enthusiasmus und deine Begeisterungsfähigkeit für wissenschaftliche Fragestellungen aller Art haben mich immer fasziniert und motiviert. Dass du dir für mich Zeit genommen hast, so trivial meine Anliegen manchmal auch gewesen sein mögen, war mir immer eine große Hilfe, zumal ich weiß, wie beschäftigt du bist.

Gleichermaßen danke ich **Claudia Payne**. Dass du dich immer kompetent um alle Formalitäten gekümmert hast und ein Auge auf alle Schäfchen deiner Herde hattest, war eine große Hilfe.

Martin Pontius danke ich für das Rechnen der FD-Ergebnisse und so manch lustige Diskussion.

Petra Knopf möchte ich für die gute IT-Betreuung danken. Du hast dich jederzeit zuverlässig und kompetent meinen Fragen und Problemen angenommen. Basierend auf dem Wissen, dass du im Hintergrund alles tust, um einen reibungslosen Ablauf zu gewährleisten, war es mir auch unter Zeitdruck möglich, zuversichtlich und daher gewissermaßen ‘entspannt’ zu arbeiten. Ein Dankeschön geht natürlich auch an alle anderen aktuellen und ehemaligen **Mitarbeiter des GPI**, die mich in vielfältiger Hinsicht in den letzten Jahren unterstützt haben.

Und dann sind da noch die unzähligen wunderbaren Menschen, die mich außerhalb des GPI in den letzten vier Jahren begleitet haben. Leider kann ich hier nicht alle beim Namen nennen. Das würde den Rahmen dieser Danksagung sicherlich sprengen. Bei einigen wenigen möchte ich dennoch nicht darauf verzichten. **Noah, Heiko, Wolle, Sarah, Aaron, Axel, Richie, Franz, Micha, Peter** und **Sebastian**: Ihr seid ganz außergewöhnlich wunderbare Menschen. Danke, dass ihr die Auffassung teilt, dass alles möglich ist.

Nicht zuletzt möchte ich ganz herzlich meinen **Eltern** und **Großeltern** für ihre permanente Unterstützung während meines Studiums und der Promotion danken. Euer bedingungsloser Glaube an mich ist die Basis dessen, was ich bisher erreicht habe. Ich danke euch dafür, dass ihr mir gezeigt habt, dass man alles schaffen kann, wenn man nur fleißig und beharrlich genug ist und stets bereit ist, sein Bestes zu geben.